

High Temperature Mechanical Properties of Cast as well as Powder Metallurgical Manufactured Metallic Foams

Von der Fakultät für Georessourcen und Materialtechnik
der Rheinisch- Westfälischen Technischen Hochschule Aachen

Zur Erlangung des akademischen Grades eines

Doktors der Ingenieurwissenschaften

genehmigte Dissertation

vorgelegt von M. Sc.

Mohamed Shehata Mohamed Abbas Aly

aus El-Giza / Ägypten

Berichter: Univ.-Prof. Dr.-Ing. Wolfgang Bleck

Univ.-Prof. Dr. rer. nat. Dr.-Ing. e.h. Winfried Dahl

Tag der mündlichen Prüfung: 03.11. 2004

Diese Dissertation ist auf den Internetseiten der Hochschulbibliothek online verfügbar

Acknowledgement

The content of this Dissertation was carried out during my work at the Department of Ferrous Metallurgy (IEHK) RWTH Aachen University, as a scholarship holder supported by the Ministry of Higher Education and Scientific Research in Egypt. I gratefully acknowledge the Egyptian government for supporting me during my study in Germany.

I would like to express my appreciation and gratitude to my supervisor Prof. Dr.-Ing. W. Bleck for the scientific guidance and his interest in my work.

I also thank Prof. Dr.-Ing. e.h. W. Dahl for taking over the co-referee.

The help of the academic director of the institute Dr.-Ing. G. Heßling as well as the plant engineer Dipl.-Ing. G. Leisten in solving all the problems related to my work is gratefully acknowledged. I also appreciate the helpful technical advice of Dr. P.-F. Scholz.

I appreciate the efforts of both of Mr. K. Hermann and Mr. H. Tschammer for their contributions in carrying out the high temperature compression tests.

I thank all my colleagues at IEHK, especially my colleagues at the office, Dipl.-Ing. Patrick Larour and M.Sc. Malek Naderi, for the comfortable working atmosphere.

A large part of this work was accomplished in many weekends and via working at the institute until late hours, so a special acknowledgement to my patient, lovely wife who has enabled me via managing a good environment to finish the Master as well as Doctorate at the RWTH Aachen University. My lovely daughters Nour and Habiba are acknowledged as well.

At least but not last, I deeply express my thanks to my lovely mother. Without her preying, I would not be able to accomplish this work. I thank her for all, what she has made for us and may ALLAH reward her in the paradise. I do not forget also to thank my brothers, Mostafa (Faculty of Medicine, Cairo Uni.), Maged (Faculty of Low, Menoufia Uni.) and my sister Mayada (secondary school) for taking care with my mother during my staying abroad.

Aachen, in November 2004

Ramadan 1425 n. H.

Mohamed Shehata Aly

Dedicated to the memory of my

father and grandparents

1	INTRODUCTION.....	4
2	METAL FOAMS.....	7
2.1	INTRODUCTION	7
2.2	PRODUCTION METHODS OF METALLIC FOAMS	7
2.2.1	<i>Casting</i>	8
2.2.1.1	Foaming in Metals.....	8
2.2.1.2	Casting Metal around Granules.....	9
2.2.1.3	Investment Casting	10
2.2.2	<i>Coating</i>	11
2.2.2.1	Chemical – electrochemical Plating	11
2.2.2.2	Physical Vapour Deposition (PVD).....	11
2.2.3	<i>Powder Metallurgy</i>	12
2.2.3.1	SRFS-Process	12
2.2.3.2	Loose Powder Sintering	14
2.2.3.3	Fibre Metallurgy.....	14
3	DEFORMATION OF METALLIC FOAMS	16
3.1	COMPRESSIVE DEFORMATION OF METALLIC FOAMS	16
3.1.1	<i>Linear Elastic Regime</i>	18
3.1.2	<i>Plateau (Collapse) Regime</i>	23
3.1.3	<i>Densification Regime</i>	27
3.2	CREEP DEFORMATION OF METALLIC FOAMS	29
4	HIGH TEMPERATURE OXIDATION	33
4.1	FUNDAMENTALS OF OXIDATION	33
4.2	FORMATION AND GROWTH OF OXIDE SCALES	35
4.3	HIGH TEMPERATURE OXIDATION OF IRON	38
5	EXPERIMENTAL WORK.....	41
5.1	TESTED MATERIALS	41
5.1.1	<i>Alporas-Foams</i>	41
5.1.2	<i>Distaloy and Astaloy Foams</i>	42
5.2	DENSITY MEASUREMENT.....	47
5.3	TESTING MACHINES.....	47
5.3.1	<i>Compressive Testing Machine</i>	47
5.3.2	<i>Schenck Equipment</i>	48
5.3.3	<i>Creep Testing Machine</i>	49
5.3.4	<i>Differential Thermal Analysis</i>	50
5.4	FOLLOW-UP EXAMINATION.....	51
5.4.1	<i>Metallographic Characterisation</i>	51

Contents

5.4.2	<i>SEM Examination</i>	52
5.4.3	<i>Electron Probe Microanalysis</i>	52
6	RESULTS & DISCUSSION	53
6.1	DENSITY MEASUREMENT	53
6.2	COMPRESSION TEST OF METALLIC FOAMS	53
6.2.1	<i>Compression Test in Normal Atmosphere</i>	53
6.2.1.1	Quasi-static Compression Test of Alporas Foams	53
6.2.1.1.1	Effect of Density	54
6.2.1.1.2	Effect of Temperature	57
6.2.1.1.3	Effect of Strain Rate on the Mechanical Properties of Alporas Foams	59
6.2.1.1.4	Microstructural Examination of Alporas Foams	60
6.2.1.1.5	SEM Characterisation of Alporas Foams	65
6.2.1.2	Quasi-static Compression Test of the Distaloy Foams	65
6.2.1.2.1	Determination of the Compression Strength of the Green Distaloy Foams	65
6.2.1.2.2	Effect of Density	67
6.2.1.2.3	Effect of Temperature	68
6.2.1.2.4	Metallographic Examination	70
6.2.1.2.5	SEM Characterisation of Distaloy Foams	76
6.2.1.3	Quasi-static Compression Test of the Astaloy Foams	77
6.2.1.3.1	Determination of the Compression strength of the Green Astaloy Foams	77
6.2.1.3.2	Effect of Density	78
6.2.1.3.3	Effect of Temperature	79
6.2.1.3.4	Metallographic Examination	81
6.2.1.3.5	SEM characterisation of Astaloy Foams	86
6.2.2	<i>Compression Test in Inert Atmosphere</i>	87
6.2.2.1	Quasi-static Compression Test of Distaloy Foams	87
6.2.2.1.1	Effect of Density	87
6.2.2.1.2	Effect of Temperature	93
6.2.2.1.3	Metallographic Examination	95
6.2.2.1.4	SEM Characterisation of the Distaloy Foams	99
6.2.2.2	Quasi-static Compression Test of the Astaloy Foams	99
6.2.2.2.1	Effect of Density	99
6.2.2.2.2	Effect of Temperature	105
6.2.2.2.3	Metallographic Examination	107
6.2.2.2.4	SEM Characterisation of the Astaloy Foams	110
6.2.3	<i>Comparison between in air- in Ar Compressive Tests</i>	112
6.2.3.1	Distaloy Foams	112
6.2.3.2	Astaloy Foams	113
6.2.4	<i>Size Effect on the Foams' Mechanical Properties</i>	118
6.2.5	<i>Strain Rate Dependence of the Foam's Mechanical Properties</i>	120
6.2.6	<i>DTA Measurement</i>	121
6.2.7	<i>X-ray Spectrometer</i>	122

Contents

6.2.8	<i>Line Scan Analysis</i>	123
6.3	CREEP TEST	126
6.3.1	<i>Creep of Alporas</i>	126
6.3.1.1	Effect of Density	126
6.3.1.2	Effect of Stress	129
6.3.1.3	Effect of Temperature	130
6.3.1.4	Microstructural Examination.....	133
7	SUMMARY & OUTLOOK	135
8	KURZFASSUNG & ABSTRACT	139
9	NOMENCLATURE	140
10	BIBLIOGRAPHY	143

1 Introduction

When nature builds large load-bearing structures, she generally uses cellular materials. Typical examples include wood, bones, coral and cork. There must be good reasons for this [Ashby].

In the past, when a large dense metal contained any kind of pores, it was considered “defect” and therefore thought unsuitable for engineering purposes. Consequently efforts were made by engineers to produce a fully dense metal, free from any kind of pores [SIM02]. In recent years a great importance has been attached a new class of engineering material, known as “Porous metals or metal foams” as a result to their unique mechanical and physical properties. Owing to their pores, metal foams are classified into open cell and closed cell metal foams [YU98]. Banhart [BAN02] has summarised the potential applications of metallic foams as a function of their porosity, as shown in **Fig. 1-1**.

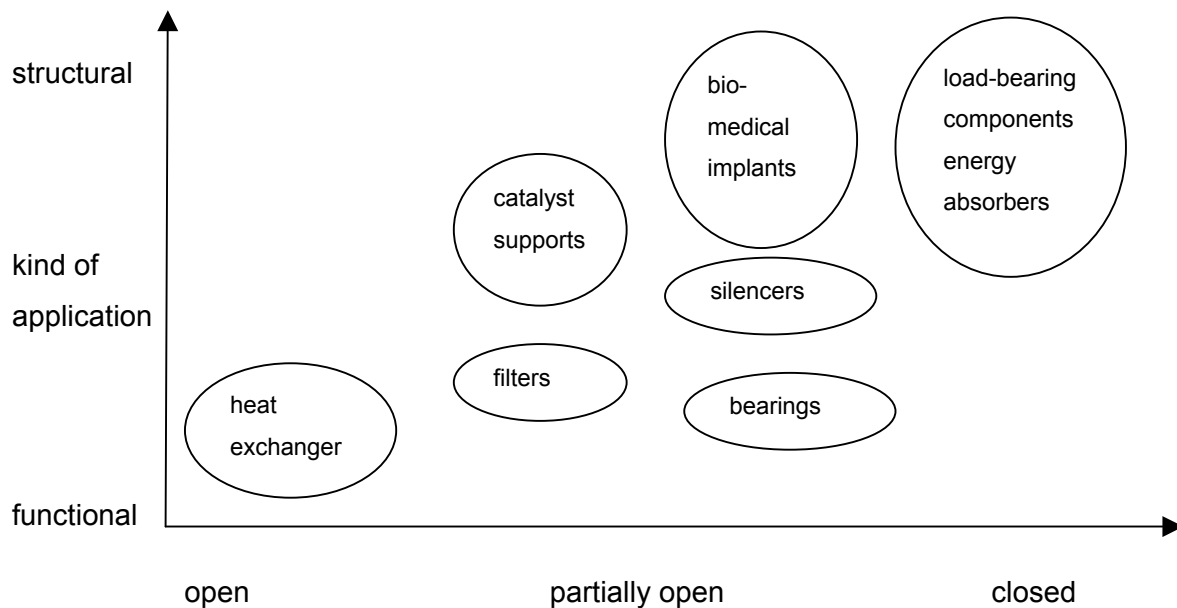


Fig. 1-1 Potential applications of metallic foams as a function of porosity [BAN02].

Closed cell foams are being used in light-weight constructions due to their high stiffness and low density [RIN71, OLU01]. Their capacity to undergo a large deformation at almost constant stress makes them ideal energy absorbers in the automobile industry and packaging applications [KES03, HAL00, KAN00]. Other potential applications of closed cell metal foams include acoustic damping [HAR99].

Open cell foams however offer a wide range of applications, e.g. as a heat exchanger [KUL73]. The high surface area and large volume of interconnected porosity of open cell

foams make them attractive for use as heat sinks in electronic devices [KES03], and in transpiration cooling [BAN02]. The interconnected porosity is of special significance for parts like filters, diaphragms, bearings [THÜ93] in addition they can also be used as membranes as well as in biomedical applications [RAU02]. Batteries, as in the case of nickel foams and jewellery, as in the case of gold and silver foams [YU98] are all potential uses of open cell foams.

Moreover metallic foams have a potential for use in applications where high temperatures are involved, e.g. the transpiration cooled rocket nozzles, a cooling system in the burning chamber of gas and steam turbines and as heat shielding for aircraft exhaust.

To date, research on the mechanical behaviour of metal foams has mainly been focused on the room-temperature behaviour. This is due to that foams are mostly used at room temperatures. However, in order to expand their applicability in the near future at high temperatures, information is required regarding their high temperature mechanical properties. At the present time, sparse information has been reported concerning the high temperature mechanical properties of aluminium foams [AND99a, AND99b, AND00].

The driving force of this research work is to assess the feasibility of the applicability of such metallic foams at high temperature applications e.g. in the transpiration cooling of the burning chamber in gas turbines or as a core for hollow engine turbine blades, thus reducing the overall weight and increasing the fuel performance. Other possible high temperature applications are as thermal and sound insulators around engine burners. For this purpose, three different types of metallic foams have been quasi-statically compressed at high temperatures in different testing atmospheres (air and/or argon). They are:

- 1- AlCaTi (trade-name ALPORAS) foams, delivered by Shinko-wire Company in Japan. This type of foams has been manufactured by the casting technique.
- 2- Distaloy foams based on low-alloy (Fe-Cu-Ni) steel powder.
- 3- Astaloy foams based on low-alloy (Fe-Mo) steel powder delivered by the company Höganäs.

Both (2, 3) have been produced by the powder metallurgical route at the Department of Ferrous Metallurgy (IEHK, RWTH Aachen). A set of parameters, e.g. foam's density, test temperature, strain rate, has been varied in order to examine the effect of each parameter on the foam response upon testing.

When temperature goes above $0.3 \cdot T_m$ (T_m is the melting point in K), a time-dependant creep

deformation becomes very important, especially for the foams which carry loads at elevated temperatures for prolonged times. The effect of the foam's density, stress as well as test temperature on the creep behaviour of AlCaTi (ALPORAS) foams was examined. By means of a conventionally light microscope, the changes within the cell-wall microstructure have been investigated. Fracture surfaces of the tested metallic foams have been examined by a scanning electron microscope.

The content of this thesis starts with giving a general review on the different production methods of metallic foams which have been used so far, followed by a detailed chapter concerning the behaviour of metallic foams under compressive deformation only at room temperature. This is due to the lack of information dealing with this topic at high temperatures. Time-dependent creep deformation of metallic foams was introduced with the help of the present literature. High temperature oxidation of iron and some properties of the wustite, Hematite and Magnetite scales are also presented.

The experimental work deals with the preparation and production of the tested materials, the testing machines, and the different instruments which have been used to examine the microstructure of the foams, through which the attained results were analysed and interpreted.

2 Metal Foams

2.1 Introduction

Before starting to talk about this new class of engineering materials, the meaning of a foam has to be firstly introduced. "Foaming" means releasing gas in a liquid, ensuring that the gas bubbles do not escape and finally stabilising the liquid foam by cooling [DUA02].

Solid metal foams are known to have many interesting combinations of physical and mechanical properties such as relative high stiffness, low specific weight and high gas permeability combined with high strength. The term (metallic foams) must be distinguished from others such as cellular metals, porous metals and metal sponges as follows:

Cellular metals refer to a metallic body with any kind of gaseous voids dispersed in it. They are characterised by their low relative densities (< 0.3) [DEG02], whereas porous metals (relative density > 0.3) is a term restricted to special types of voids, which are round and isolated from each other. Metal foams are a special class of cellular metals, originating from liquid metal foam. Metal sponges refer to a special morphology of cellular metal with usually interconnected voids [BAN00].

2.2 Production Methods of Metallic Foams

There are many methods available to produce metallic foams [GAR67]. The first attempts on foaming techniques in the past have pointed to the use of a gas as a blowing agent. Another method produced an interconnected cellular structure by using granules, which can be incorporated into the melt or introduced into a casting mould. **Fig. 2-1** shows a summary of the methods used in the production of metallic foams.

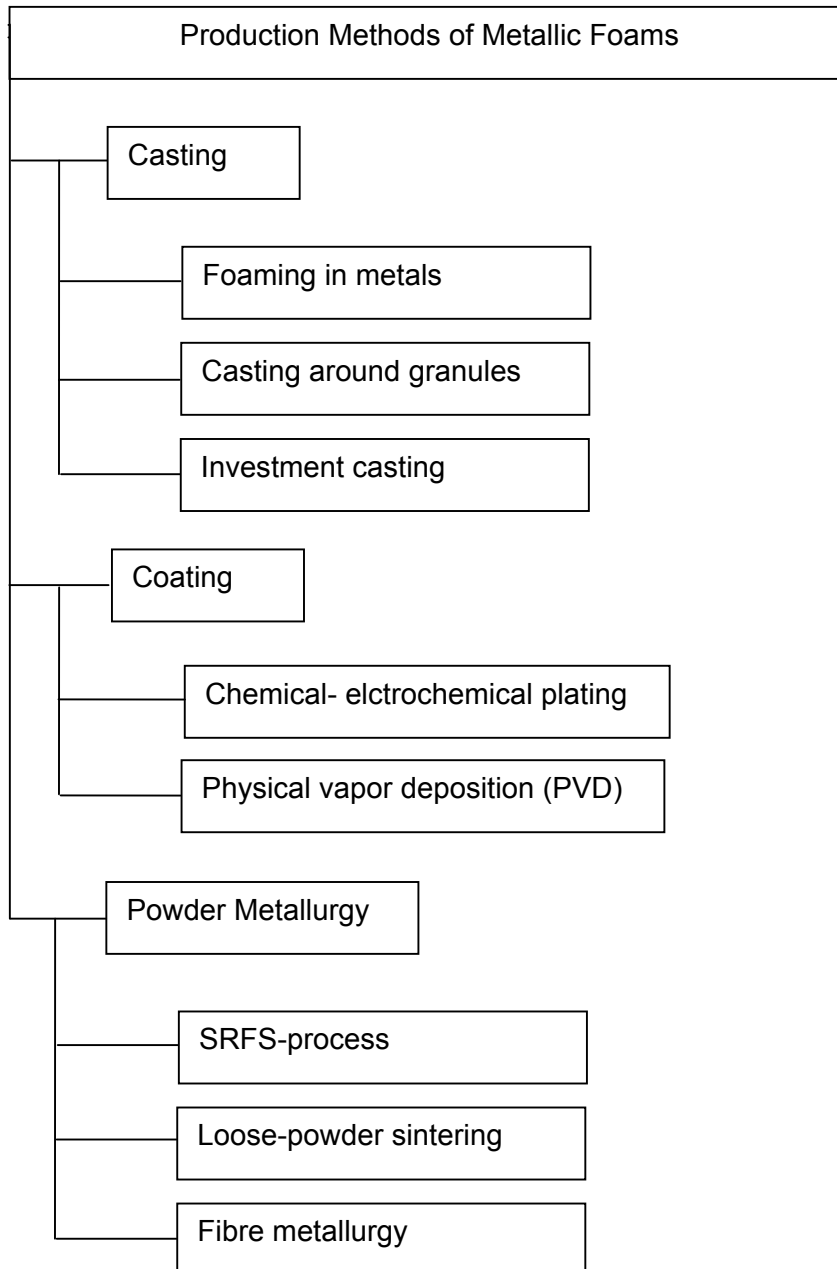


Fig. 2-1 Methods of producing metallic foams [DAV83, HAG99].

2.2.1 Casting

2.2.1.1 Foaming in Metals

According to this process, foamed metals are produced by adding a blowing agent to a molten metal and heating the mixture to decompose the blowing agent to evolve gas. The gas expands causing the molten metal to foam. After foaming the resultant body is cooled to form a foamed solid. Usually the blowing agent is a metal hydride such as TiH_2 or ZrH_2 . As an example for this technique is the production of Al-foams (ALPORAS) using the process shown in **Fig. 2-2**.

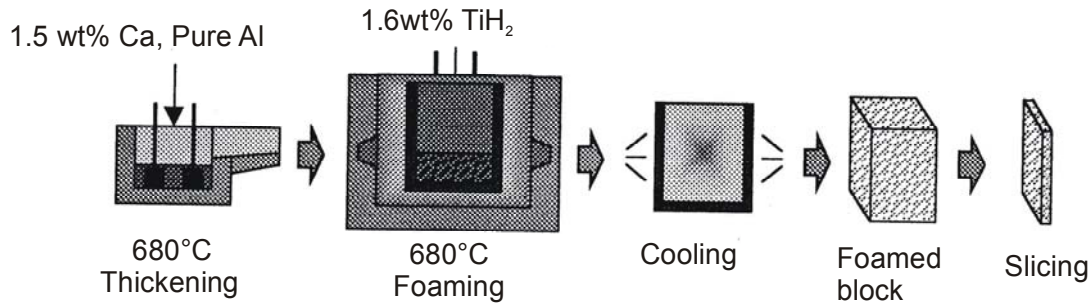


Fig. 2-2 ALPORAS manufacturing process [MIY99].

Another process which is based on foaming in a metal is the ALCAN process, illustrated in **Fig. 2-3**. This process, which was developed by Alcan and Norsk Hydro in the late 1980's, is used for the production of Al-foams.

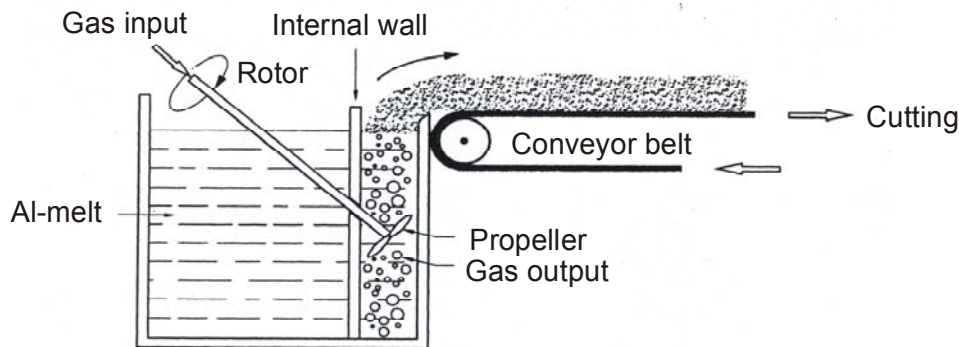


Fig. 2-3 ALCAN process [ÅSH99]

In this process, a gas is dispersed into small bubbles in an aluminium melt by a rotor impeller. The walls of the bubbles created are stabilised by refractory particles, avoiding coalescence between them. The gas bubbles rise to the surface where they accumulate. The accumulated foam on the melt surface is then transferred to a conveyor belt, where it solidifies and cools [SAN92].

2.2.1.2 Casting Metal around Granules

This method produces an interconnected cellular structure or sponge metal by casting metal around granules introduced into the casting mould, as shown in **Fig.2-4**. These granules can be soluble (but heat-resistant), such as sodium chloride, which is leached out to leave a porous metal [KUC66]. The principle of this process was developed by ACCESS e.v. in Aachen. In this process the following three steps are included:

- 1- Preparation of space-holder filler, by using either inorganic or organic granules
- 2- Infiltration of the filler with a metal
- 3- Removal of filler granules **[GRO00]**.

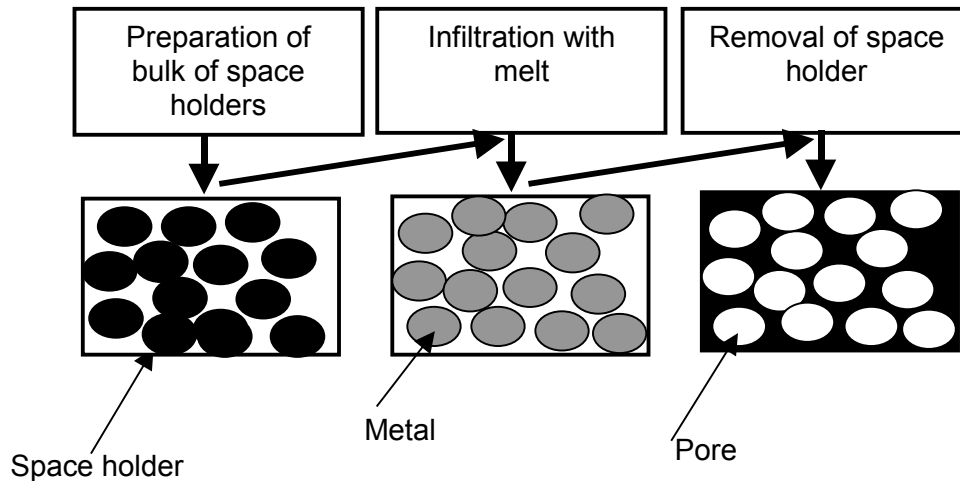


Fig. 2-4 Casting around granules **[BAN99]**.

2.2.1.3 Investment Casting

Investment casting technique has also been used to produce metallic foams **[JPN80]**. In this process, voids of spongy foamed plastic are filled with a fluid refractory material which is then hardened. Following this the integral plastic refractory material is heated so as to vaporise the plastic component and a mould having sponge lattice pores is produced. Molten metal is poured into this mould and allowed to cool and solidify. The refractory is then removed and metallic foams having the same sponge form as the original spongy plastic are obtained. This process was applied by the Foundry Department, Aachen University, in order to produce near-net shape components based on cellular metal materials.

The principles of this process are depicted in **Fig. 2-5**. A pattern of desired shape with desired dimensions is produced and embedded into a mould. Afterwards the metal is poured to fill the interstices in the mould. After cooling, the pattern is removed and a semi-product is obtained **[HIN99]**.

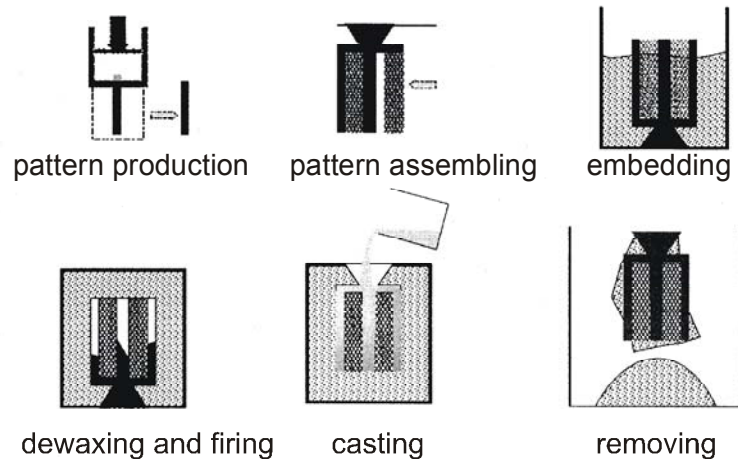


Fig. 2-5 A schematic drawing of the investment casting process for the production of porous materials [HIN99].

2.2.2 Coating

2.2.2.1 Chemical – electrochemical Plating

In this process, three stages are involved, rigidization, electroless plating and electroplating [COH68]. Rigidization is used to coat the polyurethane foam with a thin epoxy layer to provide the necessary rigidity. After rigidization, the urethane foam surface is made slightly conductive by electroless deposition of a thin film. As preparation for this the surface must be treated with a strong oxidising acidic solution (such as a chromic/sulphuric/phosphoric acid mixture) which converts the surface to the water-respective condition and selectively etches it to produce micro-roughening.

This provides a mechanical key to improve the adhesion of the subsequently-deposited metal layers. The surface is then catalysed with palladium from a palladium chloride solution. After that a continuous deposit can be obtained by immersion in an electroless plating solution [CAR77, GAB72].

2.2.2.2 Physical Vapour Deposition (PVD)

According to this method, a metal body containing atoms of entrapped inert gas evenly distributed throughout is prepared by sputtering the metal under a partial pressure of inert gas, onto a substrate. Then the metal body obtained is heated to a temperature above the melting point of the metal for a period of a time sufficient to permit the entrapped gas to expand and form individual cells. After cooling metal foam having a closed cellular structure is obtained [SOS48, SHA94].

2.2.3 Powder Metallurgy

2.2.3.1 SRFS-Process

The Slip Reaction Foam Sintering (SRFS) process is one of the recently developed methods based on the powder metallurgical route for the production of the metallic foams [SCH97]. This process, which has been developed at the Department of Ferrous Metallurgy, Aachen University, enables the production of metallic foams at room temperature with a little instrumental outlay in addition to its low environmental impact.

In this process, as shown in **Fig. 2-6**, a fine metallic powder is mixed with a dispersant, which is laminate silicate in the form of a powder having a chemical formula $[\text{Mg}_3(\text{OH})_4(\text{Si}_2\text{O}_5)]$. This dispersant stabilises the slip during the process. Concentrated ortho-phosphoric acid (H_3PO_4) which acts as a foaming agent is then mixed with the mixture. Water in different amounts is then poured. After mixing, the powder forms a slip. The foams are initiated as the reaction metal-acid is setting H_2 bubbles. Additionally, iron phosphate forms, which acts as a strong binder [CHV75, BAR68]. This binder freezes the bubbles in the slip (since it raises the viscosity of the slurry, thereby preventing the bubbles from escaping). After drying, the green samples are cut in order to remove the foams' skins. The green samples are then sintered under a reduction atmosphere, using a tube-type furnace. The resulting high strength values may be attributed to the formation of metallic bonds formed during the sintering process [MOH01].

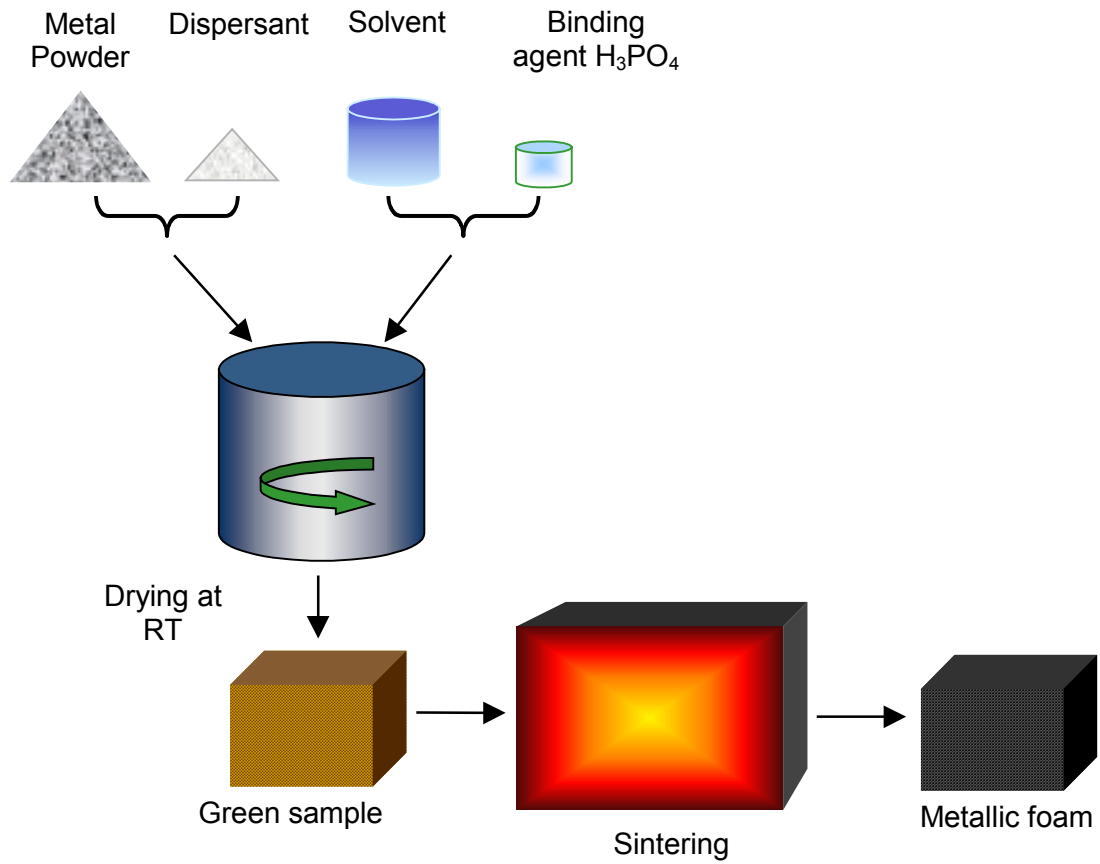


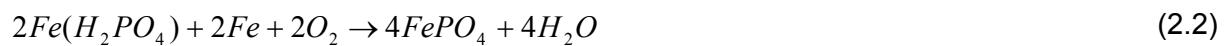
Fig. 2-6 SRFS-Process [ANG03].

The reactions which take place during the SRFS- process can be classified into [MOH03]:

1- Foaming of a slip



2- Freezing of pores (Oxide-free powder):

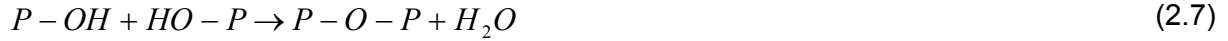


3- Freezing of pores (containing oxide powder):





4- Condensation of Fe-phosphate



Some general rules must be taken into consideration during the sintering process and can be stated as follows:

- a) A higher reduction temperature and a longer time provide: larger particle size, lower specific surface, and lower residual oxygen content.
- b) A lower reduction temperature and a shorter time provide: smaller particle size, higher specific surface, and higher residual oxygen content.
- c) A high flow rate with low dew-point results in a high reduction rate, low residual oxygen content and no, or very little, re-oxidation during the cooling period. A low flow rate with a high dew-point would produce the opposite results and would therefore be generally impracticable [THÜ93].

2.2.3.2 Loose Powder Sintering

In this process, contacts between powder particles are established and grow due to the surface tension forces. This occurs whilst the powder particles are heated in contact to each other [LEN80, FED79]. Porous metallic materials, e.g. bronze filters, porous nickel membranes used as electrodes for alkaline storage batteries and fuel cell can be manufactured by using this process. The porosities of the materials produced by this technique vary from 40 to 60 vol. %. In order to achieve high degrees of porosity, a spacing agent can be added to the charge. This spacing agent decomposes or evaporates during the sintering process or is removed by sublimation or dissolution [FED79].

2.2.3.3 Fibre Metallurgy

Instead of metal powders, metal fibres can be utilised in producing porous materials [FED79]. This process has the following advantages:

- (i) Porosity can be controlled within very wide limits
- (ii) High strength and ductility can be obtained
- (iii) High permeability.

Fibre metallurgy involves the preparation of metal fibres of ferrous or non-ferrous alloys by machining, drawing and/or other techniques. These are then processed into felts by slip casting or mechanical felting followed by sintering to develop the required strength and porosity [YAR66].

3 Deformation of Metallic Foams

Since most applications of metallic foams are concentrated in the field of energy absorption (impacts, packaging and crash protection) [FOR89], this may explain why the deformation behaviour of metallic foams under compressive testing is a recurrent theme studied by many researchers. In the next chapter, the compressive behaviour of metallic foams will be discussed further in some detail.

3.1 Compressive Deformation of Metallic Foams

Quasi-static, uniaxial compression tests are being used for characterisation of metal foams. This enables us to describe the mechanical stability of metal foams. When metallic foams are subjected to a uniaxial or hydrostatic compression test, a typical stress-strain curve, as shown in **Fig. 3-1**, is obtained.

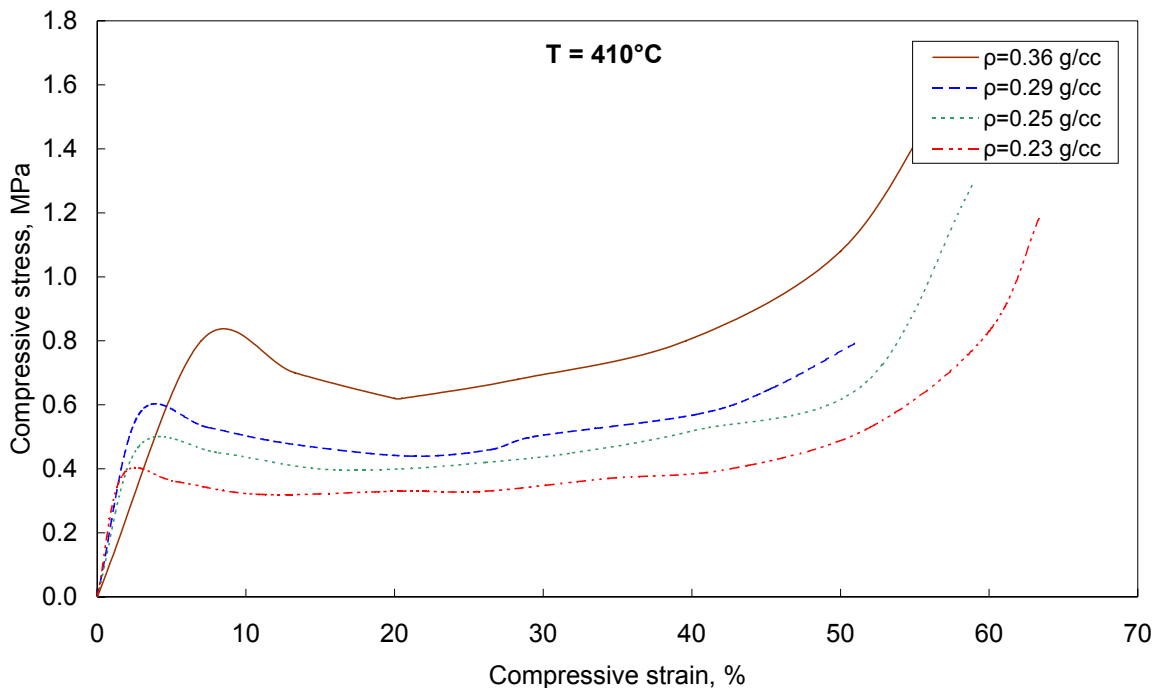


Fig. 3-1 Stress-strain curves for Al foams having four different densities compressed at 410°C [ALY03].

As **Fig. 3-1** shows, the stress-strain curve consists of three regions, linear elastic regime which ends with a maximum compression strength value, followed by a long plateau stress in which the deformation occurs at almost constant stress [GIB97]. The collapse of cell-walls and struts of cellular structure accounts for this long plateau. The deformed cells build-up deformation bands in a direction perpendicular to the direction of deformation [GRO03]. The

compression strength in case of brittle materials is defined as the first maximum value of stress in the compressive stress-strain curve, whereas in case of ductile materials, the compression strength of the material lies at that point, at which the slope of the stress-strain curve for the first time equals zero. However, there are other ductile materials showing a direct transfer to plateau regime without showing any maximum. In this case the point of intersection of the tangent drawn to the linear elastic regime and that drawn to plateau is defined as the compressive strength of the material [GRO03]. The stress-strain curve ends with a region where the stress increases rapidly. This region is known as the densification regime [GIB97]

Fig. 3-2 shows the deformation processes of metallic foams during compression. At the beginning of the compression test, zones of large pores begin to deform. With increasing the compression, new pores which lie in the already deformed zones, begin to deform [HAG99]. At the end of the compressive deformation, deformation bands with a thickness equal to a pore diameter are formed within the fractured zones [BAR98]

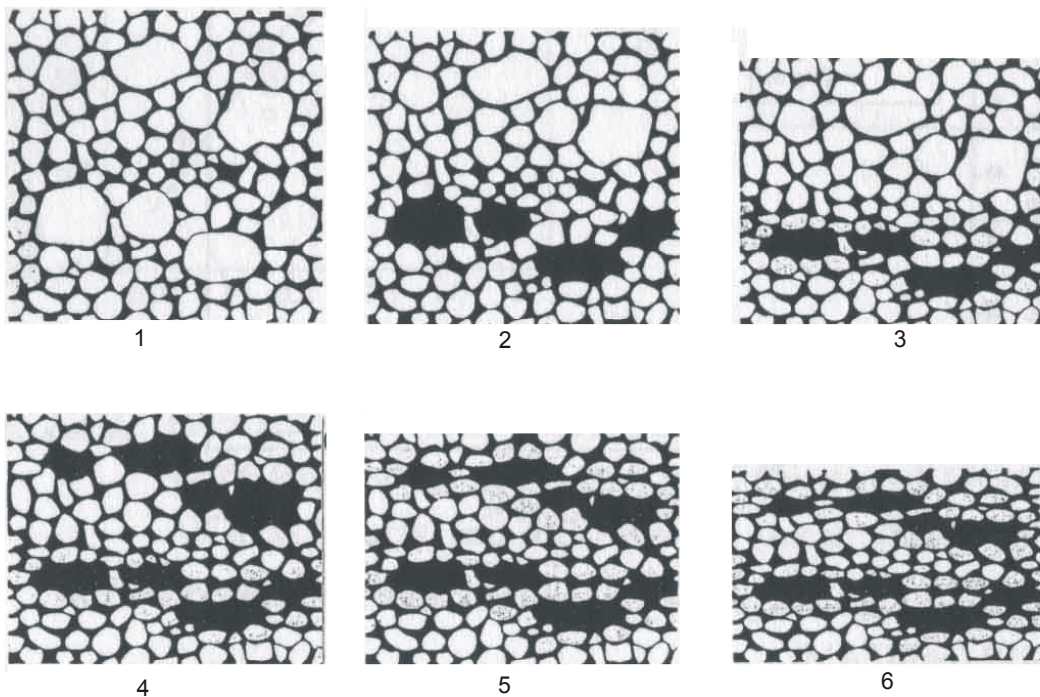


Fig 3-2 Deformation behaviour of metallic foams under compressive test (1) initial state, (2-6) with increasing compression [HUS97, HAG99].

Gibson and Ashby have studied each region of the three regions of the stress-strain curve in detail. Each region has a certain feature, e.g. in the linear elastic regime, the bending of the cell walls is the characteristic mechanism for the deformation of metallic foams, whereas the

plateau regime is associated by collapse of the cell walls. In elastomeric foams, e.g. rubber the collapse of foams occurs due to the elastic buckling. In case of metals, the collapse is caused due to the formation of plastic hinges. Ceramics which are known as brittle materials, collapse by brittle crushing. Following the approach of Gibson and Ashby, the three regions of the obtained stress-strain curves will be discussed here in more detail.

3.1.1 Linear Elastic Regime

As mentioned before there are two different types of metallic foams, as shown in **Fig. 3-3**. They are (a) closed-cell (connected), in which the faces of the cells are solid and each cell is sealed off from its neighbours, and (b) open-cell (interconnected) metallic foams, in which the cells are connected through open faces.

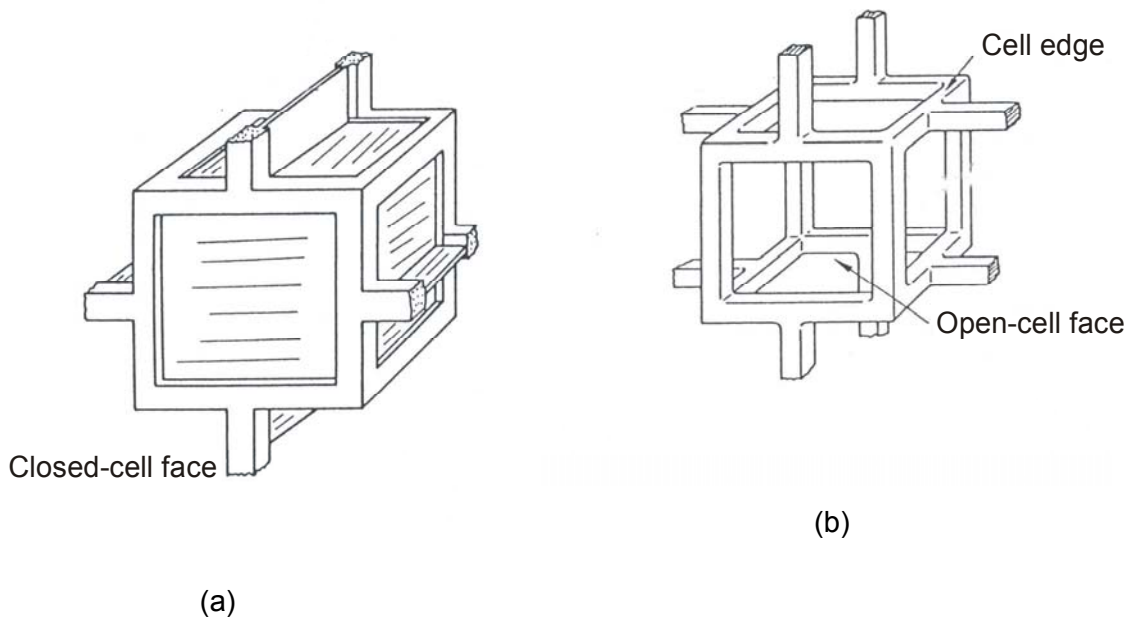


Fig. 3-3 A schematic drawing of a) closed-cell foam and b) open-cell foam [GIB97].

The mechanisms of linear elasticity depends on the porosity of the cell i.e. whether the cell is open or closed. In open-cell foams cell-edge bending is the dominant deformation mechanism, as shown in **Fig. 3-4**. When closed-cell metal foams are subjected to compressive loads greater than the collapse strength, deformation initiates via plastic bending of cell walls and stretching of the cell faces [MAR99].

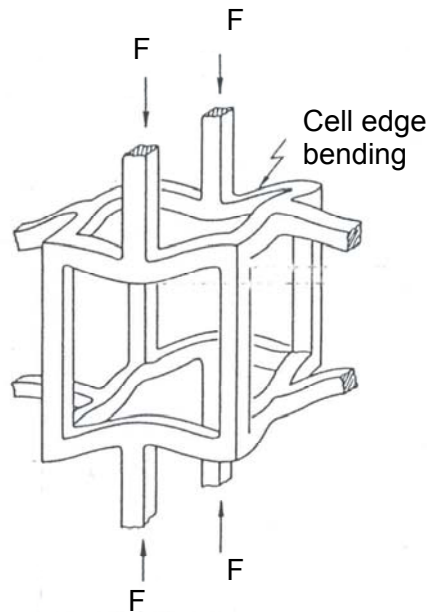


Fig.3-4 Deformation mechanisms in an open cell foam [GIB97].

Since the cell faces of conventional low relative density metallic foams are often curved or corrugated, this gives rise to poor mechanical properties. Curved cell walls result from the pressure differences between cells in the liquid metal foam before solidification. Smaller cells have a higher internal gas pressure than larger cells. The liquid cell face separating two adjacent cells has a curvature which is proportional to the difference in the internal gas pressure of the cells. Air convection within the cells can also cause cell faces to be curved in the direction of gas rise. Corrugations of the cell wall are the result of handling the liquid foam during solidification. Lower density foams with large cells are more susceptible to cell face wrinkling due to the low thickness-to-edge length ratio of their cell faces [SIM98].

Fig. 3-5 summarises the different types of cell imperfections.

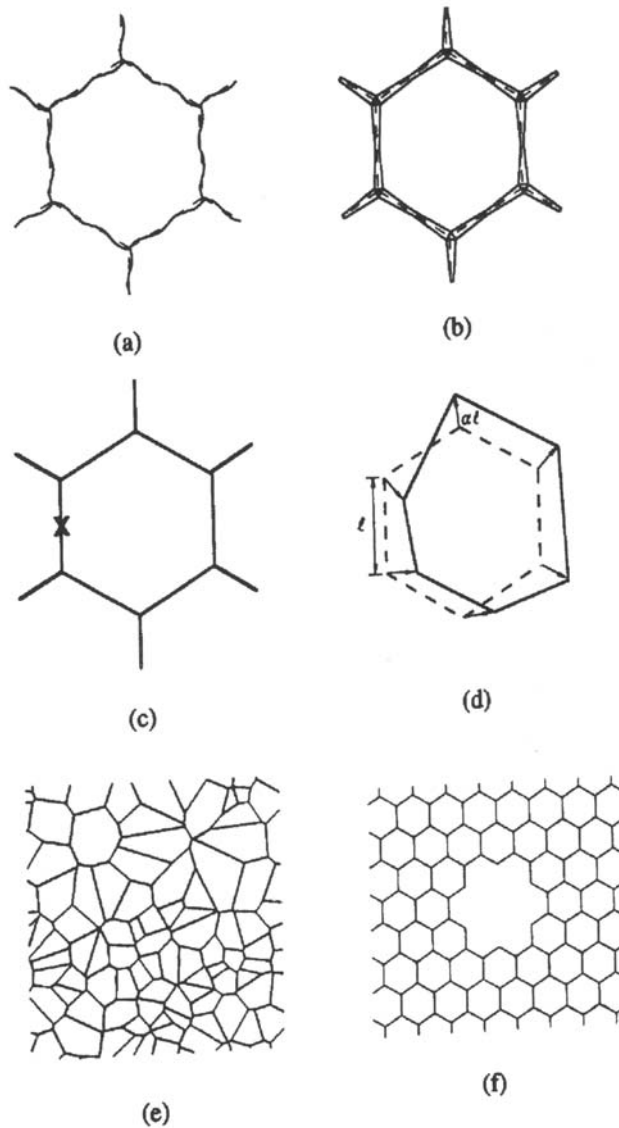


Fig. 3-5 Different types of cell imperfections a) corrugations b) non-uniform wall thickness c) fractured cell walls d) cell-wall misalignment e) Voroni structure and f) missing cells [CHE99].

It was found that face curvature and corrugations can significantly reduce the elastic modulus (which is a measure of the stiffness) and peak stress of metal foams [DAN00]. The effect of such imperfections on mechanical properties of cellular solids was modelled by Grenestedt [GRE98]. It was found that these imperfections have a negative effect on the mechanical performance of cellular solids.

For low density foams ($\rho < 0.03$), strut bending and twisting are the dominant deformation mechanisms [ZHU00]. At low densities, experimental studies indicated that the Young's modulus (E) of cellular solids is related to their density (ρ) through the following relation [GIB97]

$$\frac{E}{E_s} = C \left(\frac{\rho}{\rho_s} \right)^n \quad (3.1)$$

Where E is the Young's modulus in GPa, ρ is the density of the foam in g/cm^3 , E_s and ρ_s are the Young's modulus in GPa and density of the solid material in g/cm^3 , respectively.

If the cell walls are much thinner than the cell edges, the deformation is governed by edge-bending. In this case, E varies quadratically with density ($n= 2$). If cell-wall bending is the mechanism of deformation, Gibson and Ashby have shown that E should vary cubically ($n= 3$) with density. However, the fact that $1 < n < 2$ indicates that cell-wall stretching ($n= 1$) is actually the dominant behaviour **[ROB01]**.

Since the mechanical properties of the cellular solids depend on the geometric structure of the foams (size and shape of the cells) as well as on the properties of the solid material, from which the cell walls are made, it is important to determine the size of unit cell. A mesh sensitivity study performed by Zhu et al. **[ZHU02]** based on changing the number of cells was carried out to determine the number of cells. It was found that the larger the number, the greater the possibility of instability during compression.

Smith **[SMI98]** has examined the compressive deformation mechanisms that occur in both closed cell (Alporas) and open cell (Duocel) Al foams using X-ray tomography (CT) and surface strain mapping to determine the deformation modes and the cell morphologies that control the onset of yielding. It was found that, for Duocel, the deformations were relatively homogeneous whereas Alporas deforms heterogeneously by deformation banding, as shown in **Fig. 3-6**.

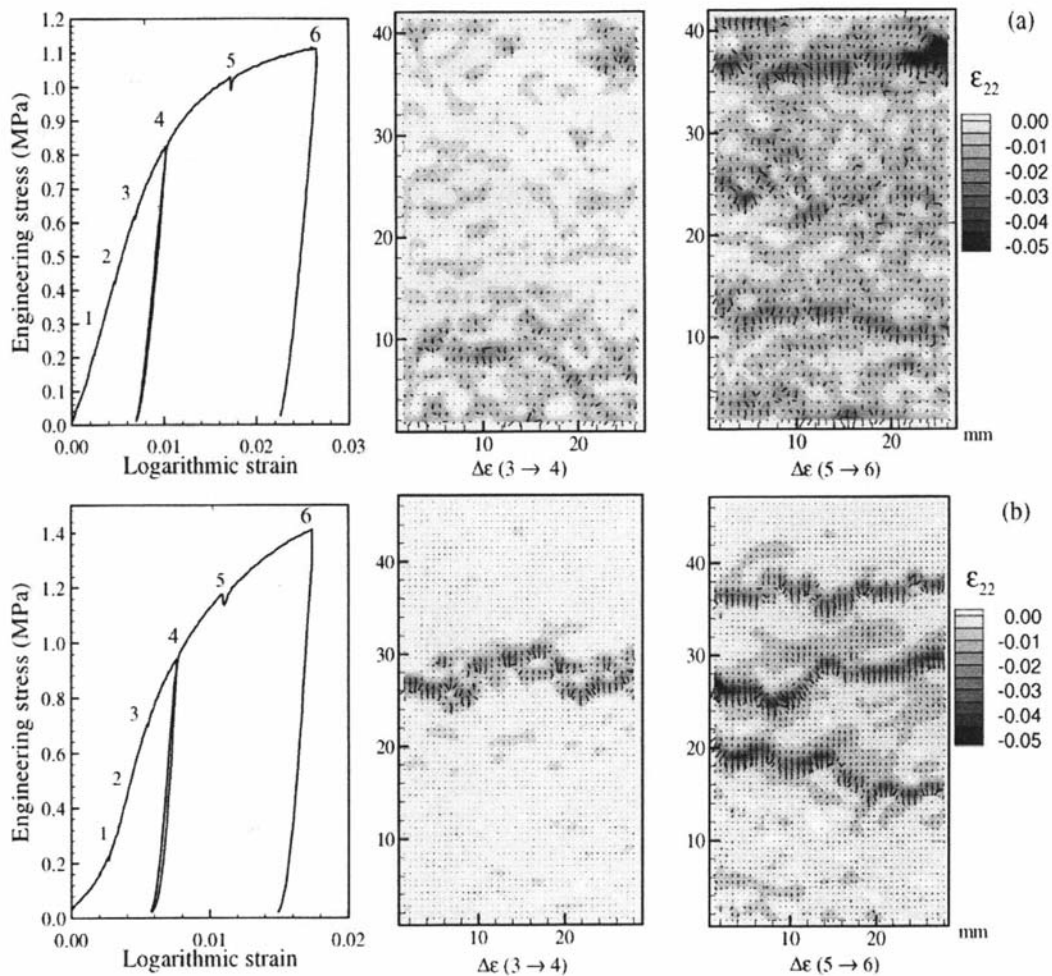


Fig. 3-6 Surface maps of incremental principle strains. Stress-strain curves are also indicated for a) Duocel and b) Alporas materials [SMI98].

In an attempt for characterisation of the 3-D structure and compressive deformation of Alporas foams using X-ray microtomography, McDonald et al. [MCD03] have observed two extreme modes of deformation in the Alporas foams: uniform crushing along a band running perpendicular to the direction of compression and a large distortion or anisotropic buckling of the sample structure. By anisotropic buckling it is meant that the specimen has had a sharp change or kink along its edges.

If the cells of the foams are quite spherical, uniaxial compression actually leads to uniaxial compaction with no lateral spreading-up to large strains. This remains true even for materials with elongated cells as long as the cells are aligned or perpendicular to the compression axis; otherwise the sample will shear and spread in various directions perpendicular to the compression axis. Samples with skin on one of their faces display a different behaviour when the skin is not perpendicular to the compression axis. The presence of a vertical skin

(parallel to the compression axis) reduces the effect of the defects found through the sample and stabilises the structure. In case of heterogeneous cells, the stress needed increases with deformation. In practice such heterogeneities are due to local variations in cell wall thickness, the geometry of the cells, the size of the connecting nodes, and the metallurgical characteristics of the material in the walls or structural features such as the cell size distribution [CHA99]. These non-uniformities may be due to the method of fabrication [FOR99].

3.1.2 Plateau (Collapse) Regime

In compression the stress-strain curve exhibits an extensive plateau stress, wherein localised collapse propagates from one cell band to another [PAU00]. This plateau stress is known as the elastic collapse stress σ_{el}^* . The foam's density determines the plateau stress which is achieved if one of the deformation bands fails [MOS03]. The energy absorption efficiency is a function of the duration of this plateau during compression [PAR00]. The long plateau stress-strain curve arises due to bending of cell walls and stretching of cell faces [PAU00] followed by cell collapse due to buckling and yielding [MOT01]. These mechanisms allow for large energy absorption at constant or slightly increasing stress. Plateau stress is of great importance in selecting foams for packaging and cushioning applications [COC00].

Gibson and Ashby have mentioned that the plateau stress (collapse stress) and post-collapse behaviour depend on whether the foam has open or closed cells. A decrease in energy absorbing efficiency of foams was found with the increase of the porosity [BIN01] whereas an enhancement in the energy absorbing efficiency of foams was obtained as a result for an increase in the aspect ratio of cell-wall thickness against the cell-edge length of the foam [MIY99a]. In open-cell foams like polyurethanes, collapse occurs at almost constant load. In closed-cell foams like polyethylenes, collapse occurs at slightly increasing stress with strain. This is due to the compression of the gas within the cells. Many experiments have proved that most foams behave as if their cells were open because the surface tension concentrates the material into the cell edges during manufacture [ASH83, GIB82].

Gibson et al. have been built a series of equations based on a cubic model of an open-cell cellular material and Euler's equation to describe each region of the stress-strain curve. Some of them are listed below

$$\text{Linear elastic regime} \quad \frac{E}{E_s} = \left(\frac{\rho}{\rho_s} \right)^2 \quad (3.2)$$

$$\text{Plateau regime for plastic foam} \quad \frac{\sigma_{pl}^*}{\sigma_y} = C_1 \left(\frac{\rho}{\rho_s} \right)^{3/2} \quad (3.3)$$

$$\text{Plateau regime for brittle foam} \quad \frac{\sigma_f^*}{\sigma_f} = C_2 \left(\frac{\rho}{\rho_s} \right)^{3/2} \quad (3.4)$$

Where E is the Young's modulus of the foam in GPa, E_s is the Young's modulus of cell wall material in GPa, σ_{pl}^* is the plastic collapse stress of the plastic foam in MPa, σ_y is the yielding strength of cell wall material in MPa, σ_f^* is the fracture strength of cell wall material in MPa, σ is the compressive stress in MPa, σ_f is the modulus of rupture of cell wall material in MPa, ρ, ρ_s are the densities of foam and cell wall material in g/cm^3 , respectively; and C_1, C_2 are constants [GIB97]

In order to measure the energy absorption of metallic foams, two methods are considered. One is the energy per unit volume, which is determined by the area under the stress-strain curve

$$C = \int_0^l \sigma d\varepsilon \quad (3.5)$$

Where σ is the compressive stress, l the limit of strain concerned, and ε is the strain.

The second method is the measurement of the energy absorption efficiency, which is defined by

$$E = \frac{\int_0^l \sigma d\varepsilon}{\sigma_{\max} \cdot l} \quad (3.6)$$

Where the numerator is the real energy absorbed after deformation over the strain l , and the dominator is the ideal energy absorption given by the product of the maximum stress applied (σ_{\max}) and the strain l [HAN98], as shown in **Fig. 3-7**.

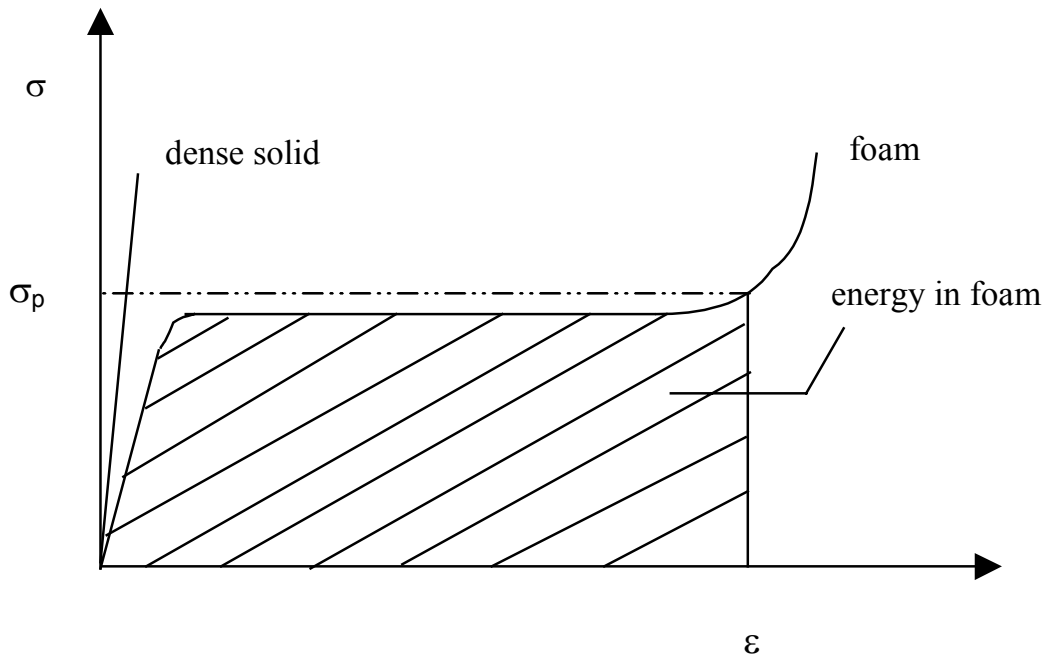


Fig. 3-7 A comparison between a real and an ideal energy absorber after 50% compression test [CHI98].

The efficiency of energy absorbing materials in crash elements is strongly influenced by their stress-strain behaviour under uniaxial compression. Experimental studies of the influence of meso-inhomogeneities of the cell structure on the crash worthiness of aluminium foams have shown that the cell sizes, the cell wall thickness and other micro-geometrical parameters should not vary too much in order to achieve optimum specific energy absorption. Strong meso-inhomogeneities lead to strain localisations and, consequently, to a decrease of the initial plateau stress and to increasing ascents in the plateau regime, both reducing the energy absorption efficiency. Specimens with comparable mean apparent density have the highest initial plateau stress when they do not show significantly varying microstructures, i.e. they are microscopically homogeneous. Metal foams which are used in energy absorbing elements exhibit a weak energy absorbing efficiency if the foam structure shows strong meso-inhomogeneities [GRA99]. For example Alporas foams have an almost constant collapse plateau stress which makes it superior for energy absorption applications. This is due to the homogeneity of their structure [SIM98a].

Mukai et al. [MUK99] have found that there is a strain rate dependence of energy absorption. For example the absorbed energy by Alporas foams under dynamic strain rate of ($2.5 \times 10^3 \text{ s}^{-1}$) is 50% greater than that at the quasi-static strain rate ($1 \times 10^{-3} \text{ s}^{-1}$).

The energy absorbed by the metallic foams depends on the density of the foams as well. Increasing the foam's density will increase the amount of the energy absorbed by the foam

[HAL00], as shown in **Fig. 3-8** and **Fig. 3-9**. In case of the foam with the lowest density ρ_3 a long plateau was achieved and a large amount of absorbed energy (W_3) was obtained. Increasing the foam's density will compensate the obtained short plateau and the same amount of energy can be absorbed, as in case of the foam with the density ρ_1 .

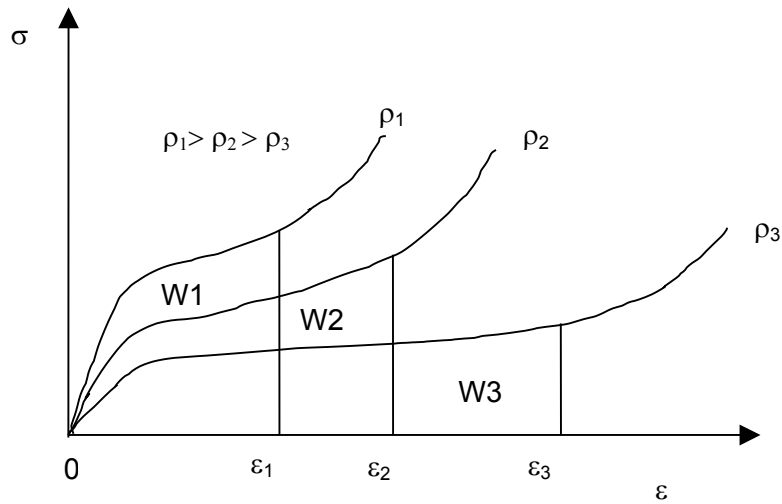


Fig. 3-8 Stress-strain curves for metallic foams having three different densities and the same amount of the absorbed energy [HAG99].

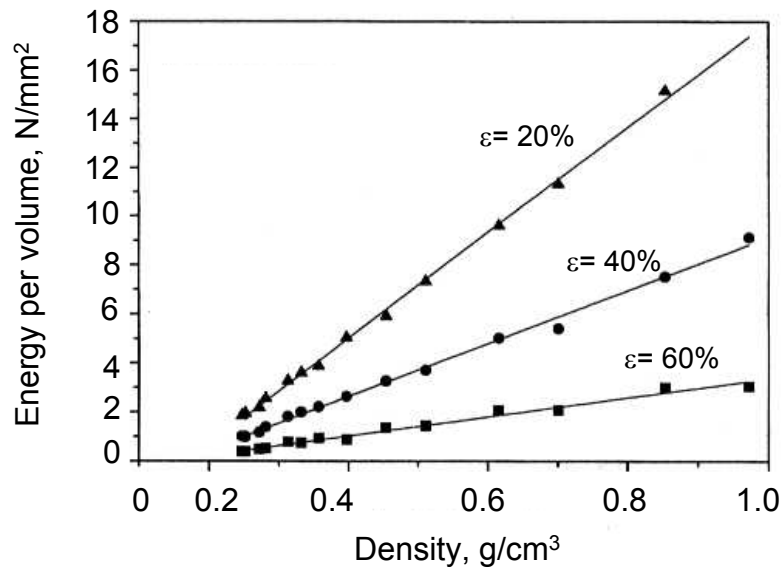


Fig. 3-9 Energy absorption of Al foam as a function of the foam's density at three different compression strains [BAU97].

3.1.3 Densification Regime

Depending on the nature of the solid making the foams and on their relative density, foams can fail by several mechanisms (elastic buckling, plastic yielding, brittle crushing or brittle fracture) [GIO00].

In case of metallic foams, which have a plastic yield point, the failure is localised in a band transverse to the loading direction which propagates throughout the foam with increasing strain.

Brittle crushing of the foams occur at large compressive strains where the opposing walls of the cells crush together and the cell wall material is compressed.

Brittle fracture of metallic foams is caused by the propagation of small cracks either along the boundaries of the grains or across the cleavage planes of the individual crystals. The cracks sometimes pre-exist in metal (a result of growth defects when the metal was cast or formed) or they are nucleated by slip when the metal starts to deform [GIB97] These cracks initiate at defects either in the cells or at the surface and extend as plane stress cracks in the thin cell walls. This process occurs beyond general yielding (strain = 2%) and is accompanied by wall thinning. **Fig. 3-10** shows a schematic of the crack growth which occurs in a tension test.

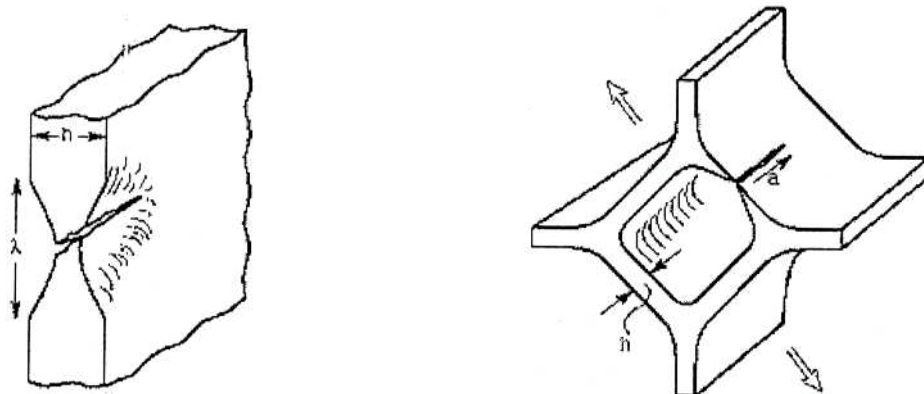


Fig.3-10 A schematic of the crack growth process a) thin sheet tearing and b) growth through the cell walls [SUG97].

The crack growth proceeds within a fracture zone, along the thinned region, via the nucleation, plastic growth and coalescence of voids. The crack meanders across adjoining walls and progresses through the material [SUG97].

Markaki et al. [MAR01] have examined the fracture surfaces of three different closed cell foams. It was found that the fracture surfaces for all three materials indicate the presence of

large cells, which probably acted as stress concentrators and favourable sites for failure initiation. In one of them a band of cell had become completely crushed. Failure in the other two foams occurred by plastic buckling of the cell walls.

Hanssen et al. [**HAN01**] have found that local and/or global failure mechanism is a reason for fracture of foams. Rupture, as in case of hollow extrusions filled with aluminium foam, is a likely mechanism.

By the examination of the failure mechanisms of aluminium foams under compressive loads, Sáenz et al. [**SÁE99**] have found that in the initial stages of failure mechanisms, crushing-shearing cell failure is associated with the interaction between non-uniform material, cell size distribution and the material's defects (cavities).

3.2 Creep Deformation of Metallic Foams

The mechanical strength of metals decreases with increasing temperature and the properties become much more time-dependent. Metals subjected to a constant load at elevated temperature will undergo creep, which is known as a time dependent change in length or in other words a time dependent plastic deformation at constant stress (or load) and temperature. The form of a typical creep curve of strain versus time is shown in **Fig. 3-11**.

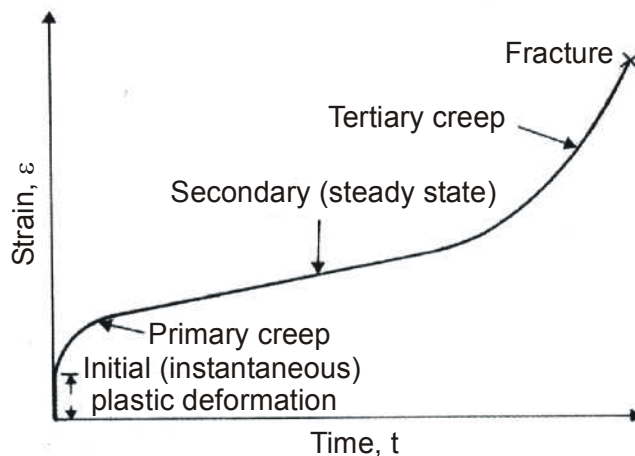


Fig. 3-11 Stages in a typical creep curve.

The slope of this curve is the creep rate $\frac{d\varepsilon}{dt}$. The curve may show the instantaneous elastic and plastic strain that occurs upon loading, followed by the plastic strain which occurs over time. Three stages of the creep curve may be identified as follows:

- a) Primary creep: in which the creep resistance increases with strain leading to a decreasing creep strain rate.
- b) Secondary (steady state) creep: in which there is a balance between work hardening and recovery processes, leading to a minimum constant creep rate.
- c) Tertiary creep: in which there is an accelerating creep rate due to the accumulating damage, which leads to creep rupture, and which may only be seen at high temperatures and stresses and in constant load machines.

The minimum secondary creep rate is interesting to design engineers, since failure avoidance is required [NN].

Solids react upon loading at high temperatures with an instantaneous strain ε_0 and a time-dependent strain ε_t . When they are completely unloaded after creep, an instantaneous contraction ε'_0 is followed by a time-dependent anelastic strain recovery ε'_t . The residual strain ε_p is called plastic creep strain, as shown in **Fig. 3-12**.

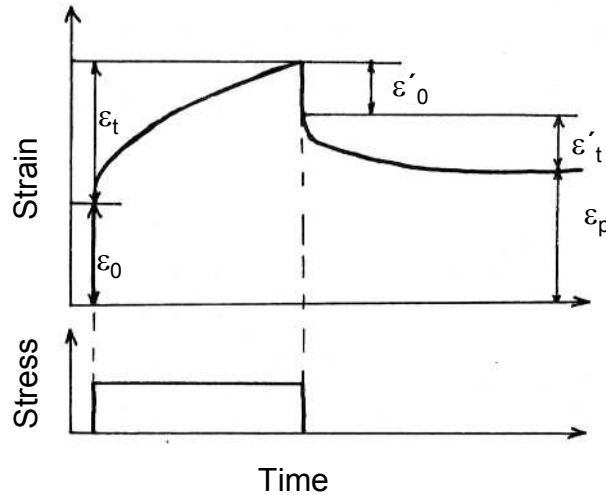


Fig. 3-12 Stages of creep strain and its partial relaxation after unloading [BRE81].

There is general agreement that creep is a thermally activated process. Thermal agitation is added locally to mechanical energy and this concurrence provides time-dependent deformation. High temperature creep ($T > 0.5T_m$) is believed to be a diffusion-controlled process [BRE81].

Several empirical models have been proposed to describe creep curves. Since the secondary creep which is of great importance for the engineering design is strongly dependent on temperature, the secondary creep rate can be determined using the following equation

$$\frac{d\varepsilon}{dt} = A \exp\left(-\frac{Q_0 - \nu\sigma}{RT}\right) \quad (3-7)$$

Where A, ν are constants, σ is the applied stress in MPa, Q_0 is the activation energy for creep in J/mole, R is the gas constant in J/K. mole, and T is the absolute temperature in K. An alternative expression is given by the equation (3-8) as follows:

$$\frac{d\varepsilon}{dt} = A\sigma^n \exp\left(-\frac{Q_c}{RT}\right) \quad (3-8)$$

Where n is creep exponent and have the values from 3-8 except at low stress where it is approximately 1. Hence the term “Power low creep” **[NN]**.

In the case of metallic foams, there is a number of existing and prospective applications in which elevated temperatures are involved, e.g. open-cell foams are used as a key component in heat exchangers or as catalyst carriers in chemical reactors. Closed-cell foams are used as core materials in light-weight sandwich components, for example in automotive and aerospace constructions, where high-temperatures exist frequently next to combustion or propellant engines. While the room-temperature plasticity of cellular metallic materials has widely been studied in recent years, relatively little research has been devoted to the high-temperature properties of this interesting class of materials.

When the foams are loaded at low temperatures ($T < 0.3T_m$), the foams deform by elastic buckling, elastic deflection and plastic collapse of their cell walls. At elevated temperatures, creep contributes to the deformation, which becomes time-dependant **[AND99a]**.

The creep behaviour of closed and open cell foams can be modelled by analysing the bending of cell edges and the stretching of the cell faces **[KES03]**. Andrews et al. **[AND99a]** have studied the creep behaviour of closed-cell aluminium foam in both tension and compression in a temperature range of 260°C-350°C and under a constant stress of 0.42 MPa. It was found that the power low creep exponent n is 5.4 in compression and 3.9 in tension for low stress values (less than 0.42 MPa) and 15.0 in compression and 14.4 in tension at higher stresses. The value of n at low stresses is close to that for aluminium ($n = 4.4$). The activation energy is 62.4 kJ/mole in compression and 133.1 kJ/mol. in tension at low temperatures (less than 300°C). At higher temperatures, the activation energy increases to 555.4 kJ/ mole. in compression and 404.0 kJ/mole in tension.

Another set of experiments has been carried out by Andrews et al. **[AND99b]** on open-cell foams (Doucel, ERG, Oakland, CA foams) at stresses ranging from 0.25 MPa to 0.68 MPa and temperatures ranging from 275°C to 350°C. The solid making up the foam is 6101-T6 aluminium alloy (0.6 Mg-0.5 Si) and it has also undergone creep tests. The creep tests were carried out at stresses ranging from 22.1 MPa to 44.0 MPa and temperatures ranging from 275°C to 325°C. The main application of this material is in heat exchangers because of its uniformity in cell size, shape and orientation. The results attained indicate that the foam should have the same activation energy Q and power low exponent n of the solid material.

Goretta et al. [GOR90] have carried out compressive creep tests on open-cell Al_2O_3 for temperatures of 1200°C-1500°C. The creep experiments were conducted at either constant load or constant cross-head speed. It was found that the data follows a general trend of linear dependence between strain rate and stress, which is characteristic for the diffusional flow with a creep exponent $n = 1 \pm 0.1$. This result was also obtained elsewhere [BRO80, FRO82].

According to Andrews et al. [AND99a] it is assumed that the creep rate of the cell-wall material can be described by the following equations:

$$\dot{\varepsilon}_{ss} = \dot{\varepsilon}_0 \left(\frac{\sigma}{\sigma_0} \right)^n \quad (3-9)$$

$$\dot{\varepsilon}_0 = A \exp\left(-\frac{Q}{RT}\right) \quad (3-10)$$

Where $\dot{\varepsilon}_{ss}$ is the steady state creep rate in s^{-1} , A is a constant, σ is the uniaxial applied stress in MPa, σ_0 and n are constants, R is the gas constant and T is the absolute temperature in K. According to the last equation it appears that, the creep rate depends on the foam's density, as shown in **Fig. 3-13**. This shows a good agreement with the results obtained by Andrews et al.

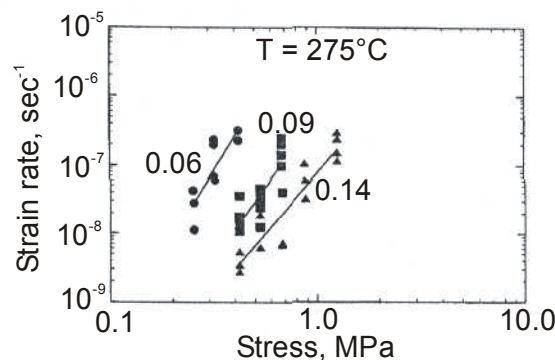


Fig.3-13 Secondary strain rate plotted against stress for different relative densities at a constant temperature [AND99b].

The increase in the strain rate is believed due to the collapse of a layer of cells, whereas the increase in stresses is due to the inhomogeneous microstructure which causes some cell walls to enter the power law breakdown regime with very rapid creep rates.

4 High Temperature Oxidation

4.1 Fundamentals of Oxidation

During exposure to elevated temperatures in air, nearly all metals react to form oxides and in some cases nitrides. The conversion of a structural component from metal to oxide can lead initially to a loss of load bearing capacity and ultimately failure [BRA00]. When a metal is oxidised at high temperatures in air, a protective oxide (scale) generally forms by a chemical reaction between the metal and the oxygen of the air according to the following equation:



Where M represents the metal component which reacts with oxygen and x, y are stoichiometric factors. When the free energy of formation ΔG° , which is defined as follows:

$$\Delta G^\circ = G_{products} - G_{reactants} \quad (4-2)$$

is negative, this reaction ends up with the metal oxide M_xO_y . When $\Delta G^\circ = 0$, a chemical equilibrium will occur [KUE92].

A graphical representation known as Richardson-Ellingham diagram, shown in **Fig. 4-1**, is of technical importance because it supplies information about several oxidation reactions [SCH00].

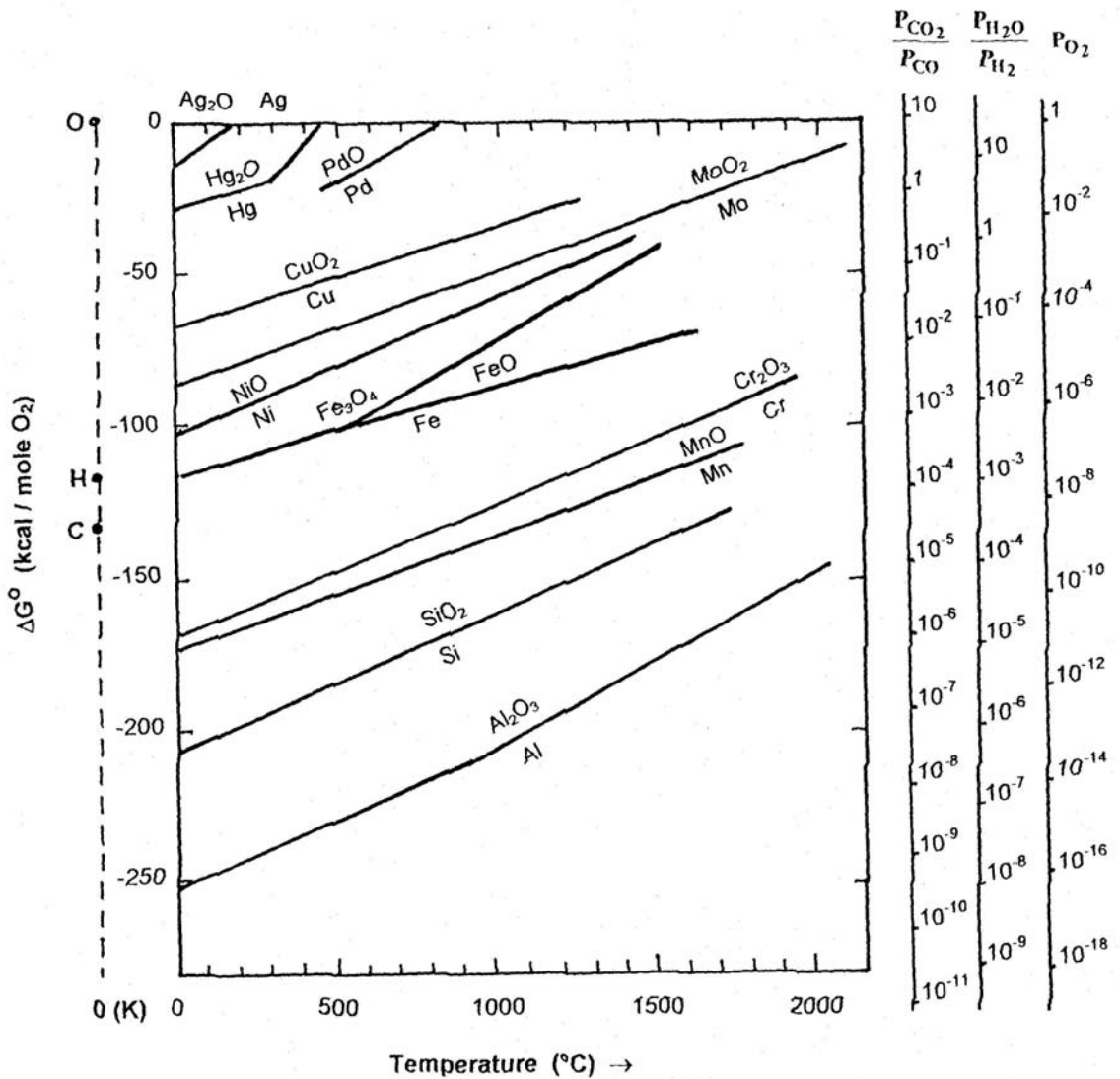


Fig.4-1 Richardson-Ellingham diagram [HOG97].

In this figure the ΔG° values are represented as a function of the temperature. Generally, ΔG° can be defined according to the following equation [KUE92]:

$$\Delta G^\circ = -RT \ln K \quad (4-3)$$

Where K is the equilibrium constant of the reaction, which is given by

$$K = \frac{a_{M_xO_y}^{2/y}}{a_M^{2x/y}} = \exp(-\Delta G / RT) \quad (4-4)$$

Where a is the activity of the different parts in the reaction, R is the general gas constant and T is the absolute temperature.

The activity for the gas phases can be approximated by the partial pressure so that for the oxygen activity the oxygen partial pressure p_{O_2} can be inserted according to the following equation:

$$P_{O_2} = \frac{a_{M_xO_y}^{2/y}}{a_M^{2x/y}} = \exp(\Delta G / RT) \quad (4-5)$$

Where P_{O_2} represents the equilibrium oxygen partial pressure at which both phases metal and oxide are stable. Below this value no oxide is formed and the metal is still stable. Above this value the oxide is stable and can form a protective scale. The most stable oxides are those where the equilibrium partial pressures take the lowest values, e.g. Al_2O_3 , Cr_2O_3 and SiO_2 . Less stable oxides are the oxides of iron and nickel [SCH00].

In order to determine the upper-use temperatures for these oxides, Perkins et al. [PER89] estimated a generalised upper-use temperature. For example, the maximum-use temperature for Cr_2O_3 is $1100^\circ C$, whereas for Al_2O_3 and SiO_2 , the maximum-use temperatures are $1425^\circ C$ and $1750^\circ C$, respectively.

4.2 Formation and Growth of Oxide Scales

The formation of an oxide scale starts with the adsorption of oxygen gas on the metal surface. During adsorption, oxygen molecules or molecules of other gaseous species in the environment dissociate and are adsorbed as atoms. These atoms initially adsorb at sites where the atom is in contact with the maximum number of surface atoms in the metal substrate. Therefore, in polycrystalline materials, grains of preferential orientation exist where the number of adsorbed atoms from the gaseous atmosphere is highest [OUD83]. This process results in a two-dimensional adsorption layer. The presence of adsorbed layers may increase the rates of the surface diffusion by orders of magnitude compared with those for surfaces with none or small amounts of adsorbate [BEN71].

When the metal surface which is saturated with adsorbed oxygen atoms or atoms from other gaseous species is further exposed to the gas, the gaseous species may dissolve in the metal and nuclei grow laterally and form a continuous film on the surface, as shown in **Fig. 4-2**.

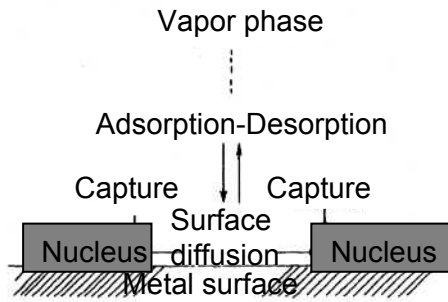


Fig. 4-2 Schematic representation of the process occurring during the nucleation of corrosion products on metal surfaces [KOF88].

Nucleation and growth of the nuclei are dependent on the composition of the substrate, the grain orientation, the temperature and the gas partial pressure. The nuclei grow in thickness and lateral direction and the reaction rate increases with time as shown in **Fig. 4-3** .

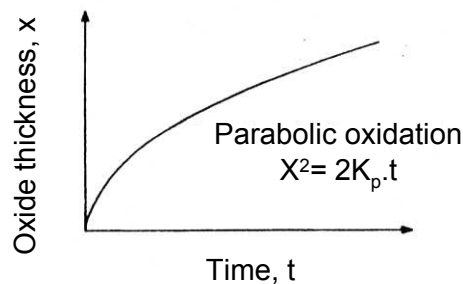


Fig. 4-3 Schematic diagram reflects the effect of time on the oxide thickness [SCH00].

The growth of oxide scales never stops as long as the material is exposed to an oxidising environment. The reason for this is the situation of the oxide scale that is determined by the ambient oxygen partial pressure at the outside surface and the equilibrium partial pressure between metal and oxide at the metal/oxide interface is considered. These two partial pressures represent fixed values as the equilibrium between oxide and metal is always maintained at the interface; thus the oxygen partial pressure always remains the same at this site, and at the outside of the oxide scale the oxygen partial pressure remains constant. The result of this situation is that there is a very strong oxygen partial pressure gradient across the scale . This gradient in oxygen partial pressure results in a defect concentration gradient across the scale. As temperatures are sufficiently high, diffusion can take place via the lattice defects. Diffusion process can be described by Fick's first law as follows:

$$j = -D \frac{\partial c}{\partial x} \tag{4-6}$$

Where j is the flux or mass diffusion per second through a unit cross section in the concentration gradient $\frac{\partial c}{\partial x}$ and D is the diffusion coefficient or diffusivity in (m^2/s) which is mainly a function of the diffusing ions, the structure in which these ions diffuse, and the temperature. If the gradient of the defect concentration is considered in the form $\Delta c/x$, where x is the thickness of the oxide, then the diffusion equation can be expressed as follows:

$$\frac{dx}{dt} = \frac{-D\Delta c}{x} \quad (4-7)$$

As Δc is a constant because it is determined by the two fixed points of the oxygen partial pressures at the two boundaries of the oxide scale (i.e. metal/oxide equilibrium pressures and oxygen partial pressure of the environment, respectively) and D is a constant as well, both can be taken together and replaced by a constant k'_p . The result is the general equation for parabolic oxidation:

$$\frac{dx}{dt} = \frac{k'_p}{x} \quad (4-8)$$

This equation in the differential form can be integrated yielding the well-known parabolic type of equation [SCH00]:

$$x^2 = 2k'_p t \quad (4-9)$$

The formation of an oxide layer on the metal surface at high temperature acts as a protection for the basis metal when the following requirements are fulfilled:

- 1- Slow growing up of the oxide layer
- 2- Good adhesion with the basis material
- 3- High thermodynamic stability
- 4- Good thermal and mechanical tolerance with the basis material
- 5- Good resistance towards the impurities in the atmosphere

Slow growing of an oxide layer means low values of the oxidation constant k'_p and thus a small diffusion constant value.

The oxide layers which are suitable for the high temperature applications are those of Al, Si and Cr [SCH00].

4.3 High temperature Oxidation of Iron

At temperatures ranging from below room temperature to temperatures of up to 1000°C, iron reacts chemically with the oxygen of the air to form a surface film of oxide. The films formed at room temperature are only a few Angstrom (Å) thick and hence invisible, but at higher temperatures, thick scales are produced [COR96].

During the oxidation of iron, the following reaction takes place:



At high temperatures, the reaction rate increases. The oxidation product, which results from the chemical reaction between iron and oxygen, is known as scale. The oxidation products can be determined by means of Fe-O phase diagram, as shown in **Fig. 4-4**.

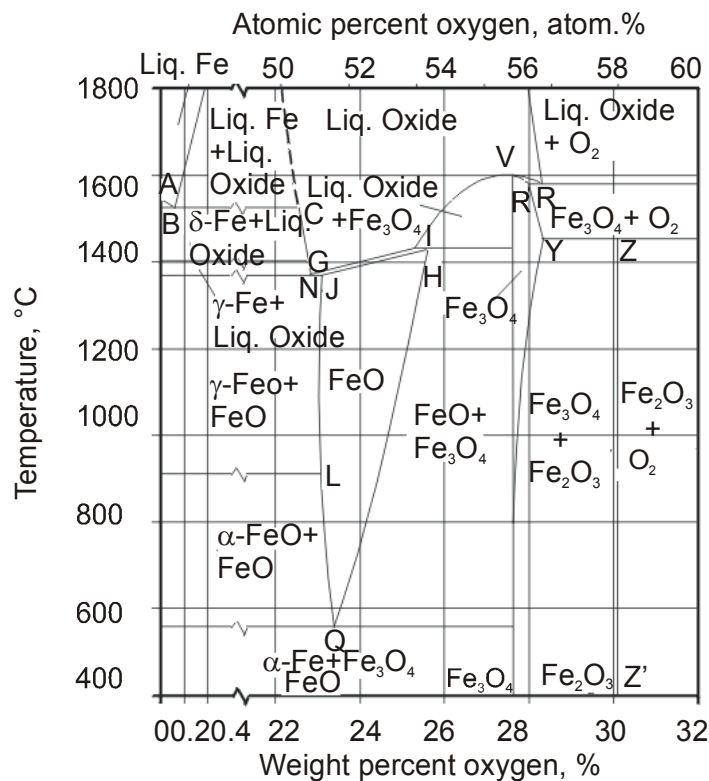


Fig. 4-4 Equilibrium Fe-O phase diagram [IEH03].

The Fe-O phase diagram shows that the maximum solubility of Oxygen in α-Fe at 700°C is

about 7 ppm (1ppm = 10^{-4} weight-%), whereas the solubility of oxygen in γ -Fe reaches about 10 ppm. Depending on the lattice defects, the solubility of oxygen can be reached 50 ppm.

The chemical reaction between Fe and oxygen results in three products, which are

FeO	Wustite	(Fe^{2+})
Fe_3O_4	Magnetite	(Fe^{2+}, Fe^{3+})
Fe_2O_3	Hematite	(Fe^{3+})

The metallic compound FeO is thermodynamically stable at temperatures above $570^\circ C$. At room temperatures, the other compounds Fe_2O_3 and Fe_3O_4 can be presented. In case of thermodynamic equilibrium, the three compounds will be formed together: $Fe / FeO / Fe_3O_4 / Fe_2O_3 / O_2$.

Tab. 4-1 summarises the different physical properties of the three oxides. The oxides differ from each other in colour, density, volume ratio, thermal expansion and hardness. It is known that the density of the oxide is smaller than that of the iron. Volume ratio between the oxide and base metal can be given by Pilling-Bedworth-Ratio which is

$$PBR = \text{volume of oxide} / \text{volume of iron}$$

The coefficient of thermal expansion of the oxide differs from that of the base metal (iron: thermal expansion coefficient at RT is about $12 \cdot 10^{-6} \text{ K}^{-1}$ and $16 \cdot 10^{-6} \text{ K}^{-1}$ at temperature $> 500^\circ C$).

	Color	Melting temperature ($^\circ C$)	Density (g/cm^3)	Pilling-Bedworth-ratio	Thermal expansion coefficient	Thermal conductivity (Cal/K.mole)	Specific heat (Cal/cm.s.K)		Electrical conductivity (W)
							To 25 $^\circ C$	To 1000 $^\circ C$	
$\alpha\text{-}Fe_2O_3$	brown/red (in divided form), black	-	5.24	2.14	$9.6\text{-}13.9 \cdot 10^{-6}$	0.035 to 30 $^\circ C$	25	36	-
Fe_3O_4	black	1600	5.18	2.10	$8 \cdot 10^{-6}$	-	36.3	48	178 at RT
FeO	black	1371-1424	5.52-7.50 (depending on vacancy content)	1.83-1.67	$11 \cdot 10^{-6}$ independent of temperature	-	11.5	14.2	90 to 200

Tab. 4-1 Physical properties of iron oxides [IEH03].

Tab. 4-2 summarises the mechanical properties of the three oxides of iron. The hardness of Fe_3O_4 as well as Fe_2O_3 is greater with respect to FeO .

Room temperature					800°C					
	Hardness		E-Modulus 10^3 Kgf/mm ²	G-Modulus 10^3 Kgf/mm ²	Hardness Kgf/mm ²	E-Modulus 10^3 Kgf/mm ²		Yield strength Kg/mm ²		Ultimate tensile strength Kg/mm ²
	Vickers Kgf/mm	Mohs				Tension	Compression	Tension	Compression	
Fe_2O_3	P 986-1219	5 to 6	M23, P 21.4 to 30.5	M 8.6 to 9, P. 9.4 to 9.6	-	-	-	-	-	-
Fe_3O_4	M 500, P 690	6	M 21.7 to 24.7 P. 23.5	M 8.9 to 9.9, P. 9.3	-	-	-	-	-	-
FeO	P 388	-	P. 12.6	$G_{FeO}=G_{Fe/2}$	P. 30	P 0.11-0.12	P 0.12-0.25	P 2.5-3.4	P 9.6-10.7	P 3-3.7

Tab. 4-2 Mechanical properties of iron oxides [IEH03].

A set of experiments has been carried out by Hidaka et al. [HID01] in order to study the deformation of FeO oxide scales at high temperatures. Tensile tests of FeO were performed at 600-1200°C under strain rates ranging from 10^{-3} to 10^{-5} s⁻¹. Test specimens of FeO scales were prepared by complete oxidation of 99.999% pure Fe before the tensile test, and gas atmospheres were adjusted through the tensile test to maintain the scale composition. It was found that oxide scales of FeO deformed plastically above 700°C, fracture elongation increased and tensile strength decreased as the temperature increases. It was also suggested that the deformation of FeO scale above 1000°C resulted from dynamic recovery associated with dislocation climb.

5 Experimental Work

5.1 Tested Materials

Three different types of metallic foams have been utilised in the present work. One of the tested foams being Alporas (AlCaTi) foams, delivered by the Shinko-wire Company in Japan. The other two types of foams are based on low alloyed steel powders, Distaloy SA and Astaloy Mo, produced by Hoganaes Company. For simplicity, During the course of this work Distaloy SA and Astaloy Mo foams will be referred to as Distaloy and Astaloy foams, respectively.

5.1.1 Alporas-Foams

Alporas foams, which have the chemical composition listed in **Tab. 5-1**, have been produced via a batch casting process, as shown in **Fig. 2-2**.

C	Si	Mn	Cu	Cr	Ti	Ca	Mg	Fe	Zn	Al
0.014	0.05	0.005	0.005	0.01	1.51	1.33	0.001	0.11	0.002	Rest

Tab.5-1 Chemical composition of Alporas **[HAG99]**.

In this process, calcium (Ca) is added to the molten Aluminium at a temperature of 680°C in order to increase the viscosity of the molten metal with the aim of stabilising the H₂ bubbles released from the thermal decomposition of TiH₂ and acts as a blowing agent. TiH₂ is the main source for this high Ti content **[MIY99]**.

The Alporas samples, which have been used in the compression test, were cut from a block with the dimensions of 2000 x 600 x150 mm³ delivered by Shinko Wire Co. Ltd. A cast Alporas block weighs 160 Kg and measures 2050 x 650 x 450 mm³ **[HAG99]**.

The mean cell size of Alporas is 4.5 mm and the cell wall thickness ~ 85 µm. The apparent density of the product varies from 0.20 g/cm³ to 0.40 g/cm³. **Fig. 5-1** shows some examples of the distribution of the apparent density along the width of Alporas foamed block.

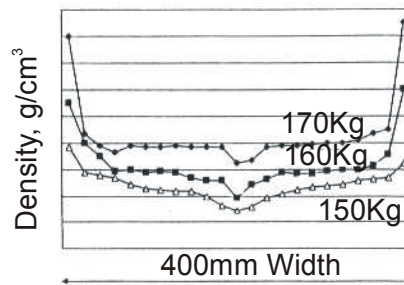


Fig. 5-1 The distribution of the apparent density along the width of foamed blocks [MIY99].

Tab. 5-2 gives the relevant properties of Alporas foams [PAU00].

Property	Value
Relative density (ρ^* / ρ_s)	0.08-0.1
Average cell size (L)	4-5 mm
Edge thickness (t_e)	75-100 μm
Elastic modulus in tension (E_t)	0.8-1.05 GPa
Elastic modulus in compression (E_c)	0.75-1 GPa
0.2% Offset strength in tension ($\sigma_{t0.002}$)	~ 1.35 MPa
0.2% Offset strength in compression ($\sigma_{c0.002}$)	~ 1.28 MPa
Tensile strength (σ_t)	1.85 -1.92 MPa
Compressive strength (first peak) (σ_c)	2 – 2.5 MPa
Fracture toughness (K_{IC})	~ 0.8 MPa m ^{1/2}

Tab. 5-2 Properties of Alporas foams.

5.1.2 Distaloy and Astaloy Foams

Based on low alloyed steel powders, two different types of powders with different chemical

compositions, Diastaloy SA and Astaloy Mo were utilised. The powders have been manufactured by Höganäs AB company. **Tab. 5-3** gives the chemical composition of both Distaloy and Astaloy powders.

	C	H ₂ -loss	Cu	Ni	Mo	Fe
Distaloy SA	0.01	0.08	1.5	1.77	0.51	Rest
Astaloy Mo	0.01	-	-	-	1.6	Rest

Tab. 5-3 Chemical composition of Distaloy and Astaloy powders, mass contents in %
[BER03].

Distaloy powder

Distaloy powders are diffusion-alloyed, sponge iron powder particles. Fine Ni-, Cu and Mo-particles are bonded to a large sponge-iron particle. **Fig. 5-2** shows three SEM micrographs with three different magnifications for the particle morphology of Distaloy powders. A characteristic feature for these particles is their spheroidal shapes. The particle's surface is craggy and uneven and the indentations within the particle were filled with the alloying elements [MOH03].

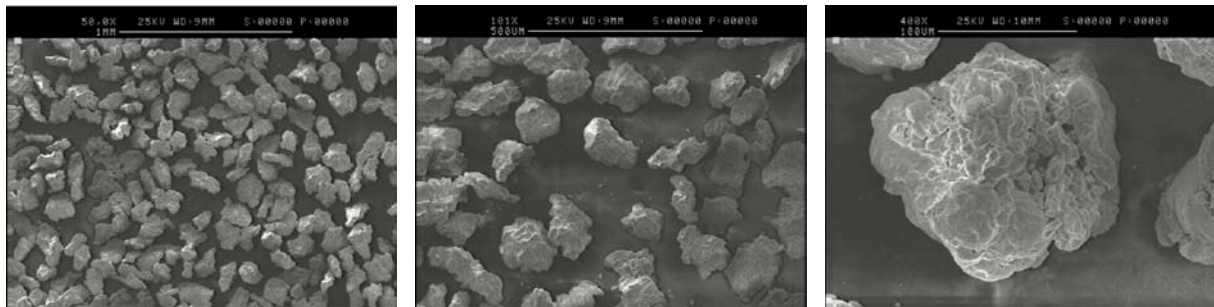


Fig. 5-2 SEM micrographs show the particle's morphology of the Distaloy powders.

Astaloy powder

Astaloy is a pre-alloyed, water-atomised steel powder free from chromium (Cr) and contains 1.5% molybdenum (Mo). This type of powder exhibits a high compressibility and a homogenous microstructure after the sintering process. This makes this powder an excellent choice for components requiring surface hardening. SEM micrographs of the Astaloy powders show that the particles' morphology of Astaloy powders has irregular shapes, as shown in **Fig. 5-3**. Irregular particles shapes provide a good green strength of the cold compacted powders and are therefore preferred in the production of iron and steel powders for structural part applications [THÜ93].

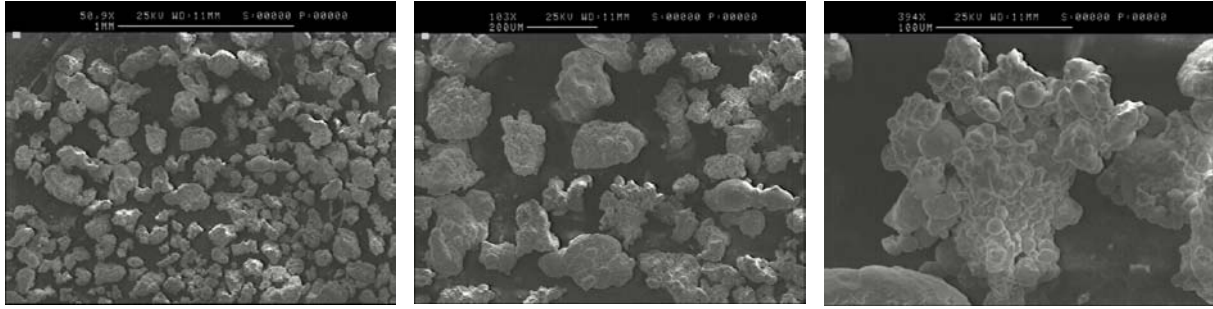


Fig. 5-3 SEM micrographs of particle’s morphology of Astaloy powders

Distaloy and Astaloy foams were produced by using the Slip Reaction Foam Sintering (SRFS) Process. In this process a metal powder was mixed with a dispersant (SiO_2). Water and a foaming agent (H_3PO_4) were added to form the slip. SiO_2 acts as a binding agent to stabilise the slip. **Tab. 5-4** gives the amounts of the used materials to produce both Distaloy and Astaloy samples, respectively.

Amount and type of metal powder	Phosphoric acid	Amount of dispersant	Amount of added water
100g Distaloy	3g H_3PO_4	2g SiO_2	17-22g H_2O
100g Astaloy	3g H_3PO_4	2g SiO_2	18-22g H_2O

Tab. 5-4 Amounts of used materials in production of Distaloy and Astaloy foams at IEHK [MOH01].

The resulted green samples are dried and then sintered. Sintering process is a heat treatment process, by which loose fine powder particles are converted into a compact material. This process takes place at a temperature ranging from $0.6-0.8T_m$ of the material. During this process, the loose powder particles bind together forming sintering bridges (sintering neck) by means of a diffusion process, i.e. the sintering process is a thermal activated process. The specific area of the particles decreases due to the enlargement of the contact areas which influences the volume of the pores and pore morphology [MOH03].

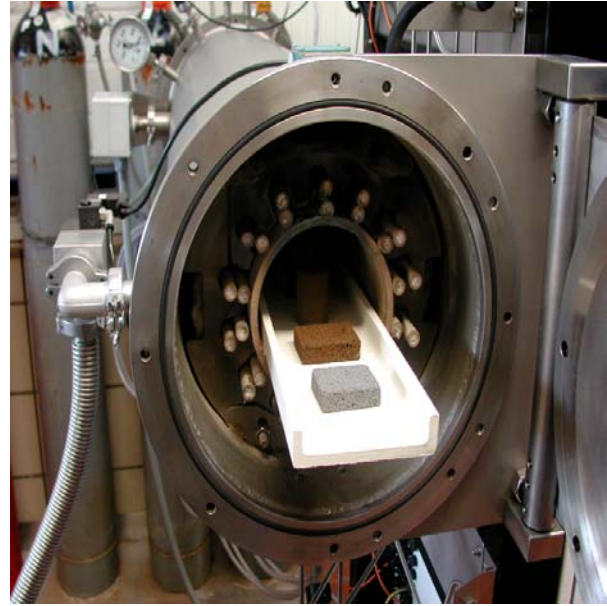
Sintering of the green samples occurs under a reduction atmosphere in the sintering furnace, depicted in **Fig. 5-4**. The furnace was manufactured by Xerion Company. As shown in **Fig. 5-4**, the furnace is of a tube-type and the maximum allowed sintering temperature is 1500°C . The furnace operating program consists of the following steps, as shown in **Fig. 5-5**; two evacuation processes take place during the sintering process as the furnace is turned on. At the end of evacuation, N_2 flows inside the furnace and afterwards H_2 starts to flow parallel with N_2 for about 1 hour. Afterwards the heating process is started. The maximum allowed heating as well as cooling rate is 10 K/min. The sintering process must not exceed

999 min; otherwise the furnace will be turned off automatically. The flow of H_2 and the cooling process take place farther in an N_2 atmosphere and the end of the sintering process at this moment is reached.

The green samples have been sintered at $1170^\circ C$ according to the scheduled temperature-time (T-t) diagram, shown in **Fig. 5-6**.



(a)



(b)

Fig. 5-4 (a) Sintering furnace at IEHK, (b) some samples are stacked on a ceramic muffle inside the furnace chamber

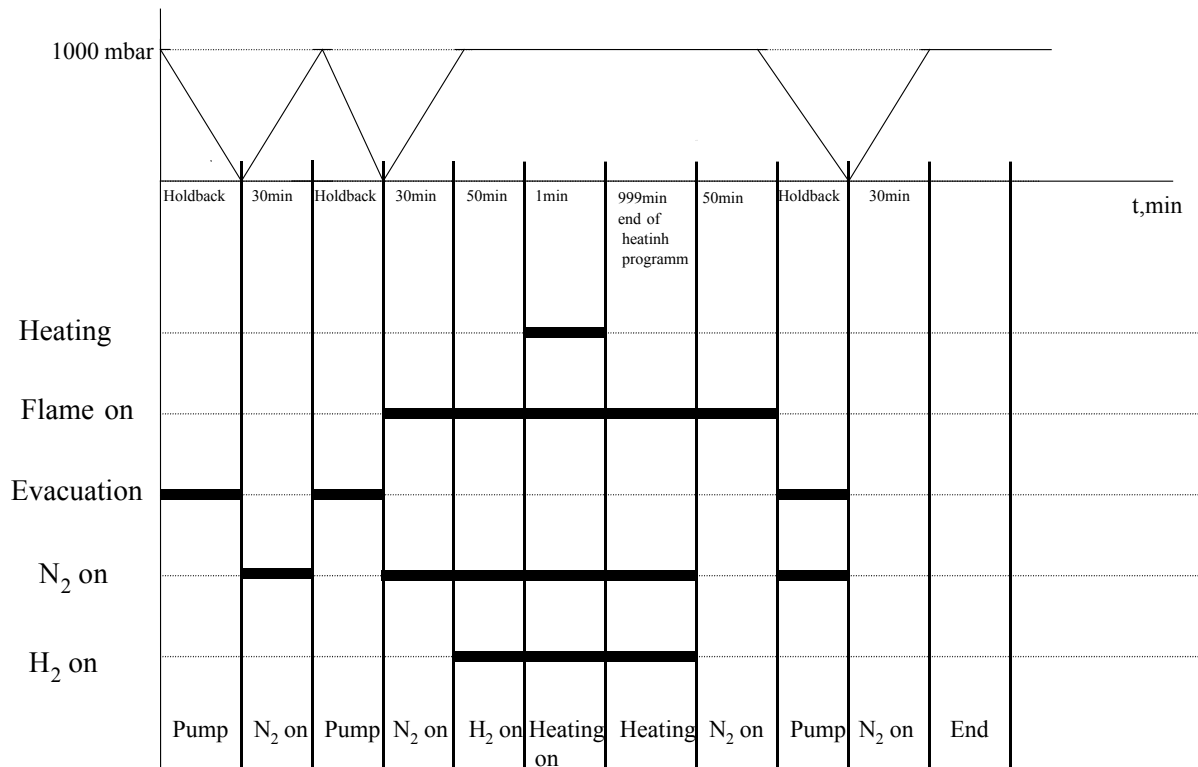


Fig. 5-5 Operating program of the sintering furnace at IEHK.

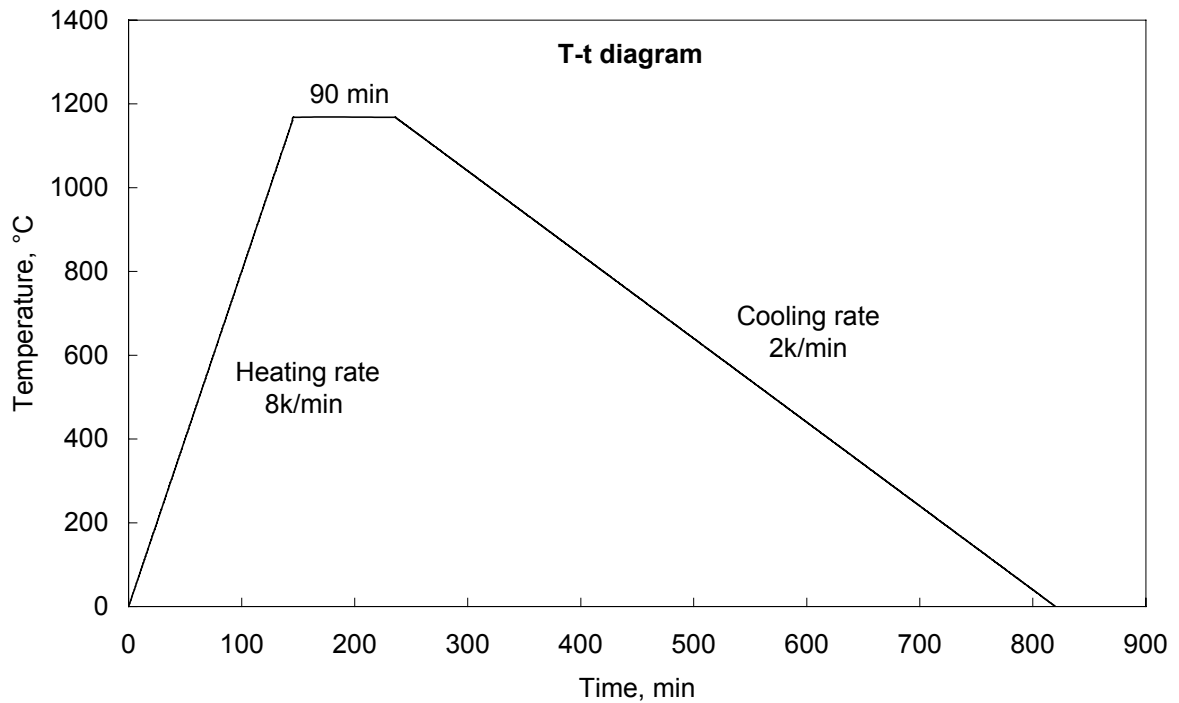


Fig. 5-6 T-t diagram of the sintering process.

5.2 Density Measurement

The utilised foams are characterized in terms of their densities since the mechanical properties of metallic foams depend largely on the density. The densities of the specimens were determined by weighing the samples using a digital balance and their dimensions were measured using a digital calliper. In order to minimise the error in measuring the specimen's density, the length, the width as well as the thickness of the sample was measured at five different positions. Multiplying the mean value of the measured dimensions, the volume is thus obtained. By dividing the weight of the sample on its volume, its density is thus determined. A maximum error of about 5% by determining the foam's density has to be taken into consideration.

5.3 Testing Machines

In order to study compressive behaviour of metallic foams, two different testing machines were used. One of them was used for testing foams in atmospheric air medium, whereas the other was equipped for testing in inert gas atmosphere.

5.3.1 Compressive Testing Machine

High temperature, quasi-static compression tests were carried out, according to DIN 53421 [DIN84], on samples having various cross sectional areas of 20 x 20, 13 x13 as well as 50 x 50 mm² over a range of temperature from 0.2-0.9*T_m (for Alporas foams) and up to 0.5*T_m (for Distaloy and Astaloy foams), where T_m is the melting temperature. The compression testing machine is a servo-hydraulic one equipped with a 100 kN load cell. A schematic sketch is clearly demonstrated in **Fig. 5-7**.

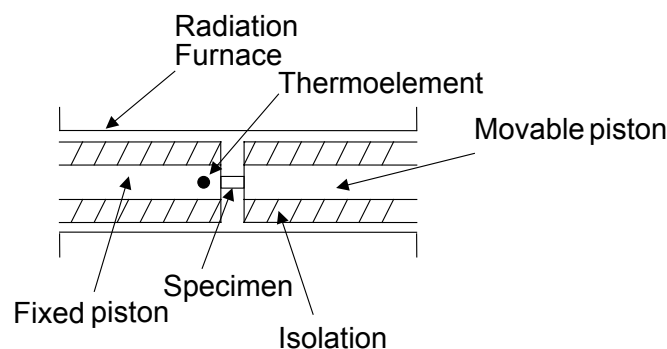


Fig. 5-7 A schematic illustration of the compressive testing machine at IEHK.

The sample was placed between a constant plate and a horizontally movable plate in

a furnace which can be folded back. The machine is connected with a heat control unit, which supplies it through 3 suppliers with the required heat. The maximum achievable temperature is about 800°C. The temperature was monitored with a thermocouple Fe-CuNi (L) DIN 43710. The specimens were maintained at the test temperature for 15 minutes prior to testing. The force was recorded as a function of the plate's displacement. The displacement of the plate was used to determine the overall strain. The displacement rate was constant at 1 mm/min.

Fig. 5-8 shows the test sample before and after compression.

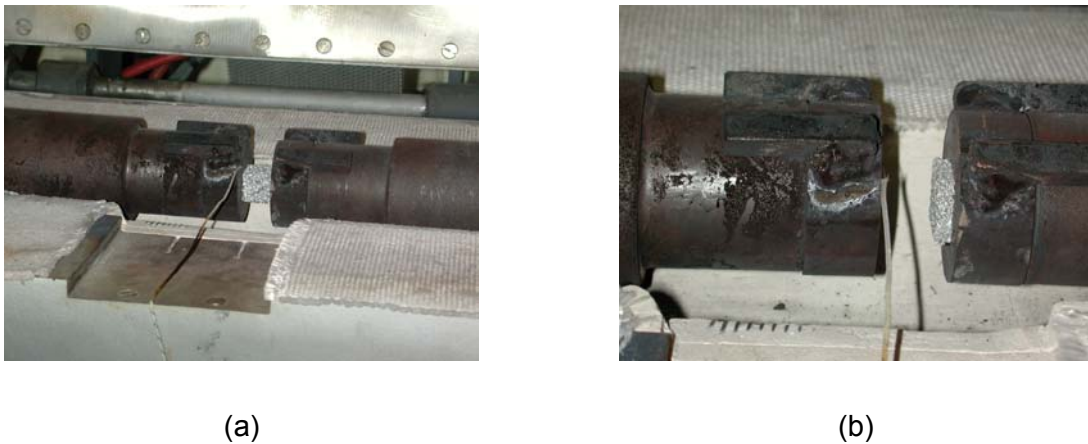


Fig. 5-8 Test sample a) before compression b) after compression.

5.3.2 Schenck Equipment

High temperature compressive tests in argon (Ar) have been carried out for the Astaloy as well as the Distaloy foams, using a servo-hydraulic testing machine equipped with 160 kN load cell. A schematic drawing of the test set-up is shown in **Fig. 5-9**. Samples having a cross sectional area of 13 x 13 mm² and 50 x 50 mm² were placed between a fixed piston and a vertically movable piston. The sample was inductively heated by a coil at a constant rate of heating of 200 K/min to the required temperature. Thermocouple type S (Pt- PtRh10%) was used to measure the temperature. As soon as the required temperature is reached, a holding time of 60 sec is done in order to achieve a homogeneous distribution of the temperature throughout the sample.

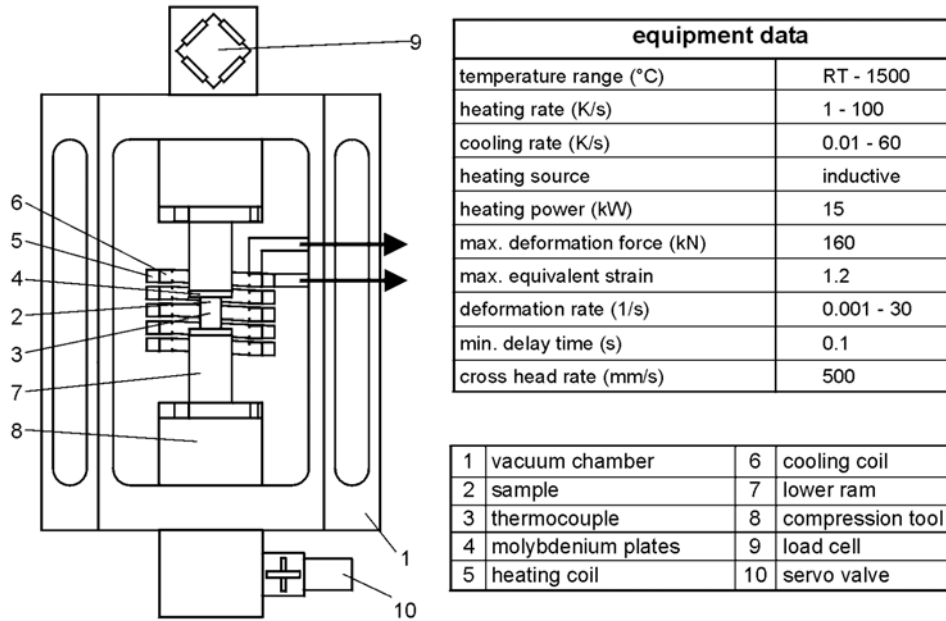


Fig. 5-9 Schenck equipment at IEHK.

5.3.3 Creep Testing Machine

The high temperature creep tests have been carried out at the Department of Materials Science (LFW), RWTH Aachen, using a biaxial testing machine, as shown in **Fig. 5-10**. This machine is suitable for both tension and torsion tests simultaneously. The maximum loading capacity of the machine is 50 kN in case of tension or compression and of 175 Nm as a maximum moment in case of torsion. The testing machine is equipped with a furnace and a heat control unit. The maximum temperature which can be reached is 1000°C.



Fig. 5-10 Creep testing machine at LFW.

With the help of a PC measuring software program; as shown in **Fig. 5-11**, the measured

data can be expressed in terms of strain, time and stress, thus the creep curves can be easily obtained.

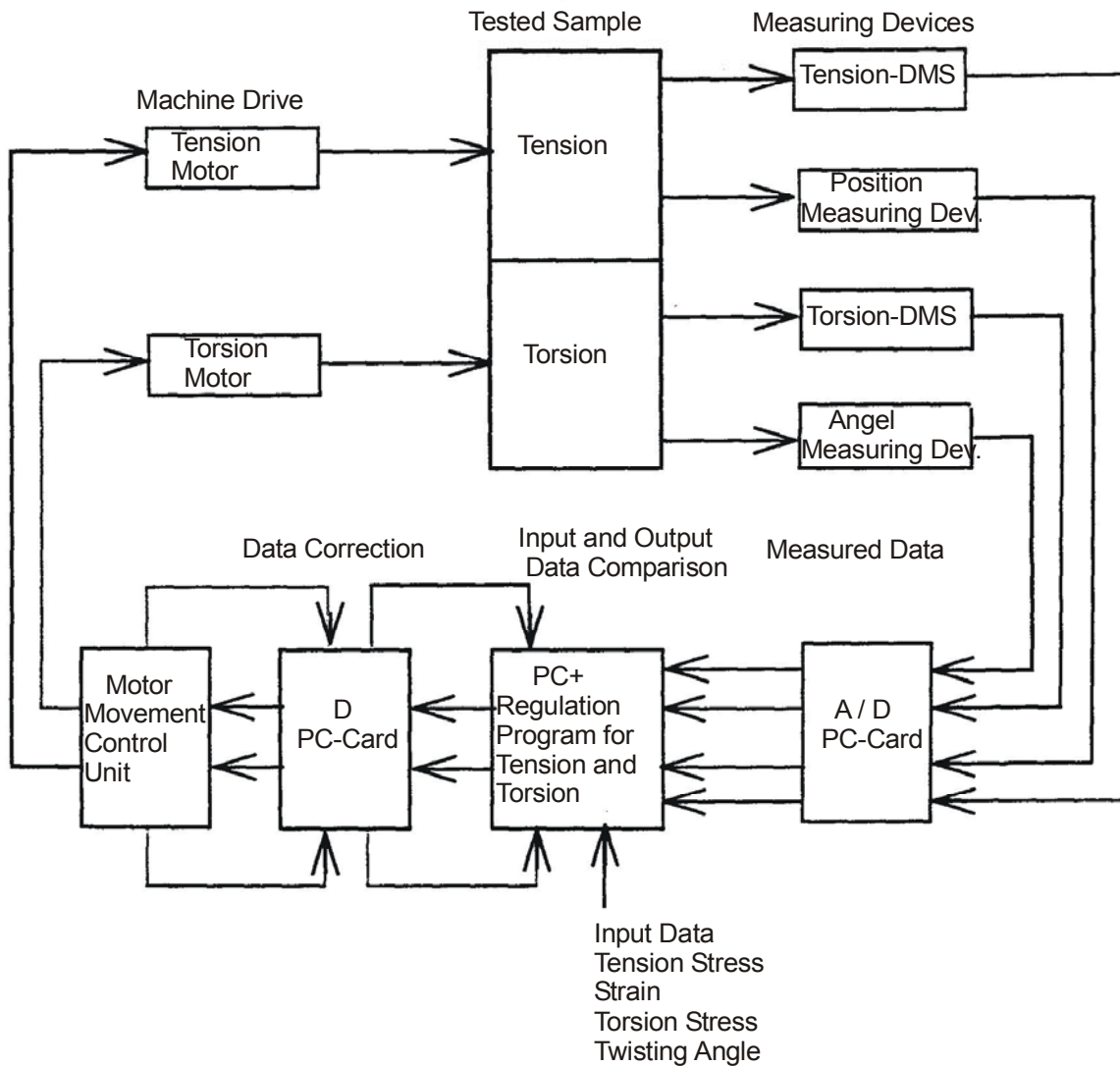


Fig. 5-11 Flow chart of the measuring system for the creep testing machine at LWK.

5.3.4 Differential Thermal Analysis

Differential Thermal Analysis (DTA) is used to investigate the phase transformations occurring during heating and/or cooling of a material via measuring the temperature difference between the material to be investigated and a reference material using Netzsch DTA 404 S type equipment, which is schematically depicted in **Fig. 5-12**. This device has the ability to determine a temperature range from room temperature to 1550°C with heating or cooling rates between 0.5 and 50 K/min. To avoid an oxidation of the specimens, the tests are performed with a constant argon flow. The reference substrate is Al₂O₃, which shows no transformation in the temperature area of interest. Since the whole bottom of the crucible

must be covered with metal in the liquid state, especially for materials with a high density, the amount of 200 mg has been proved as ideal. Only in this way is it possible to achieve the relevant accuracy, which is required upon determining the difference in temperature between the sample and the reference substrate. The sample was heated in inert atmosphere (Ar) with a rate of heating 10 K/min. The results of this experiment will be later discussed in more detail.

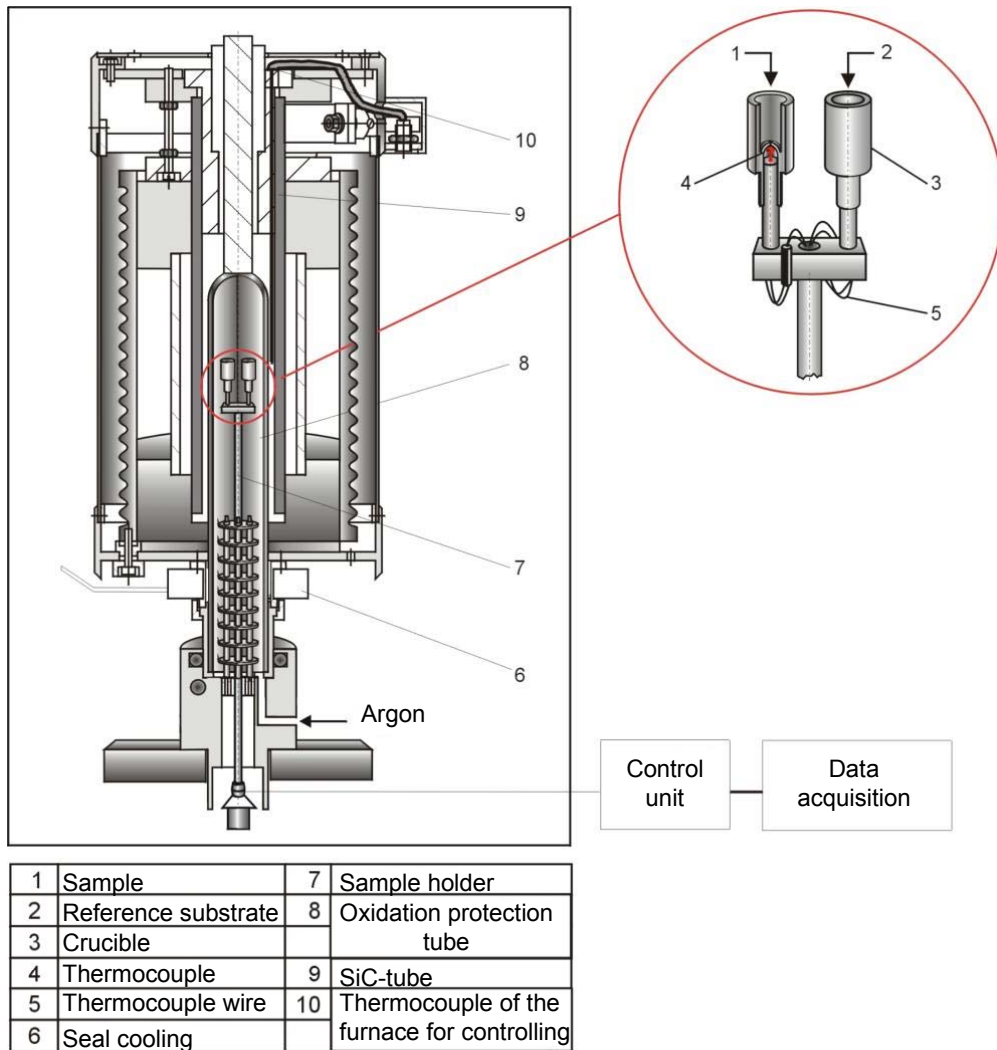


Fig. 5-12 Differential thermal analysis equipment.

5.4 Follow-up Examination

5.4.1 Metallographic Characterisation

Microstructural characterisation of samples in the green state, after sintering as well as after high temperature compression was performed using a conventional light optical microscope (LOM) working with a digital software Soft Imaging System (SIS). The samples were ground and polished using the normal grinding and polishing techniques. It is very important during

the preparation of the samples for the metallographic examination to preserve the foamed structure; i.e. the samples containing the pores have to be sawed carefully to avoid the damage of the cells [SCH88]. The samples were infiltrated in vacuum by a low viscosity resin. The resin was poured onto the samples and on admitting the air to the chamber; it was forced into the small pores. Afterwards the samples are ground and polished using the normal grinding and polishing tools.

5.4.2 SEM Examination

A scanning electron microscope (SEM), Stereoscan 90, Firm Cambridge Instruments with an acceleration voltage of 25 kV was used to characterise the particle morphology of the used powders. The topography of foams' surfaces in the green state as well as after high temperature compression was also investigated using SEM. SEM micrographs having different magnifications were taken in various directions; aiming to investigate the topography of the foams' cell-walls prior to deformation as well as after compressive deformation.

5.4.3 Electron Probe Microanalysis

Electron probe microanalysis (EPMA) investigation was carried out at the Central Facility of Electron Microscopy (GFE) - RWTH Aachen. This kind of investigation provides information about the quantitatively distribution of the alloying elements in weight (wt. %) as well as atomic percentage (at. %), respectively. The measurements were carried out by an electron microprobe (Camebax SX50) equipped with wavelength-dispersive spectrometers. For EPMA analysis the following measuring conditions were applied: electron beam energy: 15 keV; electron beam current: 40 nA; measuring time per analysing point: 10s; ~1 μm focussed electron beam.

For calibration SiO_2 , Al_2O_3 were chosen for silicon, oxygen, calcium and pure metallic standards for the other elements. Point analyses were performed in different phases, i.e. calibrated characteristic X-ray intensities were determined and transformed to chemical composition by using a matrix-correction procedure.

6 Results & Discussion

In this chapter the attained results concerning the characterisation of various metallic foams under quasi-static compressive as well as compressive creep deformation are discussed. Influence of each testing parameter e.g. foam's density, load, temperature, test medium and strain rate on the mechanical properties of metallic foams is discussed in detail.

6.1 Density Measurement

The densities of the foams were determined, as described earlier, by weighing the samples using an electronic balance. The dimensions of the samples were measured by using a digital calliper gauge. It was found that the utilised foams in this work have had a density between 0.2 g/cm³ and 0.4 g/cm³ in case of Alporas, whereas a range of density between 1.3 g/cm³ and 2.0 g/cm³ was measured in case of Astaloy and Distaloy foams.

6.2 Compression Test of Metallic Foams

The compression test of metallic foams is considered as one of the most applicable tests for the characterisation of their mechanical stability. This is due to the potential applications of metallic foams in the field of crash and energy absorption. For this purpose a set of compressive tests has been carried out on various types of metallic foams having different densities in two different atmospheres, air as well as argon (Ar) to prevent the high temperature oxidation of foams.

6.2.1 Compression Test in Normal Atmosphere

6.2.1.1 Quasi-static Compression Test of Alporas Foams

Quasi-static compression tests have been carried out according to DIN 53291. Instead of samples having a cross sectional area of 50 x 50 mm², as mentioned in the norm, small samples of a cross-sectional area of 20 x 20 mm² and thickness of 20 mm have been used. The used compressive testing machine is a universal servo-hydraulic one, as shown in **Fig. 5-8**, with a 100 kN load cell. The rate of displacement was constant at 1 mm/min (strain rate of $8.3 \cdot 10^{-4} \text{ s}^{-1}$). After compression, a result in form of a force-displacement curve is obtained. Using the following well-known relations, the force-displacement curve is converted into stress-strain curve, as shown in **Fig. 6-1**.

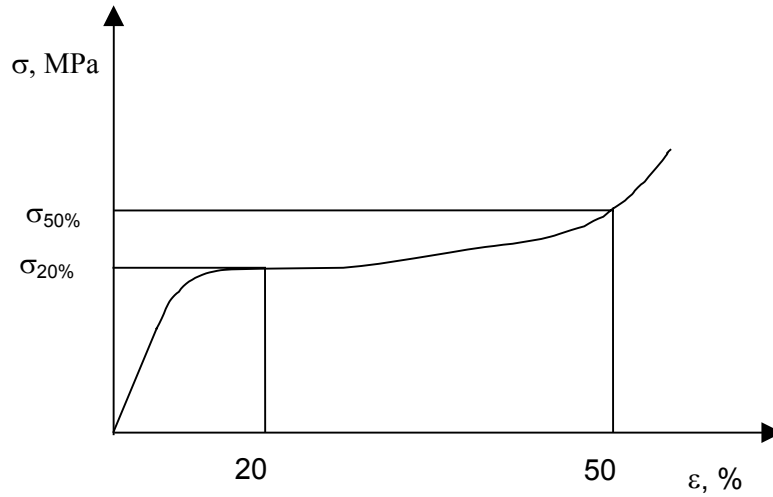


Fig. 6-1 Compressive stress-strain curve.

The stress-strain values can be easily calculated by using the following equations [HAG99]:

$$\text{Compression strength (MPa)} \quad \sigma_c = \frac{F_c}{A_o} \quad (6.1)$$

$$\text{Compression strength at 20\% strain (MPa)} \quad \sigma_{c20\%} = \frac{F_{20\%}}{A_o} \quad (6.2)$$

$$\text{Compression strength at 50\% strain (MPa)} \quad \sigma_{c50\%} = \frac{F_{50\%}}{A_o} \quad (6.3)$$

$$\text{Strain (\%)} \quad \varepsilon_c = \frac{\Delta h}{h_0} * 100 \quad (6.4)$$

Where σ_c is the compressive stress in (MPa), F_c is the compressive applied force in (N), A_o is the initial cross-sectional area of the sample in (mm^2), ε_c is the compressive strain, Δh is the change within the height of the sample in (mm) and h_0 is the initial height of the sample in (mm).

6.2.1.1.1 Effect of Density

The foam's properties are largely determined by its density. In order to study the influence of density on the mechanical properties, a set of compression tests was carried out on foams having different densities. For each density, two samples were taken and compressed.

Tab. 6-1 gives the measured compressive strength at 20% and 50% strain, respectively as a function of foam's density and temperature. It can be concluded, that the compressive

strength of Alporas foams increases linearly with increasing the foam's density, as clearly shown in **Fig. 6-2** and **Fig. 6-3**.

Temperature, °C	Density, g/cm ³	Compression strength, MPa			
		$\sigma_{20\%}$		$\sigma_{50\%}$	
25	0.20	1.14	1.30	1.72	-
	0.21	1.30	1.37	2.02	2.23
	0.22	1.47	1.18	2.38	2.17
	0.23	1.65	1.46	2.38	-
	0.24	1.49	1.59	2.64	2.17
170	0.20	0.93	0.92	1.52	1.54
	0.21	0.99	1.02	1.64	2.05
	0.22	0.99	1.12	1.91	2.17
	0.23	1.20	1.12	2.07	2.22
	0.24	1.34	1.19	2.19	1.83
270	0.20	0.64	0.43	1.04	-
	0.21	0.68	0.65	1.18	1.28
	0.22	0.74	0.72	1.36	1.40
	0.23	0.93	0.93	1.65	1.59
	0.24	0.90	0.72	1.66	1.50
340	0.20	0.42	-	0.73	-
	0.21	0.45	0.49	0.79	0.80
	0.22	0.44	0.52	0.75	0.70
	0.23	0.51	0.59	0.79	0.75
	0.24	0.52	0.46	0.92	0.94
410	0.20	0.26	-	0.41	-
	0.21	0.26	0.26	0.43	0.37
	0.22	0.32	0.24	0.51	0.43
	0.23	0.34	0.28	0.60	0.51
	0.24	0.33	0.31	0.56	0.51
480	0.20	0.18	0.21	-	-
	0.21	0.25	0.24	0.5	0.42
	0.22	0.23	0.22	0.43	-
	0.23	0.24	0.23	0.37	-
	0.24	0.26	0.23	0.54	0.44
550	0.20	0.15	0.14	0.35	0.29
	0.21	0.10	0.12	0.30	0.20
	0.22	0.13	0.13	0.30	-
	0.23	0.18	-	0.35	-
	0.24	0.16	0.15	-	-
620	0.20	0.01	0.01	0.06	-
	0.21	0.06	-	-	-
	0.22	0.02	0.02	0.06	0.03
	0.23	0.02	-	0.04	-
	0.24	0.02	0.01	-	-

Tab. 6-1 Compression strength of Alporas foams as a function of density and test temperature.

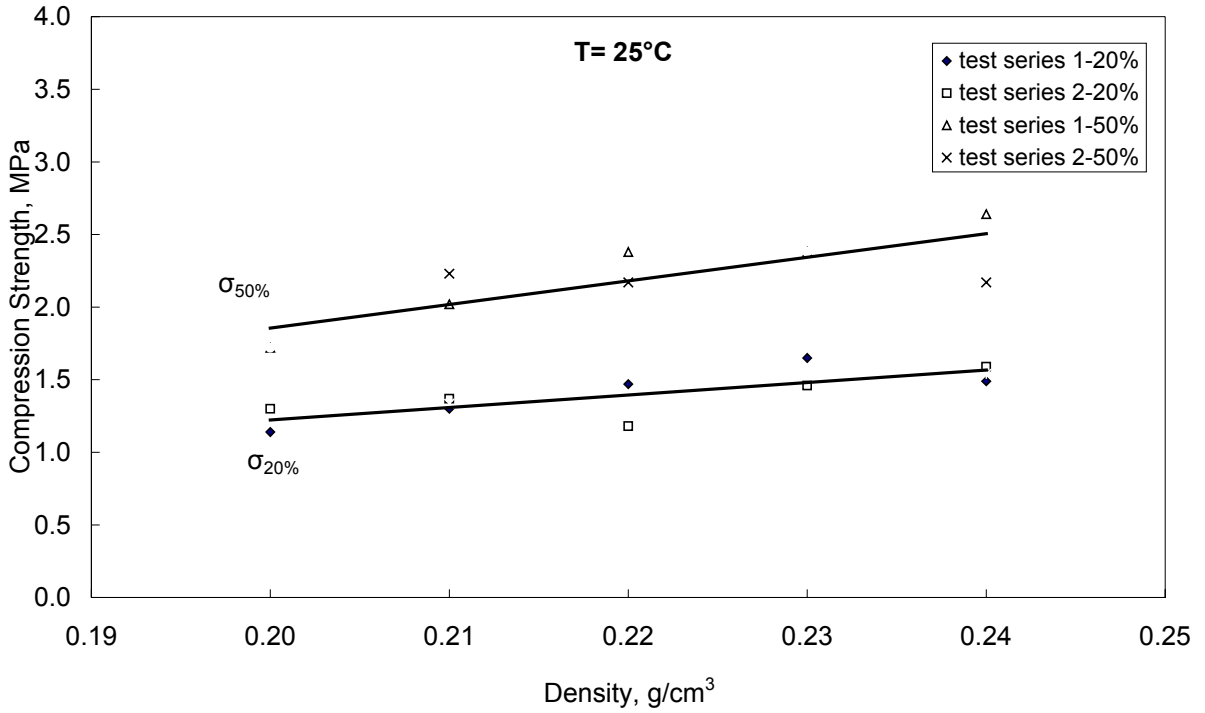


Fig. 6-2 Compression strength as a function of density of Alporas foams, tested at RT.

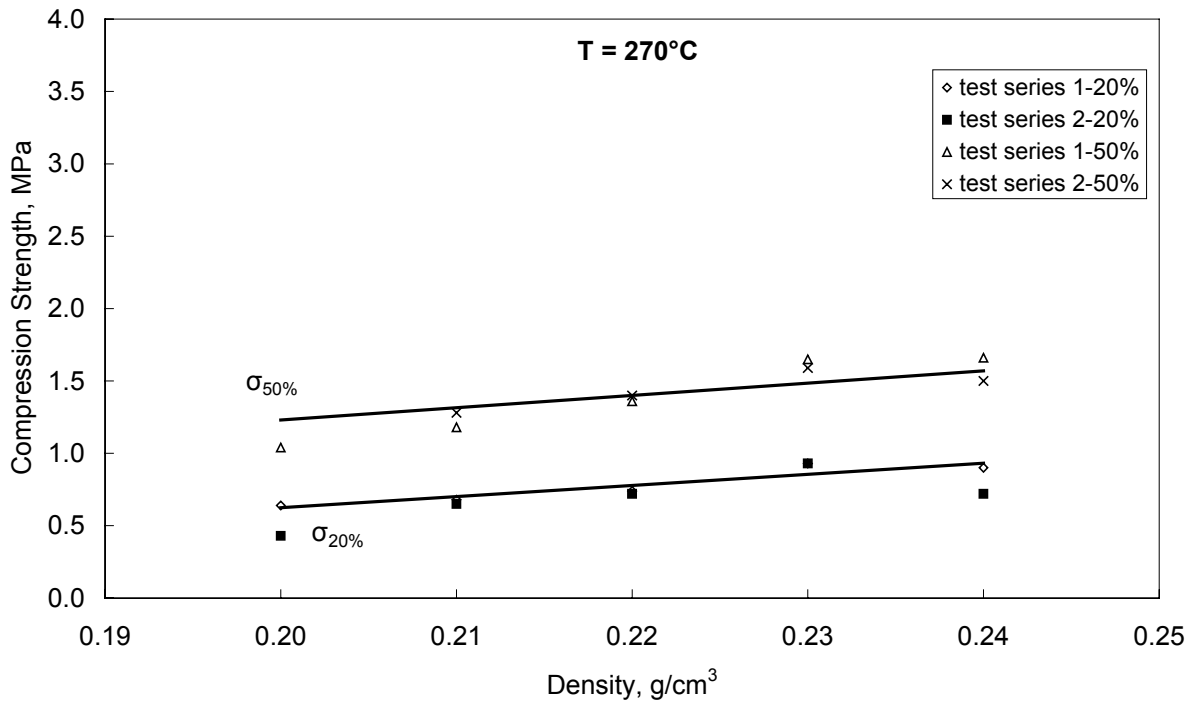


Fig. 6-3 Compression strength as a function of density of Alporas foams, tested at 270°C.

The obtained compressive stress-strain curves consist of three regions. Linear elastic regime, in which the stress attains its maximum value indicating the onset of the collapse,

followed by a softening region to a plateau regime, which is caused by the evolution of collapse bands due to buckling of individual cells [MOT01]. In this plateau regime there are distinct and quite regular stress oscillations [SMI97]. Finally, the densification regime, in which the cells crush together and the cell wall material is compressed. The stress increases rapidly, as the faces and edges are forced together [GIB97]. The duration of each region depends on the density of the foam. The magnitude (or the height) of the compression strength as well as the plateau stress of Alporas increases linearly with increasing the foam's density. A foam with lower density exhibits a longer and flatter plateau. This is because of the structure itself, which affords more opportunity for cell walls to collapse and deform [PAR00]. Moreover, the compression strain, at which the densification starts, increases with decreasing the foam's density, as shown in **Fig. 6-4**.

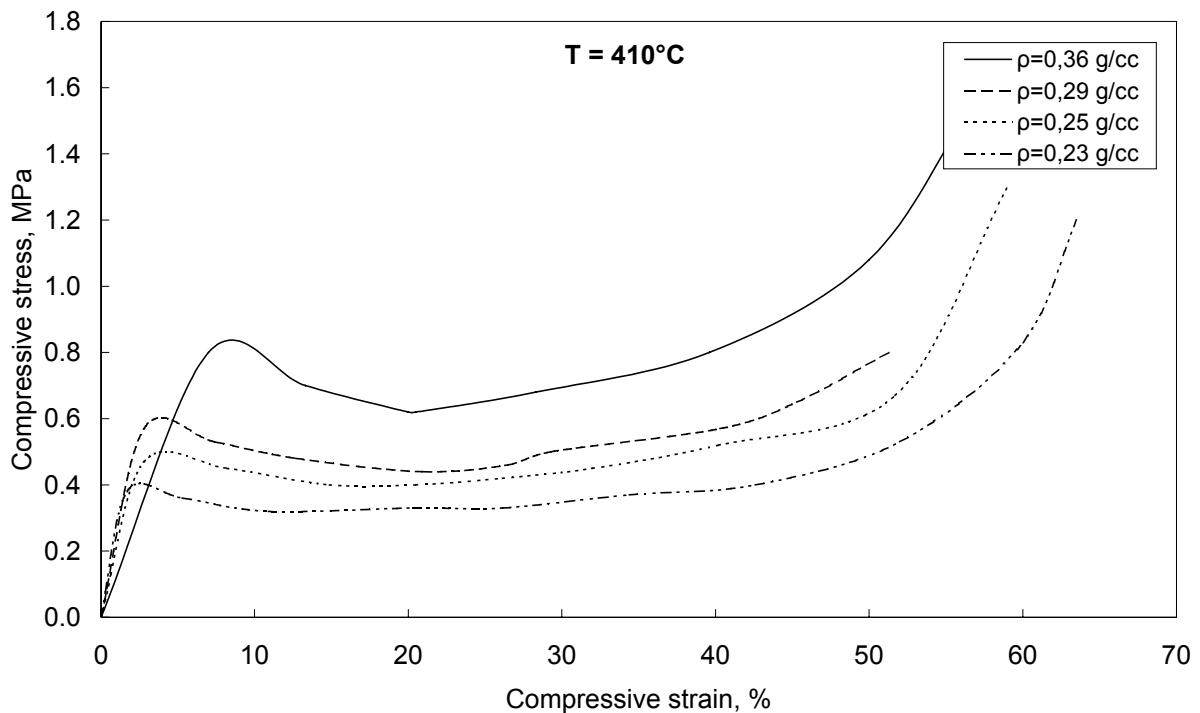


Fig. 6-4 Stress-strain curves of Alporas foams with a range of density between 0.25 g/cm^3 and 0.36 g/cm^3 .

6.2.1.1.2 Effect of Temperature

A comparison of a set of curves plotted at various temperatures clearly reveals the tendency of the Alporas foams to deform plastically. **Fig. 6-5** shows that decreasing the test temperature is accompanied with an increase within the compression strength as well as in the plateau stress, whereas the compression strain, at which densification occurs, decreases. Alporas foams with a density of 0.20 g/cm^3 having at room temperature

a compression strength value of about 1 MPa. This value decreases to its half at 410°C and to its one tenth at 620°C. The reason for this low value at room temperature may be due to the presented thin cell-walls of the structure [GRO03]. The apparent oscillations within the plateau regime of the stress-strain curve may be due to the brittle fracture of cell walls or due to the shearing of the foam walls during the deformation process [KOZ01].

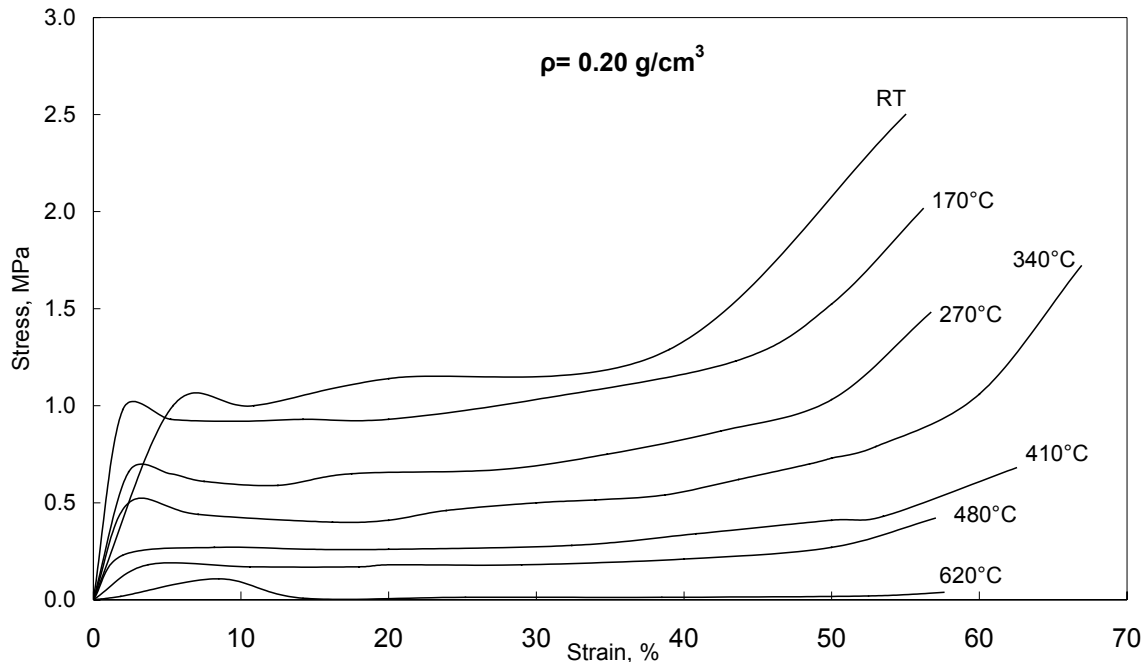


Fig. 6-5 Stress-strain curves of Alporas ($\rho = 0.20 \text{ g/cm}^3$) as a function of test temperature.

The aluminium metal has a great affinity to oxygen, so it forms an oxide layer on the surface of the metal even at room temperature. With increasing the temperature, the thickness of the oxide layer covering the surface of the metal also increases. It was found that the oxide scale at RT has a thickness around 5 nm. The oxide scale at this thickness does not affect the deformation of the foam, however, if the oxide scale becomes thicker, what is expected with increasing the temperature, it may influence the behaviour of foams having struts only a few micrometers thick. This mechanism may be consistent with the reduction in the amount of the absorbed energy (area under stress-strain curve) by the foam that is observed with increasing the temperature [DES03]

Fig. 6-6 below summarises the influence of foam's density as well as the homologous temperature on the ratio of the compressive strength of Alporas foams measured at various testing temperatures to that measured at room temperature. As expected, the compression strength of Alporas foams decreases with increasing the homologous temperature. This high temperature behaviour of Alporas foams is similar to that of compact Al metal. The poor high

temperature mechanical properties of Alporas foams may be due to the coarsening of Al_4Ca and TiAl_3 precipitates.

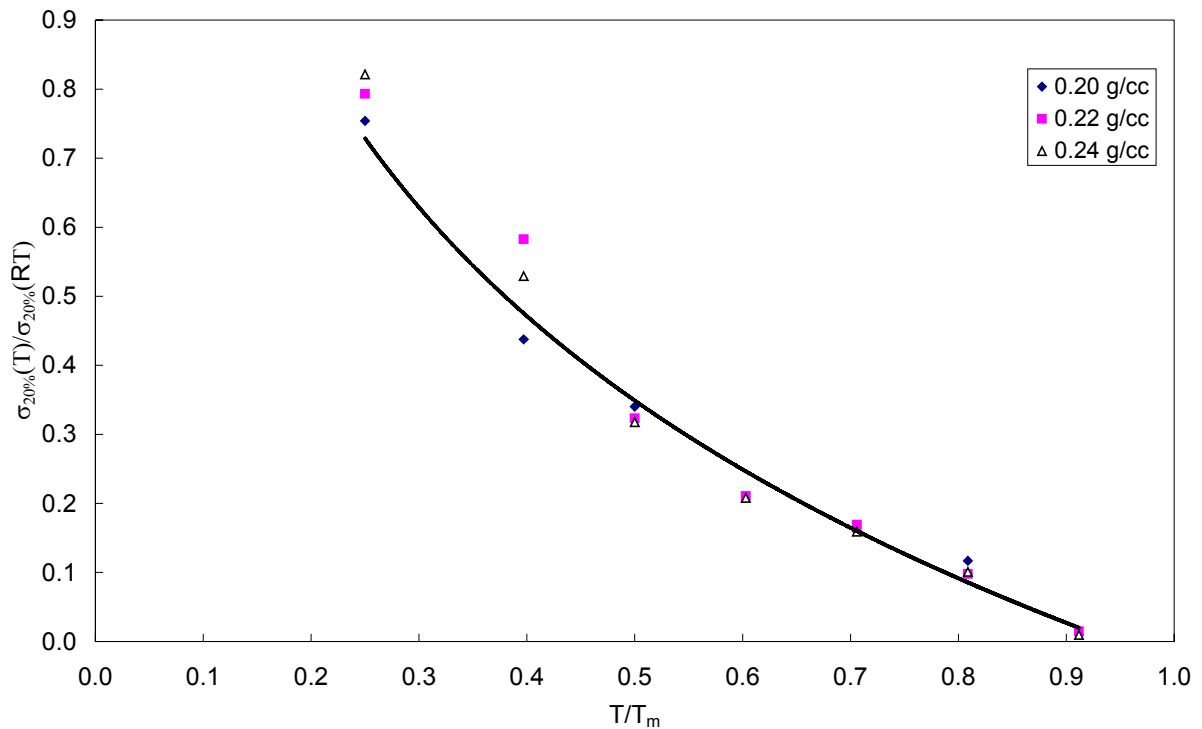


Fig.6-6 The influence of the homologous temperature on the compression strength of Alporas foams having densities of 0.20, 0.24 as well as 0.30 g/cm^3 .

6.2.1.1.3 Effect of Strain Rate on the Mechanical Properties of Alporas Foams

In order to evaluate the compressive behaviour of Alporas foams at high strain rates, compressive tests at three different strain rates, $8 \cdot 10^{-4} \text{ s}^{-1}$, $8 \cdot 10^{-3} \text{ s}^{-1}$ and $8 \cdot 10^{-2} \text{ s}^{-1}$ respectively, have been carried out on Alporas foams having a density of 0.20 g/cm^3 . **Fig. 6-7** shows that an increase of strain rate is accompanied by a slight increase of the plateau stress as well as the compressive yield strength. This slight increase was also observed in case of compact material [BÖL03]. Consequently, the foams collapse more quickly. A large densification strain (an indication for a large resistance for deformation) was obtained upon deformation at low strain rates. Two factors affecting the foam resistance against deformation upon high strain rates deformation, they are 1) the release of the entrapped gas inside the closed-cells and 2) resistance of the foam skeleton against elastic-plastic deformation (strain-rate insensitive) [BÖL03].

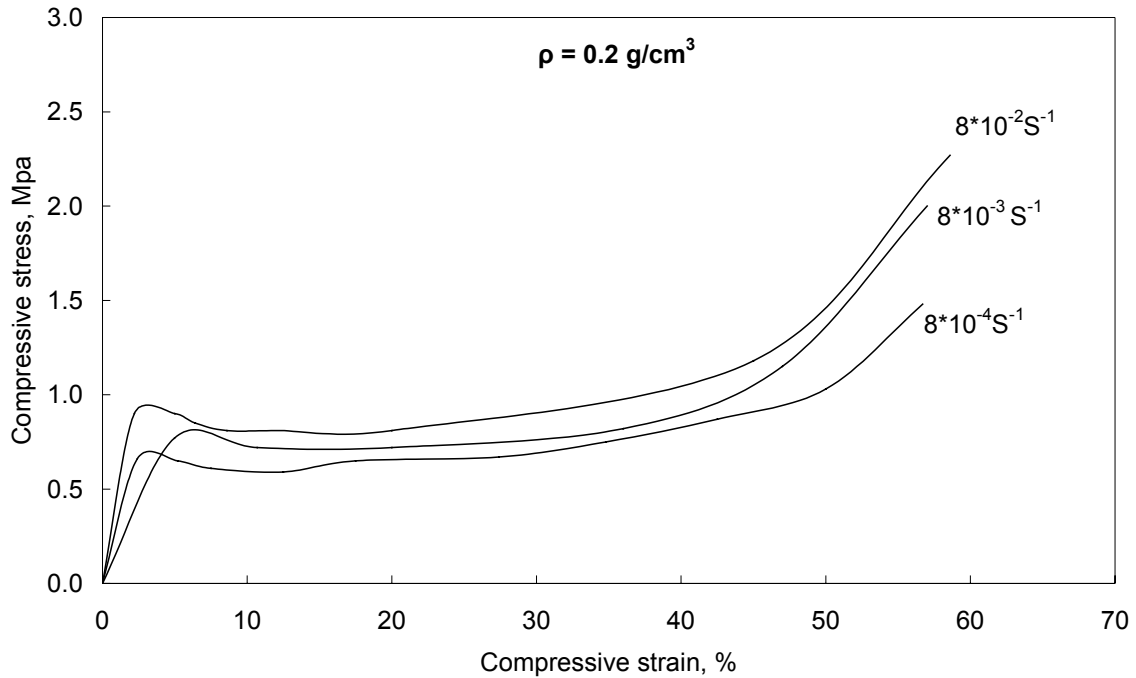
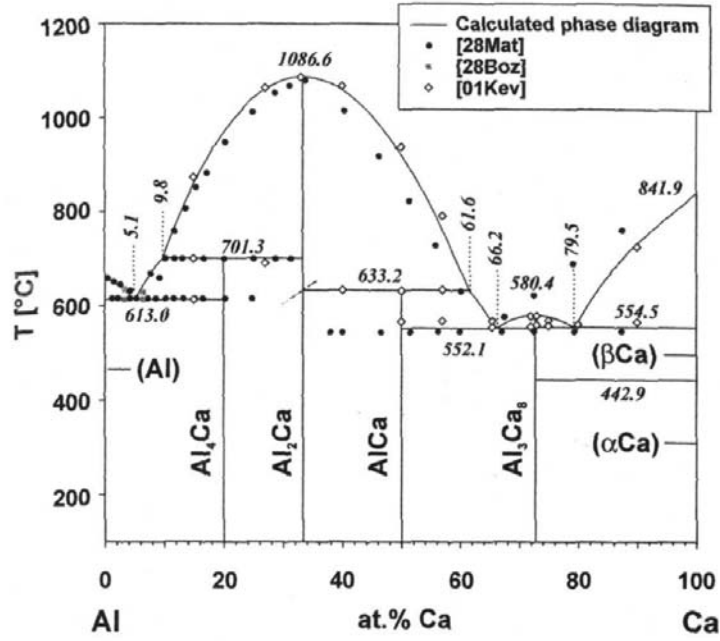


Fig. 6-7 Effect of strain rate on the stress-strain behaviour of the Alporas foams ($\rho = 0.20 \text{ g/cm}^3$), compressed at 270°C .

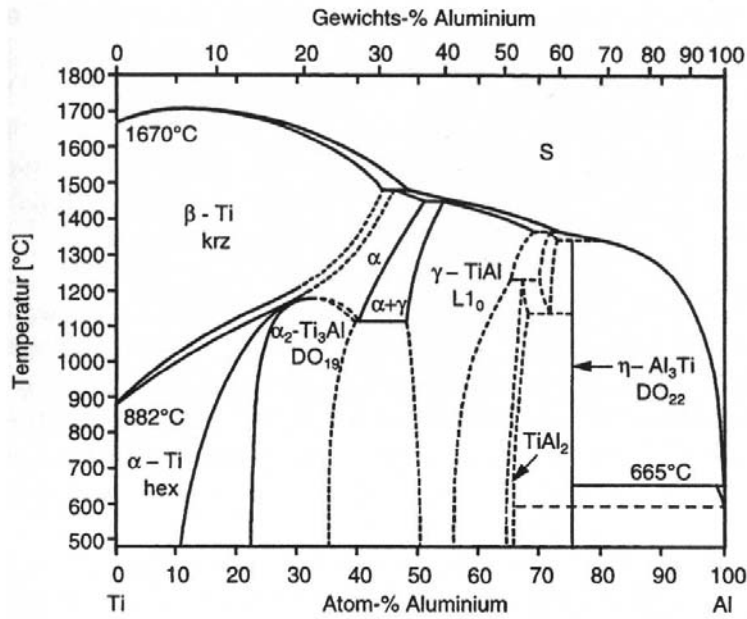
6.2.1.1.4 Microstructural Examination of Alporas Foams

The mechanical properties of foams depends mainly on the variation of the foam's density as well as on the cell geometry, e.g. shape, cell size, cell size distribution, defects within the cell structure and the cell wall thickness. The samples, which underwent the compressions tests, were examined conventionally via light microscopy. In order to preserve the foam structure during preparation, the samples were imbedded in a self-curing plastic mixture.

Fig. 6-8 illustrates the binary phase diagram of Al-Ca as well as Al-Ti systems, respectively. The cell wall microstructure of Alporas consists of Al-matrix, an eutectic phase, which is rich in Ca and Al, and a globulitic phase, which consists of Ti and Ca **[KRI00]**, as shown in **Fig. 6-9**.



(a)



(b)

Fig. 6-8 a) Calculated phase diagrams of Al-Ca [KEV01] and b) Al-Ti systems [MCC89, MUR86], respectively.

Change in cell wall thickness of Alporas was prominent in the cell structure. This change in wall thickness results from the cells, which have been elongated during the deformation, and thus results in a change in the density distribution, i.e. there are regions of higher density and

others having lower one, from which the deformation propagate to the rest of the structure [KRI99].

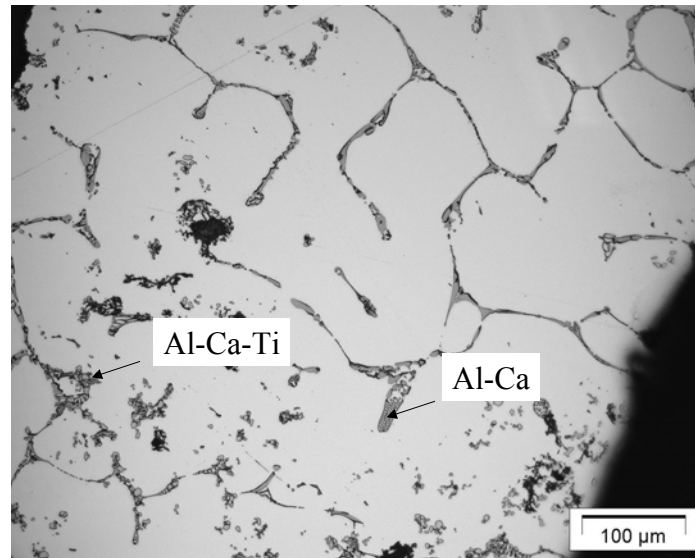


Fig. 6-9 Microstructure of a cell-wall of an Alporas sample ($\rho = 0.25 \text{ g/cm}^3$) deformed at 340°C .

Fig.6-10 (a-d) illustrates the difference within the cell-wall thickness of undeformed as well as deformed Alporas samples upon compressive loading at 340°C in the linear-elastic, plateau regimes as well as after complete densification, respectively. It can be seen that the grain sizes of Alporas foams are of several hundreds micrometer so the grains usually stretch over the whole width of the cell faces [HAA03]. It is obvious to notice that great changes within the cell-wall thickness of the sample take place upon loading. The curvature of the cell-wall also increases with increasing the load. When the load goes over a certain value, which is the maximum value that can be withstood by the cell-walls, rupture occurs, as shown in **Fig. 6-10 d**. The presence of such thin cell-walls may be the cause for this low strength of the foams [GRO03].

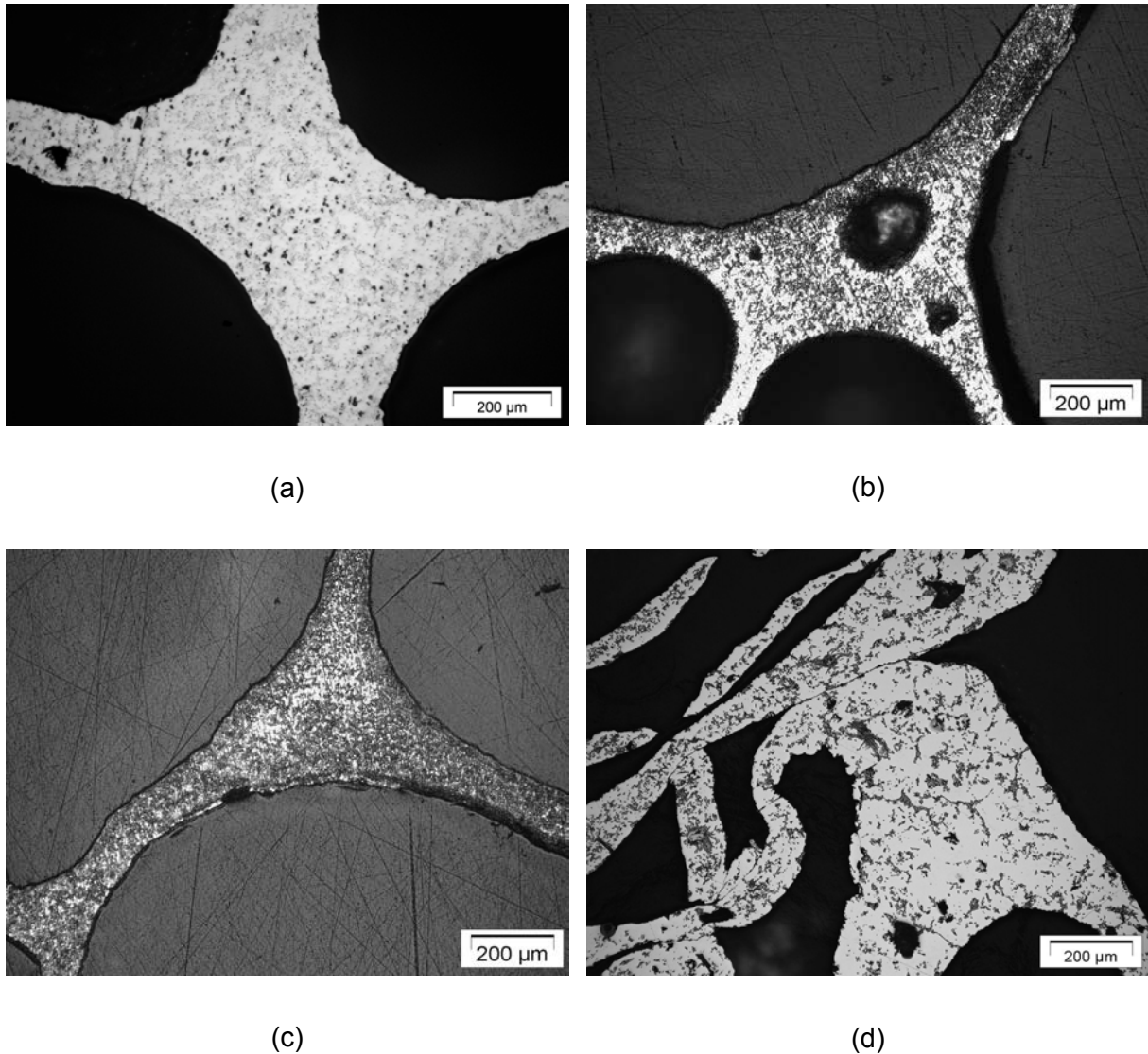


Fig.6-10 Cell wall microstructure of Alporas foams (a) undeformed, (b) in linear-elastic regime, (c) in plateau regime and (d) after densification at 340°C, respectively.

Fig. 6-11 shows the cell-wall microstructure of the Alporas foams, which have been tested at different temperatures. It is clearly visible that the cell wall of the deformed samples have been largely distorted [MCD03]. The dominant deformation mechanism was found to be the cell-wall buckling [MCD03, SAL03]. Characteristic deformation behaviour of the metallic foams is the formation of fracture zones in the form of deformation bands having a thickness equals to the pore diameter. Such deformation bands are formed in a perpendicular direction to the main deformation direction [HAG99].

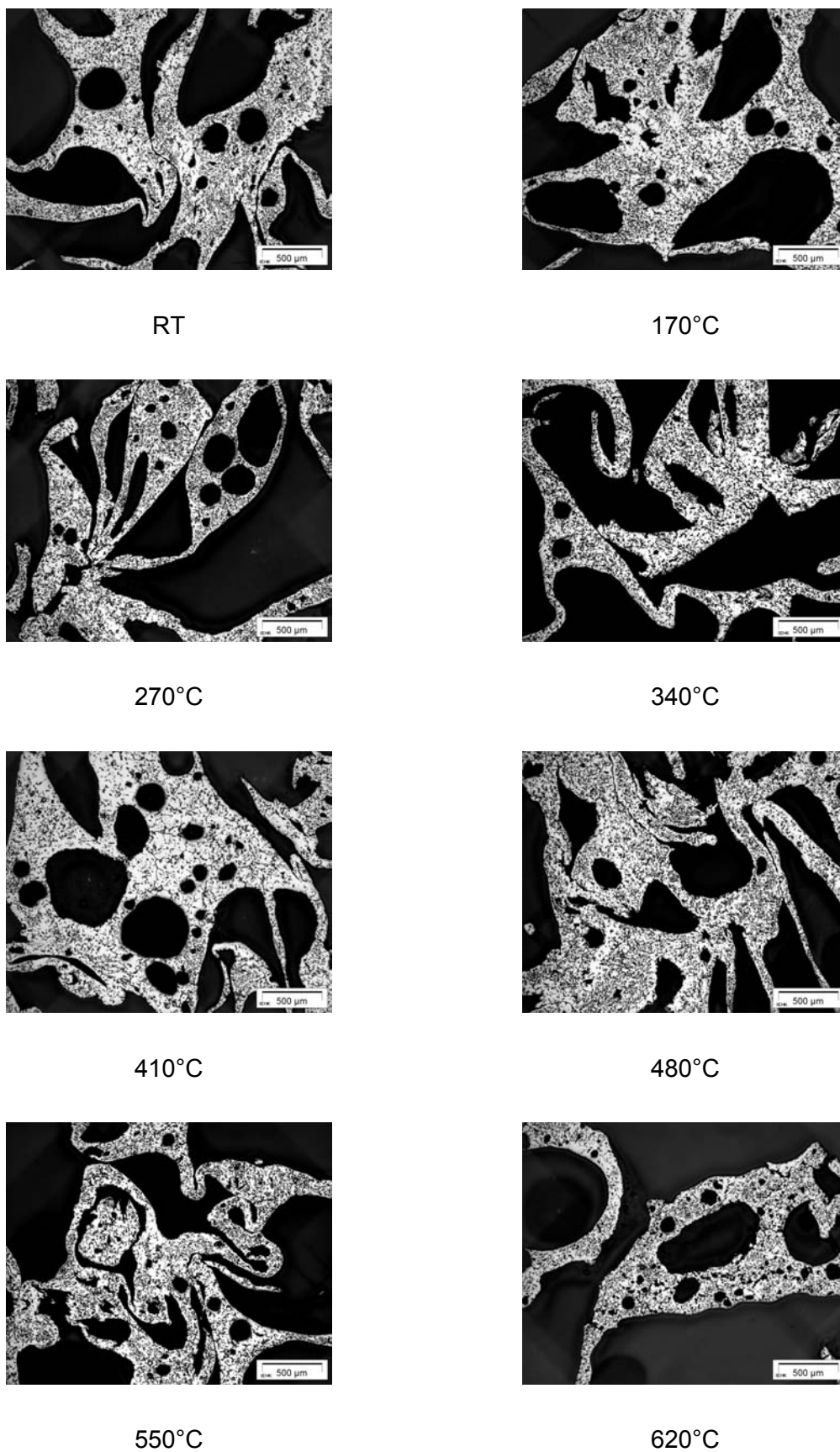


Fig. 6-11 Cell wall microstructure of Alporas foams after testing at different temperatures.

6.2.1.1.5 SEM Characterisation of Alporas Foams

After compressive deformation, the fracture surfaces of the compressed samples have been examined using a scanning electron microscope (SEM) Stereoscan 90, Firm Cambridge Instruments with an acceleration voltage of 25 kV in order to provide insight into the micro-mechanisms of the cell wall failure. Due to its closed-packed face-centred cubic crystal lattice, aluminium has a very good capacity for deformation. SEM micrograph, shown in **Fig. 6-12a**, reveals a fractured surface of a cell wall of Alporas foam. As the deformation progresses, a gradual break of interatomic bonding takes place; which results in the formation of local cracks [**SAV61**]. When the stress intensity factor in front of the crack tip exceeds a critical value (K_{IC}), cracks begin to initiate and propagate across the cell walls and a ductile fracture takes place, **Fig. 6-12b** [**NN96**, **BÖL03**].

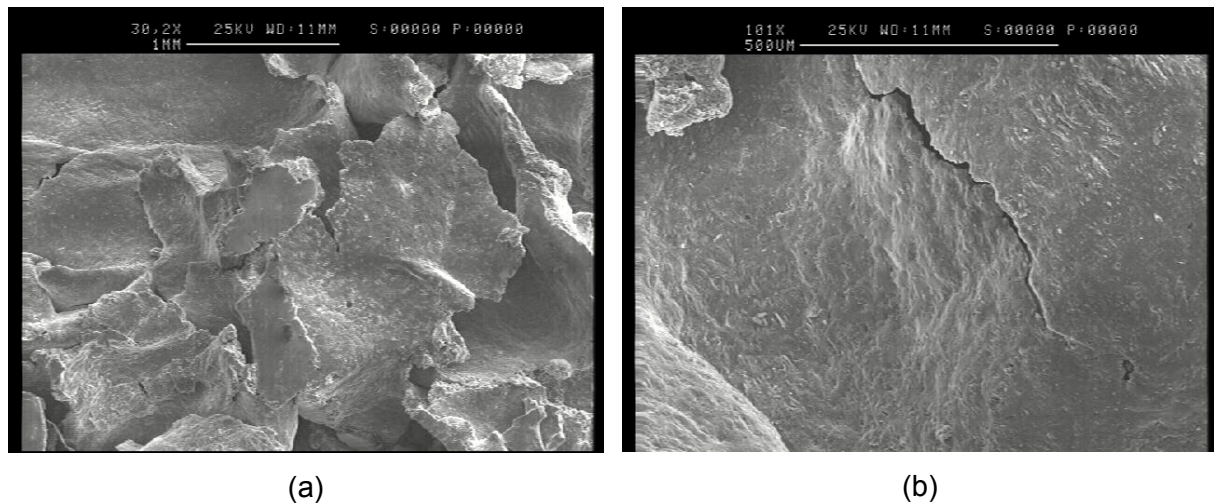


Fig.6-12 SEM-micrographs of a cell wall of Alporas foams tested at 170°C.

6.2.1.2 Quasi-static Compression Test of the Distaloy Foams

6.2.1.2.1 Determination of the Compression Strength of the Green Distaloy Foams

In order to determine the compression strength of the green samples of the Distaloy foams, room temperature quasi-static compression have been carried out on green samples of Distaloy foams having a cross sectional area of 40 x 40 mm² and with different thickness ranging from 8 mm to 10 mm. The tests were conducted at tests at a constant rate of displacement 1 mm/min. The measured $\sigma_{20\%}$ values of the Distaloy foams in the green state lie within the range of 2.0 MPa (for a foam sample having a maximum density of 1.8 g/cm³) and 1.6 MPa (for a foam sample with a minimum density of 1.5 g/cm³). **Tab. 6-2** gives the compression strength at 20% for the Distaloy foams in the green state.

Density, g/cm ³	$\sigma_{20\%}$, MPa
1.5	1.6
1.6	1.6
1.7	1.7
1.8	2.0

Tab- 6-2 Compressive strength values at 20% for Distaloy samples in the green state.

The density of the Distaloy samples was measured once more after the sintering process. A noticeable enhancement in the foam's density after the sintering process was observed, this is because of the building of a stable network (necking) during the sintering process between the particles and the compaction or the hardening of the cell walls as well [BRA04].

Fig. 6-13 shows the behaviour of the density of the samples, measured before and after the sintering process, as a function of the added amount of water. After undergoing the sintering process the samples became denser, as shown from the values listed in **Tab. 6-3**.

Added amount of solvent (water), g	Density before sintering, g/cm ³	Density after sintering at 1170°C, g/cm ³
19.0	1.8	1.9
20.0	1.7	1.7
21.0	1.6	1.7
22.0	1.3	1.5
23.0	1.3	1.4

Tab. 6-3 Density of the Distaloy foams before and after the sintering process as well.

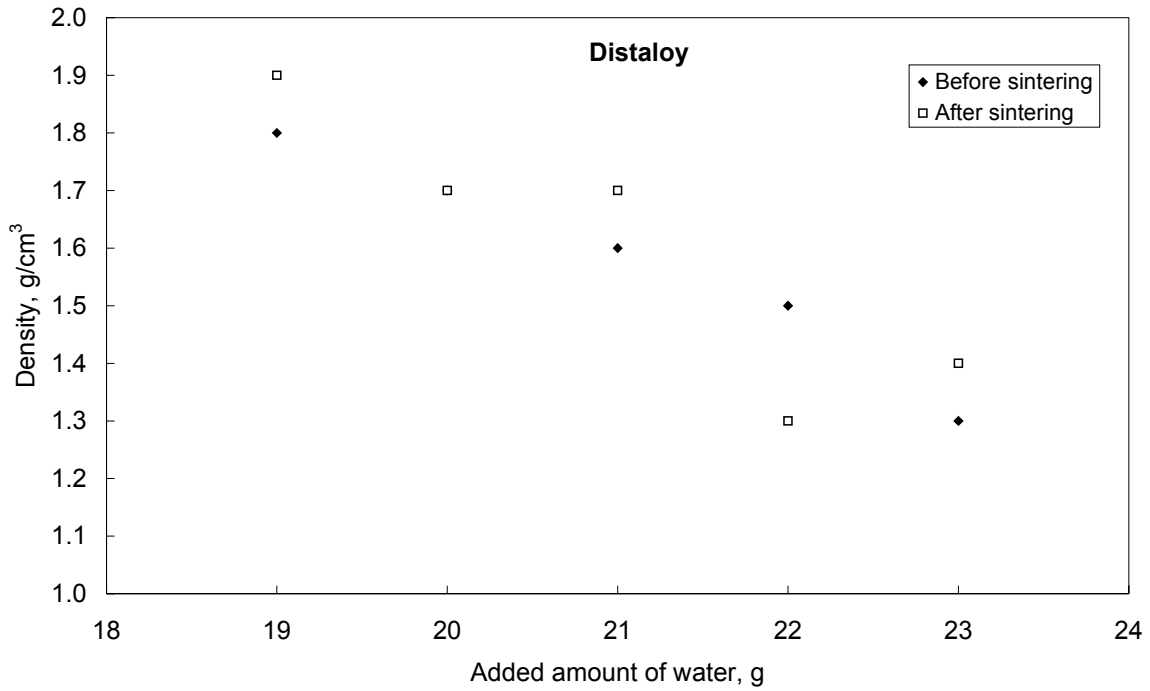


Fig.6-13 Density of the Distaloy samples measured before and after the sintering process.

In comparison with the green samples, the sintered samples have attained higher compressive strength values. This is due to the enhancement in the foam’s density resulted from the formation of metallic bonds during the sintering process. **Tab. 6-4** lists the compressive strength values at 20% for sintered Distaloy samples.

Density, g/cm ³	$\sigma_{20\%}$, MPa
1.4	5.6
1.6	9.3
1.7	10.5
1.9	18.0

Tab. 6-4 Compressive strength values at 20% for sintered Distaloy samples.

6.2.1.2.2 Effect of Density

Fig.6-14 shows the stress-strain curves of the Distaloy foams with different densities ranging from 1.4 g/cm³ to 1.9 g/cm³. Typically, compressive stress-strain curves consisting of three regions have been obtained. Linear elastic regime, a plateau regime and a densification regime. The critical stress which marked the end of linear elastic deformation and the beginning of foam collapse, is known as the compression strength. In the plateau regime, in which the cell walls buckle and collapse, stress increases slightly with an increase in the amount of strain. The attitude of the plateau stress is strongly affected by the intrinsic yield

strength of the metal, whereas the length of the plateau regime depends on the density of the foam [PAR00]. Foam with a higher density has a short plateau regime. On the other hand, foam of a lower density exhibits a longer, flatter plateau and the collapse of the cell walls takes a long time compared to the higher density one.

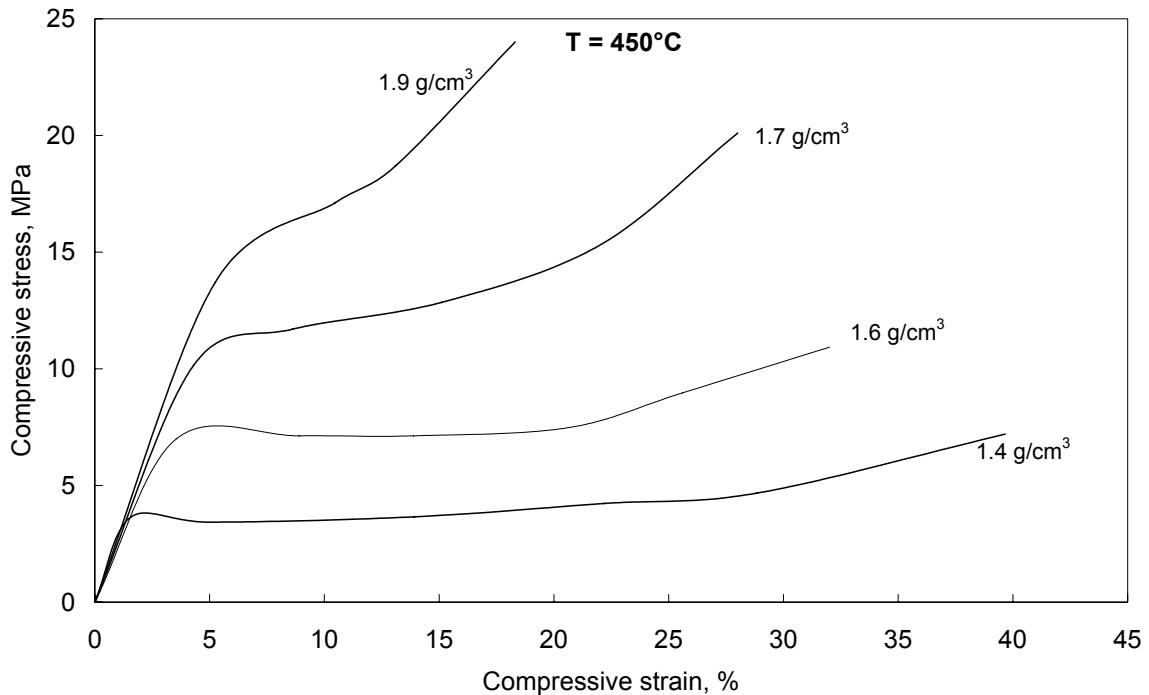


Fig. 6-14 Stress-strain curves of Distaloy foams having different densities.

6.2.1.2.3 Effect of Temperature

The previous experiments investigated the effect of the foams' density on their mechanical properties and showed that an increase within the foam's density leads to an enhancement in the mechanical properties. In the following the temperature dependence of the mechanical properties of metallic foams will be studied. Distaloy samples having a density of 1.7 g/cm^3 have been compressed at various temperatures ranging from room temperature (RT) up to 800°C . The resulting compressive stress-strain curves are depicted in **Fig. 6-15**. The compressive strength of the Distaloy foams increases with the temperature until a certain temperature (450°C) is reached. This increase in the compression strength with increasing the temperature may be due to the ageing effect, where the diffusion velocity of c-atoms increases towards the dislocations, and thus hinders the dislocation motion and consequently raises the strength of the material [BLE99]. When the temperature goes over 450°C , the foams begin to soften and a decrease in both the compressive yield strength as well as the plateau stress is observed; moreover, the densification strain has been increased.

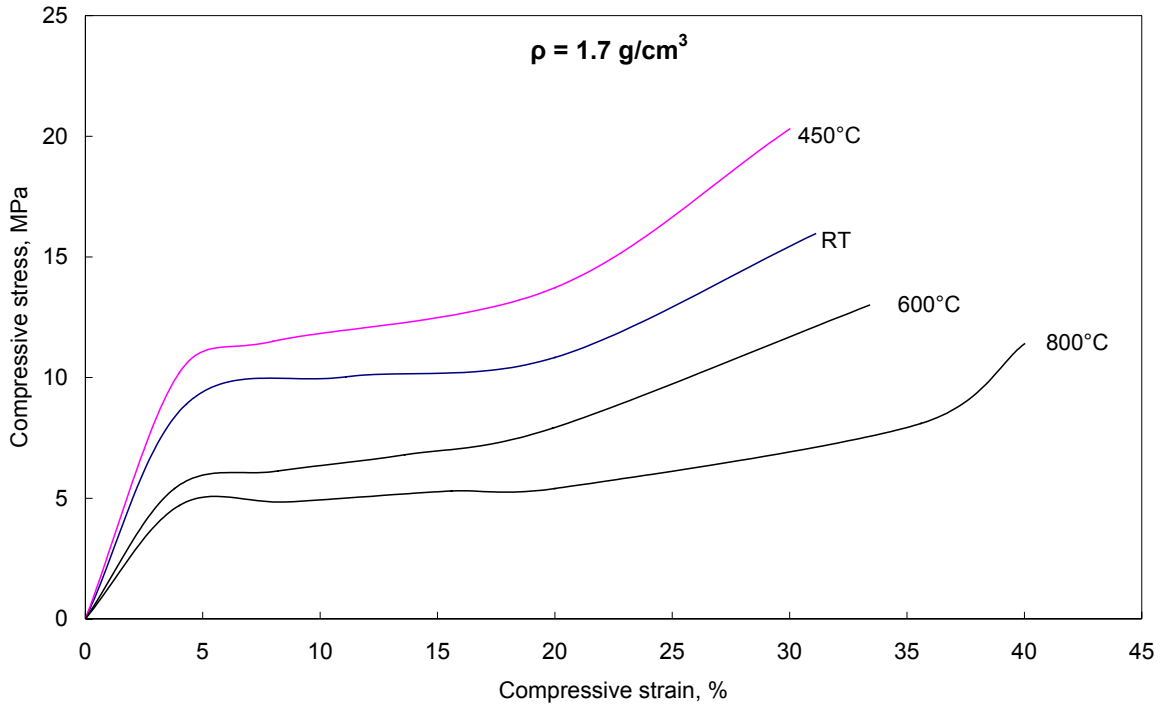


Fig. 6-15 Temperature dependence of stress-strain curves of the Distaloy foams ($\rho = 1.7 \text{ g/cm}^3$).

In **Fig. 6-16**, the ratio of the compressive strength at 20% measured at various temperatures to that measured at room temperature for different densities of the Distaloy foam is represented on the y-axis, whereas the homologous temperature is plotted on the x-axis. It can be seen that an increase within the foam's density leads to a higher compressive strength value. This is the same at all test temperatures. On the contrary, an increase in the test temperature leads to poor mechanical properties. If we consider, for example, foam with a density of 1.4 g/cm^3 compressed at RT, its compressive strength value was measured to be about 5.5 MPa; whereas about the half of this value was obtained upon compression at 800°C . This is similar in case of foams having a density of 1.9 g/cm^3 . A compressive strength value of about 16 MPa was obtained at RT, whereas about 50% of this value was obtained if the foam is compressed at 800°C . The measured compressive strength values are listed in **Tab. 6-5**. The large scattering in the obtained results are probably due to the inhomogeneous density distribution within the foam cells.

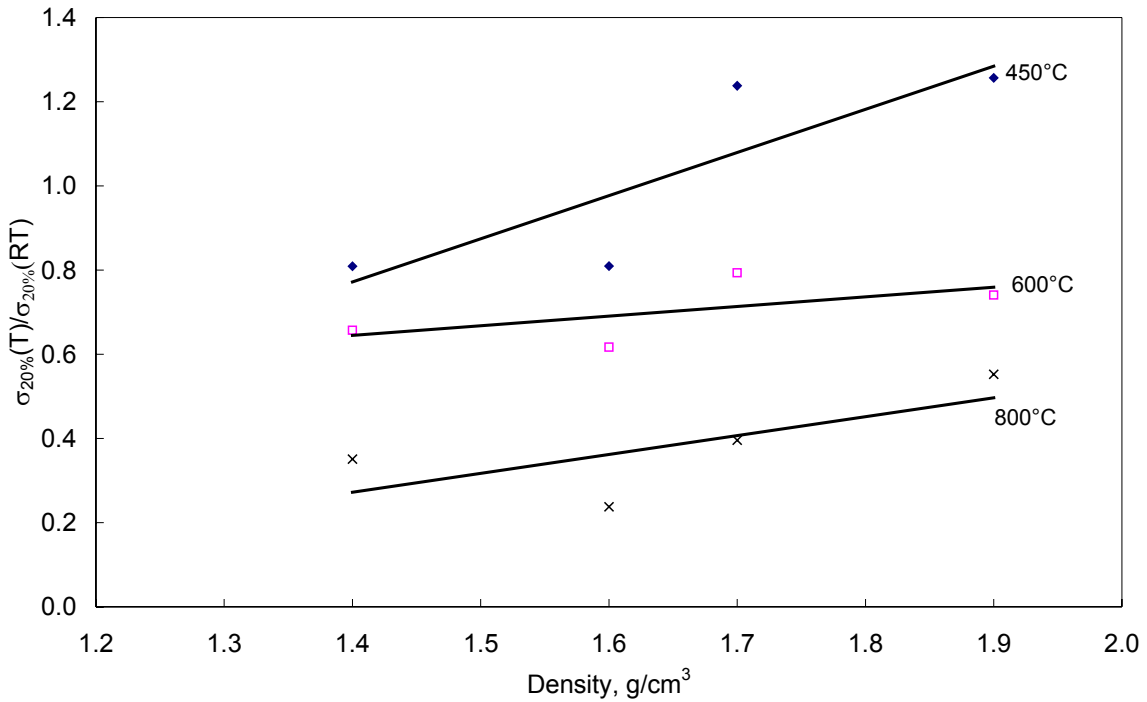


Fig. 6-16 Compression strength (mean value) of Distalloy foams as a function of temperature and foam’s density.

Density g/cm ³	Compression strength at 20% (σ _{20%}), MPa							
	RT		450°C		600°C		800°C	
1.4	6.2	4.9	4.1	4.8	3.2	4.0	1.9	2.0
1.6	9.4	9.1	7.5	7.5	6.3	5.1	2.1	1.9
1.7	10.1	10.8	13.7	12.0	7.9	8.7	5.4	2.9
1.9	20.2	15.7	24.1	21.0	13.2	13.4	-	7.4

Tab. 6-5 Density and temperature dependence of compression strength of Distalloy foams.

6.2.1.2.4 Metallographic Examination

6.2.1.2.4.1 Stereoscopic Examination of the Distalloy foams

The stereoscopic macrographs of the Distalloy foams after high temperature compression testing in air shows that the samples have been heavily oxidised due to the reaction occurring between the oxygen of the air and the iron particles and this explains the presence of this dark colour on the samples’ surfaces, as shown in **Fig. 6-17**.



Fig. 6-17 Stereoscopic macrographs of Distaloy foams having different densities, tested at RT (left), 450°C (middle) and 600°C (right), respectively.

6.2.1.2.4.2 Microstructural Examination of the Distaloy Foams

The samples for the microstructural investigation were prepared by using normal grinding and polishing techniques. The samples have firstly to be embedded under vacuum in a plastic mixture in order to protect the cell structure from damage during preparation. Microstructural examination was carried out using a light optical microscope working with a digital software soft imaging system (SIS). As shown in **Fig. 6-18**, the microstructure of Distaloy foam consists of a ferrite matrix, primary as well as secondary pores and iron oxide. The size of the primary pores ranges from 0.1 to 3.0 mm whereas the secondary pores having a size of typically 0.1 mm [ANG03]. The secondary pores are usually found within the cell walls. The iron oxide may be formed via several routes; (i) the reaction of metal particles with water molecules during the sintering process, or (ii) the reaction of the iron particles with the oxygen of the air during the heating process upon compression.

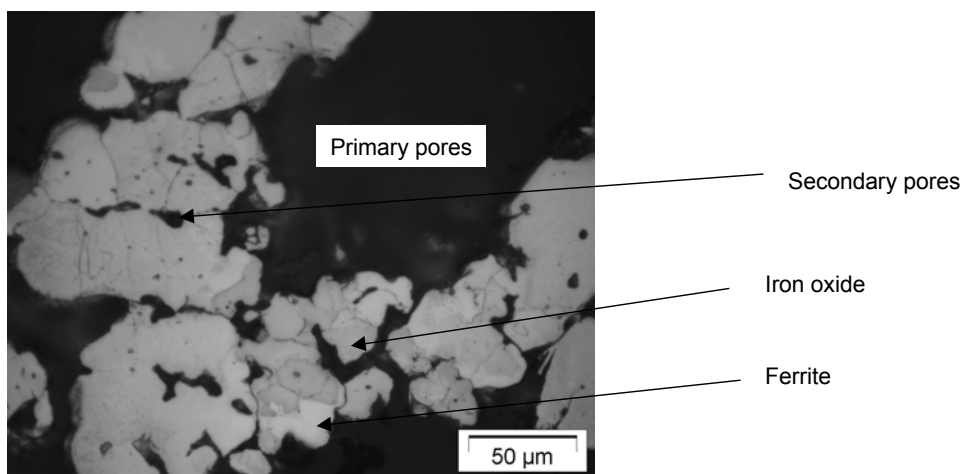


Fig. 6-18 Microstructure of Distaloy foams.

6.2.1.2.4.3 Measurement of the Oxide Scale Thickness on the Distaloy Foams

Due to their ability to build a protect layer on their surfaces, metallic materials can be used at high temperatures for prolonged times. The oxide layer growth rate must be slow in order to provide an effective protection influence. The life-time of a material used at high temperatures depends on the oxide growth rate as well as on oxide stability [LEY97].

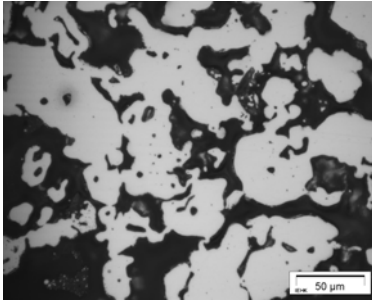
Tab. 6-6 elucidates the oxidation dependence of Distaloy foams on the temperature. After compression at high temperatures in atmospheric air, an oxide layer was formed on the surfaces of the Distaloy foams. The thickness of the oxide scales which built up on Distaloy foams of differing densities (ranging from 1.7 g/cm³ to 1.9 g/cm³), has been measured at two different positions, around the edges and in the middle of the specimens. At each position two different sites (a, b) have been determined. Increasing the oxide thickness is a matter of a diffusion process.

Position	T, °C	Oxide thickness, μm								Mean
Edge-a	25	0	0	0	0	0	0	0	0	0
	450	3.5	3.2	4.5	4.7	4.8	2.3	2.6	2.2	3.5
	600	7.4	13.5	7.2	6.9	7.8	13.6	11.0	2.7	8.8
	800	41.3	35.7	36.9	32.8	45.7	33.2	11.0	11.2	31.0
Edge-b	25	0	0	0	0	0	0	0	0	0
	450	2.8	2.5	3.0	2.3	2.4	7.1	2.1	3.6	3.2
	600	4.7	6.4	16.5	10.5	7.1	17.3	23.1	9.3	11.8
	800	42.1	37.7	28.4	10.4	24.8	13.3	21.8	34.6	26.7
Middle-a	25	0	0	0	0	0	0	0	0	0
	450	3.0	1.5	2.8	1.7	1.6	2.0	1.7	0.7	1.9
	600	5.2	6.8	4.7	10.1	3.6	4.7	5.1	2.9	5.4
	800	2.2	1.7	2.6	1.4	1.9	4.9	2.4	2.0	2.4
Middle-b	25	0	0	0	0	0	0	0	0	0
	450	2.1	3.0	2.0	1.4	1.7	1.8	2.6	1.4	2.0
	600	4.9	7.3	3.6	3.9	3.6	5.9	3.5	5.2	4.8
	800	2.4	1.4	2.4	1.5	1.1	2.7	1.4	2.6	1.9

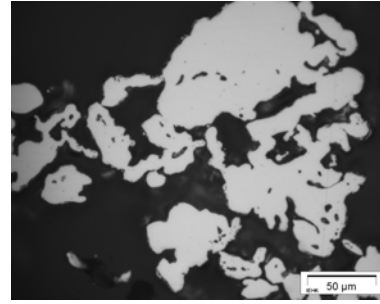
Tab. 6-6 The thickness of the scale, which has been built on the oxidised Distaloy foams.

As shown in **Fig. 6-19** and **Fig. 6-20**, there is no oxide layer, neither in the middle nor around the edges of the Distaloy samples compressed at RT. The edges of the samples have been heavily oxidised in comparison to the middle of the samples. This is illustrated by the values given in **Tab. 6-6**. A relation exists between the thickness of the built-up oxide scale and temperature - where an increase of test temperature leads to the build-up of a thicker oxide scale on the surface of the sample. Increasing the thickness of the oxide scale makes it mechanically unstable. The reason for this is the building of internal stresses, which become larger during the growth of the thickness of the oxide layer [SCH91]. If the oxide thickness exceeds a certain critical value, the growing stresses at the metal/oxide surfaces lead to build-up large normal stresses, which result in exceeding the adhesion forces of the oxide layer and thus results in delaminating of the oxide layer [LEY97]. This thick oxide layer

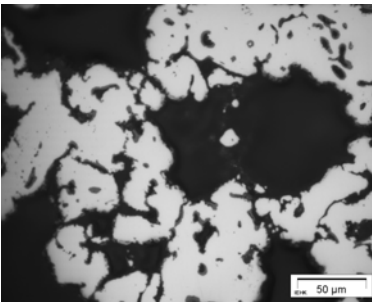
retards the inward diffusion process of the oxygen ions and therefore provides a protection against further oxidation and corrosion **[CLA]**. This leads to the formation of thinner oxide layers in the middle of the samples. The presence of copper as an alloying element in concentrations over 0.25 wt.% contributes in increasing the resistance against corrosion **[VAY97]**. Phosphor has also a positive effect on increasing the corrosion resistance **[HOU00]**. A thick oxide layer can also support the porous structure even above the melting point of the alloy, provided that no significant external force is applied on the structure **[SIM02]**.



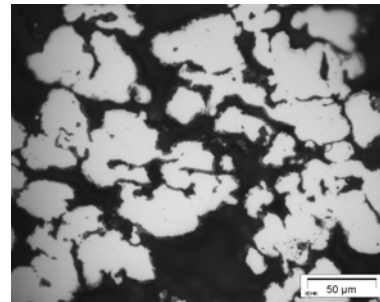
1.9 g/cm³-RT-edge-a



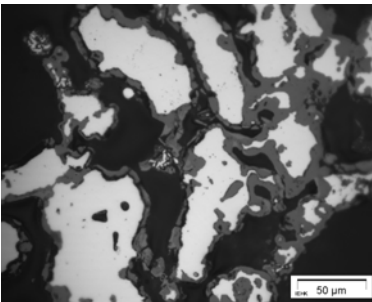
1.9 g/cm³-RT-edge-b



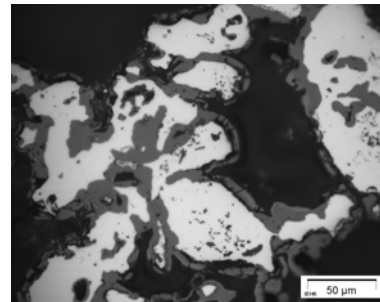
1.9 g/cm³-450°C-edge-a



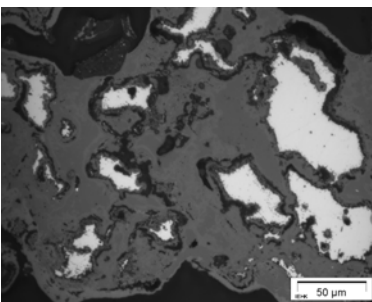
1.9 g/cm³-450°C-edge-b



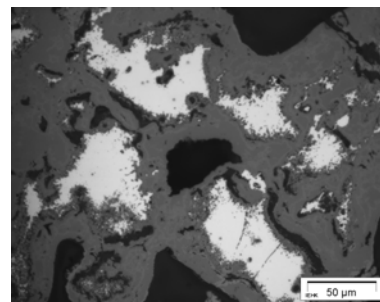
1.9 g/cm³-600°C-edge-a



1.9 g/cm³-600°C-edge-b

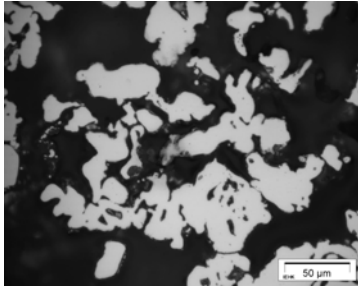


1.9 g/cm³-800°C-edge-a

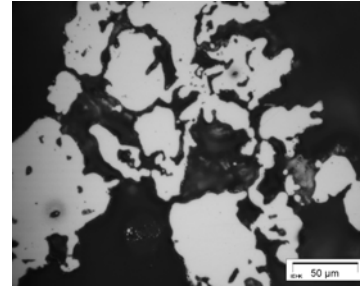


1.9 g/cm³-800°C-edge-b

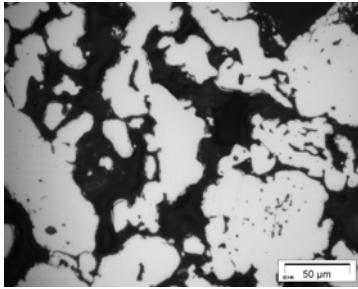
Fig.6-19 Microstructure micrographs at two different sites around the edges of Distaloy foams ($\rho = 1.9 \text{ g/cm}^3$) compressed at 1mm/min at given temperatures.



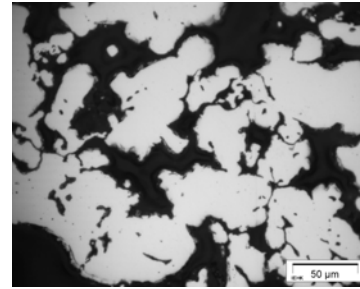
1.9 g/cm³-RT-middle-a



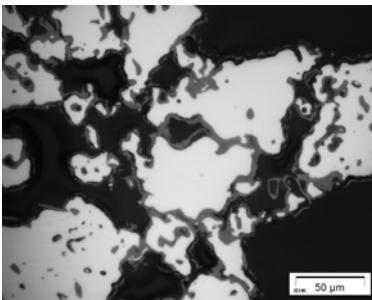
1.9 g/cm³-RT-middle-b



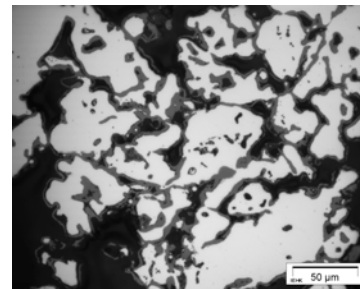
1.9 g/cm³-450°C-middle-a



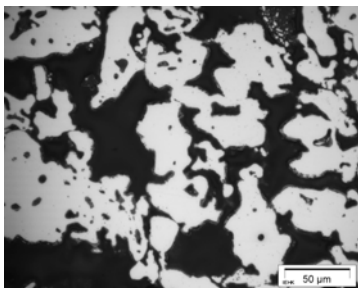
1.9 g/cm³-450°C-middle-b



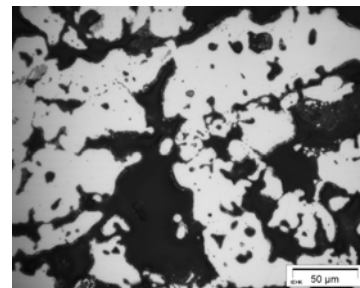
1.9 g/cm³-600°C-middle-a



1.9 g/cm³-600°C-middle-b



1.9 g/cm³-800°C-middle-a



1.9 g/cm³-800°C-middle-b

Fig.6-20 Microstructure micrographs at two different sites in the middle of Distaloy foams ($\rho = 1.9 \text{ g/cm}^3$) compressed at 1mm/min at given temperatures.

6.2.1.2.5 SEM Characterisation of Distaloy Foams

Fig. 6-21 shows a SEM-micrograph of Distaloy foam in the green state. Cell-walls separating each pore from its neighbouring are clearly to be observed. It is also easily to distinguish between the primary pores and the secondary pores. No micro cracks can be observed. On the other hand, **Fig. 6-22** reveals a post-sintering, deformed SEM-micrograph of Distaloy foam. It is difficult here to distinguish between the primary and secondary pores. The formation and propagation of cracks along the cell-walls are the dominant fracture mechanisms. Crack initiates from the weakest and thinnest cell wall and then propagates through the entire structure.

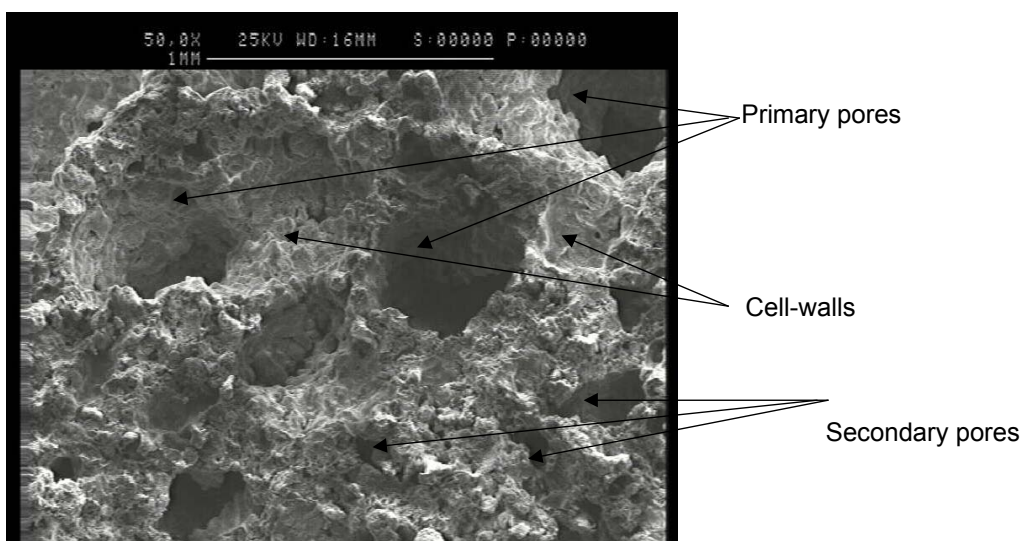


Fig. 6-21 SEM-micrograph of a Distaloy foam ($\rho = 1.8 \text{ g/cm}^3$) in the green state.

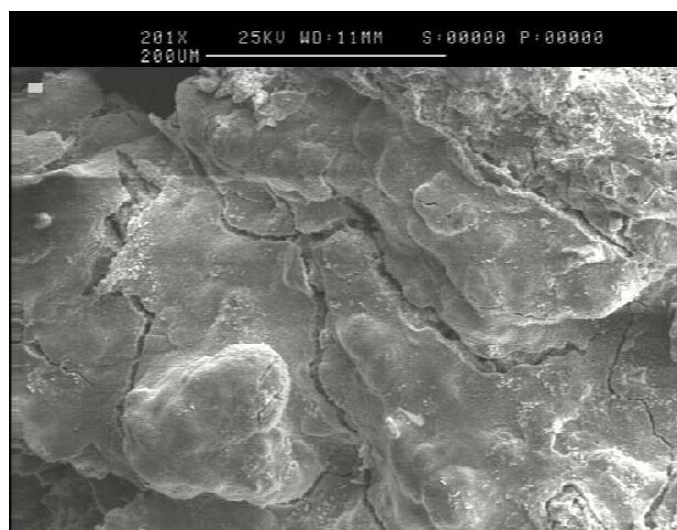


Fig. 6-22 SEM-micrograph of a Distaloy foam ($\rho = 1.8 \text{ g/cm}^3$) deformed at 800°C.

6.2.1.3 Quasi-static Compression Test of the Astaloy Foams

6.2.1.3.1 Determination of the Compression strength of the Green Astaloy Foams

The compression strength of the green Astaloy samples was measured and listed in **Tab. 6-7**. It can be noted that there is a proportional relation between the foam's density of the green samples and their compression strength. An increase within the foam's density increases the compression strength as expected.

Density, g/cm ³	$\sigma_{20\%}$, MPa
1.3	0.6
1.5	0.9
1.7	0.8
1.8	1.4
1.9	1.8

Tab. 6-7 Compressive strength at 20% for Astaloy samples in the green state.

Tab. 6-8 lists the measured values of the densities of the Astaloy foams in the green state, i.e. before the sintering process, and after sintering as well.

Added amount of water, g	Density before sintering, g/cm ³	Density after sintering at 1170°C, g/cm ³
18.0	1.7	1.8
19.0	1.5	1.7
20.0	1.4	1.6
21.0	1.2	1.4
22.0	1.2	1.4

Tab. 6-8 Density of the Astaloy foams in the green state and post-sintering process.

Like the Distaloy foams, the density of the Astaloy foams show a dependence on the added amount of water in both cases; pre- and post-sintering process as well, as shown in **Fig. 6-23**. Before the sintering process the foam's density decreases with increasing the added amount of water which in turn lowers the viscosity of the slurry and thus permit easier escaping of H₂ bubbles, meanwhile the foam's density after the sintering process increases as metallic bonds between the particles are formed.

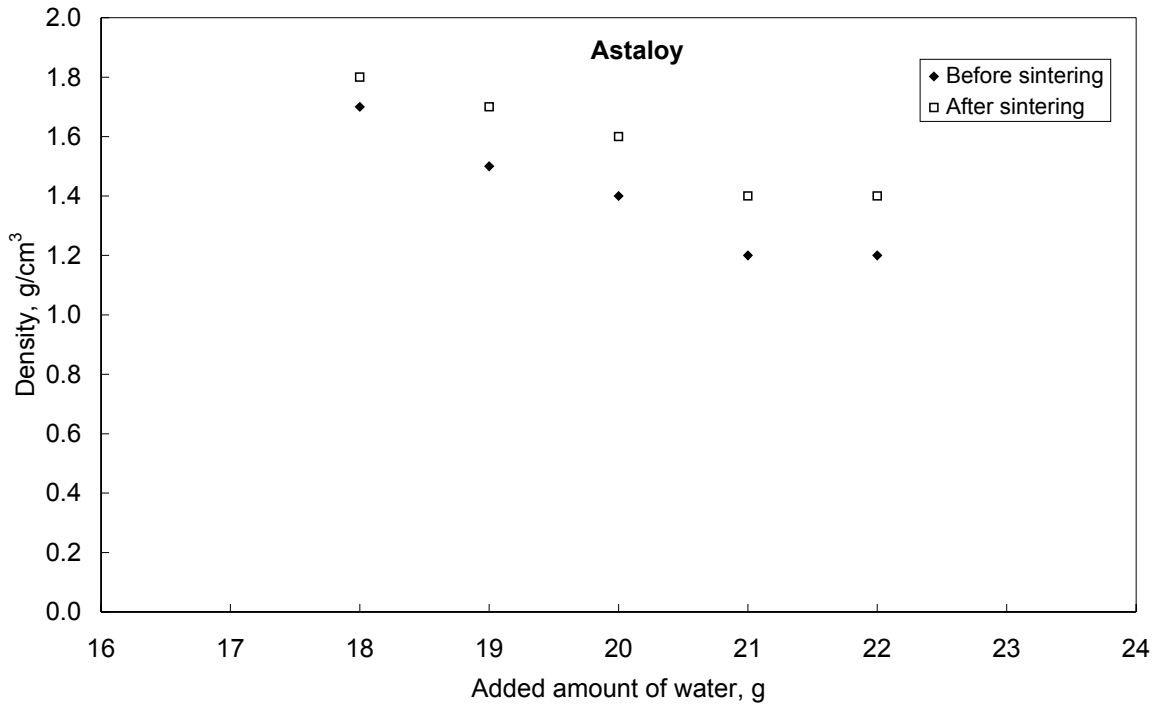


Fig. 6-23 Density of the Astaloy samples measured before and after the sintering process.

6.2.1.3.2 Effect of Density

It was observed that the Astaloy foams also exhibit the typical behaviour of stress-strain curves, namely, linear elastic regime, plateau and collapse or densification regime. Increasing the foam's density is accompanied by an increase in the compressive yield strength as well as the plateau stress, whereas the compressive strain at which the densification starts, decreases, **Fig. 6-24**. After the stress attains its maximum value, softening post-yield response was observed before the plateau stress regime appears. This softening behaviour may be due to either the presence of molybdenum (Mo) or to the buckling of the material's strut. It was found that the materials which have such like softening behaviour may be less attractive as energy absorbers, since this application requires a stress-strain response with a long, flat plateau **[DES01]**. During the plateau stress, energy is absorbed largely by the bending and collapse of cell walls in the foam **[PAR00]**. The height (or the attitude) of the plateau stress is strongly affected by the yield strength of the metal. Thus, when compared to aluminium foams, steel foams afford greater energy absorption capability because of their much higher yield stresses **[BAN95]**.

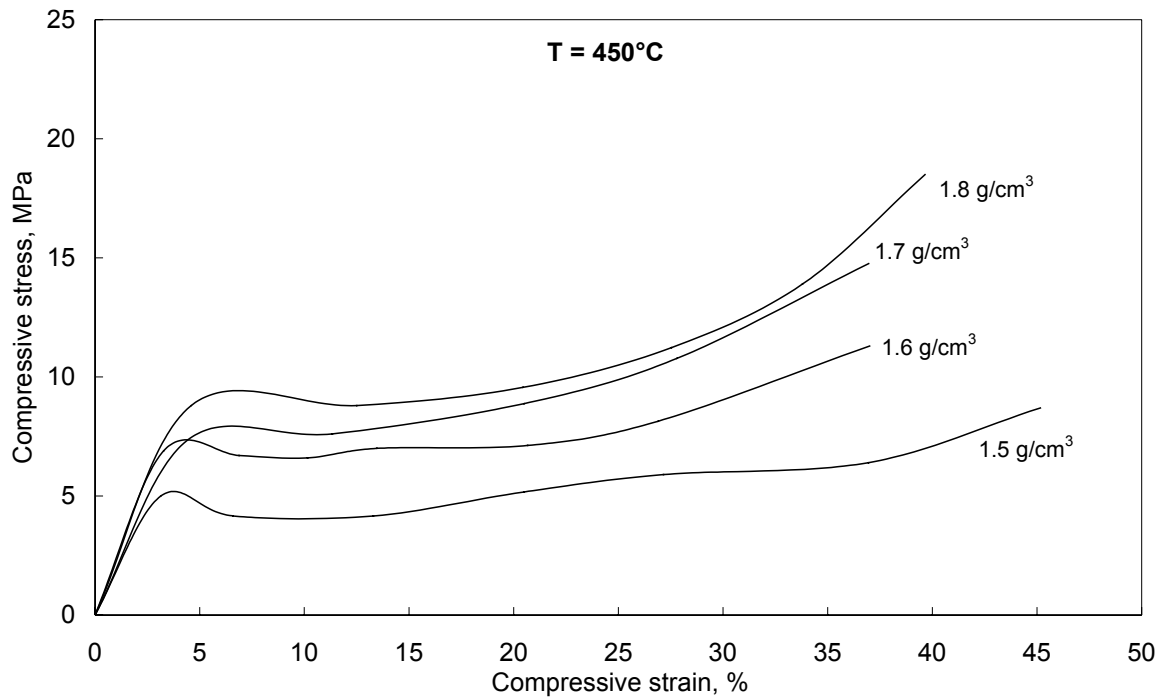


Fig. 6-24 Stress-strain curves of Astaloy samples, tested at 450°C, as a function of foam's density.

6.2.1.3.3 Effect of Temperature

Fig. 6-25 shows the stress-strain behaviour of Astaloy foams with a density of 1.7 g/cm³ after compression at various temperatures. Like the Distaloy foams, the mechanical properties of Astaloy foams are strongly dependent on the test temperature. The compressive strength of the Astaloy foams reaches its maximum value when a temperature of about 450°C is reached. When the test temperature goes over 450°C a decrease in both compressive yield strength as well as plateau stress is observed.

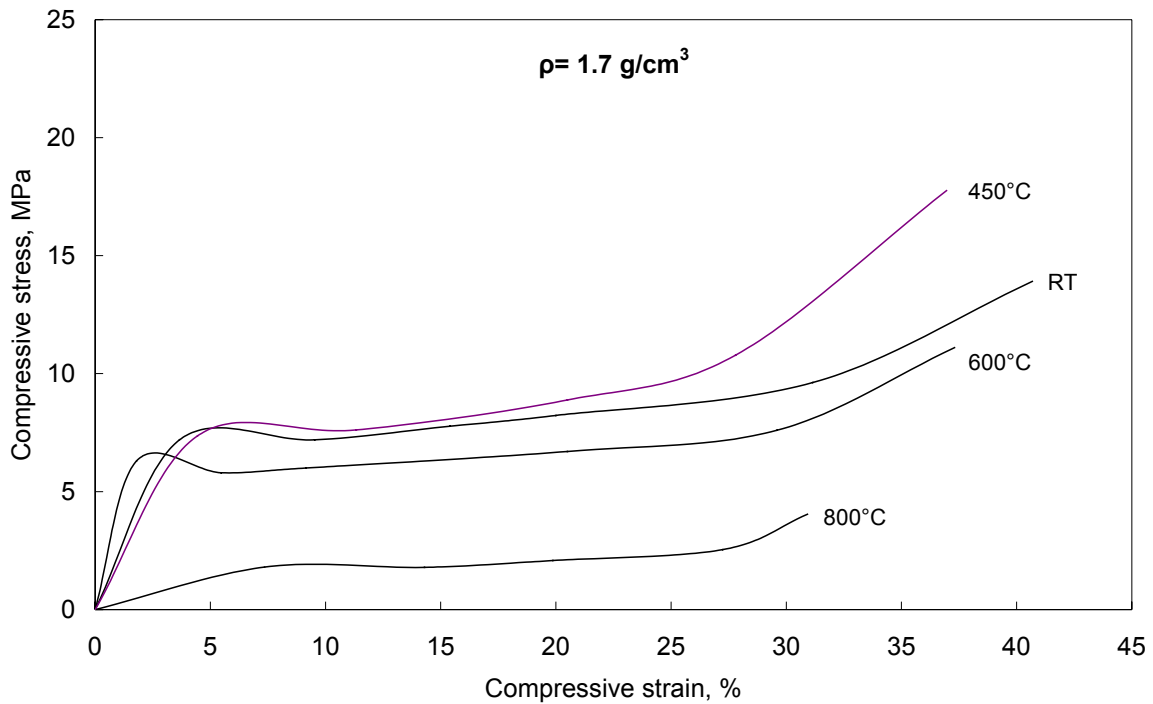


Fig. 6-25 Temperature dependence of stress-strain curves of Astaloy foams ($\rho = 1.7 \text{ g/cm}^3$).

The effect of both temperature and density on the compression strength of Astaloy foams is presented in **Fig. 6-26**. It was found that the foams have attained a maximum compression strength values at a temperature of 450°C, over which the foams begin to soften and their strengths are thus reduced. As mentioned earlier, the reason for this phenomenon may be due to the effect of the ageing. **Tab. 6-9** gives the measured compression strength of the Astaloy foams as a function of temperature and density.

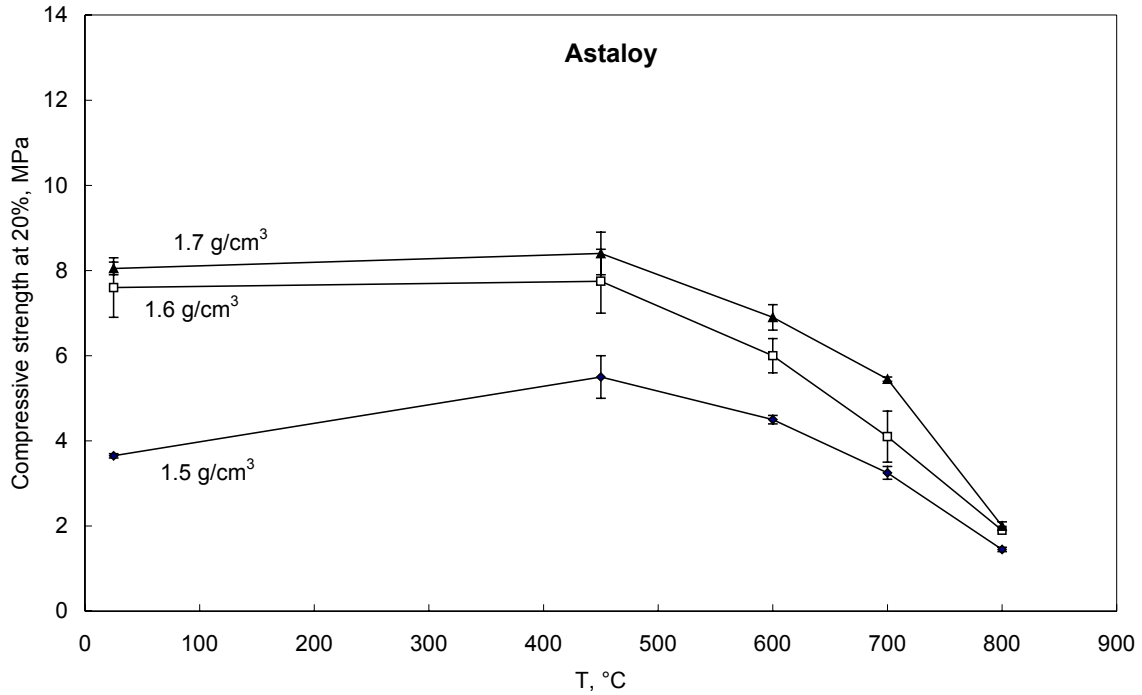


Fig. 6-26 Influence of temperature on the Compression strength of 1.5 g/cm³, 1.6 g/cm³ and 1.7 g/cm³ of Astaloy foams.

Density, g/cm ³	Compression strength at 20%, MPa									
	RT		450°C		600°C		700°C		800°C	
1.5	3.6	3.7	5.0	6.0	4.4	4.6	3.1	3.4	1.4	1.5
1.6	6.9	8.3	7.0	8.5	6.4	5.6	3.5	4.7	1.9	1.9
1.7	8.2	7.9	8.9	7.9	6.7	7.1	5.4	5.5	2.1	1.9

Tab. 6-9 Compression strength of the Astaloy foams as a function of density and test temperature.

6.2.1.3.4 Metallographic Examination

6.2.1.3.4.1 Stereoscopic Examination of Astaloy Foams

As shown in **Fig. 6-27**, the outer surface of the Astaloy samples have been strongly oxidised due to the high temperature oxidation reaction with oxygen of the air.



Fig. 6-27 Stereoscopic macrographs of Astaloy foams having different densities, tested at RT (left), 450°C (middle) as well as 600°C (right), respectively.

6.2.1.3.4.2 Microstructural Examination of Astaloy Foams

The microstructure micrograph of an Astaloy foam, shown in **Fig. 6-28**, taken by a light optical microscope reveals that the microstructure consists of a ferrite matrix. There are two different types of pores, primary-as well as secondary pores each have different sizes. Iron oxide scale has been formed as well, due to the reaction occurring between the iron particles and the oxygen of the air upon high temperature compression.

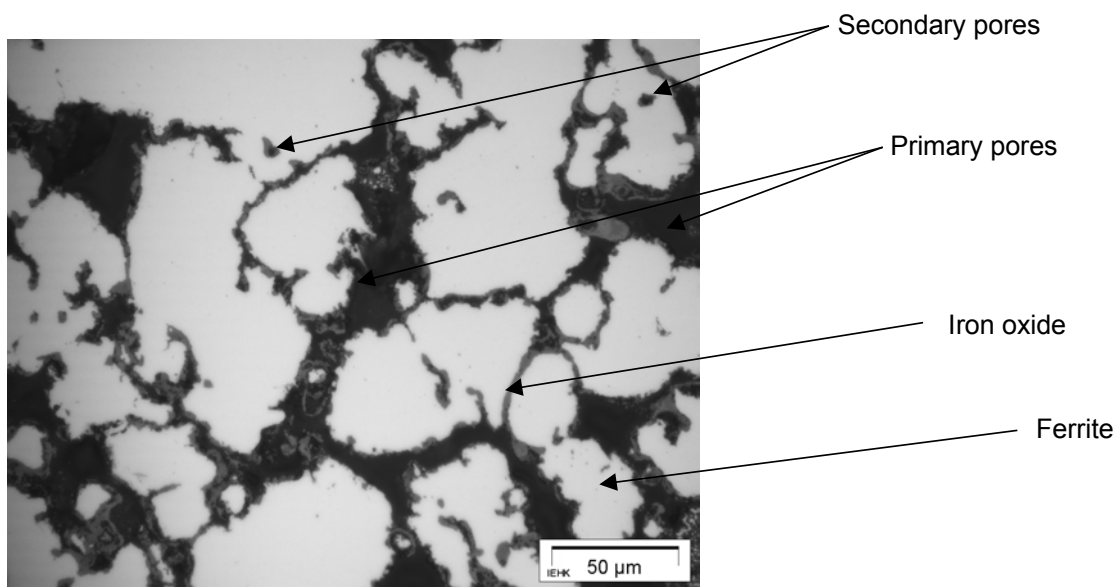


Fig. 6-28 Microstructure micrograph of an Astaloy sample compressed at 450°C.

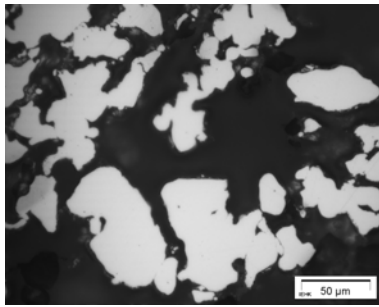
6.2.1.3.4.3 Measurement of the Oxide Scale Thickness on the Astaloy Foams

During the high temperature compressive testing of Astaloy foams, the foams have been oxidised because of the reaction of the iron particles with oxygen ions presented in air. In order to study the effect of temperature on the thickness of the built oxide layer in the cell walls at the middle as well as around the edges of the Astaloy samples, the thickness of this built layer was measured at different temperatures. **Tab. 6-10** gives the measured thickness at the middle as well as around the edge at different temperatures.

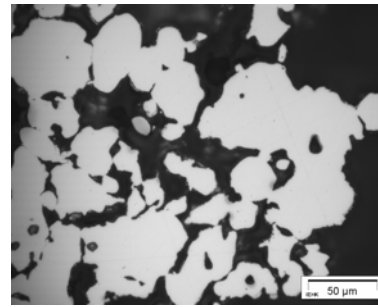
Position	T, °C	Oxide thickness, μm								Mean
Edge-a	RT	0	0	0	0	0	0	0	0	0
	450°	1.2	1.3	0.9	1.6	1.9	0.9	-	-	1.3
	600°	13.3	6.7	10.0	9.9	10.0	9.7	7.0	7.5	9.1
	800°	7.7	10.7	14.6	20.1	16.5	10.1	9.2	19.9	13.6
Edge-b	RT	0	0	0	0	0	0	0	0	0
	450°	4.7	1.5	2.1	2.1	1.4	1.4	3.0	2.0	2.3
	600°	6.5	6.1	7.3	5.8	8.0	8.4	6.2	7.6	5.9
	800°	20.1	19.0	18.3	13.0	19.5	12.2	12.7	13.1	16.0
Middle-a	RT	0	0	0	0	0	0	0	0	0
	450°	1.7	1.5	1.8	1.1	2.5	2.0	1.8	1.2	1.9
	600°	2.3	2.7	2.5	3.3	1.9	2.9	2.4	3.4	2.7
	800°	2.7	2.5	1.5	2.2	3.0	5.1	1.7	5.2	3.0
Middle-b	RT	0	0	0	0	0	0	0	0	0
	450°	1.5	2.1	1.8	1.8	1.5	1.7	3.2	1.7	1.9
	600°	3.3	3.8	3.0	3.4	5.0	1.5	2.5	2.9	3.3
	800°	4.5	5.1	5.3	5.8	3.3	3.4	3.6	2.4	4.2

Tab. 6-10 Measured oxide thickness of Astaloy samples at different temperatures

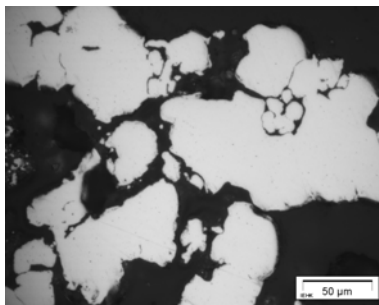
The microstructure micrographs of the Astaloy samples in **Fig. 6-29** and **Fig. 6-30**, illustrate the changes within the thickness of the built oxide scales at two different sites as a function of the temperature. It can be seen that the Astaloy samples compressed at RT, have no oxide scales neither in the middle of the sample nor around the edges. With increasing temperature, a thick oxide layer is built on the surface of the samples. The formation of such scales increases the resistance of the material against corrosion, which is also enhanced by molybdenum as well as phosphorus [HOU00].



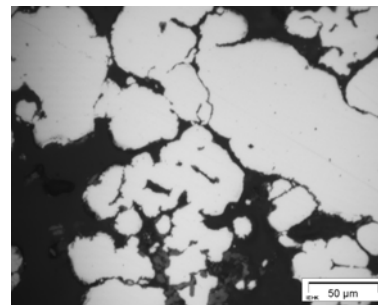
1.8 g/cm³-RT-edge-a



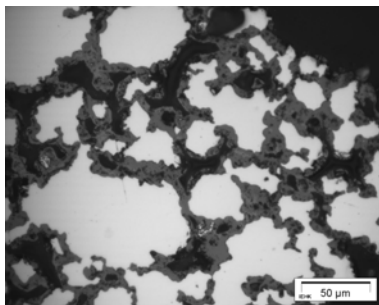
1.8 g/cm³-RT-edge-a



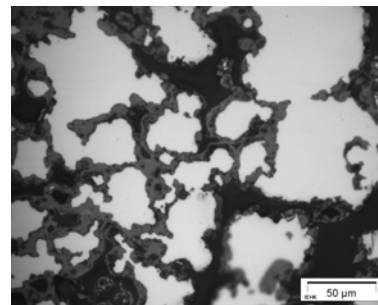
1.8 g/cm³-450°C-edge-a



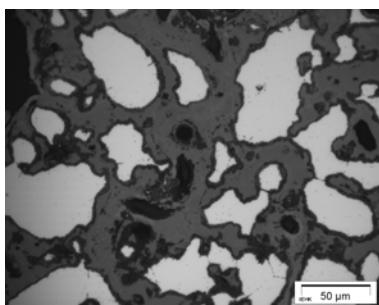
1.8 g/cm³-450°C-edge-b



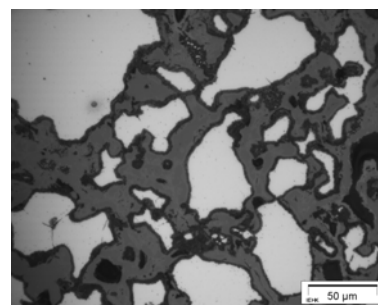
1.8 g/cm³-600°C-edge-a



1.8 g/cm³-600°C-edge-b

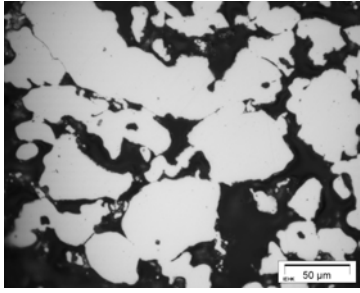


1.8 g/cm³-800°C-edge-a

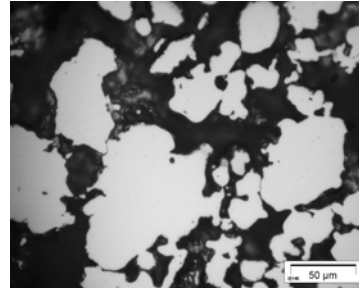


1.8 g/cm³-800°C-edge-b

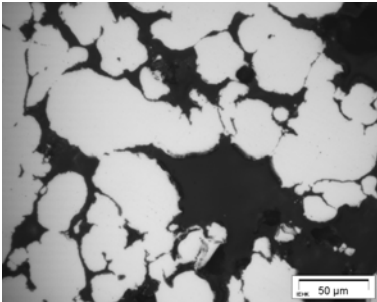
Fig. 6-29 Microstructure micrographs around the edges of the Astaloy samples (having a density of 1.8 g/cm³) compressed at different temperatures.



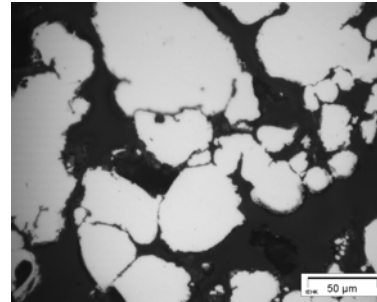
1.8 g/cm³-RT-middle-a



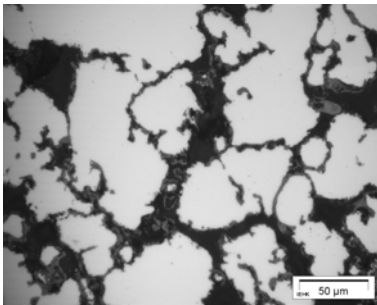
1.8 g/cm³-RT-middle-b



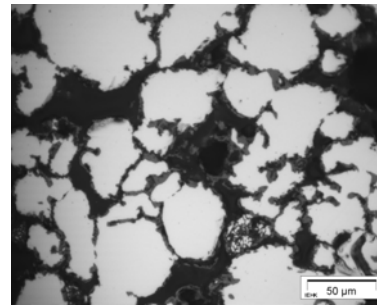
1.8 g/cm³-450°C-middle-a



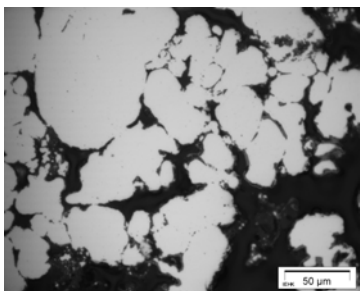
1.8 g/cm³-450°C-middle-b



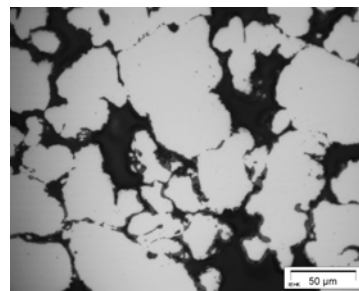
1.8 g/cm³-600°C-middle-a



1.8 g/cm³-600°C-middle-b



1.8 g/cm³-800°C-middle-a



1.8 g/cm³-800°C-middle-b

Fig. 6-30 Microstructure micrographs at two different sites in the middle of Astaloy samples (having a density of 1.8 g/cm³) deformed at different temperatures.

6.2.1.3.5 SEM characterisation of Astaloy Foams

SEM micrograph of a non-deformed green sample of Astaloy foams reveals obviously the foamy structure, wherein the pores are separated from each other via the cell-walls, as shown in **Fig. 6-31**, meanwhile **Fig. 6-32** shows a SEM micrograph of the Astaloy foam in sintered, deformed state. it can be seen a dense agglomerate with no more primary pores but too many secondary pores are observed. The cell-walls have been completely destroyed. The formation of trans-agglomerate cracks is the dominant fracture mechanism. These cracks formed as a result of the nucleation of small voids, which coalesce together forming large cavities.

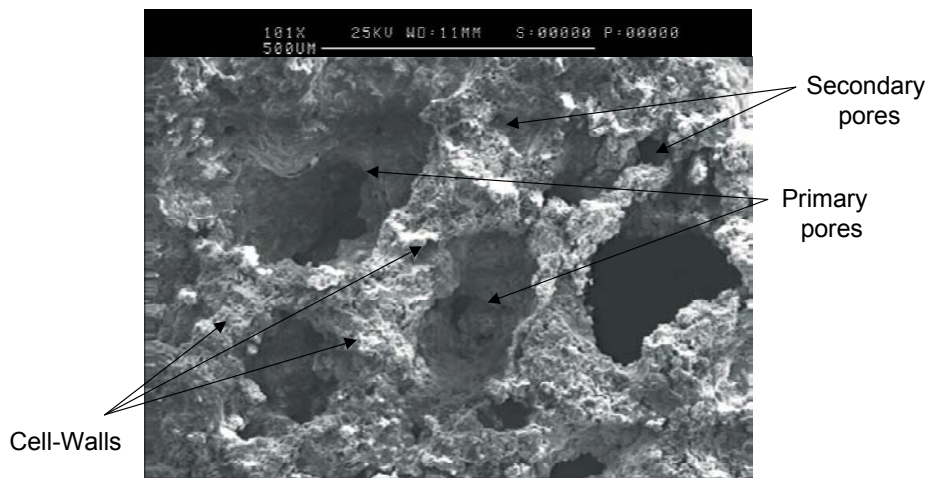


Fig. 6-31 SEM-micrograph of a non-deformed Astaloy foam ($\rho = 1.8 \text{ g/cm}^3$) in the green state.

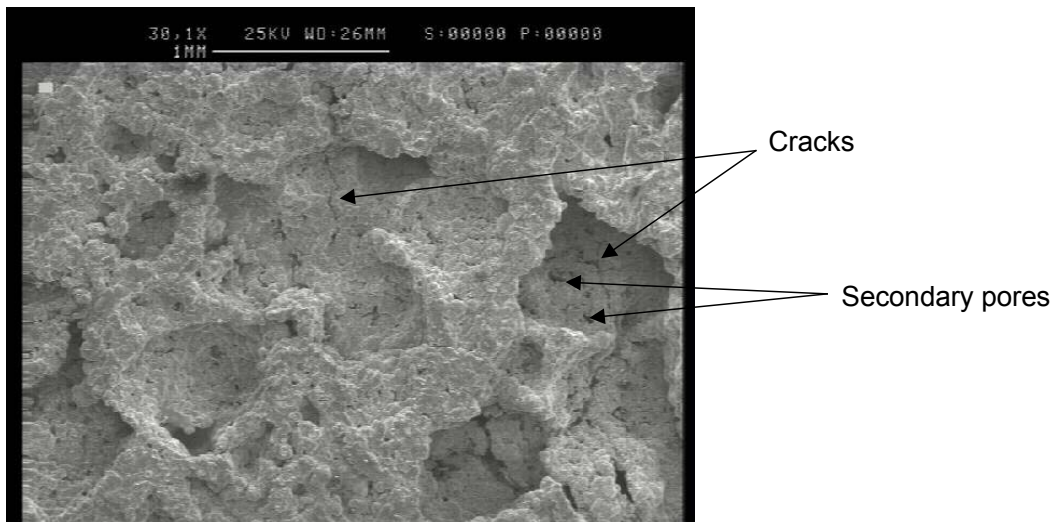


Fig. 6-32 SEM-micrograph of an Astaloy foam ($\rho = 1.8 \text{ g/cm}^3$) deformed at 800°C.

6.2.2 Compression Test in Inert Atmosphere

The past chapter showed that high temperature compression test in atmospheric air has led to the formation of an oxide scale on the surfaces of the tested foams.

In order to study the behaviour of these foams without the influence of the built oxide layers on their surfaces, a new set of compression tests was carried out in inert atmosphere (Ar) at different temperatures, ranging from RT up to 800°C and constant rate of displacement 1mm/min, using the servo-hydraulic testing machine (illustrated in **Fig. 5-9**). The high temperature compression tests have been carried out only for the Distaloy and Astaloy foams, since for Al-foams (Alporas) an oxide layer already exists, even at RT, because of the high affinity of Al to react with the oxygen of the air.

6.2.2.1 Quasi-static Compression Test of Distaloy Foams

6.2.2.1.1 Effect of Density

As mentioned earlier, compression tests have been conducted for Distaloy foams having different densities. At each test temperature, compression tests have been conducted twice for two samples having the same density. The stress-strain behaviour should be similar and the difference in the level of the stress-strain curves should not be expected to be large.

Fig. 6-33 to **Fig. 6-37** shows the typical compressive stress-strain curves for different densities of the Distaloy foams at different testing temperatures.

RT

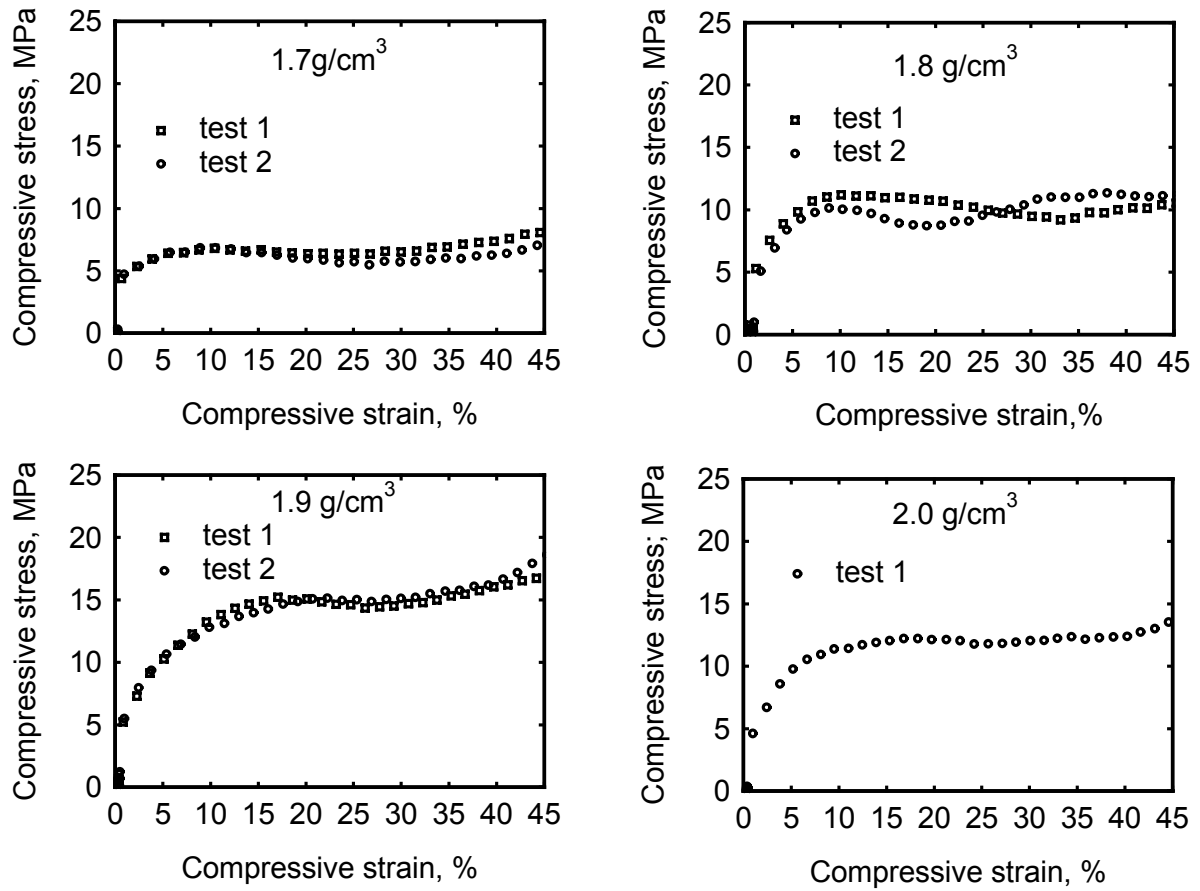


Fig. 6-33 Stress-strain curves of different densities of the Distaloy foams, compressed at RT in Ar atmosphere.

200°C

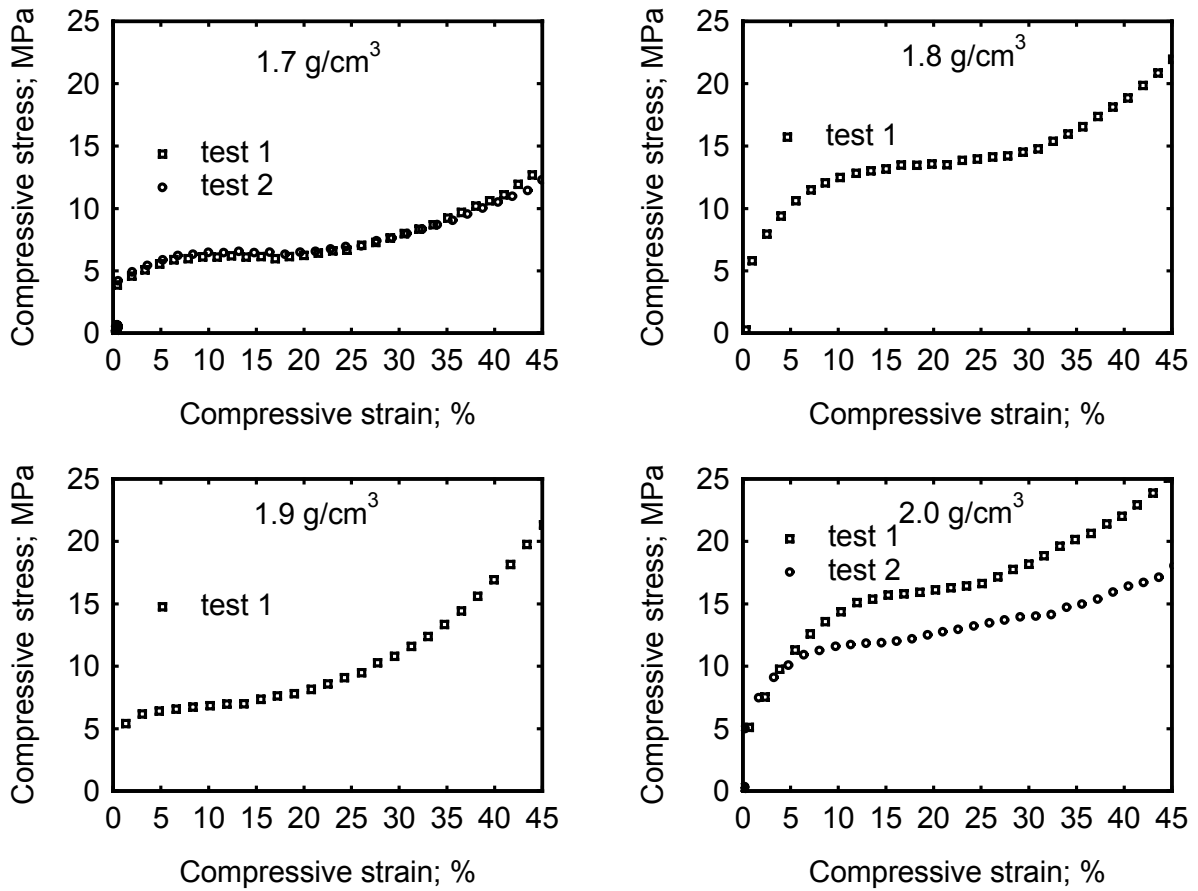


Fig. 6-34 Stress-strain curves of different densities of the Distaloy foams, compressed at 200°C in Ar atmosphere.

450°C

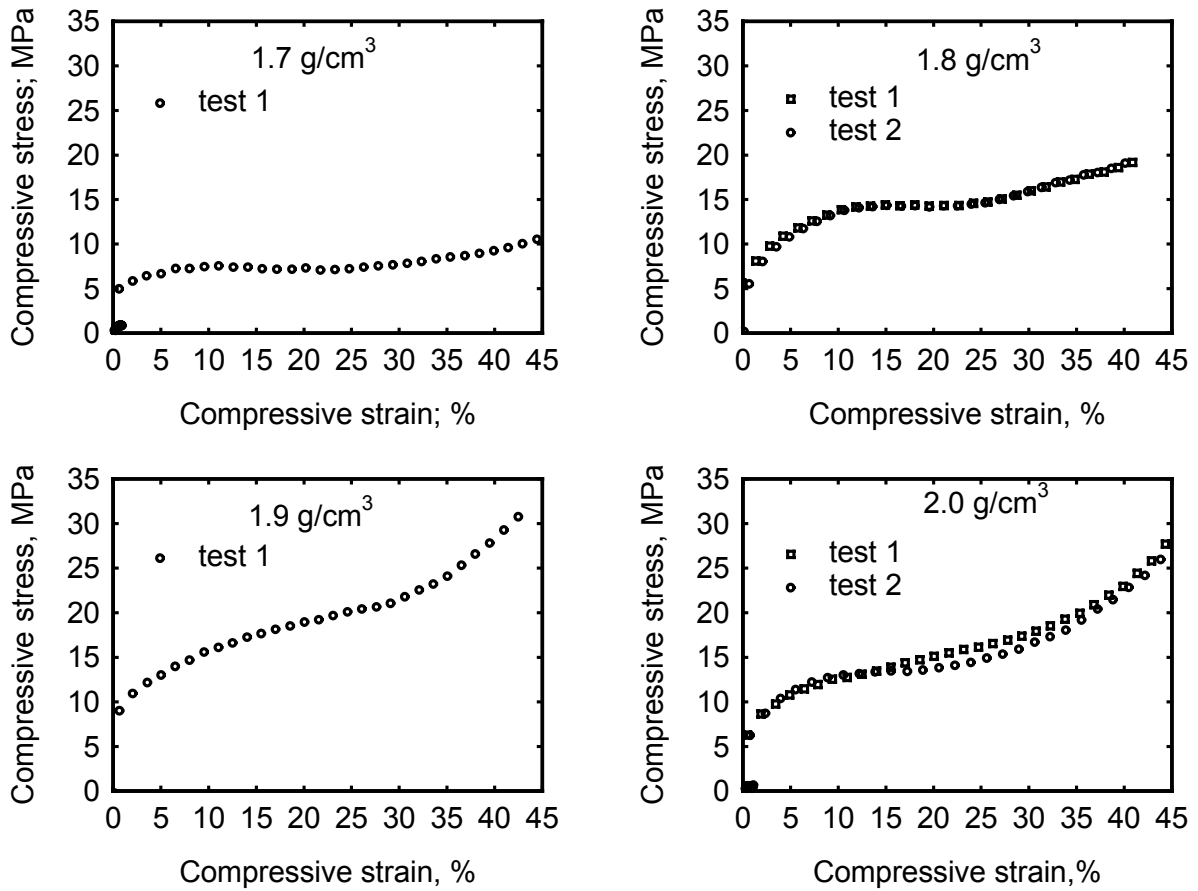


Fig. 6-35 Stress-strain curves of different densities of the Distaloy foams, compressed at 450°C in Ar atmosphere.

600°C

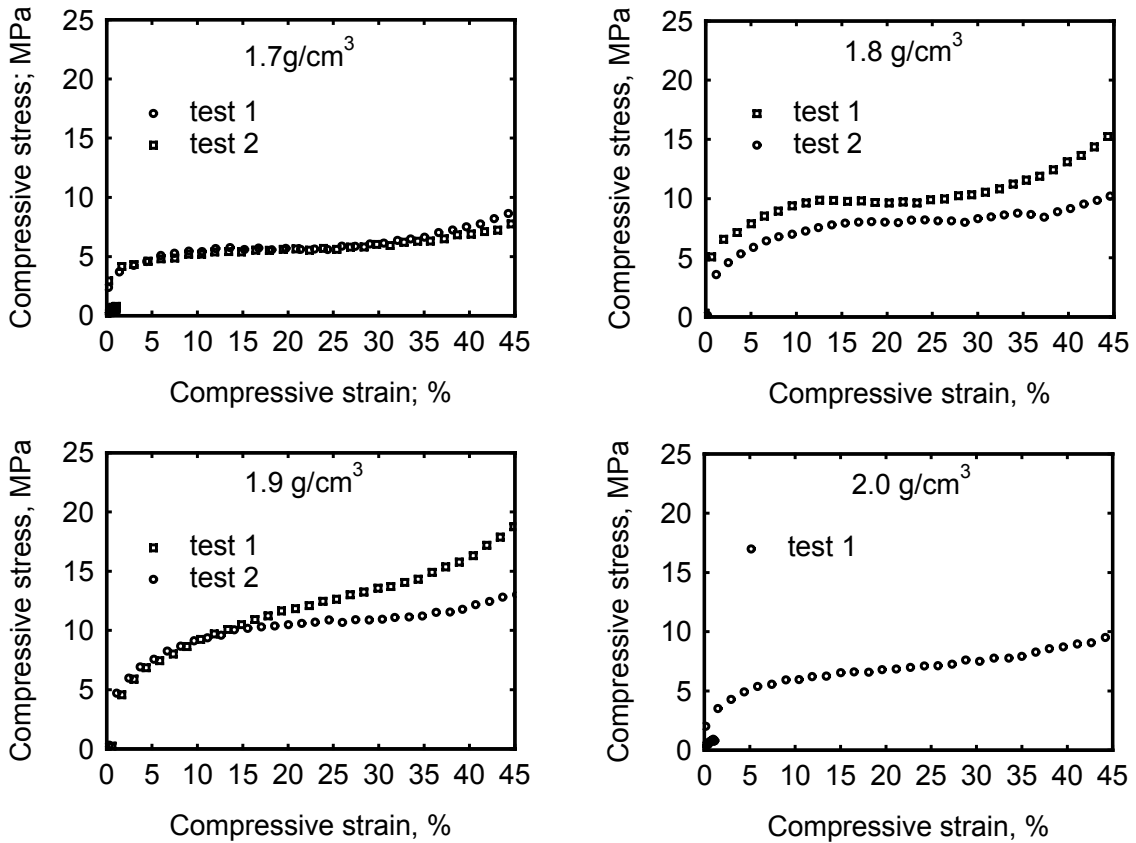


Fig. 6-36 Stress-strain curves of different densities of the Distaloy foams, compressed at 600°C in Ar atmosphere.

800°C

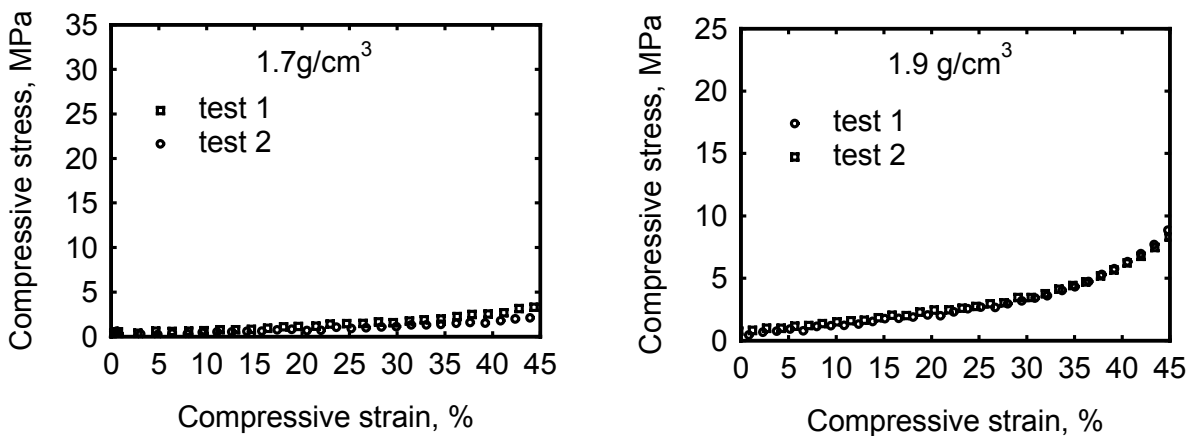


Fig. 6-37 Stress-strain curves of different densities of the Distaloy foams, compressed at 800°C in Ar atmosphere.

The previous curves reveal that for most of the tested samples, the stress-strain curves coincide with respect to each other. The deviation in the level of the two stress-strain curves for certain samples with densities for example 1.7 g/cm^3 and 1.8 g/cm^3 (tested at RT), as well as 1.9 g/cm^3 (tested at 600°C), may result from the inhomogeneous distribution of the density.

Fig. 6-38 summarises the effect of the density on the stress-strain behaviour of the Distaloy foams. The increase in the foam's density shifts the stress-strain curves to an upper level, which implies that a higher levels of the compressive strength as well the plateau stress are achieved, meanwhile the densification strain is shifted to the left, i.e. the higher the density of the foam, the more quickly the collapse of its cells.

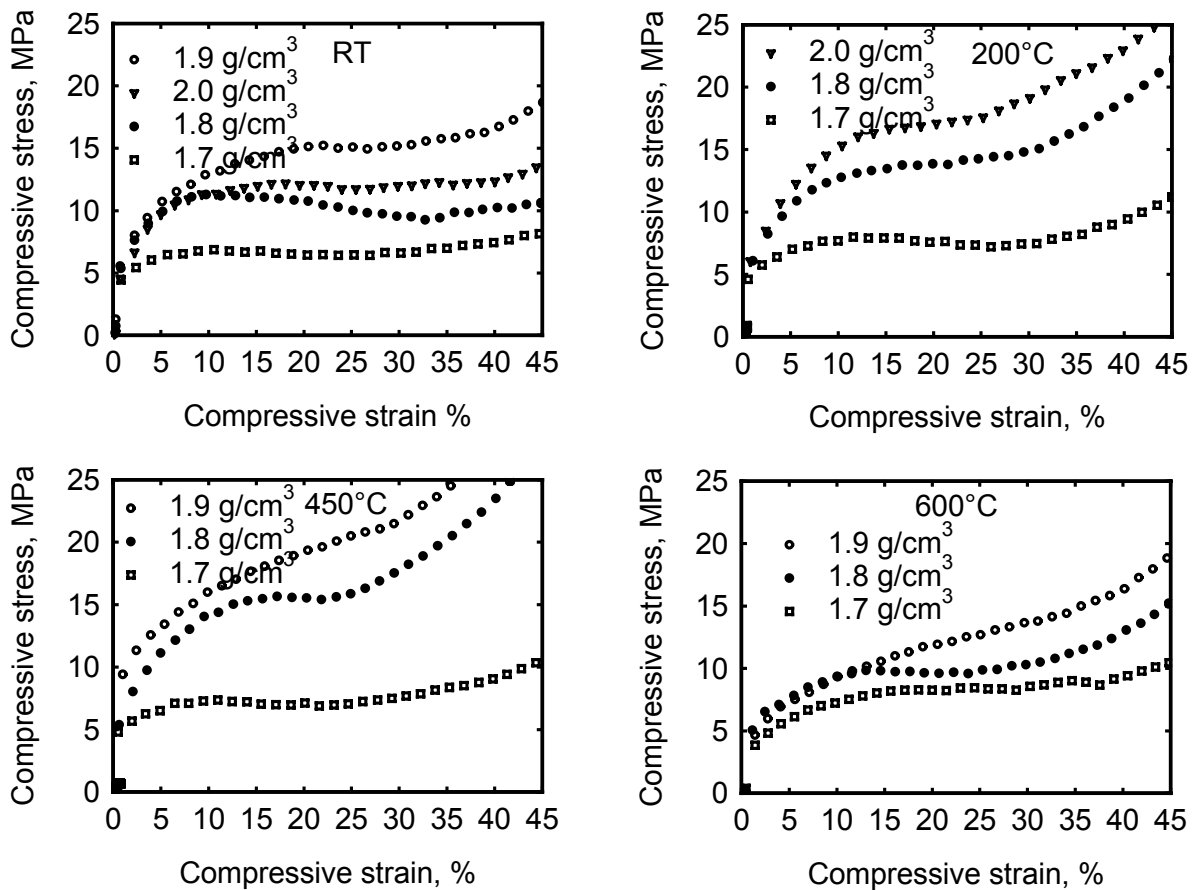


Fig. 6-38 Influence of the density of the Distaloy foams on the stress-strain behaviour at different test temperatures.

6.2.2.1.2 Effect of Temperature

Fig. 6-39 summarises the effect of test temperature upon the stress-strain behaviour of the Distaloy foams as a function of the foam's density. It is well-known from the physical metallurgy of metals and alloys that the strength of solid metals decrease with increasing temperature. However, it was observed that the compressive strength of foams at 200°C as well as 450°C, respectively, was larger than that at RT. This was observed for all foams under study. The reason for the increase in the compressive strength of the Distaloy foams in this range of temperature (200°C-450°C) may result from the interaction between C-element and immigrating dislocations. This phenomenon is known as „age-hardening“ [BLE99].

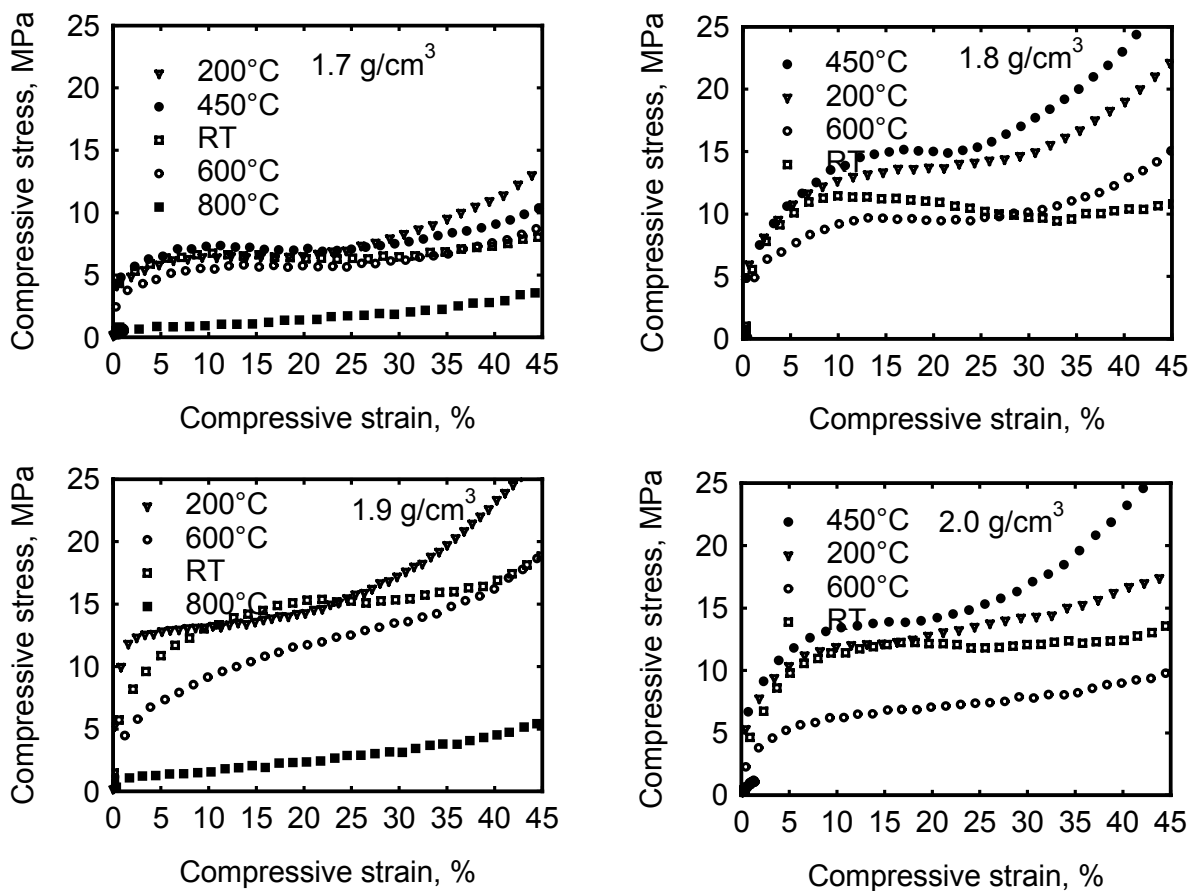


Fig. 6-39 Stress-strain curves for different densities of Distaloy foams at different test temperatures.

The compression strength values of the Distaloy foams as a function of the foam's density and of the test temperature are given in **Tab. 6-10**.

Density, g/cm ³	Compression strength at 20%, MPa									
	RT		200°C		450°C		600°C		800°C	
1.7	5.8	6.5	6.3	7.0	-	6.8	5.7	5.6	0.7	1.1
1.8	8.6	10.7	13.7	-	14.2	14.2	9.7	8.0	-	-
1.9	15.0	15.0	7.8	-	18.9	-	11.8	10.4	2.3	2.1
2.0	12.1	-	16.9	12.7	15.1	13.8	6.7	-	-	-

Tab. 6-11 Compressive strength of Distaloy foams at 20% as a function of foam’s density and test temperature.

Fig. 6-40 illustrates the relation between the mean values of the compressive strength at 20% strain for Distaloy foams having two different densities as a function of test temperature. It is obvious to see that there are two different mechanisms - strengthening and softening – taking place during the compression test. Like the Distaloy foams, the compressive strength of the Astaloy foams increases as the temperature increases until it reaches 450°C, afterwards the foams begin to soften with increasing the temperature. As mentioned before, an interpretation for this increase in the compressive strength values over this range of temperature may be due to the ageing effect [BLE99, MEM89]. On the same diagram, the compressive strength at 20% of 0.24 g/cm³ Alporas foam is plotted in order to compare between the behaviour of the Distaloy foams and that of the Alporas foams. Unlike the Distaloy foams, the compressive strength of Alporas foams decreases with increasing the test temperature. An interpretation for this softening may be due to the coarsening of the precipitates which have been formed during the manufacturing process.

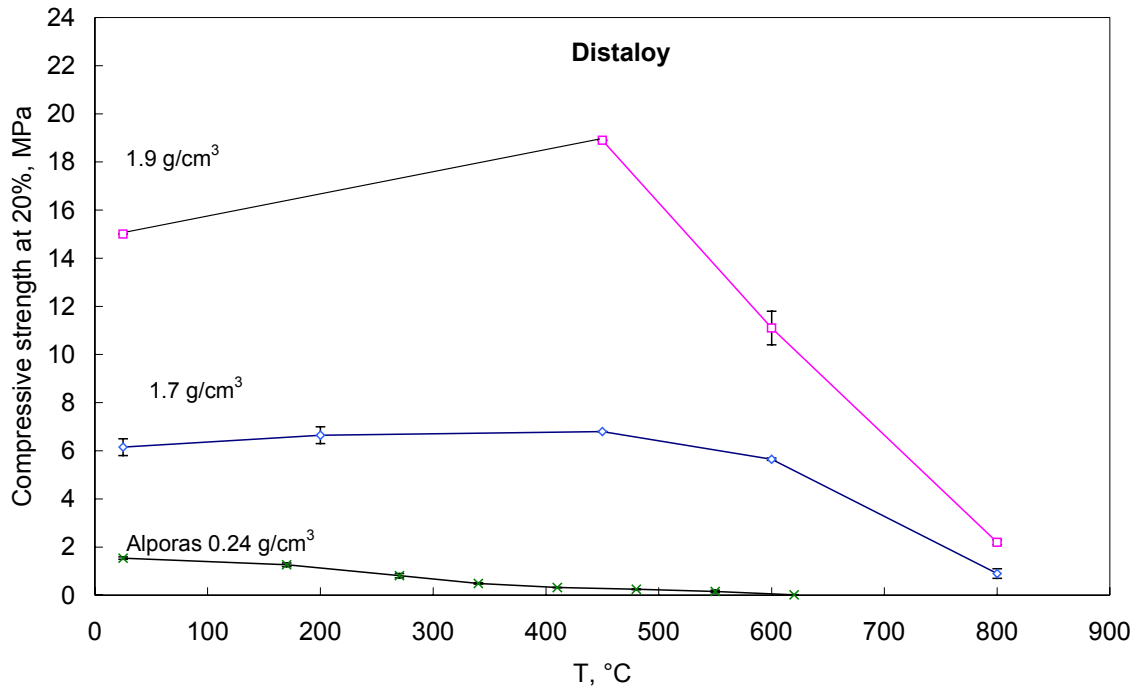


Fig. 6-40 Compressive strength of Distaloy foams as a function of foam's density and test temperature in comparison to Alporas foams.

6.2.2.1.3 Metallographic Examination

6.2.2.1.3.1 Stereoscopic Examination of the Distaloy Foams

Observing the stereoscopic macrographs of the tested Distaloy samples, shown in **Fig. 6-41** to **Fig. 6-44**, it was found that each sample has had certain characteristic features, e.g., in some samples some pores with different sizes were found, whereas in others very fine pores were present. Some samples showed some kind of agglomeration or clustering of particles in certain areas than the other, while others did not exhibit it. The number, size and distribution of pores influence undoubtedly the homogeneity of the foam's density and consequently their mechanical properties.

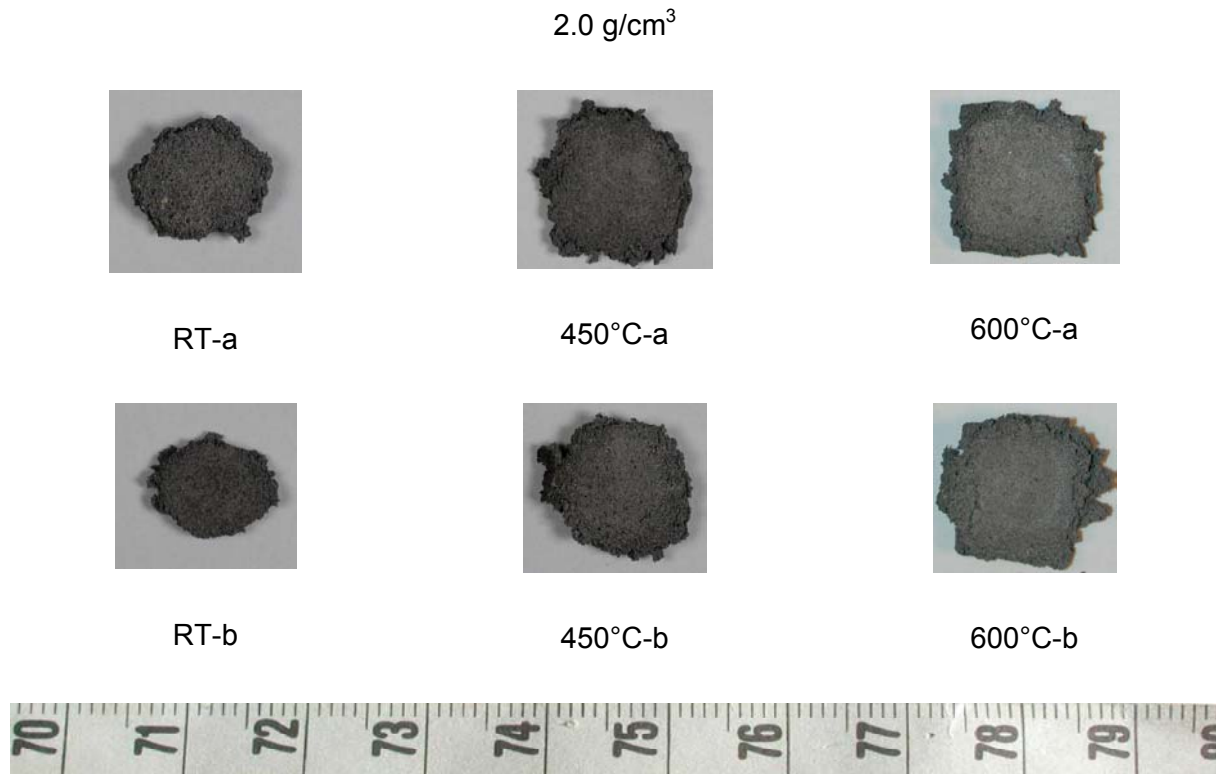


Fig. 6-41 Macrographs of the Distaloy foams ($\rho = 2.0 \text{ g/cm}^3$).

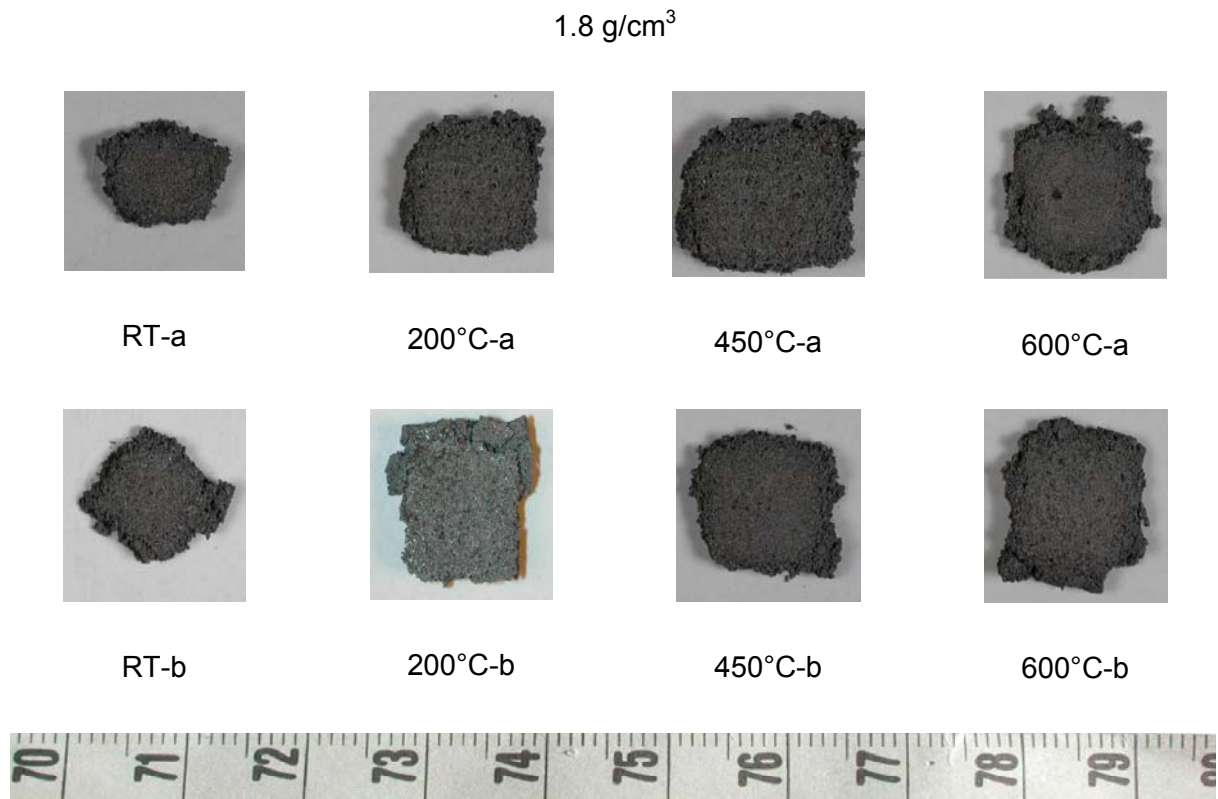


Fig. 6-42 Macrographs of the Distaloy foams ($\rho = 1.8 \text{ g/cm}^3$)

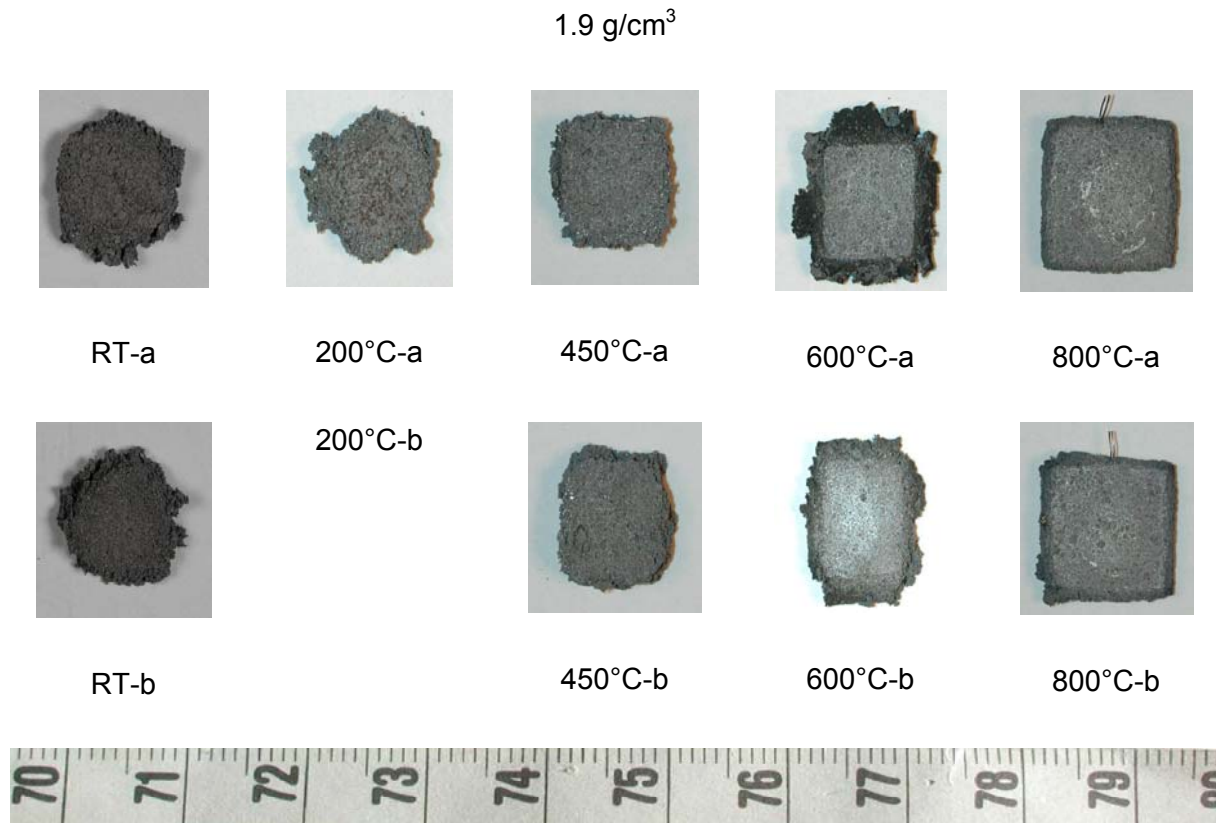


Fig. 6-43 Macrographs of the Distaloy foams ($\rho = 1.9 \text{ g/cm}^3$)

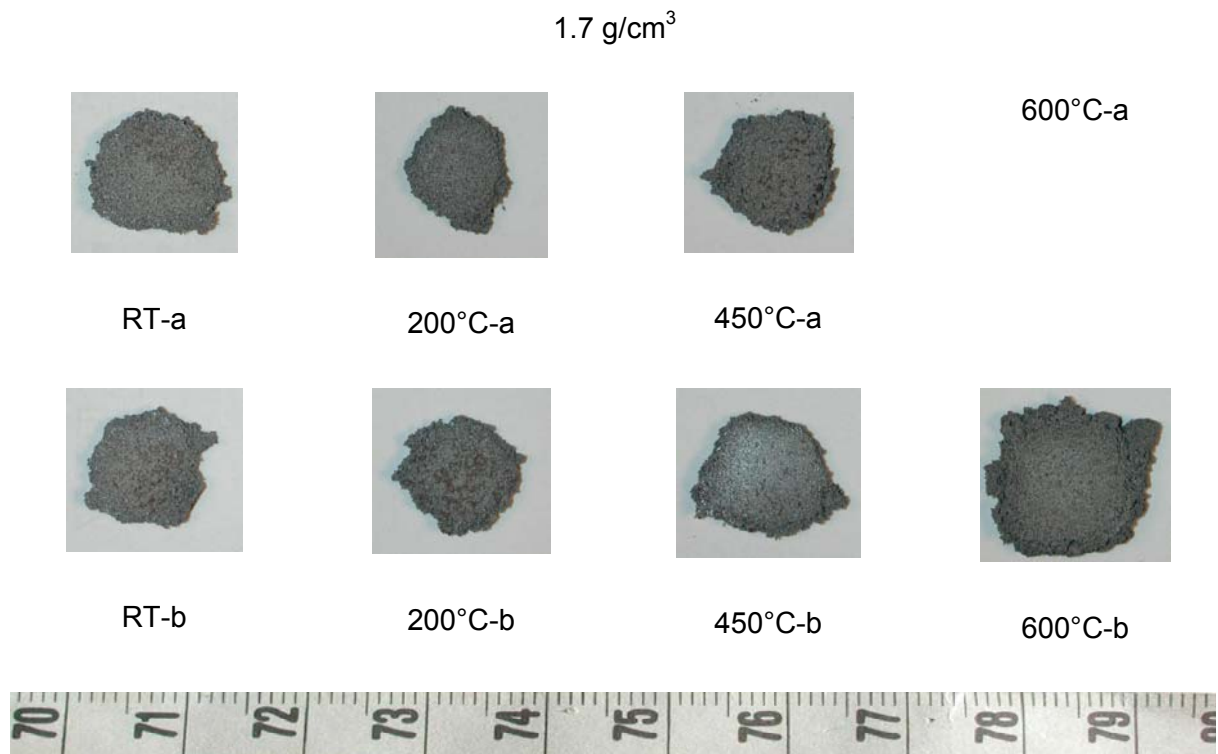


Fig. 6-44 Macrographs of the Distaloy foams ($\rho = 1.7 \text{ g/cm}^3$)

6.2.2.1.3.2 Microstructural Examination of the Distaloy Foams

Fig. 6-45 shows the light optical microscope (LOM) micrographs of the Distaloy foams at a magnification of 500 μm at each test temperature. The micrograph of the Distaloy foam compressed at RT has a large number of primary pores with small sizes. Primary pores with larger sizes and of irregular shapes have been appeared at higher temperatures. This causes inhomogeneous distribution of the local density within the sample. A neck (sintering-bridge) has been formed between some particles. This indicates that the sintering process was not completely carried out, i.e. the samples should be sintered either at high sintering temperatures or at long sintering times. The interconnection between some pores was also observed.

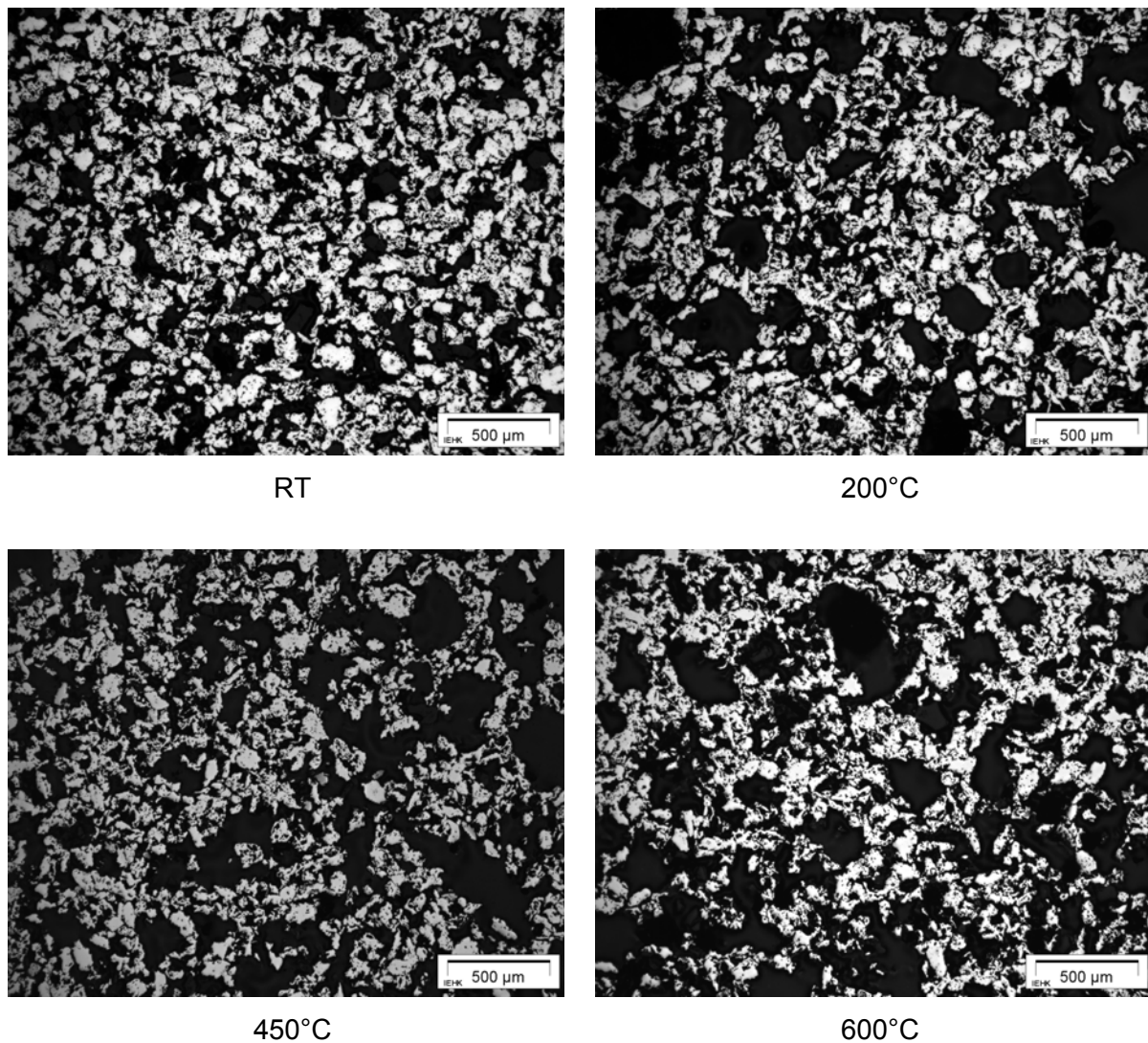


Fig. 6-45 Microstructure micrograph of the deformed Distaloy foams ($\rho = 1.8 \text{ g/cm}^3$) at different testing temperatures.

6.2.2.1.4 SEM Characterisation of the Distaloy Foams

Fig. 6-46 shows a micrograph of a cell wall of Distaloy foam. After deformation, pores were still found in certain sites of the cell wall, whereas the rest of the cell wall of the foam has been completely compressed into a compact material. The coalescence of small pores leads to the formation of micro-cracks. The particles have been completely stuck with each other. As will be seen later in case of Astaloy, this sticking effect has not appeared; therefore this phenomenon may be due to either the nature of the powder or its chemical composition.

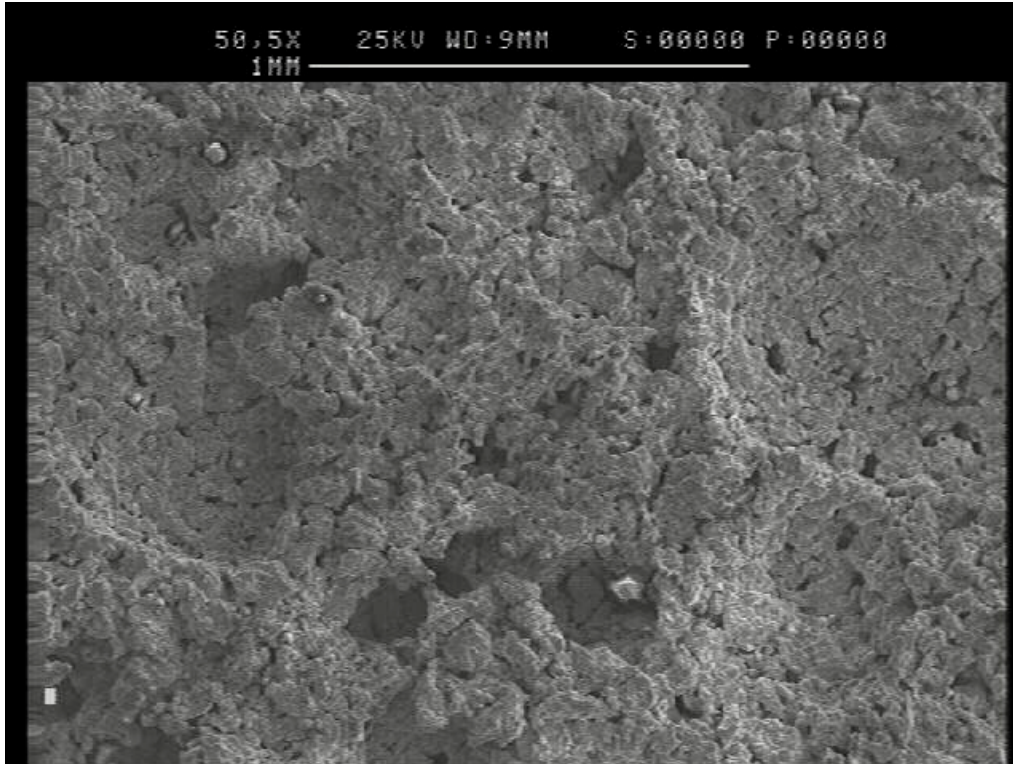


Fig. 6-46 SEM micrograph of a Distaloy foam tested at 200°C ($\rho = 1.8 \text{ g/cm}^3$).

6.2.2.2 Quasi-static Compression Test of the Astaloy Foams

6.2.2.2.1 Effect of Density

Like the Distaloy foams, compression tests on different densities of Astaloy foams were carried out under similar conditions. **Fig. 6-47** to **Fig. 6-50** shows the compressive stress strain behaviour for different densities of the Astaloy foams at each given test temperature. The compression test was carried out twice for each density. The deviation in the obtained stress-strain curves in some cases is possibly resulting from the inhomogeneous distribution of the density.

RT

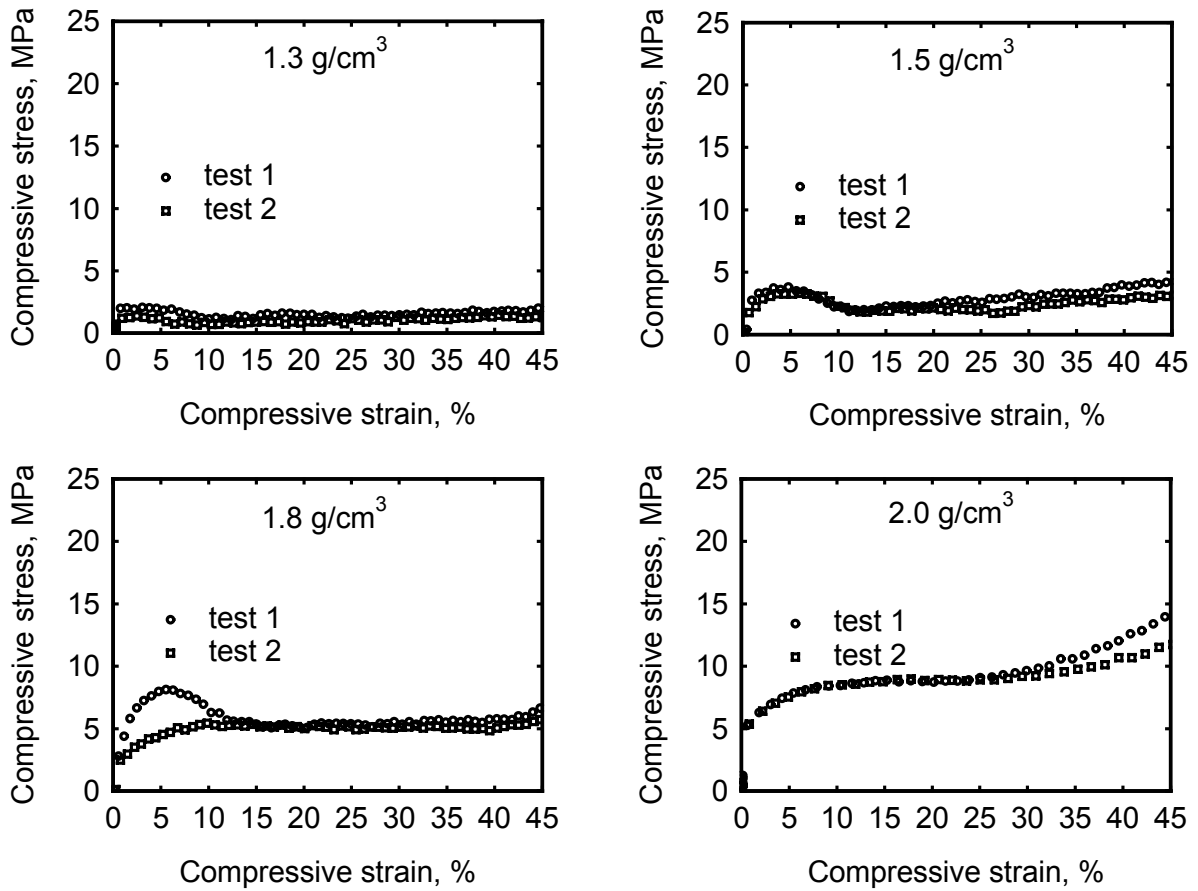


Fig. 6-47 Stress-strain curves for different densities of the Astaloy foams, compressed at RT in Ar atmosphere.

200°C

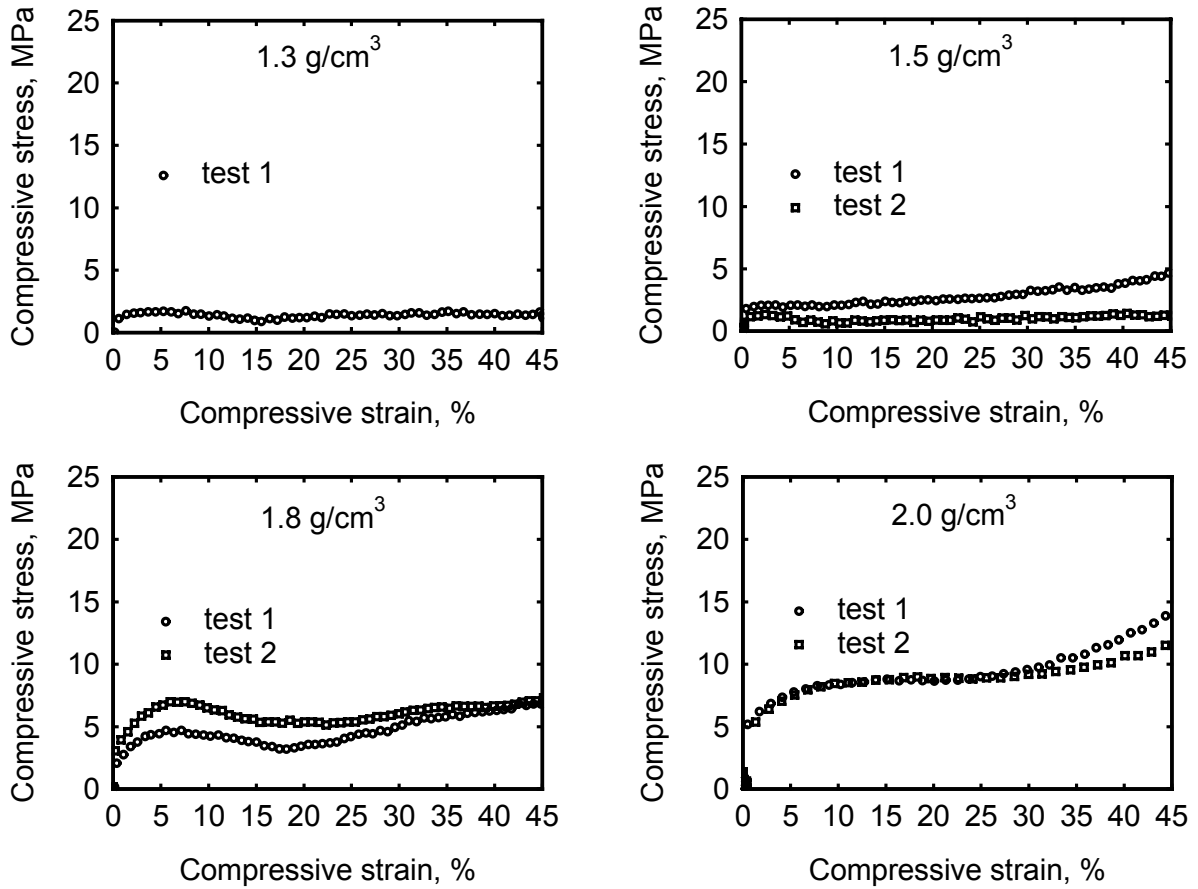


Fig. 6-48 Stress-strain curves for different densities of the Astaloy foams, compressed at 200°C in Ar atmosphere.

450°C

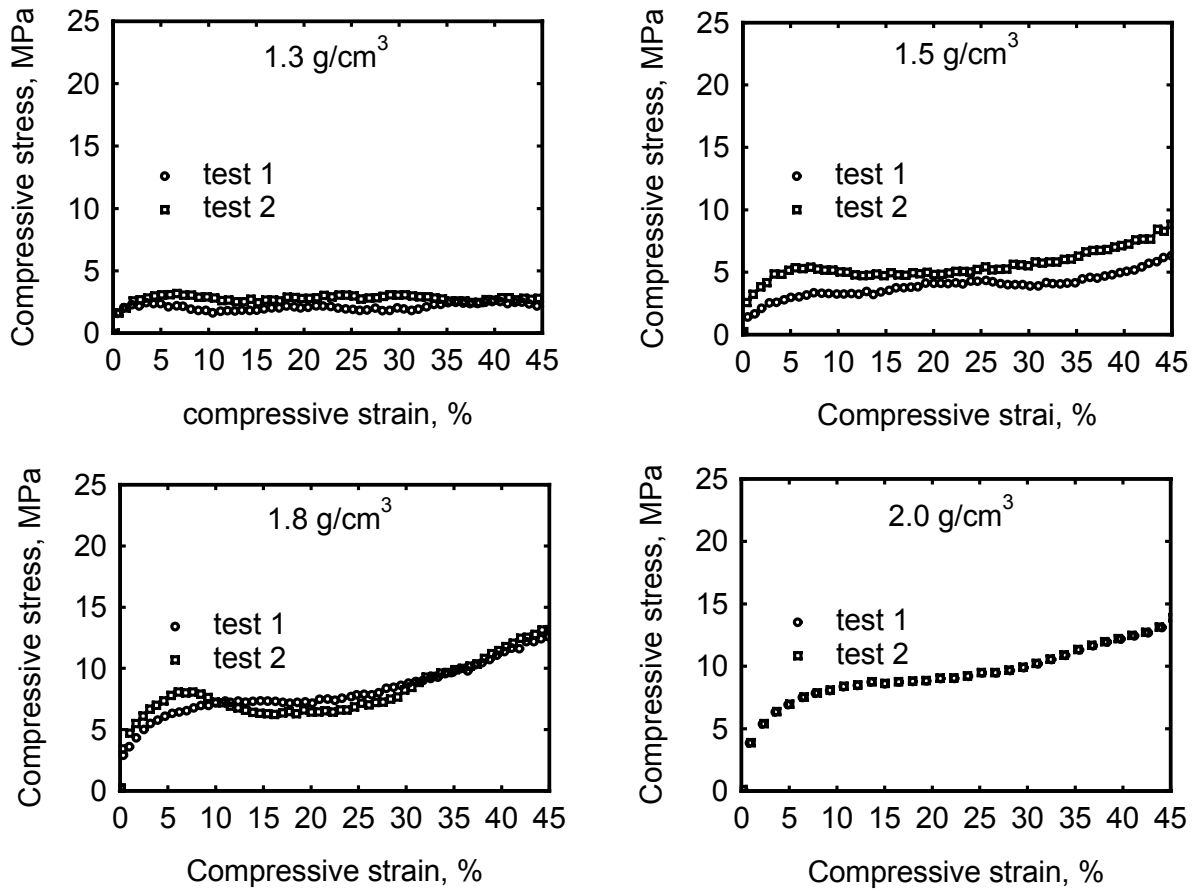


Fig. 6-49 Stress-strain curves for different densities of the Astaloy foams, compressed at 450°C in Ar atmosphere.

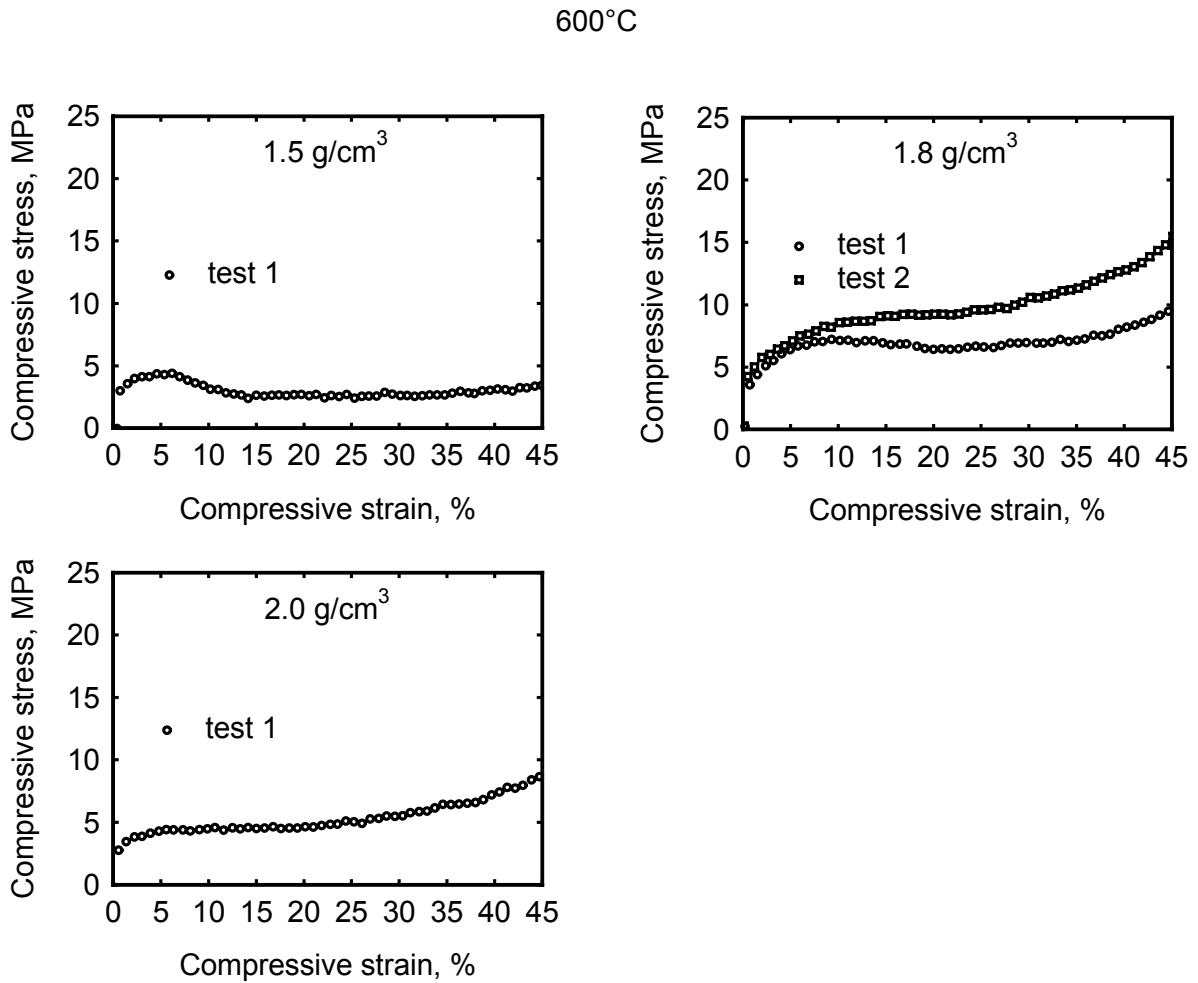


Fig. 6-50 Stress-strain curves for different densities of the Astaloy foams, compressed at 600°C in Ar atmosphere.

Fig. 6-51 represents the effect of the foam's density on the stress-strain behaviour of the Astaloy samples at different test temperatures. The compressive strength increases with increasing foam density. Non-homogeneous distribution of the density may be a cause for the deviation in the obtained results.

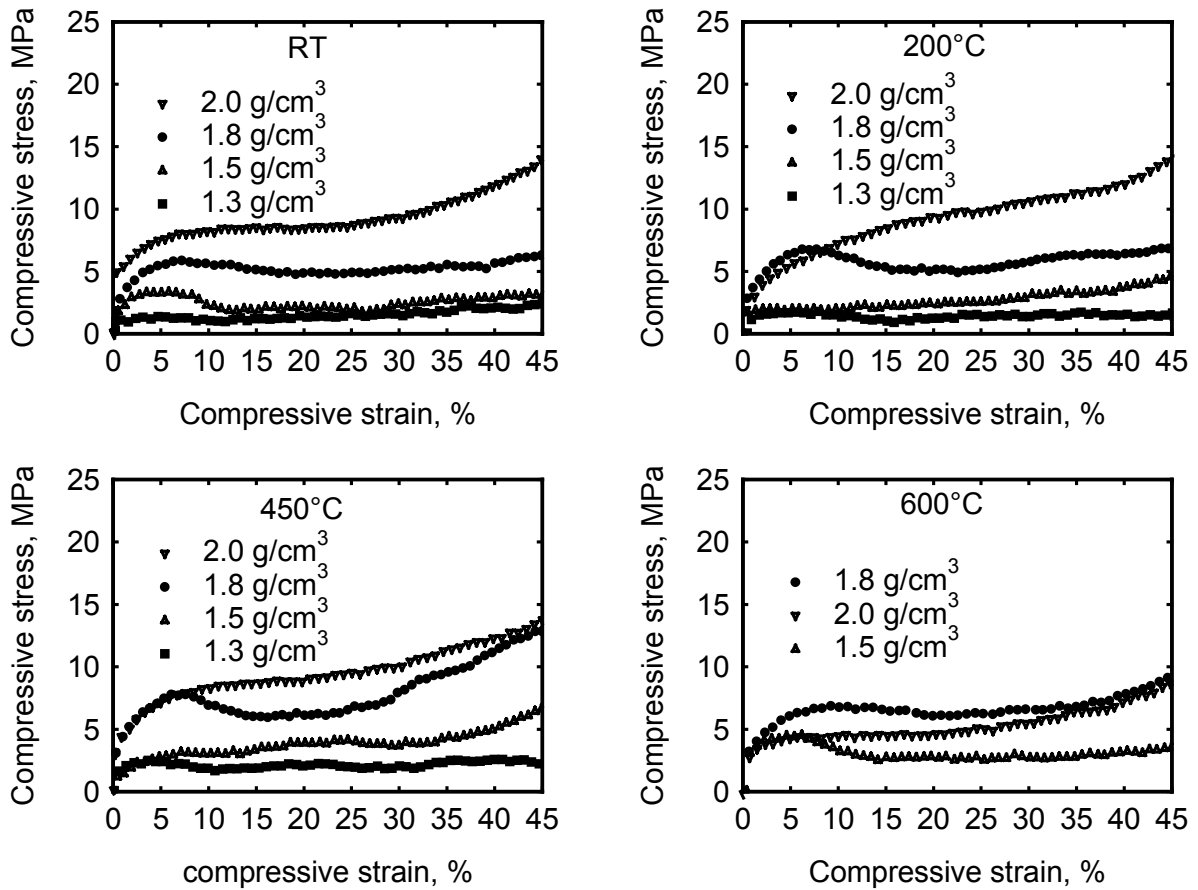


Fig. 6-51 Density dependence of the stress-strain curves of the Astaloy foams, compressed at different temperatures.

6.2.2.2.2 Effect of Temperature

Fig. 6-52 represents the effect of the temperature on the stress strain curves of different densities of the Astaloy foams

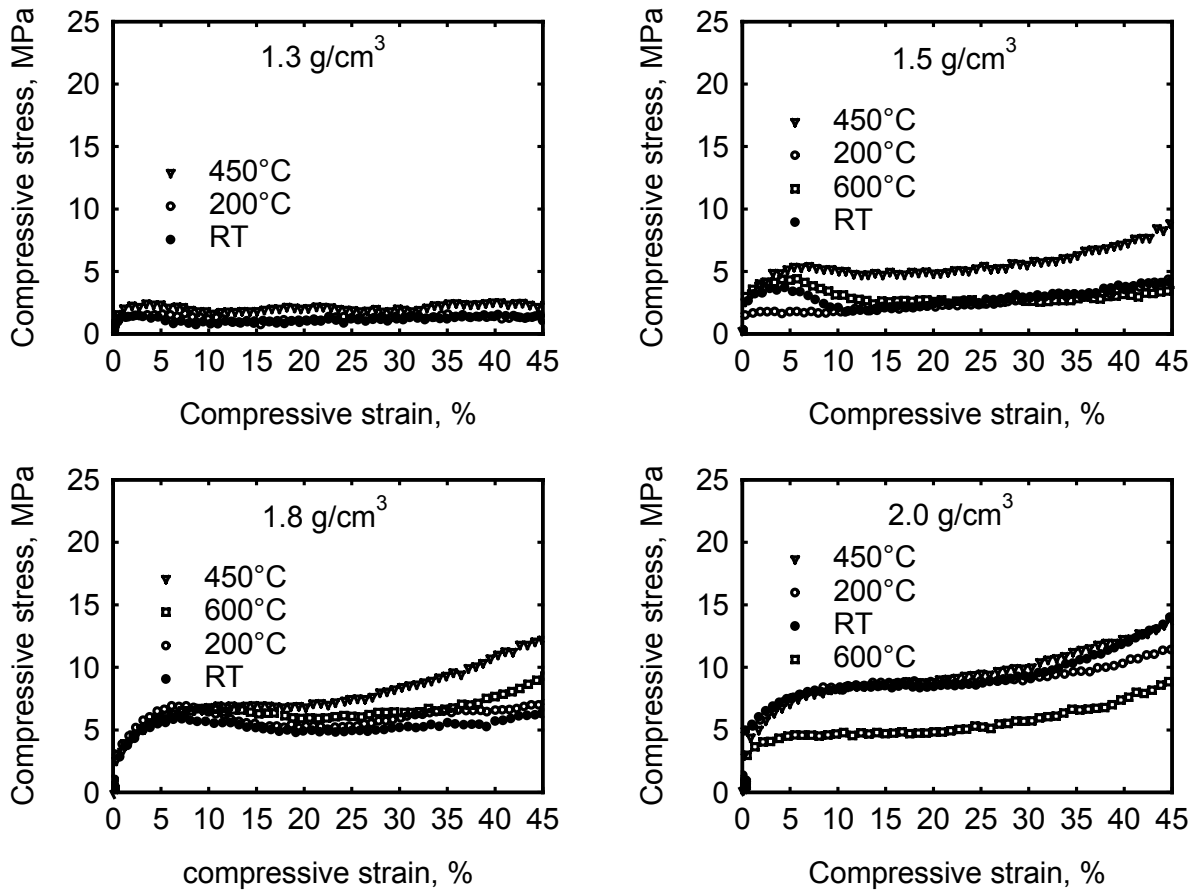


Fig. 6-52 Temperature dependence of stress-strain curves of different densities of Astaloy foams.

Tab 6-12 gives the compressive strength of the Astaloy foams at 20% strain as a function of the foam's density and temperature. It is worth noting that the compressive strength values of the Astaloy foams at higher temperatures (until 450°C) compared with those at RT are relatively large, as illustrated in **Fig. 6.53**. The Astaloy foams begin to soften when the temperature goes over 450°C. Experiments on low and high alloyed steels revealed that the presence of molybdenum increases the high temperature strength as well as the creep resistance of the material. Experiments carried out on Fe-Mo alloys revealed that molybdenum increases the creep resistance of α -solid solution as well as it decreases the recrystallisation temperature after cold working. This may explain why Mo-alloyed steels have better properties than Mo-free steels. In case of steels with low carbon content as well as low alloying elements, the formation of an intermediate structure (bainite), which has

better properties than those of perlite as well as martensite, may explain this important role of molybdenum on the mechanical properties of materials especially at high temperatures [ARC51].

Like the behaviour of the Distaloy foams compared with that of Alporas foams, the Astaloy foams have been found to behave in the same manner, as shown in **Fig. 6-53**, wherein the compressive strength of Astaloy foams having two different densities 1.5 and 2.0 g/cm³, respectively as well as of 0.20 g/cm³ Alporas foams was plotted as a function of the temperature. Alporas foams soften with increasing the test temperature unlike the Astaloy foams, whose compressive strength increases with the temperature (untill 450°C) and then decreases with increasing the temperature. As noted above the coarsening of the precipitates may be the reason for this softening effect in case of Alporas foams.

Density, g/cm ³	Compression strength at 20%, MPa							
	RT		200°C		450°C		600°C	
1.3	0.7	1.7	1.2	-	2.3	2.9	-	-
1.5	2.1	2.4	3.2	2.4	3.9	5.0	2.7	-
1.8	5.0	5.3	3.4	5.3	6.5	7.3	6.4	9.2
2.0	8.8	8.8	8.9	8.7	9.2	8.8	4.5	-

Tab. 6-12 Density and temperature dependence of compression strength of the Astaloy foams

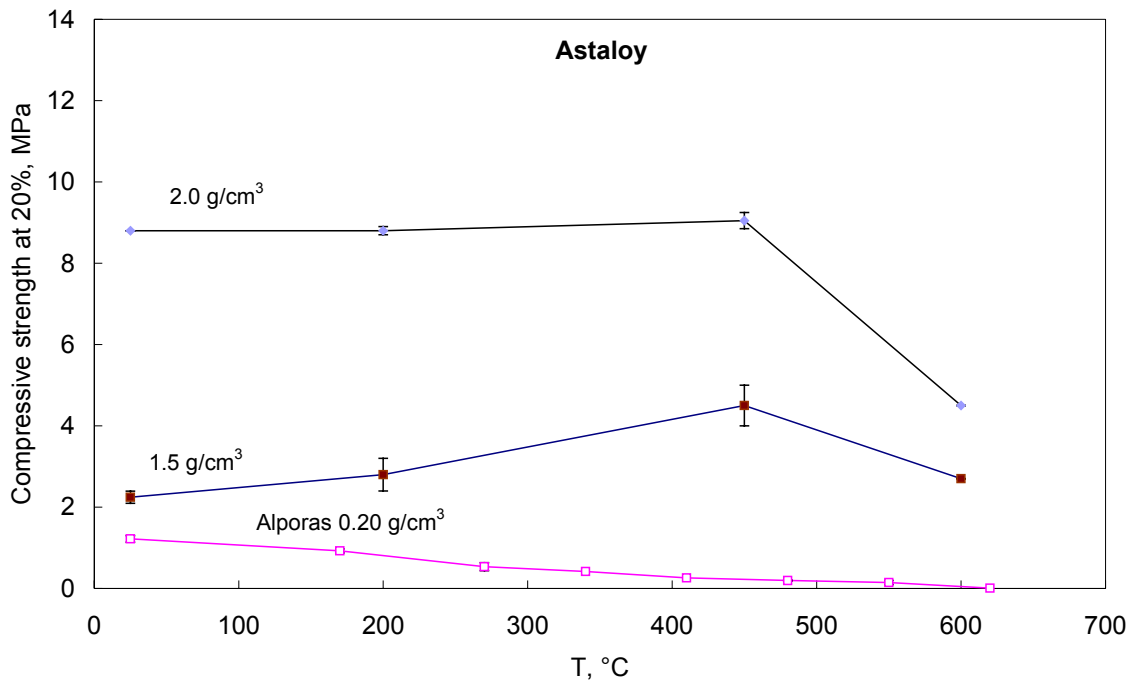


Fig. 6-53 Compression strength as a function of foam’s density and test temperature.

6.2.2.2.3 Metallographic Examination

6.2.2.2.3.1 Stereoscopic Examination of the Astaloy Foams

The stereoscopic macrographs of the upper surfaces of the tested Astaloy samples, **Fig. 6-54** to **Fig. 6-58**, show that some samples have pores of various sizes. Others having regions, in which a cluster of material is found and the foam looks like to be a compact one. This may have resulted from the effect of stirring of the mixture during the manufacturing process. All these factors may be the reasons for that scattering in the obtained results.

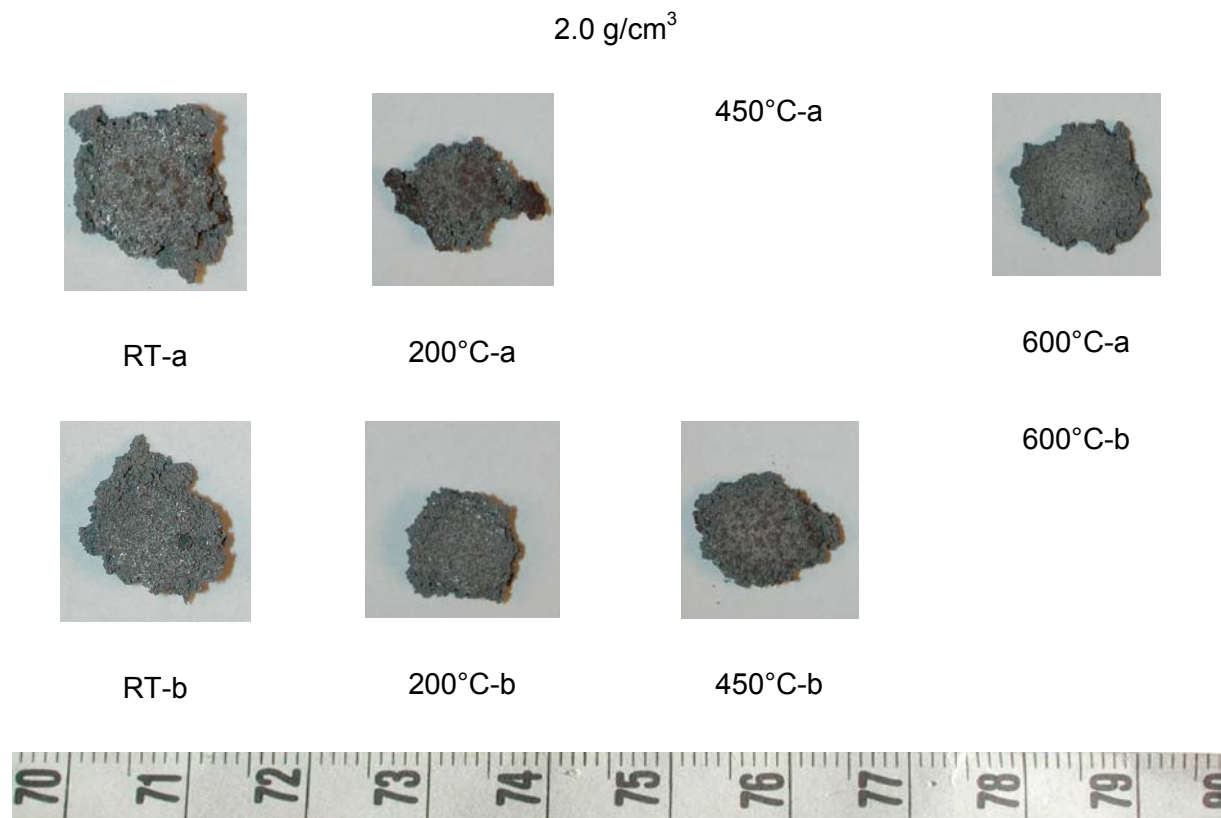


Fig. 6-54 Stereoscopic macrographs of the Astaloy foams ($\rho = 2.0 \text{ g/cm}^3$).

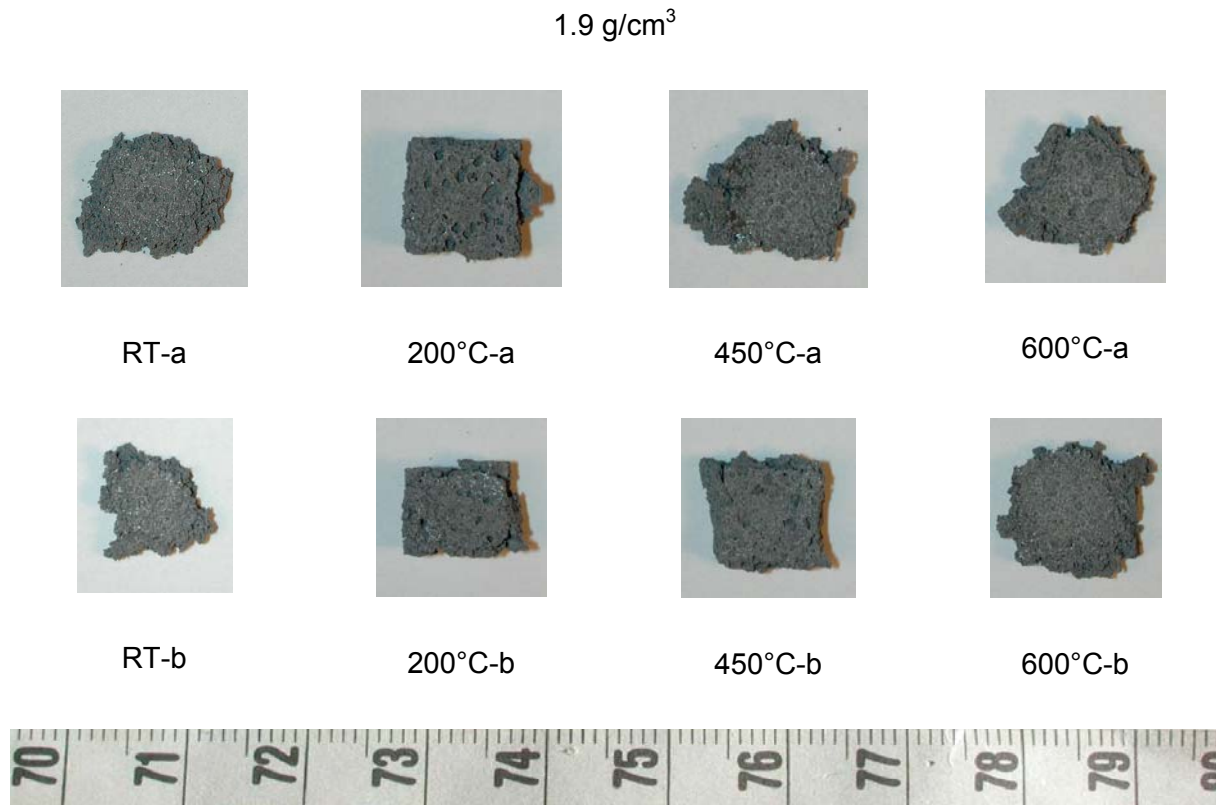


Fig. 6-55 Stereoscopic macrographs of the Astaloy foams ($\rho = 1.9 \text{ g/cm}^3$).

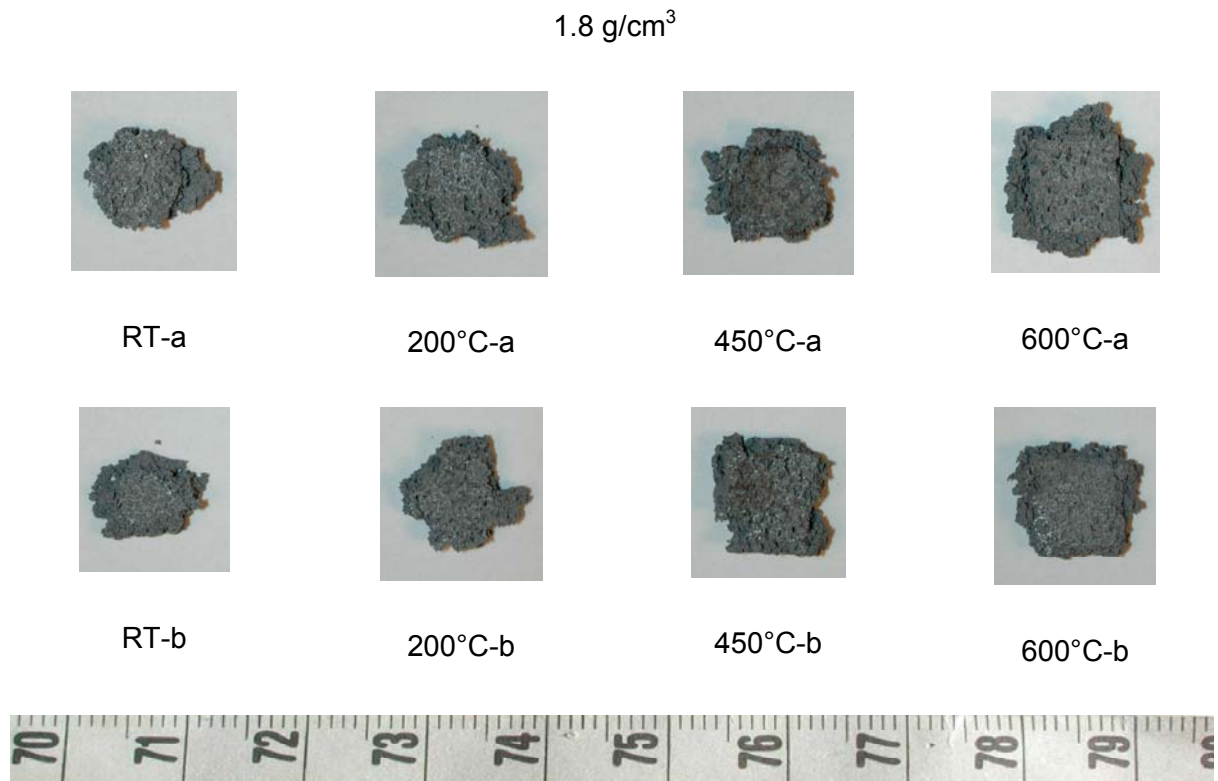


Fig. 6-56 Stereoscopic macrographs of the Astaloy foams ($\rho = 1.8 \text{ g/cm}^3$).

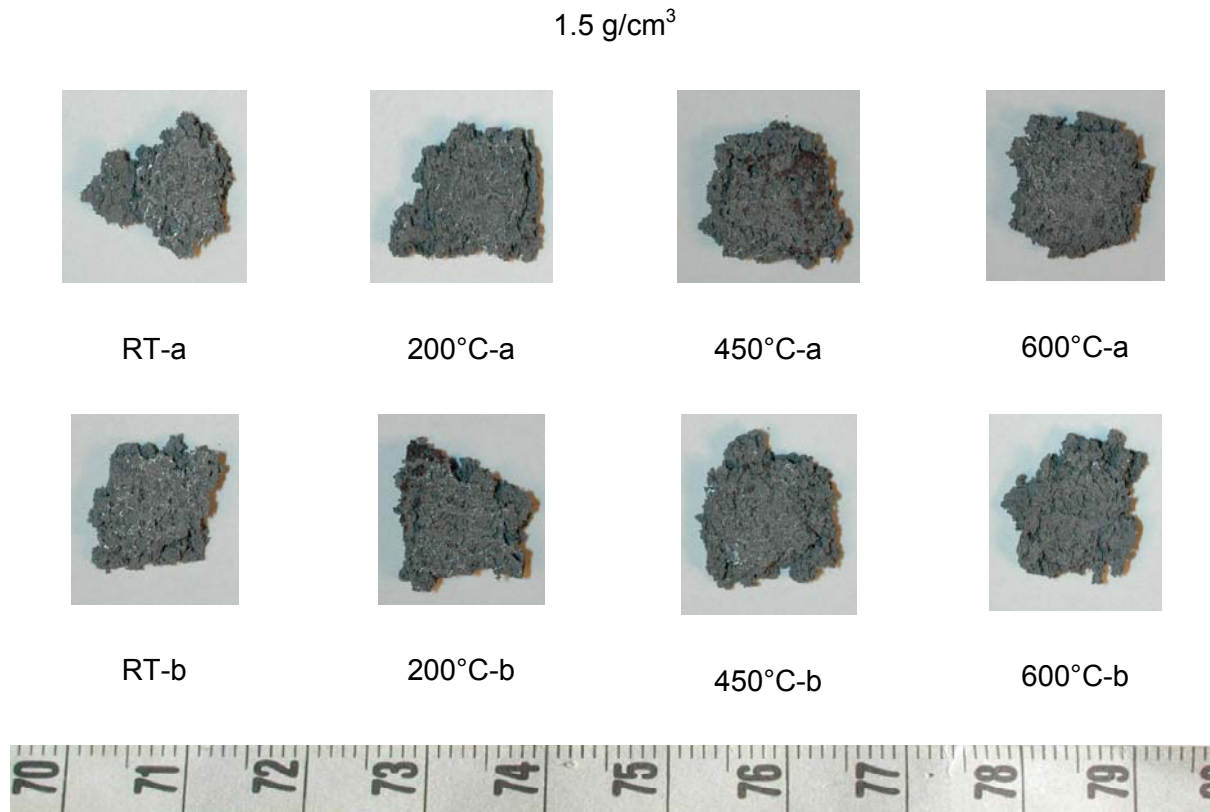


Fig. 6-57 Stereoscopic macrographs of the Astaloy foams ($\rho = 1.5 \text{ g/cm}^3$).

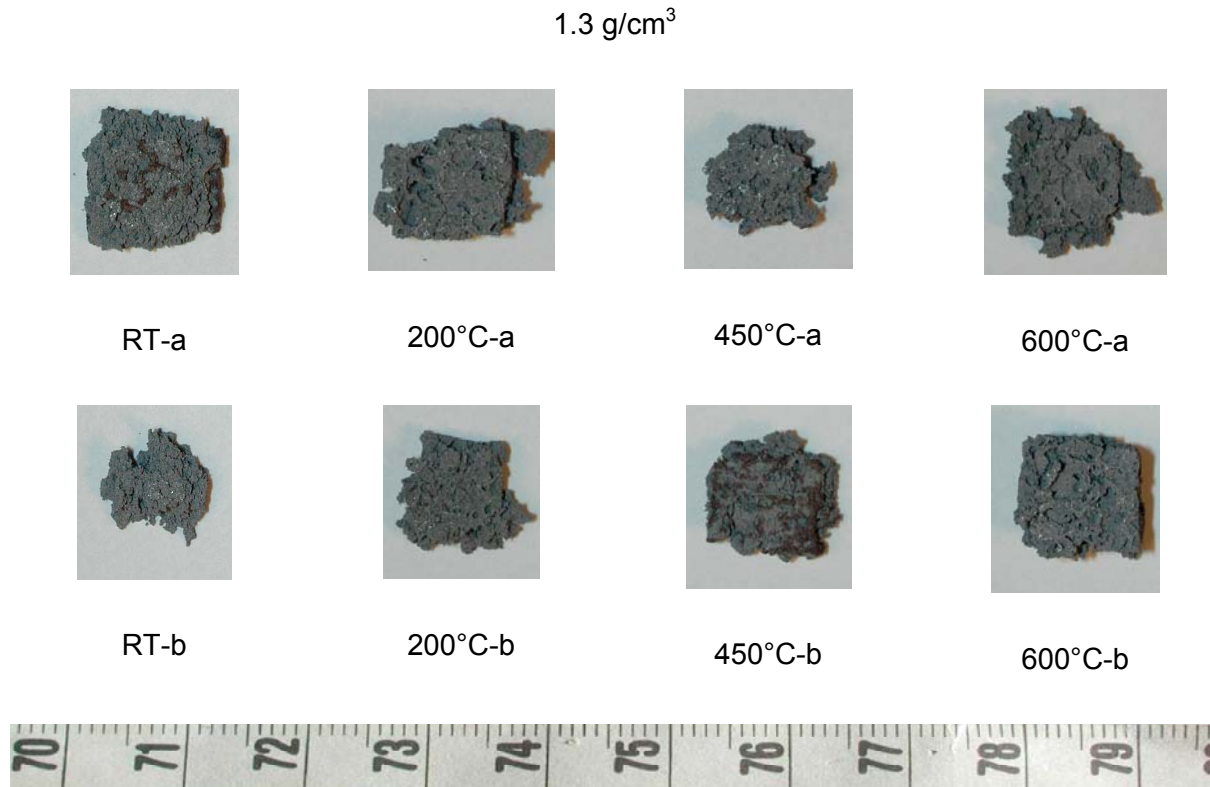


Fig. 6-58 Stereoscopic macrographs of the Astaloy foams ($\rho = 1.3 \text{ g/cm}^3$).

6.2.2.2.3.2 Microstructural Examination of the Astaloy Foams

Fig. 6-59 shows the microstructure of deformed Astaloy foams after testing at various temperatures. It can be observed that the pores having large sizes are not homogeneously distributed. Some partial connections (sintering bridges) between the powder particles are also observed. The irregularities of the pore size as well as pore distribution within the foams influence their mechanical properties.

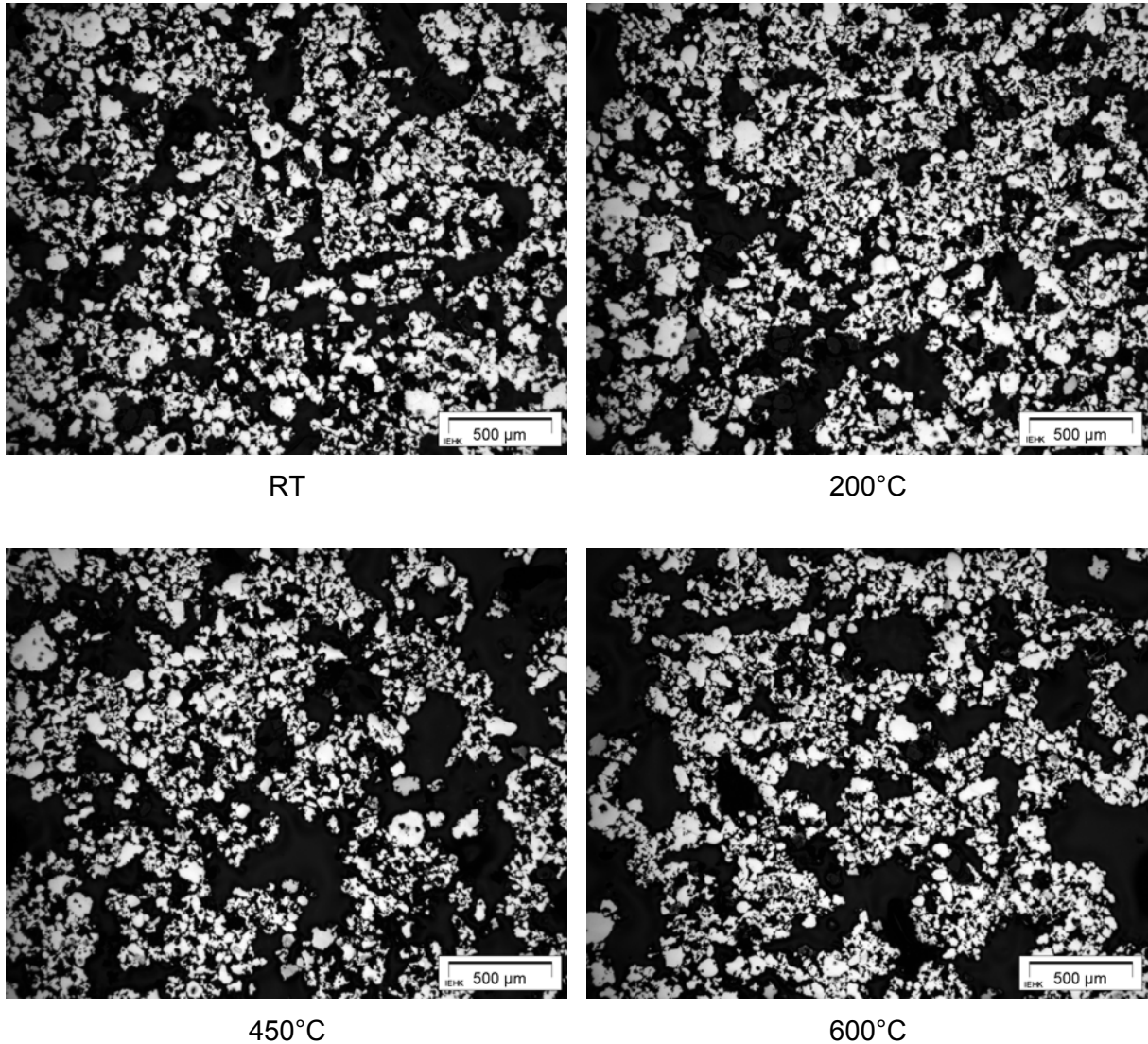


Fig. 6-59 Microstructure micrographs of the deformed Astaloy foams ($\rho = 1.8 \text{ g/cm}^3$) at different test temperatures.

6.2.2.2.4 SEM Characterisation of the Astaloy Foams

An Astaloy sample having a density of 1.8 g/cm^3 and compressed at 450°C was taken as an example for the investigation by means of a scanning electron microscope. **Fig. 6-60** shows a typical irregular morphology of the Astaloy powders. The particles have not completely

stuck with each other, as for Distaloy. The irregular shapes of Astaloy particles and their clogged surfaces do not allow the particles to get stuck with each other.

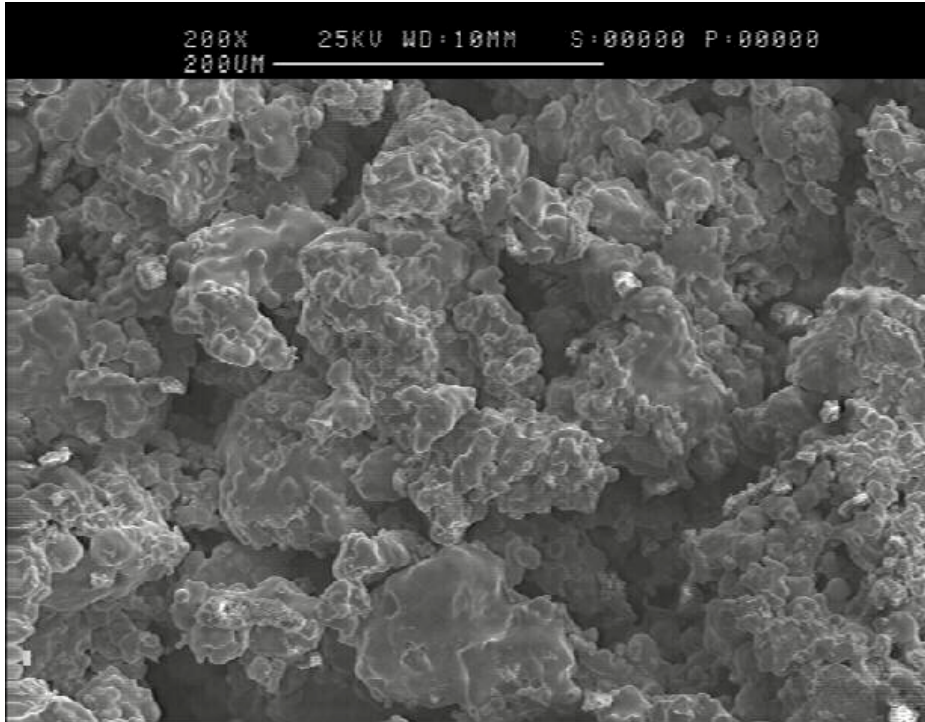


Fig. 6-60 SEM micrograph of an Astaloy foam ($\rho = 1.8 \text{ g/cm}^3$) compressed at 450°C .

6.2.3 Comparison between in air- in Ar Compressive Tests

6.2.3.1 Distaloy Foams

Compared with tests conducted in Ar, compression strength values of the Distaloy foams which were compressed in atmospheric air were enhanced, as illustrated in **Fig. 6-61**. The formation of an oxide scale on the surface of the foam affects its mechanical properties and increases its resistance against corrosion.

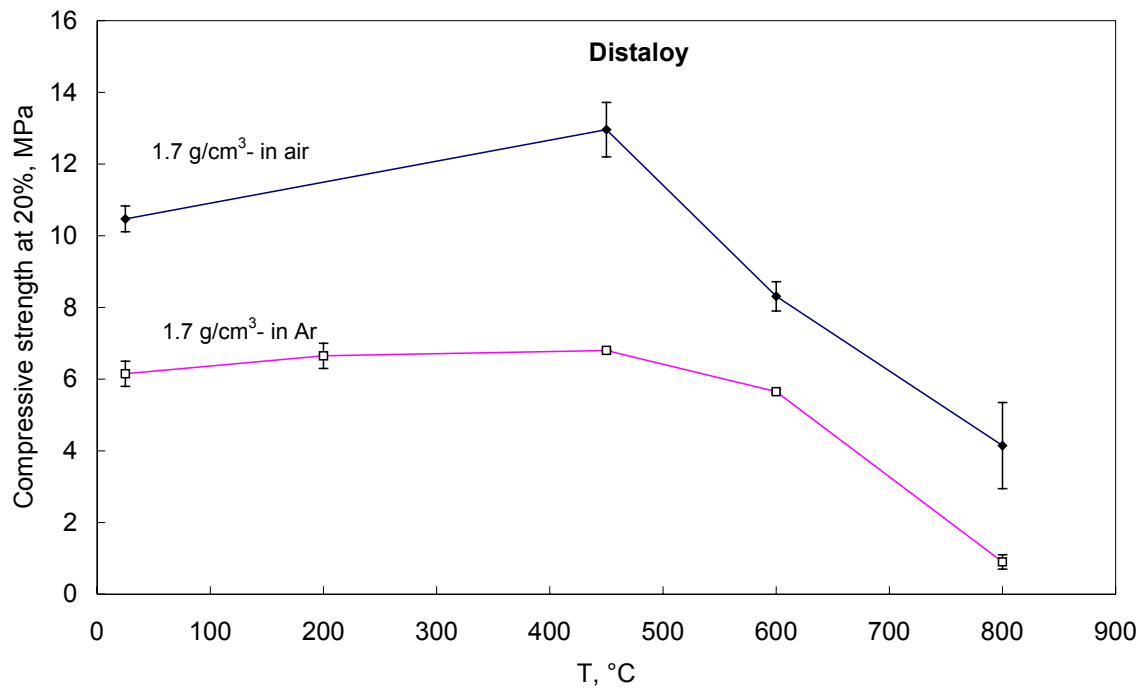


Fig. 6-61 Temperature dependence of the compression strength of Distaloy foams ($\rho = 1.7 \text{ g/cm}^3$) at 20% strain after testing in air as well as Ar atmosphere.

6.2.3.2 Astaloy Foams

A similar trend for Astaloy foams having a density of 1.5 g/cm^3 was observed, as shown in **Fig. 6-62**.

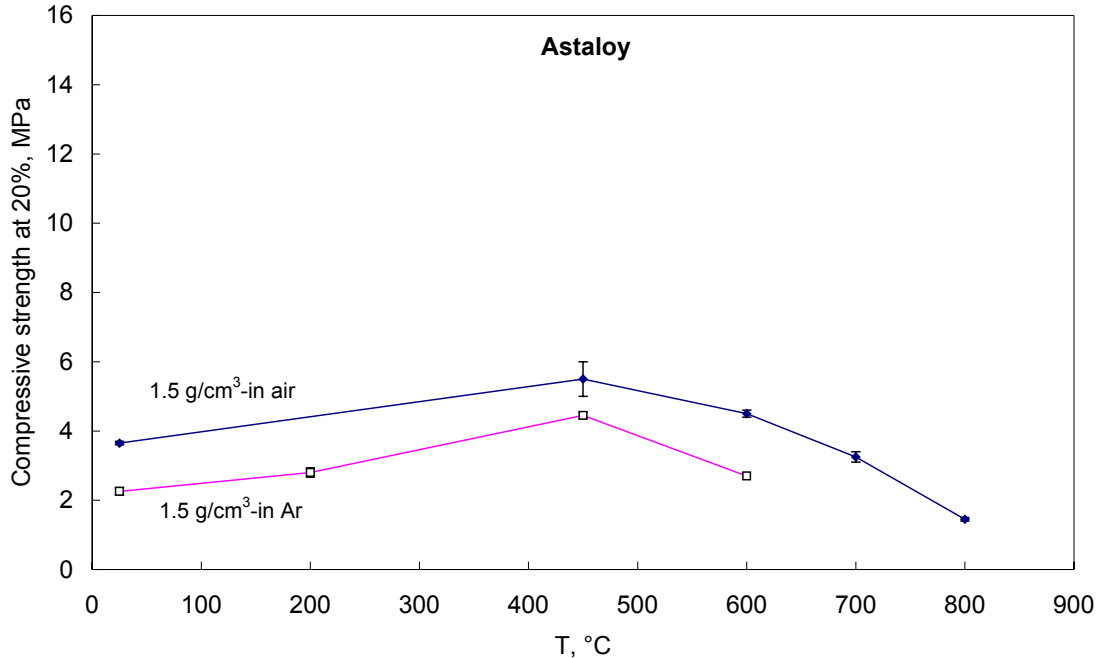


Fig. 6-62 Temperature dependence of the compression strength of the Astaloy foams ($\rho=1.5 \text{ g/cm}^3$) at 20% strain after testing in air as well as Ar atmosphere.

It is clearly noticeable from the last two figures, that the compressive strength of the Distaloy foams is larger than that of the Astaloy foams in both test conditions, namely air and Ar atmospheres, respectively. An explanation for this discrepancy may be due to the effect of the alloying elements, where it was found that the presence of Cu as an alloying element in the chemical composition of Distaloy powders increases the corrosion resistance of the material by means of building-up a thick oxide scale on the surface of the material [VAY97]. Another explanation that may clarify the behaviour of both foams upon high temperature compression may be explained by the difference in the particle morphology of the two powders. To clarify this cause, a set of metallographical as well as SEM examinations has been carried out on samples of Distaloy and Astaloy foams in the green state as well as after sintering. The chemical composition of these samples is given in **Tab. 6-13**

Sample No.	Material	Added amount of H ₂ O (g)	Added amount of H ₃ PO ₄ (g)	Added amount of SiO ₂ (g)
1123	Astaloy	17.0	1.0	2.0
1124	Astaloy	17.0	1.5	2.0
1125	Astaloy	17.0	2.0	2.0
1126	Astaloy	17.0	2.5	2.0
1127	Astaloy	17.0	3.0	2.0
1128	Astaloy	19.0	1.0	2.0
1129	Astaloy	19.0	1.5	2.0
1130	Astaloy	19.0	2.0	2.0
1131	Astaloy	19.0	2.5	2.0
1132	Astaloy	19.0	3.0	2.0
1133	Astaloy	22.0	1.0	2.0
1134	Astaloy	22.0	1.5	2.0
1135	Astaloy	22.0	2.0	2.0
1136	Astaloy	22.0	2.5	2.0
1137	Astaloy	22.0	3.0	2.0
1138	Distaloy	16.0	1.0	2.0
1139	Distaloy	16.0	1.5	2.0
1140	Distaloy	16.0	2.0	2.0
1141	Distaloy	16.0	2.5	2.0
1142	Distaloy	16.0	3.0	2.0
1143	Distaloy	18.0	1.0	2.0
1144	Distaloy	18.0	1.5	2.0
1145	Distaloy	18.0	2.0	2.0
1146	Distaloy	18.0	2.5	2.0
1147	Distaloy	18.0	3.0	2.0
1148	Distaloy	21.0	1.0	2.0
1149	Distaloy	21.0	1.5	2.0
1150	Distaloy	21.0	2.0	2.0
1151	Distaloy	21.0	2.5	2.0
1152	Distaloy	21.0	3.0	2.0

Tab. 6-13 Composition of Distaloy and Astaloy foams used for metallographical and SEM examinations.

Considering the microstructural micrographs of the Distaloy as well as the Astaloy foams, **Fig. 6-63** to **Fig. 6-66**, it can be seen that the particles of the Distaloy samples are existing in round forms, compared to the irregular shapes of Astaloy one. In the green state, a loose-powdered structure was observed in case of the Distaloy as well as the Astaloy foams respectively. In the sintered state, however, the particles became closer to each other and necking (sintering bridges) have been observed. After sintering the cell walls have been compacted as well. The cell structure of the Distaloy powders seems to be more homogeneous than that of Astaloy one. Astaloy samples have a thick-walled cell structure, i.e. large pores and isolated particles are dominant within the structure. Some large pores were found locally in certain sites beside other small pores. This difference in pore sizes as well as pore distribution within the foams has certainly a significant influence on their mechanical properties. Large pores will lead to poor mechanical properties. A sign for foams' irregularity can be immediately observed with the necked eye upon detecting the upper surfaces of the samples (stereoscopic micrographs).

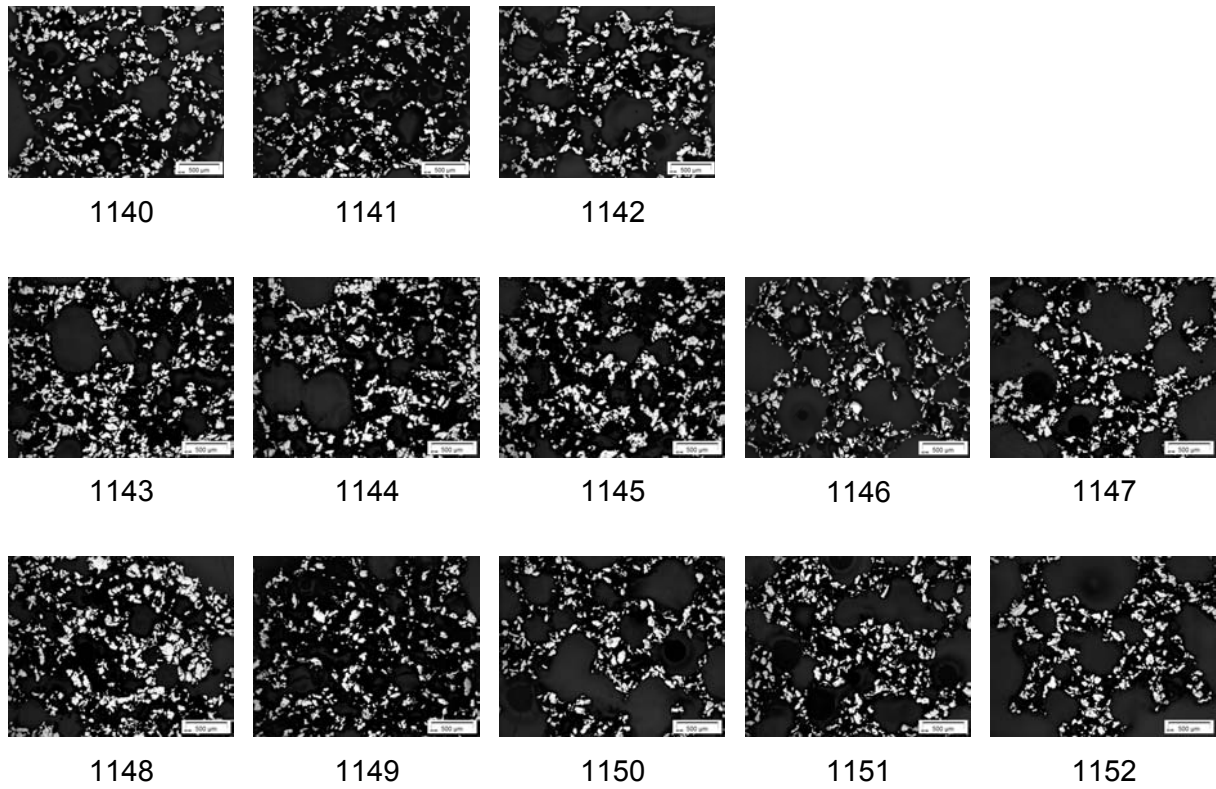


Fig. 6-63 Microstructural micrographs of Distaloy foams in the green state.

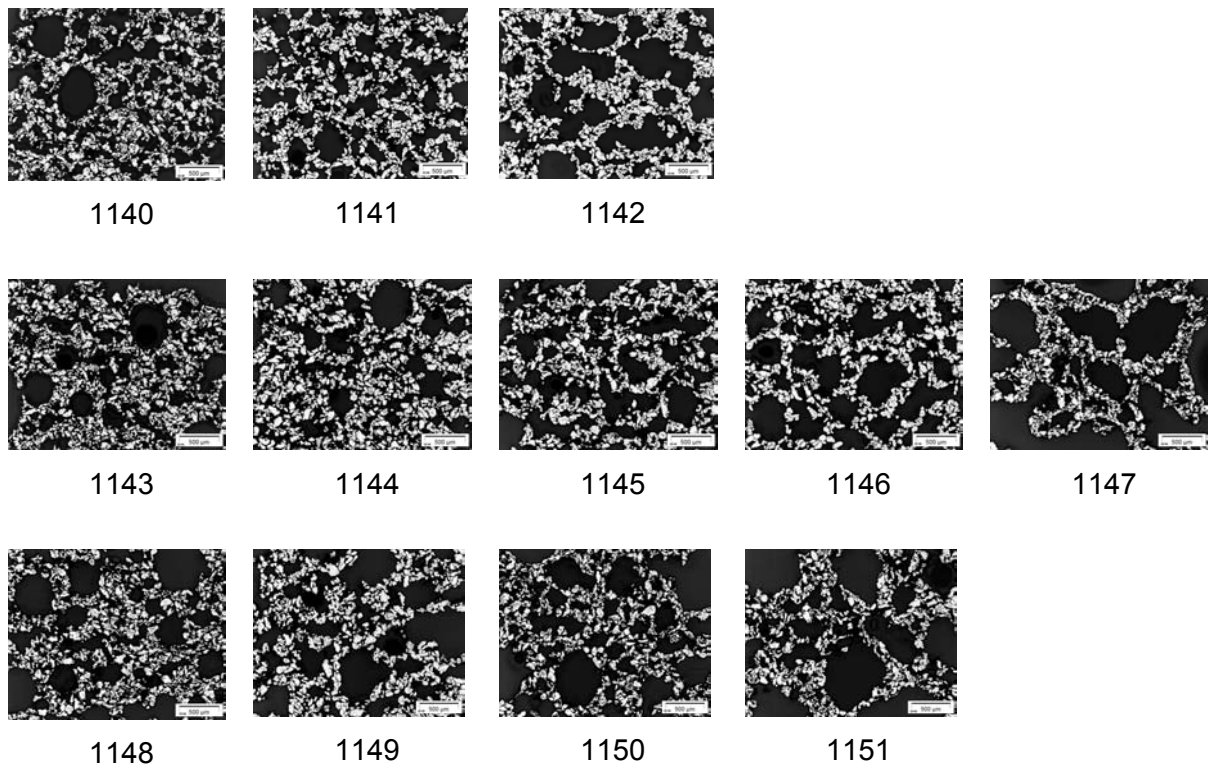


Fig. 6-64 Microstructural micrographs of Distaloy foams in the sintered state.

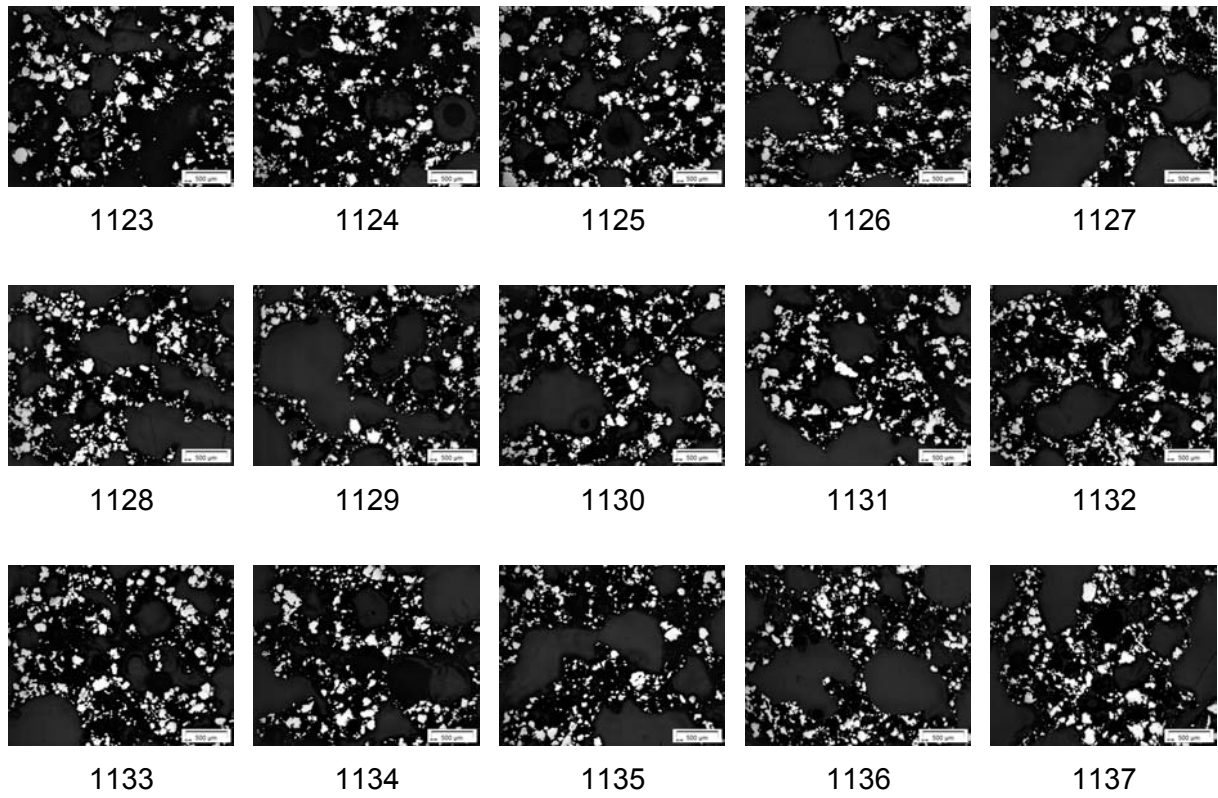


Fig. 6-65 Microstructural micrographs of Astaloy foams in the green state.

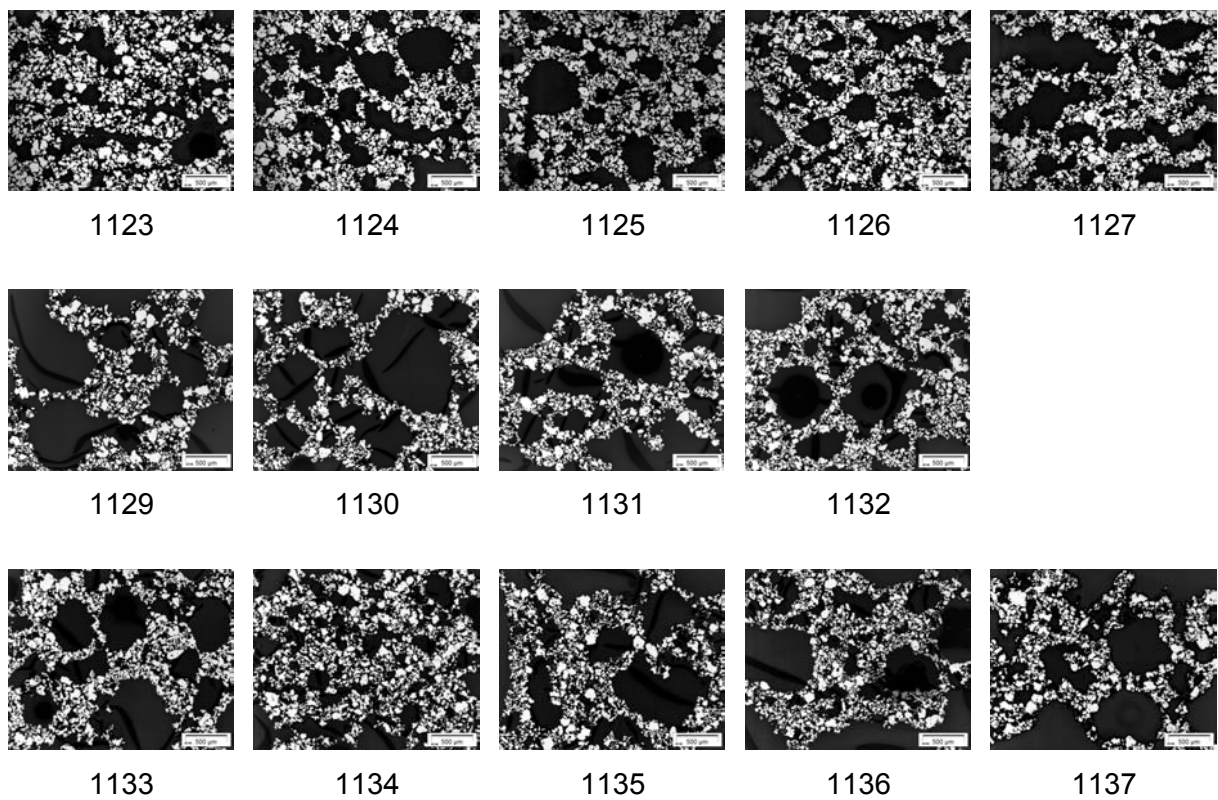


Fig. 6-66 Microstructural micrographs of Astaloy foams in the sintered state.

Considering the SEM-micrographs of the Distaloy as well as the Astaloy foams in the green and in the sintered state as well, shown in **Fig. 6-67** to **Fig. 6-70**, it can be seen that both foams in the green state have had a characteristic foamy structure. Post-sintering SEM-micrographs of Distaloy and Astaloy foams show a larger number of micro-pores than that existing in green state. The number written beneath each micrograph indicates the sample number. Via this number, the chemical composition of each sample can be easily known by referring to **Tab. 6-13**.

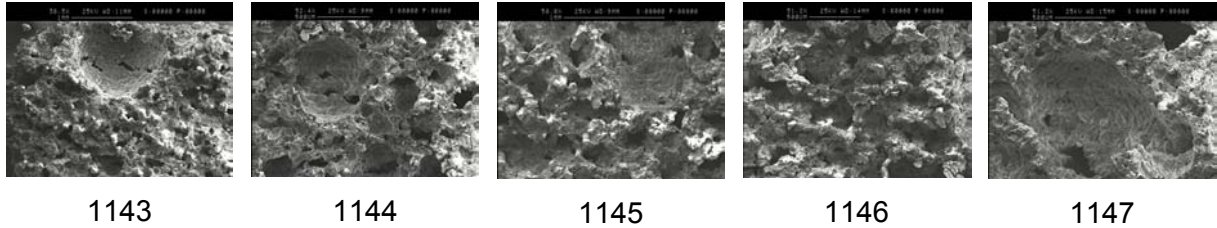


Fig. 6-67 SEM-micrographs of Distaloy foams in the green state.

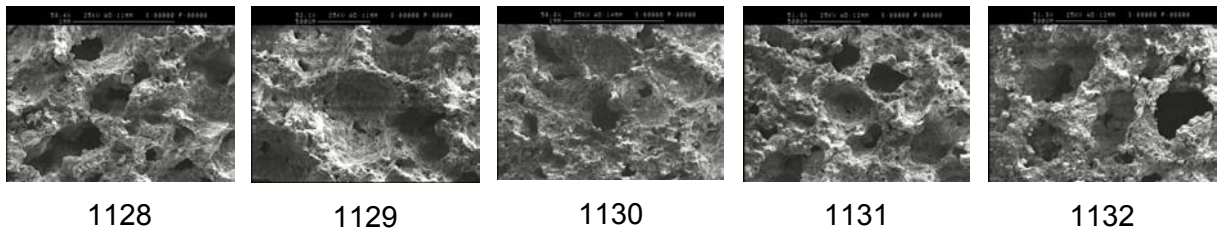


Fig. 6-68 SEM-micrographs of Astaloy foams in the green state.

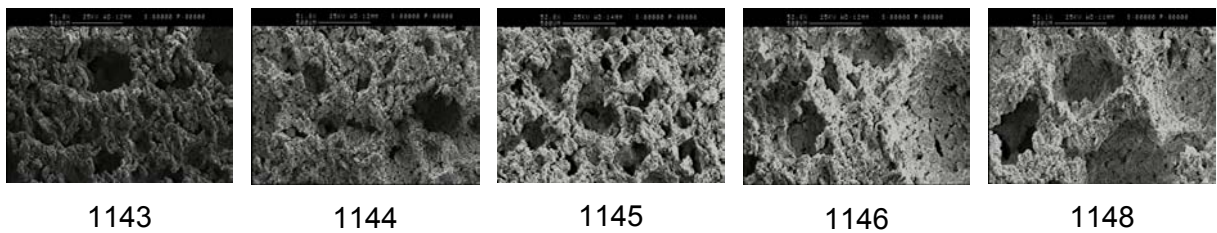


Fig. 6-69 SEM-micrographs of Distaloy foams in the sintered state.

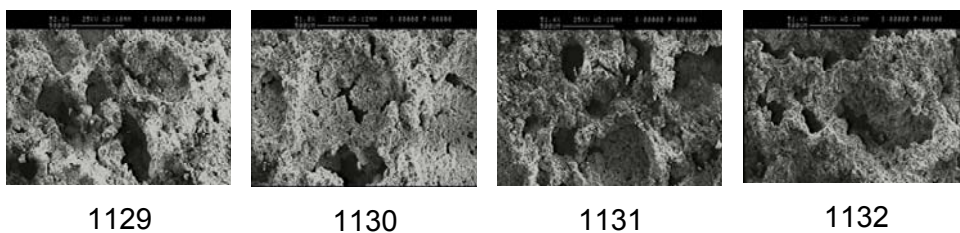


Fig. 6-70 SEM-micrographs of Astaloy foams in the sintered state.

6.2.4 Size Effect on the Foams' Mechanical Properties

A new set of experiments was carried out on large samples of Astaloy foams consisting of several thousand cells. The samples have a cross sectional area of $50 \times 50 \text{ mm}^2$. A thermocouple type S (Pt-Pt Rh 10%) is conducted to the sample in three positions in order to monitor accurately the temperature of the sample, as shown in **Fig. 6-71**. The difference between the nominal as well as the measured temperature was found to be $\pm 10^\circ\text{C}$, as shown in **Fig. 6-72**. The samples were compressed under the same conditions like the small ones, i.e. at a constant rate of displacement of 1 mm/min . After reaching the required test temperature, the samples were held at this temperature for approximately 1 min in order to achieve a homogeneous temperature distribution throughout the sample.

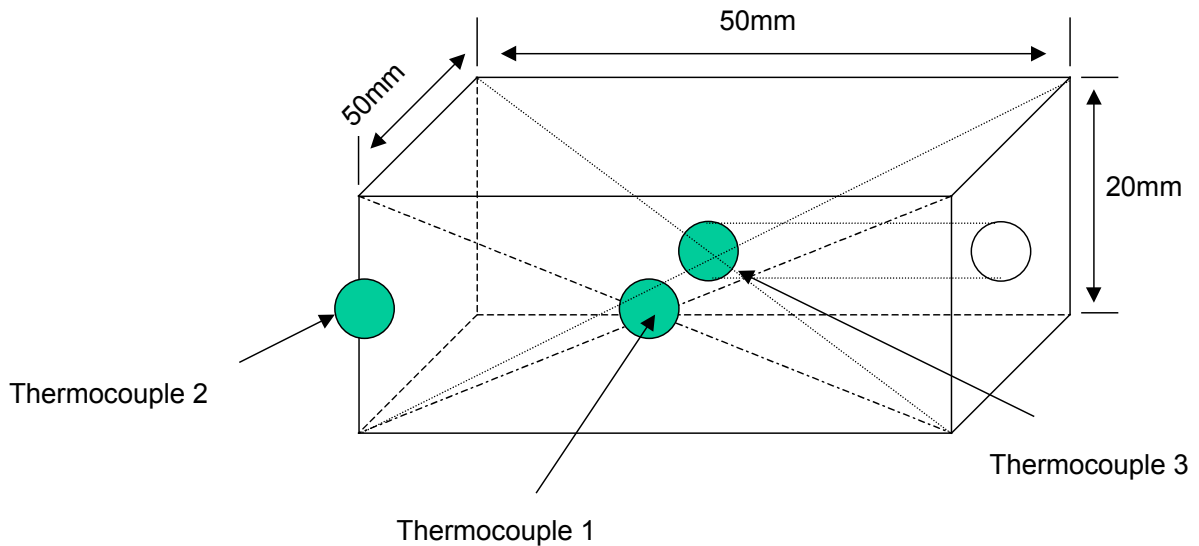


Fig. 6-71 A schematic illustration of three thermocouples conducted to a foam sample having a cross sectional area of $50 \times 50 \text{ mm}^2$.

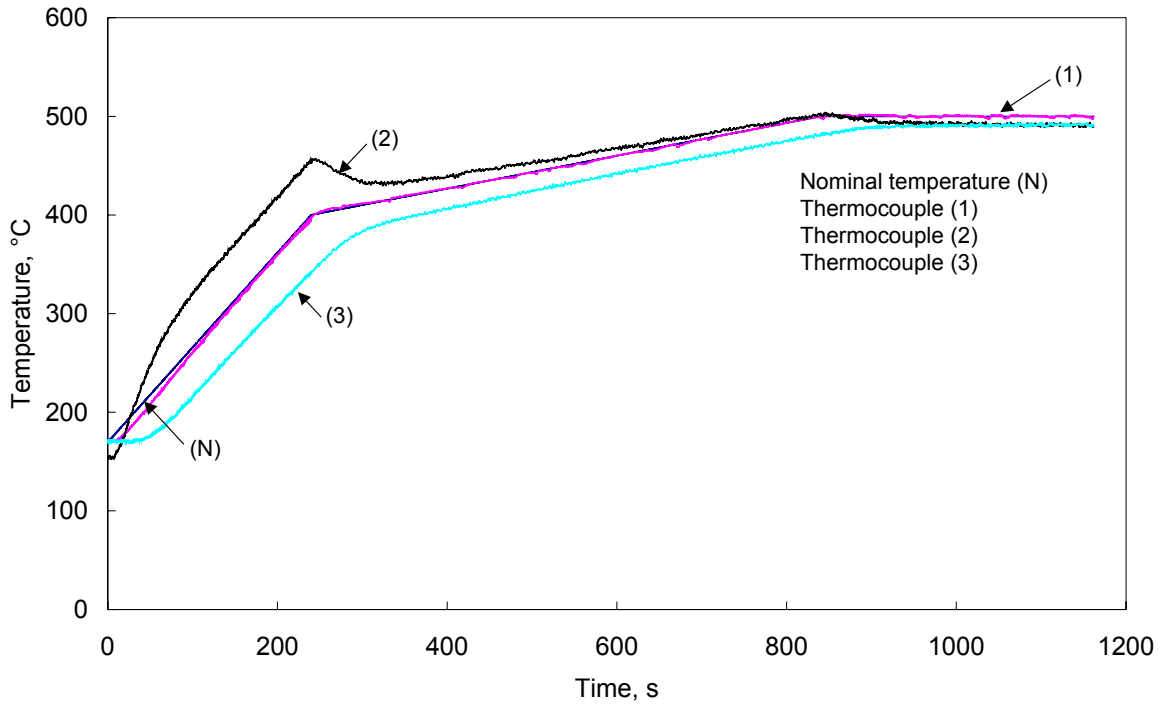


Fig. 6-72 Temperature monitoring in a foam sample using three different thermocouples.

Two different densities of Astaloy foams, namely 1.5 and 1.9 g/cm³, respectively, were compressed in an inert atmosphere (Ar) at various temperatures. The compression strength at 20% was measured at the correspondent testing temperature and listed in **Tab. 6-13**.

Density, g/cm ³	Compression strength at 20%, MPa							
	25°C		200°C		450°C		600°C	
1.5	3.3	4.8	4.1	8.1	5.2	9.1	5.0	7.6
1.9	9.6	10.9	12.1	7.4	12.7	12.0	11.9	8.5

Tab.6-13 compression strength at 20% for large samples of Astaloy foams as a function of temperature.

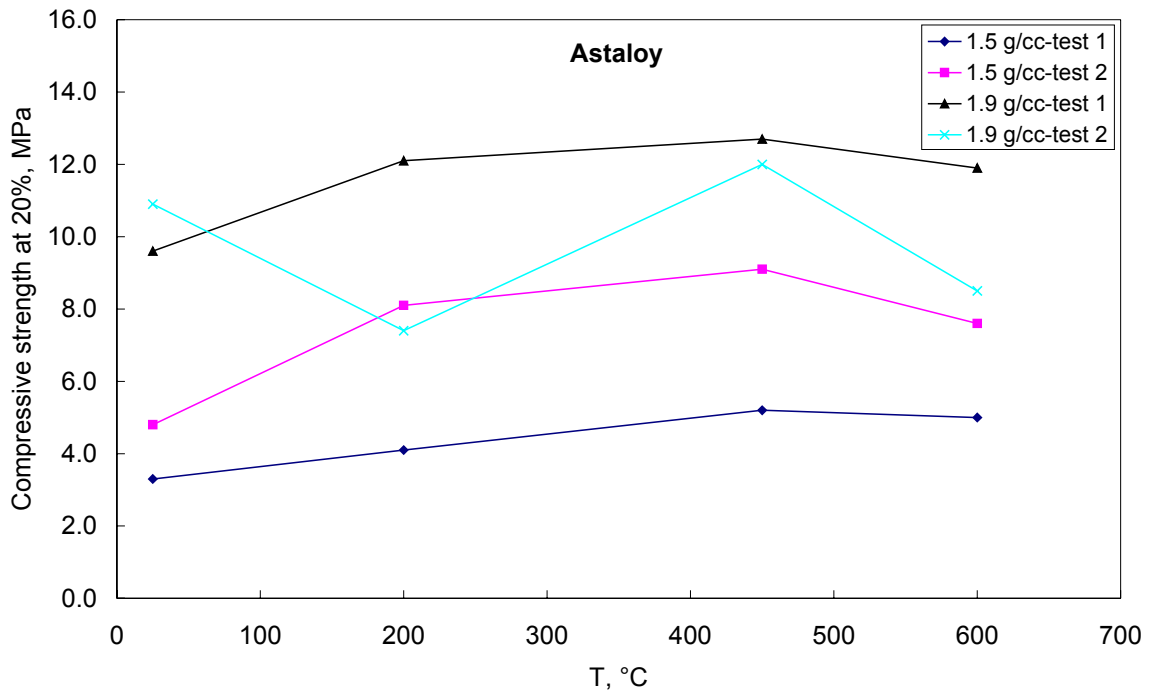


Fig. 6-73 Temperature dependence of compressive strength (mean value) of large samples of Astaloy foams ($\rho = 1.5$ and 1.9 g/cm^3) having a cross sectional area of $50 \times 50 \text{ mm}^2$ (after compression in Ar-atmosphere).

As clearly shown from the past results, listed in **Tab. 6-13** and represented in **Fig. 6-73**, the dependence of the compressive strength of the Astaloy foams, having large cross sectional area, and consequently large number of cells, on the temperature is similar to that of small ones.

6.2.5 Strain Rate Dependence of the Foam's Mechanical Properties

In order to examine the effect of the dynamic age hardening, a new set of compressive tests was carried out on samples of Astaloy (1.5 g/cm^3) as well as Distaloy (1.9 g/cm^3) foams having a cross sectional area of $50 \times 50 \text{ mm}^2$ by using the Schenck equipment with a maximum load cell of 160 kN. The tests were carried out at the same conditions but the difference here is that the specimens were deformed under high strain rate. The tests were performed at a fixed rate of displacement of 100 mm/min.

It can be seen from **Fig. 6-74** that the metallic foams show, at higher temperatures, the same behaviour like that of the compact materials. As the temperature increases, the compressive strength of the foams decreases. This degrading in the foam's mechanical properties may be regarded to the softening mechanisms (recovery and recrystallisation) taking place during the high temperature testing. The disappearance of the ascending compressive strength of

the foams at 200°C as well as 450°C, respectively indicates clearly that the mechanical properties of Distaloy as well as Astaloy foams are strongly dependant on the rate of strain at which the test was carried out and this ensures the assumption that the reason for the enhancement within the foam's mechanical properties which have been deformed at 1 mm/min over this range of temperature was because of the well-known phenomenon "age-hardening" [MEM89].

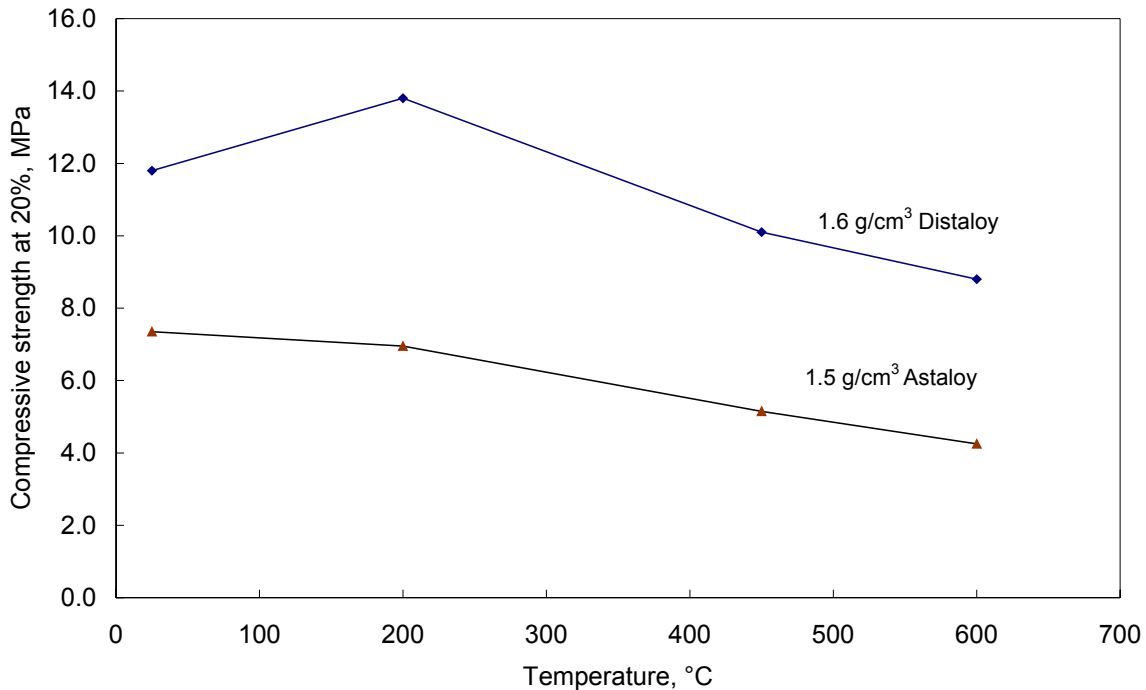


Fig. 6-74 Temperature dependence of the compressive strength of Astaloy and Distaloy foams (50 x 50 mm²) after compressive testing in Ar atmosphere at 100 mm/min.

6.2.6 DTA Measurement

In order to have an insight on the thermal events taking place upon heating during the high temperature compression tests, a sample of Distaloy foam (250 mg) was investigated by means of a Differential Thermal Analysis (DTA). A device Netzsch 404 S, shown in **Fig. 5-12**, was used to measure the temperature difference between a reference material (Al₂O₃) and the material which has to be investigated, as described in the past chapter. 200 mg of a Distaloy foam has to be finely ground so as to guarantee a homogeneous distribution over the entire crucible and accurate measurements are thus obtained. The sample was heated with a rate of heating of 10 K/min.

Fig. 6-75 shows the results obtained from DTA measurements for Distaloy foam as well as the Distaloy powder (as delivered), respectively. DTA measurements were carried out for

powder, which is previously melted, cooled and then reheated, and for another one which was only heated, i.e. without any previous melting. It can be seen that the powder in both cases has almost the same behaviour. Compared to the powder, the powdered foam sample exhibited a completely different behaviour. It can be observed that an endothermic reaction takes place upon heating the foam sample. The reaction starts at approximately 210°C and ends at approximately 470°C. The phase transformations occurring over this range of temperature are still unclear so far, but it has been supposed to be due to the decomposition of H_3PO_4 , involved in the foam processing, which starts at approximately 213°C. This probably represents another interpretation for this enhancement within the compressive strength of the foams measured over this range of temperature.

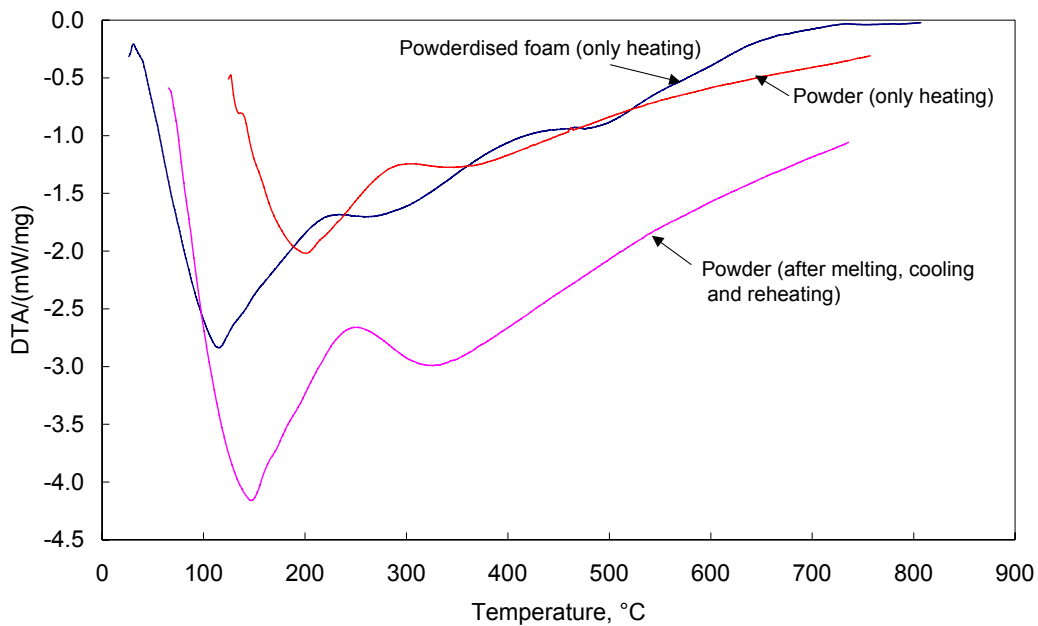


Fig. 6-75 DSC scans for samples of Distaloy powder and Distaloy foam as well.

6.2.7 X-ray Spectrometer

A set of experiments was carried out at the Department of Glass, Ceramics and Building materials (GHI, RWTH-Aachen) using a Philips PW 1830 X-ray powder spectrometer device. This device aims at measuring the intensity of the X-ray reflections from a crystal with an electronic device, such as a Geiger counter tube. The measurements were carried out at a constant rate of 0.005 s^{-1} in a 2θ range from 5 up to 70° .

Two samples of Distaloy as well as Astaloy foams were finely ground into powders. These fine powders were characterised using the X-ray spectrometer. The reflected intensity is recorded as a function of 2θ (Bragg angle) as shown in **Fig. 6-76** and **Fig. 6-77**, respectively.

The presence of the Bragg diffraction peaks, appeared in the two diffraction diagrams, indicates that the structure of the Distaloy as well as Astaloy foams is pure crystalline.

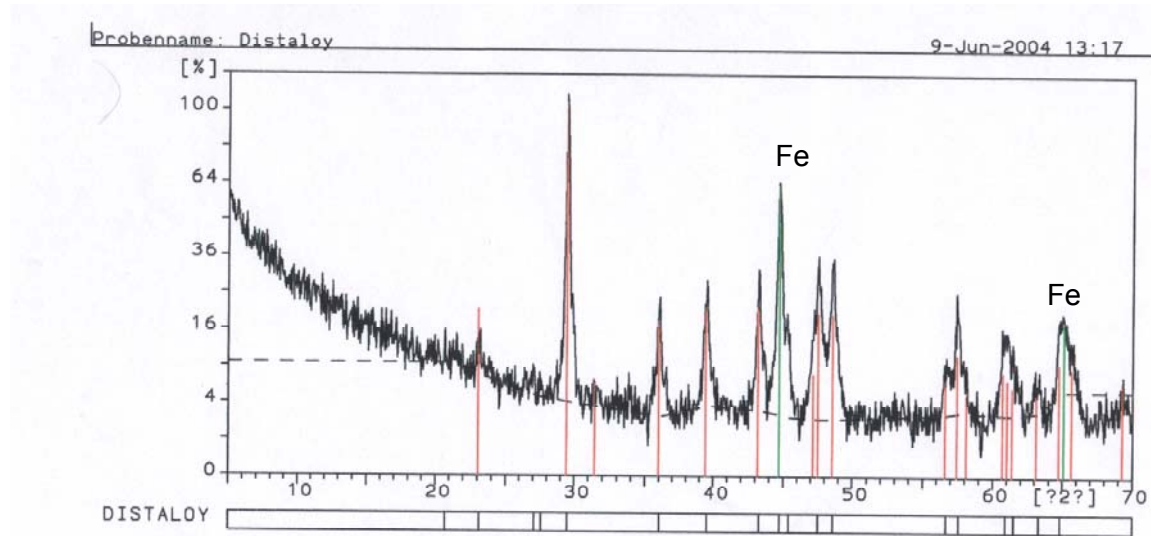


Fig.6-76 X-ray diffraction diagram of Distaloy sample.

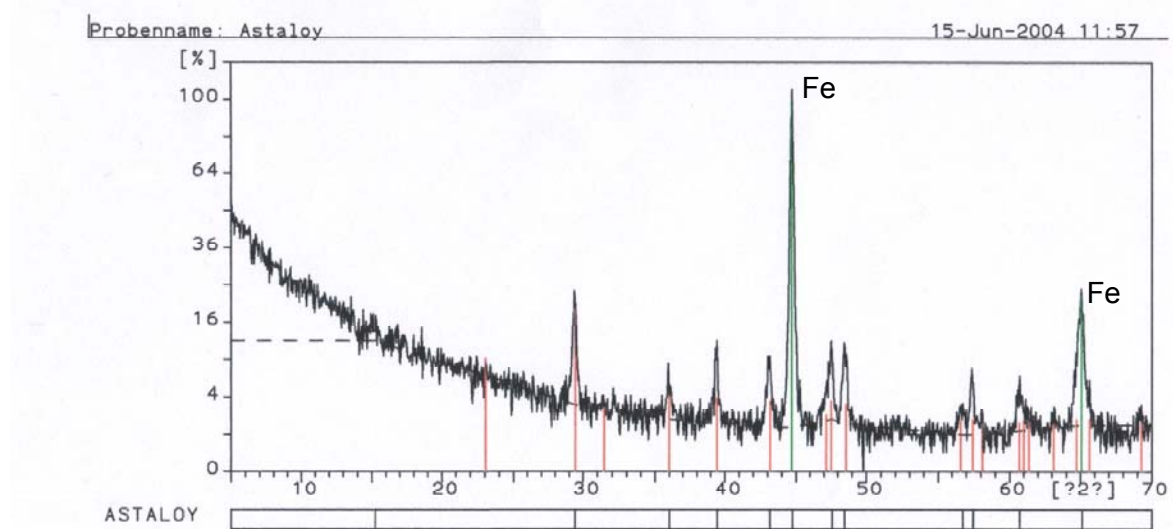


Fig.6-77 X-ray diffraction diagram of Astaloy sample.

6.2.8 Line Scan Analysis

A line scan analysis was carried out at the Central Facility of Electron Microscopy (GFE), RWTH Aachen using an electron microprobe (Camebax SX 50) equipped with wavelength dispersive spectrometers. This kind of investigation aims at determining the quantitative distribution of the elements over the microstructure of the foam.

Fig. 6-78 shows Element X-ray Mapping micrographs of a cell-wall microstructure of Distaloy foam in the sintered state. It is clearly visible that the contact areas between the iron particles are enriched with Si, P and O atoms. The diffusion of phosphorous atoms between the iron particles indicates that H_3PO_4 has wetted all the iron particles, i.e. H_3PO_4 has good wetting properties.

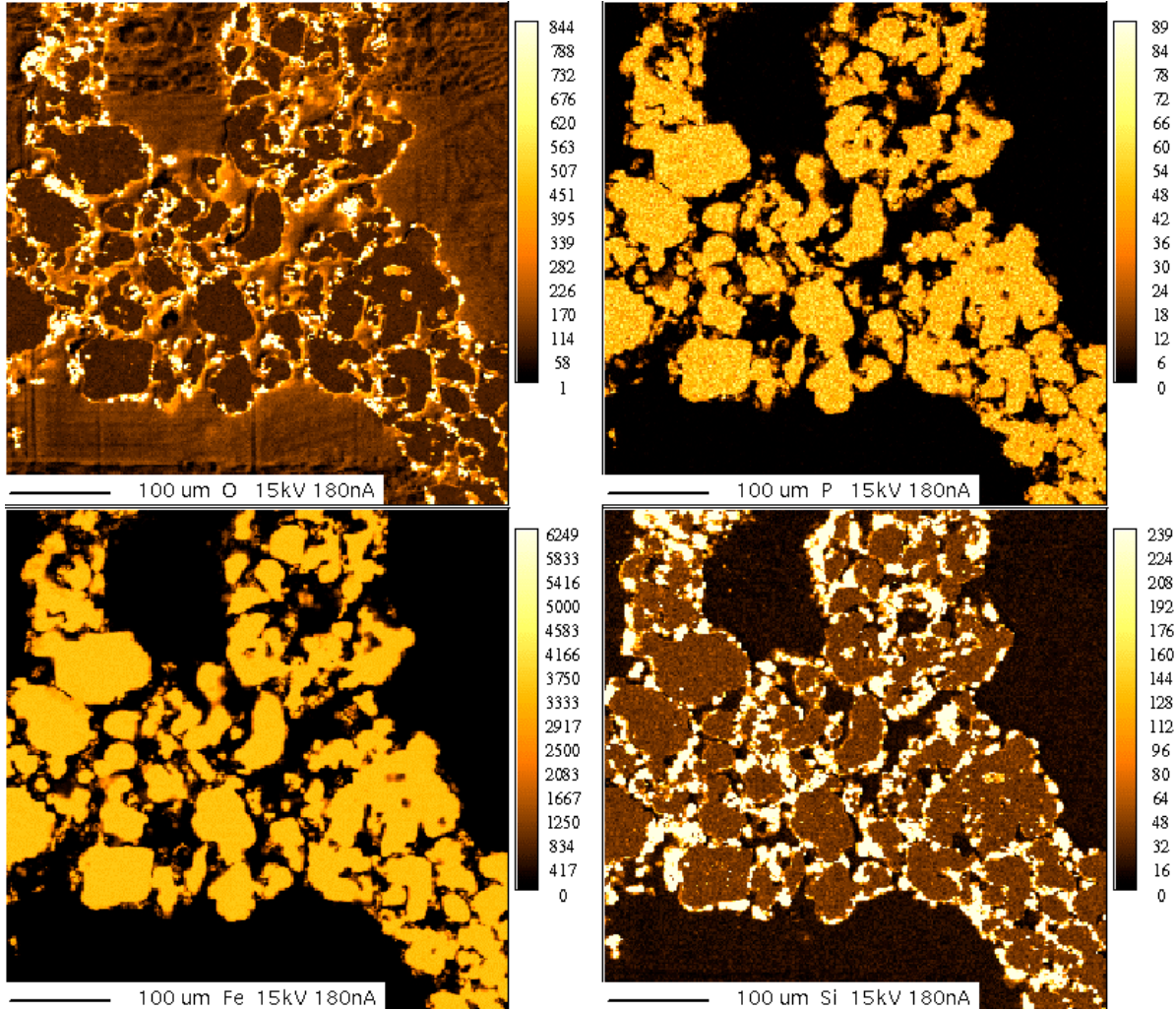
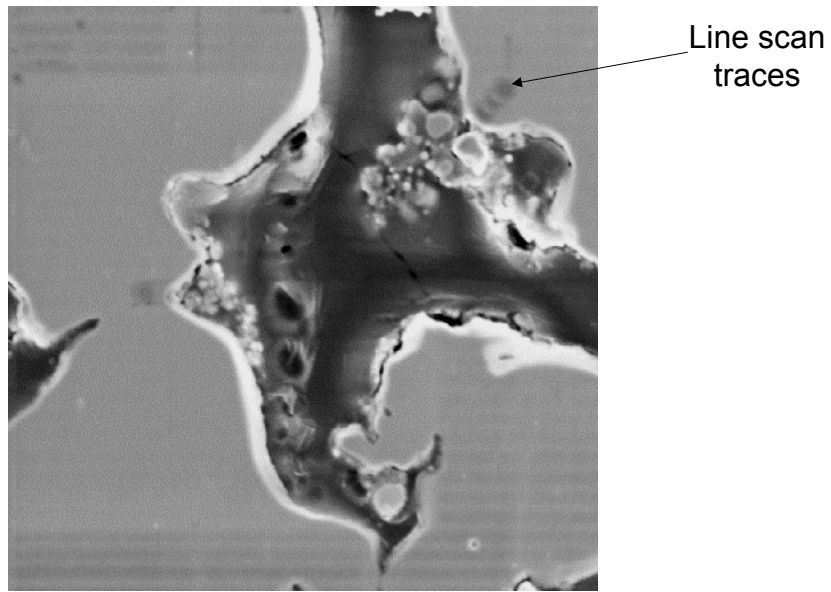
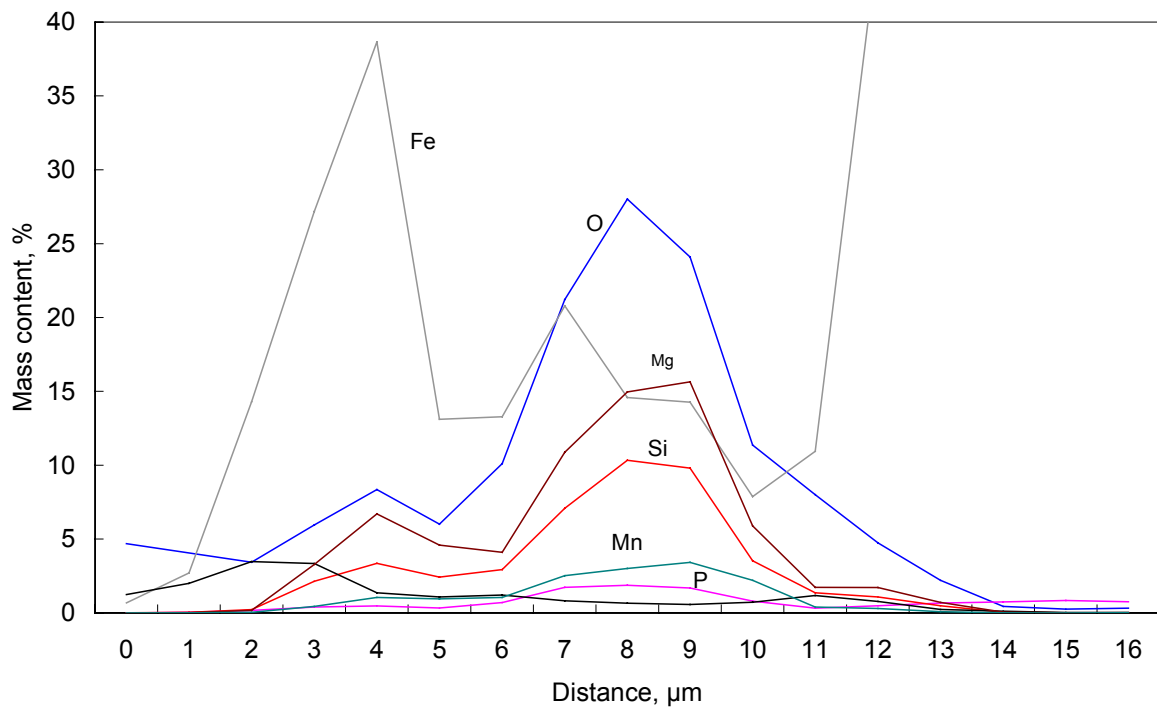


Fig. 6-78 Element X-ray Mapping micrographs for a cell-wall microstructure of Distaloy foam.

Considering for example a section in the cell-wall microstructure, as shown in **Fig. 6-79a**, the quantitative line scan measurements related to this section is illustrated in **Fig. 6-79b**. It is obviously shown that Fe, Mg, Si, Mn and P form certain types of ceramic oxides or glass phase consisting of the oxides of the past mentioned elements. The smoothing effect caused by glass solder results in an enhancement within the mechanical properties of SRFS foams upon heating until the softening temperature of this glass phase is reached [**ALYxx**].



(a)



(b)

Fig. 6-79 Quantitative line scan measurements.

6.3 Creep Test

Because of the high melting points of metallic foams in comparison to polymer foams, metallic foams can be utilised in high temperature applications as heat exchangers or heat sinks in electronic devices. If the temperature exceeds $0.3 \cdot T_m$, a time-dependent creep deformation takes place. This is of great importance particularly for such components that carry loads for prolonged times.

Since the biaxial testing machine, **Fig. 5-11**, at the Department of Material Science (LFW) is not equipped with a set-up which enables us to carry out tests in an inert atmosphere, the compressive creep tests were carried out only on Alporas foams in normal air in a range of temperatures and applied stresses regardless the formation of an oxide scale on the surface of foams. The tested samples were of dimensions $45 \times 45 \times 20 \text{ mm}^3$. The tests were carried out in atmospheric air since the thickness of the oxide scale covering pure Al is around 5 nm thick and it is not expected that the formation of an oxide scale having such thickness affects the foam deformation **[DES03]**. The effect of the foam's density, the test temperature as well as the applied stress on the creep behaviour of the Alporas foams was examined. Each parameter's influence was studied and will be discussed in the following section.

6.3.1 Creep of Alporas

6.3.1.1 Effect of Density

In order to gain information about the influence of the foam's density upon the foam's behaviour during creep test, a set of compressive creep experiments at a constant stress of approximately 0.6 MPa and at 300°C was performed on samples of Alporas foams with different densities, ranging from 0.25 g/cm^3 up to 0.32 g/cm^3 .

Typical creep curves, with the well-known primary, secondary and tertiary creep regimes were obtained, as depicted in **Fig. 6-80**. The shape of the curve of the creep rate versus strain plot is similar to that obtained by Zhang *et al.* **[ZHA02]** and Andrews *et al.* **[AND99a, b]**. In the primary creep regime, the creep rate decreased over a period of time until the minimum creep rate was reached. In the secondary creep regime, the creep rate increased to a maximum value with increasing the strain. According to Andrews *et al.*, the occurrence of such a peak is associated with the formation of a crush band in which the cells collapse quickly while the material outside the band appears to creep in a steady fashion **[ZHA02]**. The tertiary creep is terminated by rupture. Various plots, strain versus time, creep rate versus strain and creep rate versus time, for different densities of Alporas foams are illustrated in **Fig. 6-80** to **Fig. 6-83**.

0.25 g/cm³

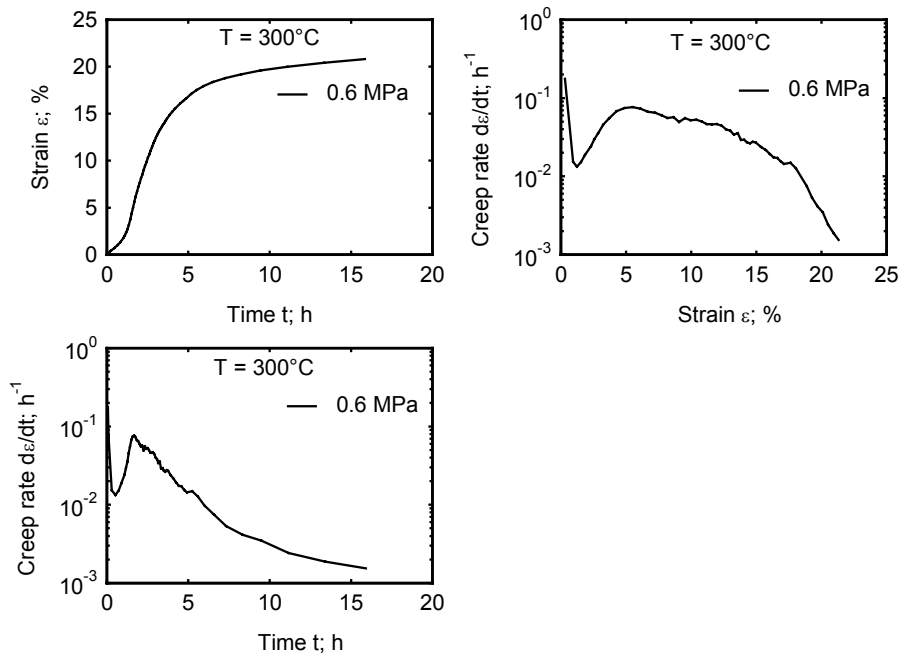


Fig. 6-80 Creep behaviour of Alporas foams having a density of 0.25 g/cm³.

0.27 g/cm³

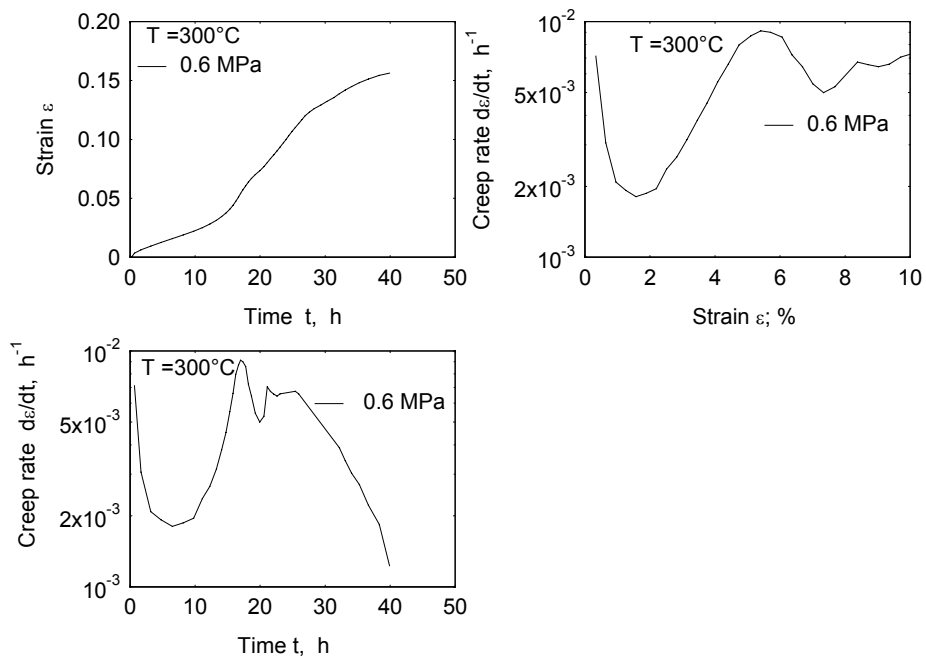


Fig. 6-81 Creep behaviour of Alporas foams having a density of 0.27 g/cm³.

0.30 g/cm³

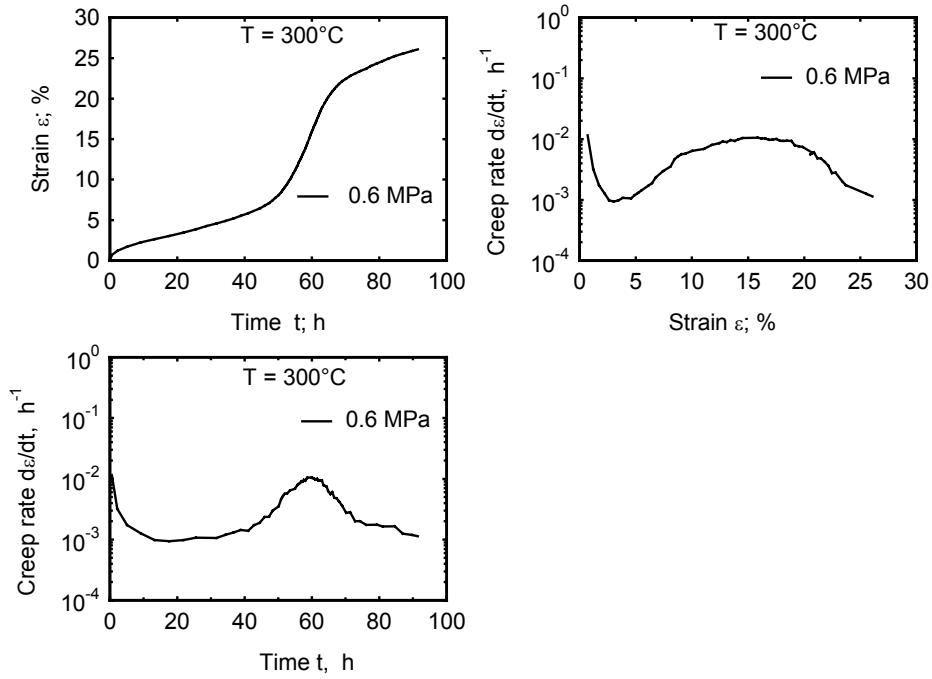


Fig. 6-82 Creep behaviour of Alporas foams having a density of 0.30 g/cm³.

0.32 g/cm³

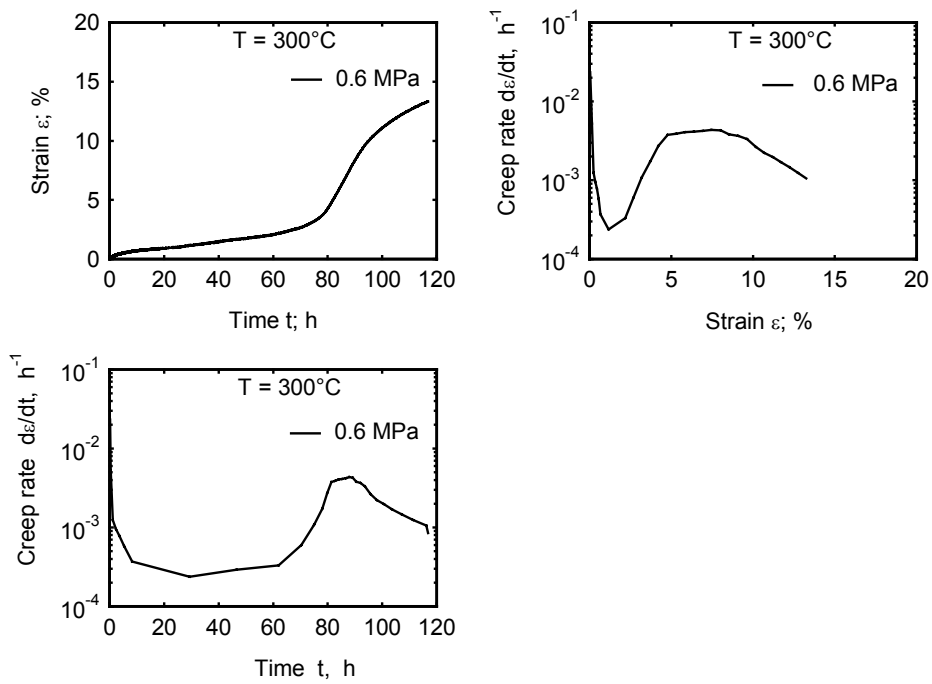


Fig. 6-83 Creep behaviour of Alporas foams having a density of 0.32 g/cm³.

Fig. 6-84 summarises the effect of the foam's density on the compressive creep behaviour of the Alporas foams. The increase in the foam's density leads to a higher resistance of the material to creep and consequently to fracture. Time of rupture varies from as short as 1 hour to as long as 80 hours.

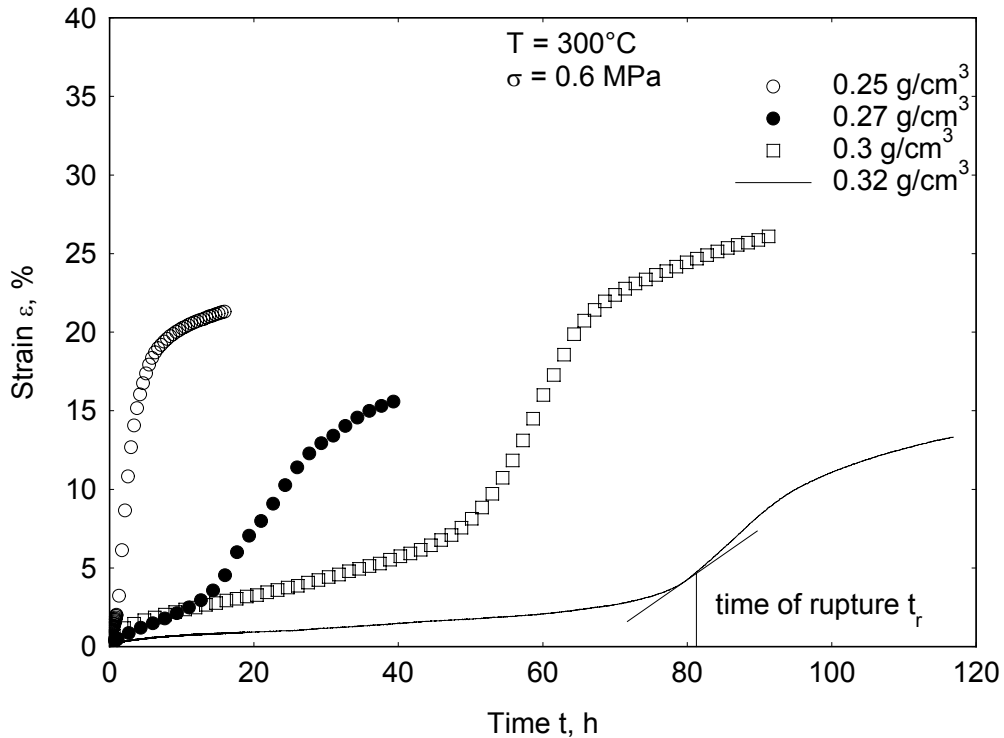


Fig. 6-84 Density dependence of strain-time curves of Alporas foams.

6.3.1.2 Effect of Stress

A set of creep experiments was carried out on Alporas foams of a certain density under different applied stresses in order to study the influence of the stress on the creep behaviour. Typical creep curves were obtained, **Fig. 6-85**. It can be clearly noticed that with decreasing applied stress on the foam, a longer life-time is achieved. A higher creep strain rate was achieved with increasing the applied stress. This increase within the creep strain rate corresponds to the collapse of a layer of cells and the formation of crush band **[AND99b]**.

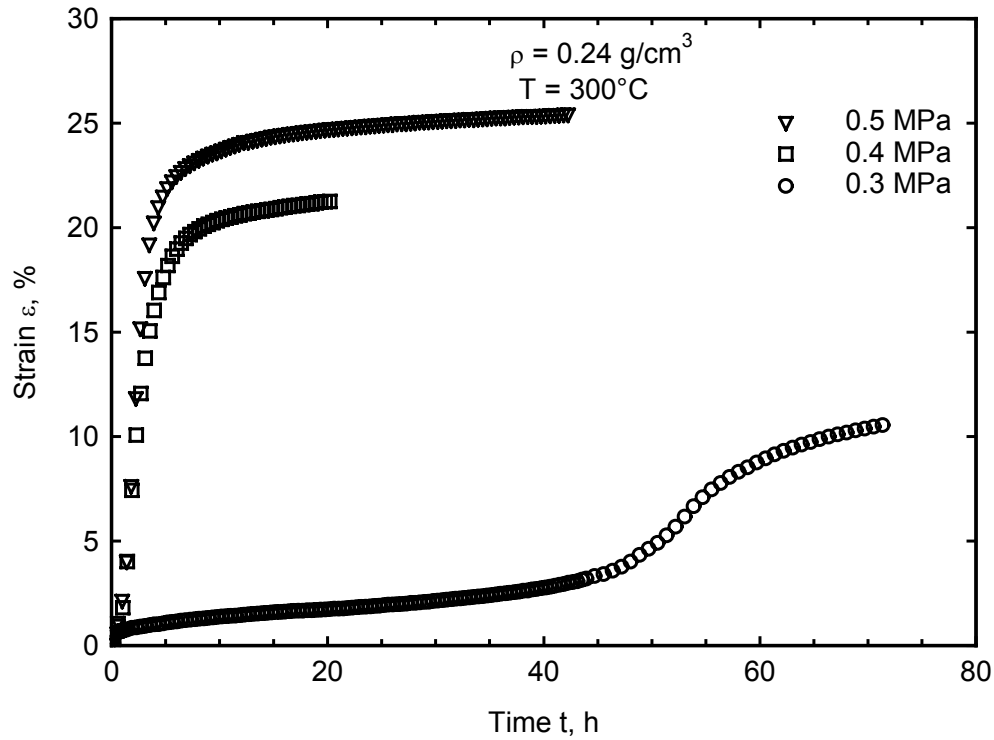


Fig. 6-85 Influence of the stress on the creep of the Alporas foams.

6.3.1.3 Effect of Temperature

Alporas samples having a density of 0.24 g/cm^3 have been undergone creep tests at different temperatures and under an applied stress which was fixed at approximately 0.6 MPa. **Fig. 6-86** to **Fig. 6-88** represents the strain-time curves at temperatures of 275°C , 325°C and 350°C respectively.

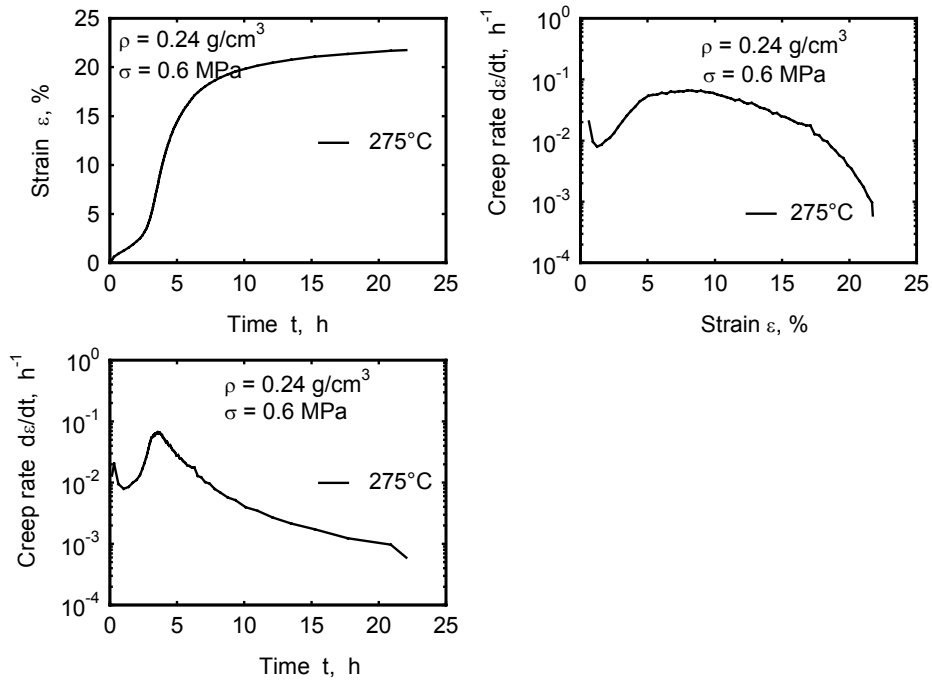


Fig. 6-86 Creep behaviour of 0.24 g/cm^3 Alporas foam at 275°C.

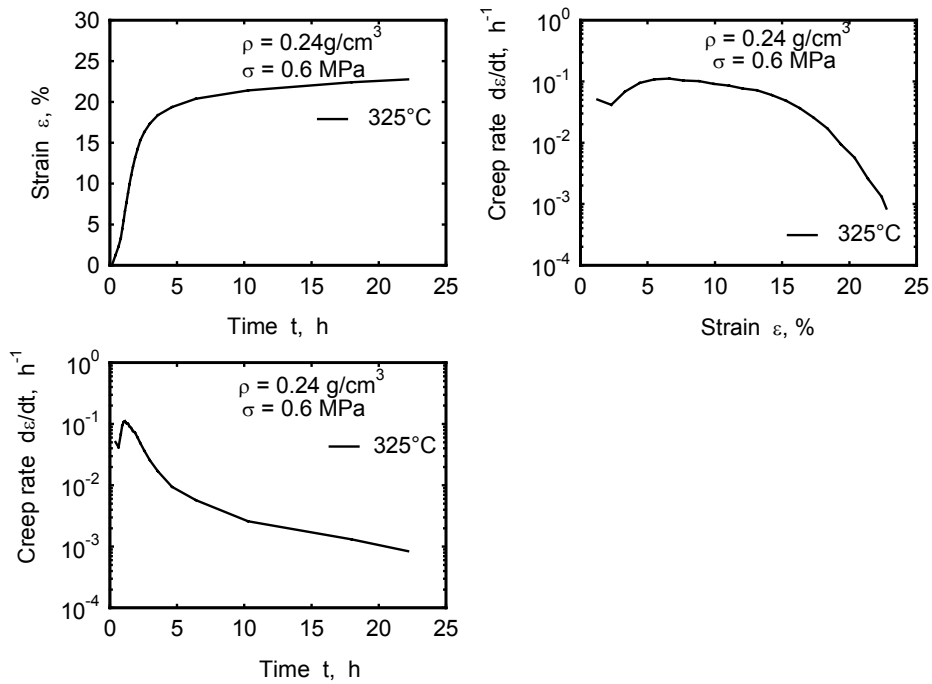


Fig. 6-87 Creep behaviour of 0.24 g/cm^3 Alporas foam at 325°C.

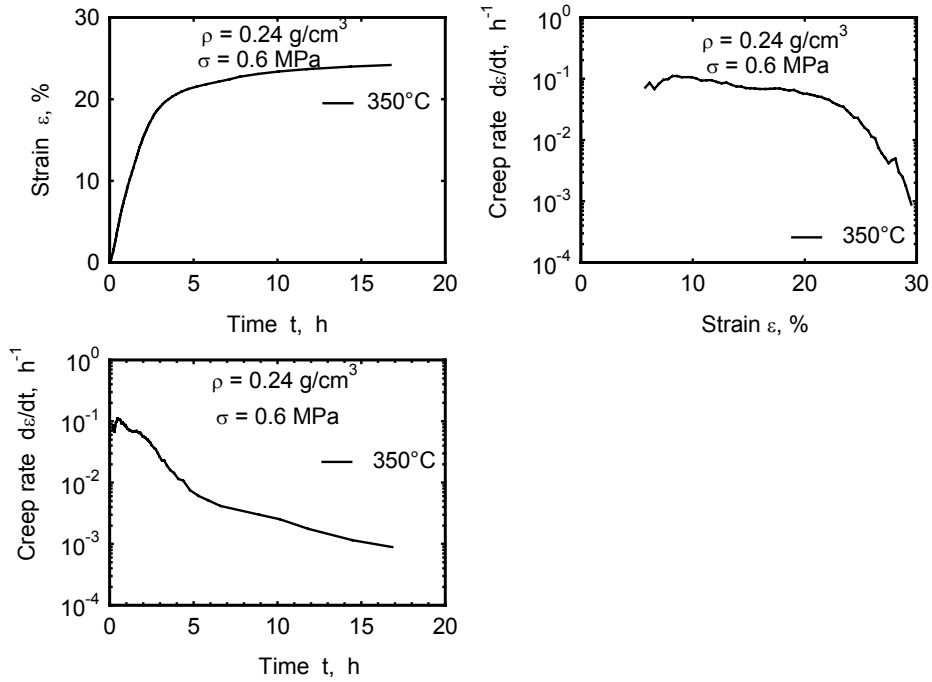


Fig. 6-88 Creep behaviour of 0.24 g/cm^3 Alporas foam at 350°C .

As shown in **Fig. 6-89**, a decrease in the test temperature results in a longer lifetime of the foam, i.e. the resistance of the foam to creep deformation decreases with increasing temperature and the on-set of fracture takes place in shorter time-frame at higher temperatures.

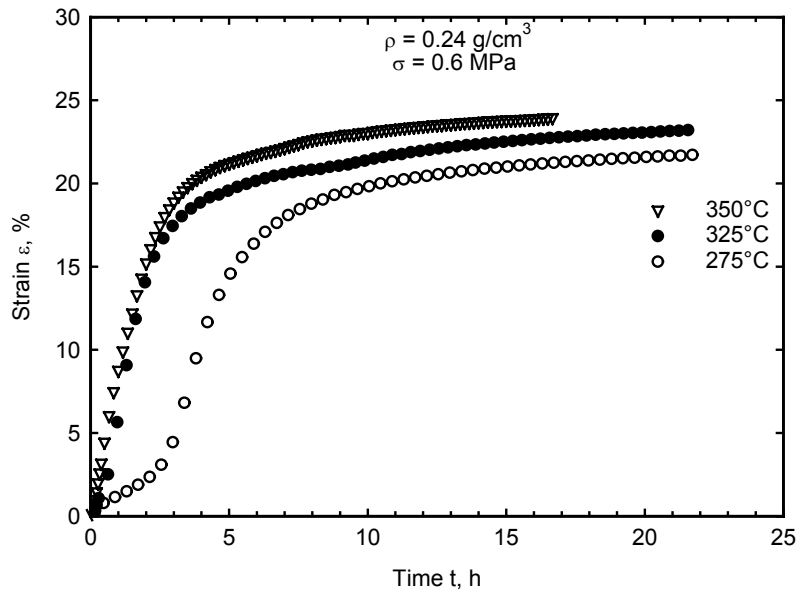


Fig. 6-89 Temperature dependence of creep of 0.24 g/cm^3 Alporas foam.

In an attempt to determine the activation energy, described by equation 3-9, strain rate against inverse of temperature is plotted in **Fig. 6-90** for Alporas foams (0.24 g/cm^3) which have been undergone compressive creep tests at a constant stress of 0.6 MPa. An activation energy of about 100 kJ/mole is obtained. Andrews *et al.* [AND99b] found the activation energy to be about 62.4 kJ/mole. An activation energy of slightly above 71 kJ/mole between 260°C and 350°C was expected [AND99b]. The activation energy of the solid material making up the foams is about 140 kJ/mole. The obtained results showed that Alporas foams have attained an activation energy which is rather equal to that of the solid material making up the foams.

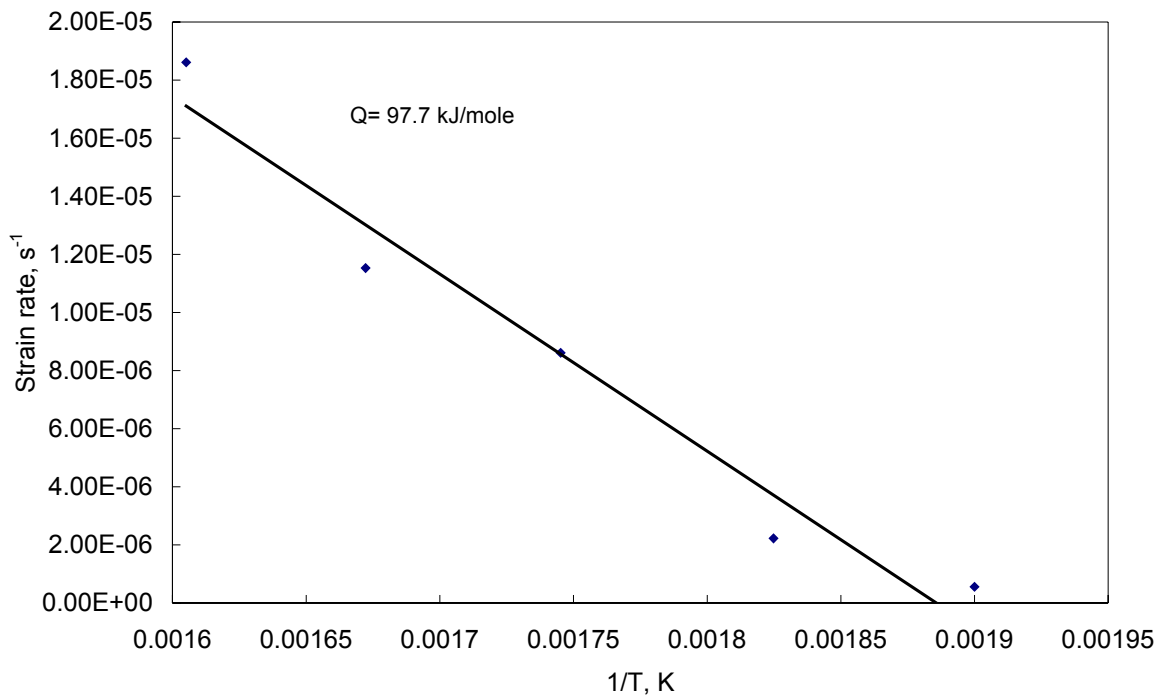
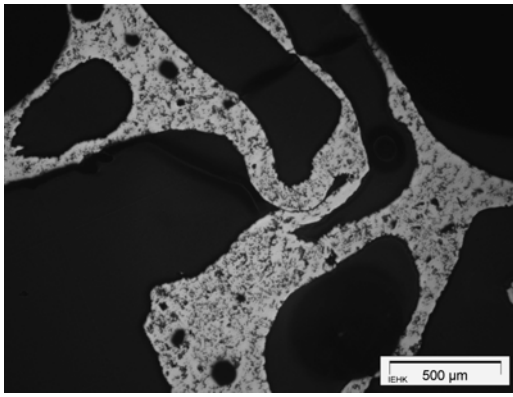


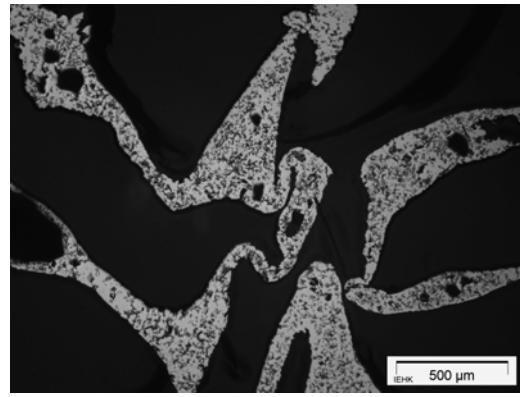
Fig. 6-90 strain rate plotted against inverse of temperature for Alporas foams ($\rho = 0.24 \text{ g/cm}^3$) at a constant stress of 0.6 MPa.

6.3.1.4 Microstructural Examination

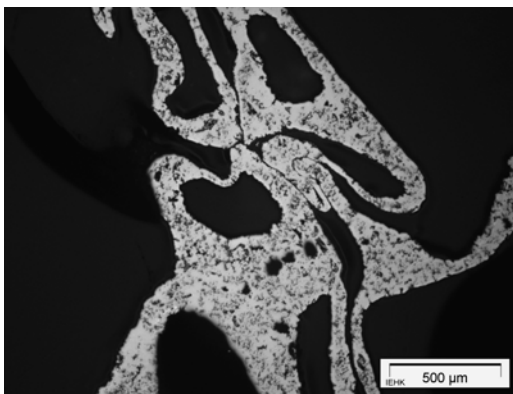
Fig. 6-91 shows cell wall microstructures of 0.24 g/cm^3 deformed Alporas samples under a constant stress of 0.6 MPa and at different temperatures. The cell-wall consists of granular microstructure with a grain size of several hundreds of micrometers. The small and large holes were produced during the manufacturing process. Bending of cell walls indicate that they have been strongly deformed.



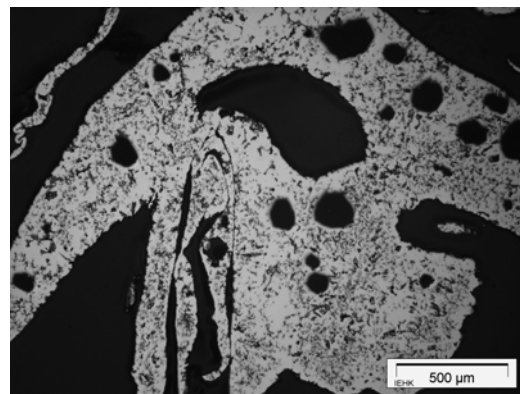
250°C



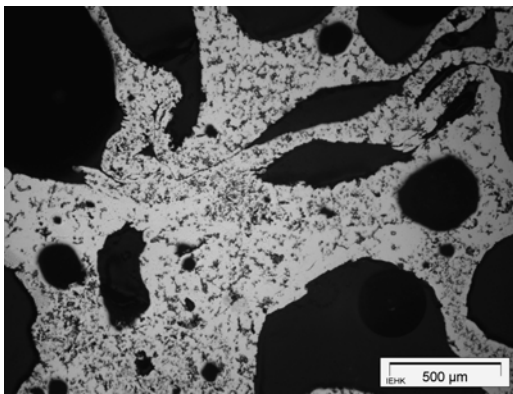
275°C



300°C



325°C



350°C

Fig. 6-91 Cell wall microstructure of Alporas foams ($\rho = 0.24 \text{ g/cm}^3$) after compressive creep deformation at different test temperatures ($\sigma = 0.6 \text{ MPa}$).

7 Summary & Outlook

The present work has aimed to characterise the mechanical properties of different types of foams at high temperatures. For this goal, three different types of foams have been used. AlCaTi foams (trade-name ALPORAS) were processed by a casting technique and they were delivered by the company Shinko Wire Co. Ltd. in Japan. The other two types of foams are made from low-alloyed steel powders having different chemical compositions, Distaloy SA with small traces of copper as well as nickel and Astaloy Mo with molybdenum. The powders were delivered by the company Höganäs AB, Sweden. Distaloy and Astaloy foams were manufactured at the Department of Ferrous Metallurgy (IEHK), RWTH Aachen University, by means of a powder metallurgical route. The developed method is known as Slip Reaction Foam Sintering process (SRFS). In this process, a certain amount of powder is mixed with a dispersant SiO_2 . Water which acts as a solvent is added to the mixture in order to make a slip. Afterwards a binder, ortho-phosphoric acid H_3PO_4 , is then added. A chemical reaction takes place between the metal powder and acid resulting in H_2 bubbles, which are the main cause for foaming process. The slip is then poured in a form and dried at RT for 24h. The green samples are then obtained. The surfaces of the samples are removed by using a sawing machine and the samples are then introduced into a tube-type furnace, in which they undergo a sintering process under reductive atmosphere. After sintering, the samples become more strength due to the formation of metallic bonds. Samples are then ready to be handled and examined.

High temperature compressive tests were performed on the above mentioned types of foams, namely Alporas, Distaloy as well as Astaloy foams. The tests were conducted at various temperatures (up to 620°C in case of Alporas foams, and 800°C for the low-alloy steel foams, Distaloy and Astaloy). Several parameters were varied, e.g. the testing medium (air, Ar), foam's density, testing temperature, loading velocity as well as the applied stress. The influence of each variable upon the behaviour of the metallic foams was studied.

Typical compressive stress-strain curves were obtained. Like that of compact materials, the compressive stress-strain curves consist of three different regions. A linear elastic regime, which ends with the maximum compressive strength, before the curve changes its direction to the plateau regime. This regime is of great importance, especially for design engineers, because the amount of the absorbed energy by the foam is related to this region. The last region, which is called the densification region, is featured by an increase of the stress level due to the collapse of the cell walls and faces touching each other, i.e. the foam becomes more dense- like a compact metal.

The mechanical properties of (SRFS) foams are strongly dependent upon many parameters e.g. particle shape, foam's density, test temperature, pore size, pore size distribution, cell wall thickness as well as the sintered contact areas between the particles (secondary pores).

Compared with particles of irregular shapes, round particles provide good mechanical properties.

With increasing the foam's density, the compressive strength of the foam increases, the magnitude of the plateau strength also increases. The length of the plateau depends upon the foam's density as well. Foam with a low density is characterised by its long and flat plateau. Foams having higher densities collapse more quickly than that of lower ones. This means that foams with low densities are more suitable for energy absorption applications than that of high densities. A similar effect of the foam's density on the mechanical properties of the (SRFS) foams was obtained upon testing them in an inert atmosphere.

As with the foam's density, the mechanical properties of the (SRFS) foams were affected by the test temperature, however, here the trend is reversed. A foam with a higher compressive strength (and therefore, a higher magnitude of plateau stress) was obtained by decreasing the test temperature. It was also found that the length of the plateau was affected by the test temperature. A more decrease of test temperature, resulted in a longer plateau.

Compared with the compressive strength of the Astaloy and Distaloy foams at room temperature, their compressive strengths at 200°C and 450°C were found to be a little bit larger. An explanation for this increase is probably due to the well-known phenomenon "ageing effect" caused by the C-element over this temperature range. The strain rate dependence of the foam's compressive strength shows that Distaloy as well as Astaloy foams exhibit no enhancement within its compressive strength over this range of temperature, which ensures strongly the assumption that the reason for the obtained increase within the mechanical properties was the "age hardening effect" **[ALYxx]**.

The presence of certain alloying elements e.g. molybdenum as well as copper increase the high temperature strength in this range of temperature **[ARC51]**. Another explanation for this enhancement in the compression strength of the foams with increasing the temperature may be due to the presence of a mixture of ceramic oxides- glass phase- consisting of FeO, MgO, MnO, SiO₂ and P₂O₅ found in the contact areas between the iron particles. The smoothing effect caused by glass solder results in an enhancement within the mechanical properties of SRFS processed foams upon heating until the softening temperature of this glass phase is reached.

The large scatter in the obtained results may be due to the density gradients within the structure, since there is no exact method to guarantee the production of a metallic foam with a homogeneous density distribution.

The examination the cell-wall microstructure of the deformed ALPORAS samples indicated that the buckling of the cell walls was the main deformation mechanism at each test temperature.

The microstructure micrographs of the Distaloy as well as Astaloy foams show that the porosity of the samples increased with increasing test temperature.

The compression strength values of the Distaloy as well as Astaloy foams which have been compressed in atmospheric air are large compared with those compressed in argon. An oxide scale of varying thicknesses built-up on the surface of the foams tested in atmospheric air. This scale acts as a protective layer from further oxidation and makes the base material more stable [SIM02]. The thickness of the built scale at the edge of the sample is larger than that formed at the middle of the sample. Compared with the oxide scales formed on the surfaces of the Astaloy foams, the Distaloy foams have thicker scales. This may be due to the difference in chemical composition, where the presence of Cu in concentrations over 0.25 wt% increases the corrosion resistance of the material [VAY97]. Molybdenum as well as phosphorus has also been found to have a positive effect in increasing the corrosion resistance of the material [HOU00].

Increasing the thickness of the oxide scale makes it mechanically unstable. The reason for this is the building of internal stresses, which become larger during the growth of the thickness of the oxide [SCH91]. If the oxide thickness exceeds a specified critical value, the growing stresses at the metal/oxide surfaces lead to build large normal stresses, which result in exceeding the adhesion forces of the oxide layer and thus results in delamination of the oxide layer [LEY97].

The micrographs of the fractured surfaces of the tested samples have shown that the failure of the foams resulted from the initiation of cracks which further propagate through the whole structure.

Using the metal foams as load carriers over long periods at applied temperatures larger than 0.3 of their melting points, a time-dependant creep deformation takes place. The creep tests were carried out for Alporas foams having different densities in temperature range between 250°C-350°C and under different stresses from 0.2 MPa to 0.6 MPa, respectively.

A foam with a larger density exhibits more resistance against creep, i.e. the higher the

density of the foam, the larger the time needed to fracture. On the other hand, when the foam is subjected to large stresses, it fails relatively quickly. Higher temperatures have a similar effect as that of stress upon the metallic foams. With increasing temperature, the strain-time curves are shifted to shorter times.

The Alporas foams deformed by bending their cell-walls when subjected to creep deformation at different temperatures.

The results indicated also that the Alporas foams are insensitive to large deformation velocities. The difference in the stress-strain response at different strain rates was not large.

Outlook

The results obtained at the end of this work from the quantitative line scan analysis opened the door for more questions which require further deep investigation for better understanding. One of the most interesting points, which should be studied later, is the effect of SiO_2 , H_3PO_4 on the mechanical properties of (SRFS) foams. Foams having various amounts of SiO_2 and H_3PO_4 have to be compressed at elevated temperatures.

If we consider again the ageing phenomenon, further tests should be carried out under high strain rates because it may also share in finding a good interpretation for the effect of the test temperature on the mechanical properties of foams.

8 Kurzfassung & Abstract

In dieser Arbeit werden die mechanischen Eigenschaften verschiedener metallischer Schäume bei erhöhten Temperaturen charakterisiert. Die untersuchten Schäume wurden mittels zweier unterschiedlicher Methoden hergestellt. Alporas Schäume wurden durch ein schmelzmetallurgisches Verfahren hergestellt, während die auf niedriglegierten Stahlpulvern basierenden Distaloy- bzw. Astaloy-Schäume unter Anwendung einer neu entwickelten Methode erzeugt wurden. Diese Methode, das SchlickerReaktionSchaumSinter (SRSS)-Verfahren, gehört zu den pulvermetallurgischen Verfahren.

An proben dieser Schäume wurden Hochtemperaturdruckversuche in normaler Atmosphäre sowie unter Argonatmosphäre durchgeführt. Die mechanischen Eigenschaften wurden in Abhängigkeit von Dichte, Temperatur, Probengröße und Dehngeschwindigkeit ermittelt. Zusätzlich wurden Alporas-Schäume Kriecheversuchen unterzogen. Dabei wurde die Abhängigkeit der mechanischen Eigenschaften von Dichte, Temperatur sowie Spannung ermittelt.

This work deals with studying the high temperature mechanical properties of different types of metallic foams. The foams which have been used in this work were manufactured by two different processing methods. Al-foams (trade-name Alporas) were processed by a melt metallurgical route whereas Distaloy as well as Astaloy foams which are based on low-alloyed steel powders, were manufactured by a newly developed method. This method which is known as Slip Reaction Foam Sintering (SRFS)-process, belongs to the powder metallurgical route.

High temperature compressive tests were carried out, in air as well as in argon, on foams having different densities in a variable range of temperature. The effect of the foam density, test temperature, size of the specimen as well as the strain rate on the mechanical properties was studied. Moreover, Alporas foams have been undergone creep tests in air. The effect of the foam density, test temperature and the applied stress on determining the creep properties was studied as well.

9 Nomenclature

Symbol	Definition	Unit
A_0	Initial cross sectional area of the specimen	mm ²
E	Young's modulus of a foam	GPa
E_s	Young's modulus of a cell wall material	GPa
ρ	Density of a foam	g/cm ³
ρ_s	Density of cell wall material	g/cm ³
$\frac{\rho}{\rho_s}$	Relative density	
σ_{pl}^*	Plastic collapse stress	MPa
σ_y	Yield strength of cell wall material	MPa
σ_f^*	Crushing strength of cell wall material	MPa
σ_f	Modulus of rupture of cell wall material	MPa
σ_c	Compressive stress	MPa
ε_c	Compressive strain	%
Δh	Change in height of the specimen	mm
h_0	Initial height of the specimen	mm
l	Limit of strain concerned	
$\frac{d\varepsilon}{dt}$	Creep rate	s ⁻¹
ε_0	Instantaneous strain	%

Nomenclature

ε_t	Time-dependent strain	%
ε'_0	Instantaneous contraction	%
ε'_t	Time-dependent anelastic strain recovery	%
ε_p	Plastic collapse strain	%
Q_0	Activation energy	J/mole
R	Gas constant	J/mole.K
T	Absolute temperature	K
T_m	Melting temperature	°C
n	Creep exponent	
X, y	Stoichiometric factors	
ΔG°	Free energy of formation	Joule
K	Equilibrium constant	
P_{O_2}	Oxygen partial pressure	atm.
a	Activity	
j	Flux or mass diffusion	mol./m ² .s
$\frac{\partial c}{\partial x}$	Concentration gradient	
D	Diffusion coefficient	m ² /s
x	Thickness of the oxide	μm
L	Average cell size	mm
t_e	Edge thickness	μm

Nomenclature

E_t	Elastic modulus in tension	GPa
E_c	Elastic modulus in compression	GPa
$\sigma_{t0.002}$	0.2% offset strength in tension	MPa
$\sigma_{c0.002}$	0.2% offset strength in compression	MPa
K_{IC}	Fracture toughness	MPam ^{1/2}

10 Bibliography

- [ALY03] Aly, Mohamed Shehata; Bleck, Wolfgang.: High Temperature Compressive Deformation of Alporas (AlCaTi) Foams, Proceeding International Conference on Cellular Metals and Metal Foaming Technology: Manufacture, Properties, Applications, Metfoam 2003 (ed. J. Banhart et al.), Berlin, Germany, 2003, pp. 355-358.
- [ALYxx] Shehata Aly, Mohamed; Bleck, Wolfgang; Scholz, Paul-Friedrich.: High Temperature Compressive Deformation of Slip Reaction Foam based on Low-alloy Steel Powders, will be submitted to the Journal of steel research.
- [AND00] Andrews, E.W.; Gibson, L.J.: The Role of Cellular Structure in Creep of two-dimensional Cellular Solids, Materials Science and Engineering A 303, 2001, pp.120 - 126.
- [AND99a] Andrews, E.W.; Huang, J.-S; Gibson, L.J.: The Creep Behaviour of a Closed-Cell Aluminium Foam, Acta Mater., Vol. 47, 1999, No.10, p. 2927-2935.
- [AND99b] Andrews, E.W.; Gibson, L.J.; Ashby, M.F.: The Creep of Cellular Solids, Acta Mater., Vol. 47, 1999, No.10, pp. 2853-2863.
- [ANG03] Angel, S.; Bleck, W.; Mohr, U.; Aly, M.S.; Scholz, P.-F.: Herstellung und Eigenschaften von Stahlschaum nach dem SchlickerReaktionsSchaumSinter (SRSS)-Verfahren. Hagener Pulvermetallurgisches Symposium, eingeladener Vortrag, 27-28.11.2003.
- [ARC51] Archer, R.S; Briggs, J.Z.; Loeb, C.M.JR.: Molybdän, Stähle-Gußeisen Legierungen, Calimax Molybdenum Company, Zürich.1951.
- [ASH83] Ashby, M.F.: Metal Transaction A, 14 A , 1983, pp. 1755-1769.
- [ASH99] Asholt, P.: Aluminium Foam Produced by the Melt Foaming Route Process, Properties and Applications, Proceeding International Conference on Metal foam and porous metal structures, Bremen, Germany, June 1999.
- [BAN00] Banhart, J.: Metallic Foams:Challenges and Opportunities, Eurofoam 2000, Editors: Zitha, P.; Banhart, J.; Verbist, G.; Mit-Verlag, Bremen, 2000, pp.13-20.

- [BAN02] Banhart, J.: Functional Applications, "Handbook of Cellular Metals, Production, Processing, Applications", edited by Hans-Peter Degischer and Brigitte Kriszt, WILEY-VCH Verlag GmbH, 2002.
- [BAN99] Banhart, J.: Properties and applications of cast aluminium sponges, Proceeding International Conference on Metal foam and porous metal structures, Bremen, Germany, June 1999.
- [BAR68] Bartha, P.; Lehmann, H.; Koltermann, M.; Verhalten phosphategebundener Werkstoffe bei hohen Temperaturen, Glas-Email-Keramo-Technik, Heft 8, pp. 282, 1968.
- [BAR98] Bart-Smith, H.; Bastrawos, A.F.; Mumm, D.R.; Evans, A.G.; Sypeck, D.J.; Wadley, H.N.G.: Compressive Deformation and Yielding Mechanisms in Cellular Al Alloys Determined Using X-Ray Tomography and Surface Strain Mapping, in: Schwartz, D.S.; Shih, D.S.; Wadely, H.N.G., Evans, A.G.: Materials Research Society MRS Proceedings, Vol. 521: Porous and Cellular Materials for Structural Applications, 1998, pp .71-81.
- [BAU97] Baumeister, J.; Banhart, J.; Weber, M.: Aluminium Foams for Transport Industry, Materials Design, Vol. 18 (1997), pp. 217-220.
- [BEN71] Benard, J.: in : Oxidation of Metals and Alloys, 1971.
- [BER03] Bericht " Entwicklung von offenporigen Schäumen aus Nickelbasislegierungen und intermetallischen Phasen", IEHK, RWTH-Aachen, 2003.
- [BIN01] Bin, W.; Deping, H.; Guangji, S.: Compressive Properties and Energy Absorption of Foamed Al Alloy, Proceeding International Conference on Cellular Metals and Metal Foaming Technology (ed. J. Banhart et al.), Bremen, Germany, June 2001, pp. 351-354.
- [BLE99] Bleck, W. (Hrsg.): Werkstoffprüfung in Studium und Praxis, Aachen, 1999.
- [BÖL03] Böllinghaus, T.: Werkstoffeigenschaften und Verarbeitung von Aluminumschäumen, Dr.-Ing Dissertation, RWTH Aachen, Shaker Verlag, 2003.
- [BRA00] Brady, M.P.; Pint, B.A.; Tortorelli, P.F.; Wright, I.G.: High Temperature Oxidation and Corrosion of Intermetallics, Materials Science and Technology, Corrosion and Environmental Degradation, Ed. M. Schuetz, Vol. II, Wiley-VCH Verlag, 2000.

- [BRA04] Bram, M.; Laptev, A.; Buchkremer, H.P.; Stöver, D.: Herstellung von hochporösen, endkontournahen Titan-Formkörpern für biomedizinische Anwendungen, *Mat.-wiss. U. Werkstofftech.*, Vol. 35, No. 4, 2004, pp. 213-218.
- [BRE81] Bressers, J.: *Creep and Fatigue in High Temperature Alloys*, Galliard Printers Ltd, Great Britain, 1981.
- [BRO80] Brown, A.M.; Ashby, M.F.: *Scr. Metall.*, 14 (1980), pp. 1297.
- [CAR77] Carter, V.E.: *Metallic Coatings for Corrosion Control*, Butterworths, London, 1977.
- [CHA99] Chastel, Y.; Hudry, E.; Forest, S.; Peytour, C.: Mechanical Behaviour of Aluminium Foams For Various Deformation Paths. Experimental and Modelling, *Proceeding International Conference on Metal foam and porous metal structures*, Bremen (Germany), June 1999, pp. 263-268.
- [CHE99] Chen, C.; Lu, T.J.; Fleck, N.A.: Effect of Imperfections on the Yielding of Two-Dimensional Foams, *Journal of Mechanics and Physics of Solids*, 47, 1999, pp. 2235-2272.
- [CHI98] Chin, J.Y.; Eifert, H.; Banhart, J.; Baumeister, J.: Metal Foaming by a Powder Metallurgy Method: Production, Properties and Applications, *Mat Res Innovat*, 2, 1998, pp. 181-188.
- [CHV75] Chvatal, T.: Stand der feuerfesten Phosphatbindung heute, *Sprechsaal 108. Jahrgang, Internat. Ceramics & Glass Magazine*, Coburg, 1975, pp. 576-588.
- [CLA] Clarke, D.R.: Stress Generation during High-Temperature Oxidation of Metallic Alloys, *Materials Dep., College of Eng., Uni. Of California*, CA 93160-5050.
- [COC00] Cocks, A.C.F.; Ashby, M.F.: Creep-Buckling of Cellular Solids, *Acta Mater.*, Vol. 48, 2000, pp. 3395-3400.
- [COH68] Cohen, L.A.; Power, W.A.; Fabel, D.A.: *Mater. Eng.*, Vol. 67, 1968, pp. 44.
- [COR96] Cornel, R.M.; Schwertmann, U.: *The Iron Oxides, Structure, Properties, Reactions, Occurrence and Uses*, VCH Verlag GmbH, Germany, 1996.

- [DAN00] Dannemann, K.A.; Lankfordjr, J.: High Strain Rate Compression of Closed-Cell Aluminium Foams, *Materials Science and Engineering A*, Vol. 293, Issues 1-2, 2000, pp. 157-164.
- [DAV83] Davies, G.J.; Shu Zhen.: Review Metallic foams: Their Production, Properties and Applications, *Journal of Materials Science* , Vol.18, 1983, pp. 1899-1911.
- [DEG02] Degischer, H.P.: Materials Definitions, Processing, and Recycling, *Handbook of Cellular Metals, Production, Processing, Applications*, Edited by Degischer, H.-P. and Kriszt, B., Wiley-VCH Verlag GmbH, Weinheim, 2002.
- [DES03] Despois, J.-F; Conde, Y.; San Marchi, C.; Mortensen, A.: Tensile Behaviour of Replicated Aluminium Foams, *Proceeding International Conference on Cellular Metals and Metal Foaming Technology: Manufacture, Properties, Applications* (ed. J. Banhart et al.), Berlin, Germany, June 2003, pp. 375-380.
- [DIN84] DIN 53421: Prüfung von harten Schaumstoffen, Druckversuch, Berlin, 1984.
- [DUA02] Duarte, I.; Banhart, J.: A Study of Aluminium Foam Formation Kinetic and Microstructure, *Acta mater.*, 48, 2002, pp. 2349-2362.
- [FED79] Fedorchenko, I.M.: *Sov. Powder Metall. Met. Ceram.* 18625, 1979.
- [FOR89] Fortes, M.A.; Fernandes, J.J.; Serralheiro, I; Rosa, M.E.: Experimental Determination of Hydrostatic Compression versus Volume Change Curves for Cellular solids, *Journal of Testing and Evaluation JTEVA*, Bd.17, 1989, Nr.1, pp. 67-71.
- [FOR99] Fortes, M.A.; Ashby, M.F.: The Effect Of Non-Uniformity On The In-Plane Modulus Of Honeycombs, *Acta Mater.*, Vol. 47, No. 12,1999, pp. 3469-3473.
- [FRO82] Frost, H.J.; Ashby, M.F.: *Deformation Mechanism Maps: The Plasticity and Creep of Metals and Ceramics*, Pergamon Oxford, 1982.
- [GAB72] Gabe, D.R.: *Principles of Metal Treatment and Protection*, Pergamon Press, Oxford, 1972.
- [GAR67] Gardner, A.R.: *Prod. Eng.*, 38, 141, 1967.
- [GIB97] Gibson, J.; Ashby, F.: *Cellular Solids : Structure and Properties*, 2nd edition, Cambridge University Press, 1997.

- [GIO00] Gioux, G.; McCormack, T.M.; Gibson, L.J.: Failure of Aluminium Foams Under Multiaxial Loads, *Int. Journal of Mech. Sci.*, 42, 2000, pp. 1097-1117.
- [GOR90] Goretta, K.C.; Brezny, R.; Dam, C.Q.; Green, D.G.: High Temperature Mechanical Behaviour of Porous Open-cell Al₂O₃, *Materials Science and Engineering*, A124, 1990, pp. 151-158.
- [GRA99] Gradinger, R.; Rammerstorfer, F.G.: On The Influence Of Meso-Inhomogenities On The Crush Worthiness Of Metal Foams, *Acta Mater.*, Vol. 47, 1999, No. 1, pp.143-148.
- [GRE98] Grenstedt, J.L.: Influence of Imperfections on Effective Properties of Cellular Solids, in: D.S. Schwarz; D.S. Shih, A.G. Evans, H.N.G. Wadley (Eds.), *Porous and Cellular Materials for Structural Applications*, Materials Research Society Symposium Proceedings, 521, 1998, pp. 3-13.
- [GRO03] Grote, F.: *Offenporige Metallstrukturen nach dem Platzhalterverfahren*, Dr.-Ing. Dissertation, RWTH Aachen, Shaker Verlag, 2003.
- [HAA03] Haag, M.; Wanner, A.; Clemens, H.; Zhang, P.; Kraft, O.; Arzt, E.: Creep of Aluminium-Based Closed-Cell Foams, *Metallurgical and Materials Transactions A*, Vol. 34A, 2003, pp. 2809-2817.
- [HAG99] Hagen, H.Von.: *Werkstoffeigenschaften eines Sandwichverbundes aus Stahldeckblechen mit einem Aluminiumschaumkern*, Dr.-Ing. Dissertation, RWTH Aachen, Shaker Verlag, 1999.
- [HAL00] Hall, I.W.; Guden, M.; Yu, C.-J.: Crushing of Aluminium Closed Cell Foams: Density and Strain Rate Effects, *Scripta Mater.*, 43, 2000, pp. 515-521.
- [HAN01] Hanssen, A.G.; Langseth, M.; Hopperstad, O.S.: Crash Behaviour of Foamed-Based Components: Validation of Numerical Simulations, *Proceeding International Conference on Cellular Metals and Metal Foaming Technology* (ed. J. Banhart et al.), Bremen, Germany, June 2001, pp. 329-338.
- [HAN98] Han, F.; Zhu, Z.; Gao, J.: Compressive Deformation and Energy Absorbing Characteristic of Foamed Aluminium, *Metallurgical and Materials Transactions A*, 29A, 1998, pp. 2497.
- [HAR99] Harte, A.-M.; Fleck, N.A.; Ashby, M.F.: Fatigue Failure of an Open Cell and a Closed Cell Aluminium Alloy Foam, *Acta Mater.*, Vol. 47, 1999, pp. 2511-2524.

- [HID01] Hidaka, Y.; Anraku, T.; Otsuka, N.: Deformation of Feo Oxide Scales upon Tensile Tests at 600-1200°C, Materials Science Forum, Vol. 369-372, , 2001, pp. 555-562.
- [HIN99] Hintz, C.; Wagner, I.; Sahm, P.R.; Stoyanov, P.: Investment Cast Near-net Shape Components Based on Cellular Metal Materials, International Conference on Metal Foams and Porous Metal Structures, Bremen, Germany, June 1999, pp. 153-158.
- [HOG97] Hogaenaes.: Handbook for Sintered Components, 1997.
- [HOU00] Hou, B.; Li, Y.; Li, Y.; Zhang, J.: Effect of Alloy Elements on the Anti-Corrosion Properties of Low Alloy Steel, Bull. Mater. Sci., Vol. 23, No. 3, 2000, pp. 189-192.
- [HUS98] Huschka, S.; Hicken, S.; Arendts, F.-J.: Modellierung der Spannungs-Stauchungs-Kurven von Aluminiumschaum unetr der Berücksichtigung der Porengrößenverteilung, in: Banhart; J. (Hrsh.): Metallschäume, Symposium Metallschäume, Bremen, Deuschalnd, MIT-Verlag 1997, pp. 37-57.
- [IEH03] Skript Oberflächentechnik, Institut für Eisenhüttenkunde, RWTH- Aachen, 2003.
- [JPN80] Jpn. Ind. Tech. Bull., 8, 19, 1980.
- [KAN00] Kanahashi, H.; Mukai, T.; Yamada, Y.; Shimojima, K.; Mabuchi, M.; Nieh, T.G.; Higashi, K.: Dynamic Compression of an Ultra-Low Density Aluminium Foam, Materials Science and Engineering A 280, 2000, pp. 349-353.
- [KES03] Kesler, O.; Crews, L.K.; Gibson, L.G.: Creep of Sandwich Beams with Metallic Foam Cores, Material Science and Engineering A, 341, 2003, pp. 264-272.
- [KOF88] Kofstad, P.: High Temperature Corrosion, London: Applied Science, 1988.
- [KUC66] Kuccheck, H.A.: US Patent 3236706, 1966.
- [KUE92] Kueppenbender, I.: Verhalten der Oxidschicht auf Nickel bei Druckbelastung des Verbundsystems, Ph.D thesis, RWTH-Aachen, 1992.
- [KUL73] Kulkarni, S.B.; Ramakrishnan, P.: Foamed Aluminium, Int. J. Powder Met., Vol. 9, 1973, pp. 41.

- [LEN80] Lenel, F.V.: Powder Metallurgy Principles and Applications, Metal Powder Industries Federation, London, 1980.
- [LEY97] Leyens, Ch.: Oxidationsverhalten und Oxidationsschutz von Titanlegierungen für den Hochtemperatureinsatz in Flugtriebwerken, Dr.-Ing Dissertation, RWTH Aachen, Shaker Verlag, 1997.
- [MAR01] Markaki, A.E.; Clyne, T.W.: The Effect of Cell Wall Microstructure on the Deformation and Fracture of Aluminium-Based Foams, *Acta mater.*, Vol. 49, 2001, pp.1677-1686.
- [MAR99] Markaki, A.E.; Clyne, T.W.: The Effect of Impact Velocity on the Deformation of Layered Metal Foam / Ceramic Composites, *Proceeding International Conference on Metal foam and porous metal structures* (ed. J. Banhart et al.), Bremen, Germany, June 1999, pp. 359-364.
- [MEM89] Memhard, D.: Festigkeits- und Zähigkeitsverhalten von ferritischen Baustählen im Temperaturbereich zwischen 20°C und 400°C, Dr.-Ing Dissertation, RWTH Aachen, 1989.
- [MCD03] McDonald, S.A.; Mummery, P.M.; Johnson, G.: Characterisation of the 3-D Structure and Compressive Deformation of Metallic Foams, *Proceeding International Conference on Cellular Metals and Metal Foaming Technology: Manufacture, Properties, Applications* (ed. J. Banhart et al.), Berlin, Germany, June 2003, pp. 289-294.
- [MIY99] Miyoshi, T.; Itoh, M; Akiyamy, S.; Kitahara, A.: Aluminium Foam (ALPORAS): The Production Process, Properties and Applications, *Proceeding International Conference on Metal foam and porous metal structures*, Bremen, Germany, June 1999, pp. 125-132.
- [MIY99a] Miyoshi, T.; Itoh, M; Mukai, T.; Kanahashi, H.; Kohzu, H.; Tanabe, S.; Higashi, K.: Enhancement of Energy Absorbtion in a Closed-Cell Aluminium by the Modification of Cellular Structures, *Scripta Materialia*, Vol. 41, 1999, pp. 1055-1060.

- [MOH01] Mohr, U.; Scholz, P-F.; Bleck, W.: Production of SlipReactionFoam (SRF) and Influence of Production Parameters on the Mechanical Properties, Proceeding International Conference on Cellular Metals and Metal Foaming Technology (ed. J. Banhart et al.), Bremen, Germany, 2001, pp. 209-214.
- [MOH03] Mohr, U.: Herstellung und Charakterisierung von offenporigem Stahlschaum, Dr.-Ing. Dissertation. RWTH Aachen, 2003.
- [MOS03] A statistic Approach to Estimate the Compression Strength of Aluminium Foams, Proceeding International Conference on Cellular Metals, Manufacture, Properties, Applications, Metfoam 2003 (ed. J. Banhart et al.), Berlin, Germany, 2003, pp. 387-392.
- [MOT01] Motz, C.; Pippan, R.; Ableidinger, A.; Böhm, H.; Rammerstorfer, F.G.: Deformation and Fracture Behaviour of Ductile Aluminium Foams in the Presence of Notches under Tensile Loading, Proceeding International Conference on Cellular Metals and Metal Foaming Technology (ed. J. Banhart et al.), Bremen, Germany, 2001, pp. 299-304.
- [MUK99] Mukai, T.; Kanahashi, H.; Miyoshi, T.; Mabuchi, M.; Nieh, T.G.; Higashi, K.: Experimental Study of Energy Absorption in a Closed-Cell Aluminium Foam Under Dynamic Loading, Scripta Materialia., Vol. 40, 1999, No. 8, pp. 921-927.
- [NN] www.tec.plym.ac.uk
- [NN96] Erscheinungsformen von Rissen und Brüchen metallischer Werkstoffe, Verlag Stahleisen, Düsseldorf, 1996.
- [OLU01] Olurin, O.B.; Fleck, N.A.; Ashby, M.F.: Tensile and Compressive Failure of Notched Cellular Foams, Advanced Engineering Materials, Vol. 3, 2001, No.1-2, pp. 55-58.
- [OUD83] Oudar, J.: in: High Temperature Corrosion, 1983.
- [PAR00] Park, C.; Nutt, S.R.: PM Synthesis And Properties Of Steel Foams, Materials Science and Engineering A 288, 2000, pp.111-118.
- [PAU00] Paul, A.; Ramamurty, U.: Strain Rate Sensitivity of a Closed-Cell Aluminium Foam, Materials Science and Engineering A 281, 2000, pp. 1-7.

- [PER89] Perkins, R.A.; Chiang, K.T.; Meier, G.H.; Miller, R.: Effect of Alloying, Rapid Solidification, and Surface Kinetics on the High Temperature Environmental Resistance of Niobium AFOSR Contract F49620-86-C-0018. Washington, DC: Bolling Air Force Base.
- [RAU02] Raush, G.; Banhart, J.: Making Cellular Metals from Metals other than Aluminium, "Handbook of Cellular Metals, Production, Processing, Applications", edited by Hans-Peter Degischer and Brigitte Kriszt, WILEY-VCH Verlag GmbH, 2002.
- [RIN71] Rinde, J.A.; Hoge, K.G.: Time and Temperature Dependence of the Mechanical Properties of Polystyrene Bead Foam, Journal of Applied Polymer Science, Vol. 15, 1971, pp. 1377-1395.
- [ROB01] Roberts, A.P.; Garboczi, E.J.: Elastic Moduli of Model Random Three Dimensional Closed-Cell Cellular Solids, Acta Mater., Vol. 49, 2001, pp. 189-197.
- [SÁE99] Saenz, E.; Villate, A.; Garuz, I; Irisarri, A.M.; Rausch, G; Weber, M.: Failure Mechanisms of Aluminium Foams under Compressive Loads, Proceeding International Conference on Metal foam and porous metal structures (ed. J. Banhart et al.), Bremen (Germany), 1999, pp. 269-273.
- [SAL03] Salvo, L.; Belestin, P.; Douillard, T.; Maire, E.; Jacquesson, M.; Vecchionacci, C.; Boller, E.: Structure and Mechanical Properties of AFS Sandwiches Studied in Compression Tests by In-situ X-ray Micro-tomography, Proceeding International Conference on Cellular Metals and Metal Foaming Technology: Manufacture, Properties, Applications (ed. J. Banhart et al.), Berlin, Germany, June 2003, pp. 319-324.
- [SAN92] Sang, H.; Kenny, L.D.: Process and Apparatus for Producing Shaped Slabs of Particle Stabilized Foamed Metal, European Patent EP 0587619B1, 1992.
- [SAV61] Savitsky, E.M.: The Influence of Temperature on the Mechanical Properties of Metals and Alloys, Stanfold, California, 1961.
- [SCH00] Schuetz, M.: Corrosion and Environmental Degradation Vol. I, Materials Science and Technology, Editors: Cahn; R.W., Hassen; P., Kramer; E.J., Wiley-VCH, 2000.
- [SCH88] Schatt, W.: Pulvermetallurgie, Sinter- und Verbundwerkstoffe, 3. Auflage, Deutscher Verlag für Grundstoffindustrie, Leipzig, 1988.

- [SCH91] Schuetz, M.: Die Korrosionsschutzwirkung oxidischer Deckschichten unetr thermisch-chemischer Werkstoffbeanspruchung, Materialkundliche Reihe 10, G. Petzow und F. Jeglitsch (Hrsg.), Gebrüder Borntraeger, Berlin, Stuttgart, 1991.
- [SCH97] P.-F. Scholz: Patent DE 197 16 514 C 1, Verfahren zum pulvermetallurgischen Herstellen und damit hergestellte Bauteile, 1997.
- [SHA94] Shapovalov, V.I.: Porous Metals, MRS Bulletin, Bd.19, 1994, Nr.4, pp. 24-28.
- [SIM02] Simancik, F.: The Strange World of Cellular Metals, " Handbook of Cellular Metals, Production, Processing, Applications", Ed. Hans-Peter Degischer, Brigitte Kriszt, WILEY-VCH Verlag GmbH, 2002.
- [SIM98] Simone, A.; Gibson, L.J.: The Effects Of Cell Face Curvature and Corrugations on the Stiffness and Strength of Metallic Foams; Acta Mater., Vol. 11, 1998, pp. 3929-3935.
- [SIM98a] Simone, A.E.; Gibson, L.J.: Aluminium Foams by Liquid-State Processes, Acta Metall., Vol. 46, 1998, pp. 3109-3123.
- [SMI98] Smith, H.B.; Bastaworse, A.-F.; Mumm, D.R.; Evans, A.G.: Compression Deformation and Yielding Mechanisms in Cellular Al Alloy Determined Using X-Ray Tomography and Surface Strain Mapping, Acta Mater., Vol. 46, 1998, No. 10, pp. 3583-3592.
- [SOS48] Sosnik, A.:US patent 2434775, 1948.
- [SUG97] Sugimara, Y.; Meyer, J.; He, M.Y.; Bart.Smith, H.; Grenestedt, J.; Evans, A.G.: On the Mechanical Performance of Closed Cell Al Alloy Foams, Division of Eng. and Applied Sci., Harvard University, Cambridge, 1997.
- [THÜ93] Thümmeler, F; Oberacker, R.: Introduction to Powder Metallurgy, The Institute of Materials, London, 1993.
- [VAY97] Vayman, S.; Guico, R.S.; Fine, M.E.; Manganello, S.J.: Estimation of Atmospheric Corrosion of High-Strength, Low-Alloy Steels, Metallurgical and Materials Transactions A: Physical Metallurgy and Materials Science, Vol. 28A. No. 5, 1997.

- [YAR66] Yarnton, D.: Eng. Mater. Des., 9, 83, 1966.
- [YU98] Yu, C.-J.; Eifert, H.H.; Banhart, J.; Baumeister, J.: Metal Foaming By a Powder Metallurgy Method: Production, Properties and Applications, The first Innovations in Materials Conference (Imn), Washington D.C., July 19-22, 1998.
- [ZHA02] Zhang, P.; Haag, M; Kraft, O.; Wanner, A.; Arzt, E.: Microstructural Changes in the Cell Walls of a Closed-Cell Aluminium Foam during Creep, Philosophical Magazine A, Vol. 82, No. 16, 2002, p. 2895-2907.
- [ZHU00] Zhu, H.X.; Hobdell, J.R.; Windle, A.H.: Effects Of Cell Irregularity on The Elastic Properties of Open-Cell Foams, Acta Mater., Vol. 48, 2000, pp. 4893-4900.
- [ZHU02] Zhu, H.X.; Windle, A.H.: Effects Of Cell Irregularity on the High Strain Compression of Open-Cell Foams, Acta Mater., Vol. 50, 2002, pp. 4893-4900.

Mohamed Shehata Aly

Persönliche Daten:

Familienstand: Verheiratet + 2 Kinder
Staatsangehörigkeit: ägyptisch
Geburtsdatum: 15.03.1975 in El-Giza, Ägypten

Ausbildung:

1989 –1992	Gymnasium, (Abschluß: Abitur)	El-Giza, Ägypten
1992-1997	Faculty of Eng., Cairo Uni., Mining; Petroleum and Metallurgical Dep. (Abschluß: B. Sc.)	El-Giza, Ägypten

Berufserfahrung:

Sommer 1995	Praktikum in El-Nasr Casting Company	Ägypten
Sommer 1996	Auslandspraktikum am Institut für Eisenhüttenkund (IEHK)	Aachen, Deutschland
1997 - 1998	Wissenschaftlicher Mitarbeiter am Central Metallurgical Research and Development Institut (CMRDI)	Helwan, Ägypten
Ende 1998	Stipendiat der ägyptischen Regierung für Promotion an der RWTH Aachen University	Aachen, Deutschland
July1999 - October 1999	Deutsch Kurse am Goethe Institut, Bonn	Bonn, Deutschland
October 1999 - Februar 2002	Masterstudiengang Metallurgie und Werkstofftechnik an der RWTH Aachen University	Aachen, Deutschland
Februar 2002	Abschluß: M. Sc. in Metallurgie und Werkstofftechnik	Aachen, Deutschland
Ab März 2003	Stipendiat am Institut für Eisenhüttenkunde.	Aachen, Deutschland